

DOTTORATO DI RICERCA IN
FISICA

Ciclo XXXI

Settore Concorsuale: 02/A1 - FISICA Sperimentale delle interazioni fondamentali

Settore Scientifico Disciplinare: FIS/01 - FISICA Sperimentale

TITOLO TESI

Production and nuclear modification factors of pions, kaons and protons in pp and AA collisions at the LHC

Presentata da: Nicolò Jacazio

Coordinatore Dottorato

Silvia Arcelli

Supervisore

Luisa Cifarelli

Co-supervisore

Francesca Bellini

Esame finale anno 2019

Production and nuclear modification factors of pions, kaons and protons in pp and AA collisions at the LHC

Author: **Nicolò Jacazio**

Supervisor: Prof. Luisa Cifarelli

Advisor: Dr. Francesca Bellini

Department of Physics and Astronomy
Bologna University

This dissertation is submitted for the degree of
Doctor of Philosophy

April 2019

A tutti i miei nonni e a chi prima di loro ha combattuto compiendo sacrifici e fatiche nella
speranza di un mondo migliore.

Acknowledgements

I would like to thank all the people who accompanied me during my adventure. I especially owe all my colleagues who helped me, through endless and boring (for them) discussions, to discover new points of view and understand the real essence of science. I thank Biella for being the proof that with time and sacrifice anything can be done and undone. I thank my supervisor Prof. Luisa Cifarelli and co-supervisor Dr. Francesca Bellini, for helping me write this work by steering my efforts in the right way. I would like to warn the reader that there is no special order in the list of people I will thank below, anyway I would like to apologize in advance as I surely missed someone. Please, do not take this the wrong way as I could not possible fit everyone in one thesis alone. I thank Roberto, Pietro, Francesco, Manuel, Andrea, Francesca, Gilda, Rosario, Maximiliano, Federico, Luigi, Matteo, Anastasia, Nico, Luca, Stefano, Fabrizio, Alexander, Riccardo, Massimo, Stefania, Ivan, Livio, Giacomo for all the wonderful time they shared with me. I would also like to thank my family for all the support and patience that they have shown in the last 29 years. Finally I thank Giulia, who was always there when I needed help.

Thank to all of you. I wish I could someday repay your kindness.

Ringraziamenti

Vorrei ringraziare tutte le persone che mi hanno accompagnato durante la mia avventura. Sono infinitamente debitore di tutti i miei colleghi che mi hanno aiutato, tramite interminabili e noiose (per loro) discussioni, a scoprire nuovi punti di vista e a carpire la vera essenza della scienza. Ringrazio la mia Biella per esser prova vivente del fatto che tramite il sacrificio e il giusto tempo, tutto può esser fatto e disfatto. Ringrazio il mio relatore Prof. Luisa Cifarelli e correlatore Dr. Francesca Bellini, per avermi aiutato a completare questo lavoro indirizzando i miei sforzi nel modo più produttivo. Avverto il lettore che non esiste alcun ordine preciso nella lista delle persone citate di seguito, ad ogni modo, mi scuso in anticipo in quanto sicuramente avrò omesso qualcuno. Vi prego di non prendere questa cosa troppo sul serio, in quanto il compito di contenere tutti in un'unica tesi si rivela particolarmente difficile. Ringrazio Maximiliano, Manuel, Alexander, Massimo, Francesco, Giacomo, Gilda, Federico, Andrea, Francesca, Livio, Luigi, Roberto, Rosario, Nico, Pietro, Matteo, Luca, Anastasia, Riccardo, Stefania, Stefano, Ivan, Fabrizio per tutto il tempo che mi hanno dedicato. Colgo l'occasione per ringraziare la mia famiglia per tutto il supporto e la pazienza che hanno dimostrato negli ultimo 29 anni. Per ultima cosa (ma non per questo meno importante) ringrazio Giulia, che sempre è stata presente quando avevo bisogno di aiuto.

Un sincero grazie a tutti voi. Mi auguro di poter un giorno ricambiare la vostra gentilezza.

Abstract

In heavy-ion collisions at relativistic energies, a deconfined strongly-interacting state of matter is created. The elementary degrees of freedom of this state are the ones of Quantum Chromodynamics (QCD), namely quarks and gluons, hence its name Quark-Gluon Plasma (QGP). At the CERN Large Hadron Collider (LHC), protons and heavy-ions are accelerated at the highest energies ever achieved in the laboratory. The detector of A Large Ion Collider Experiment (ALICE) at the LHC, was especially designed to study the physics of the QGP produced in heavy-ion collisions. The extensive Particle IDentification (PID) capabilities of the ALICE detector allow for the study of a wide set of observables related to particle production mechanisms and sensitive to the properties and the evolution of the QGP. The “bulk” of the produced particles is constituted by hadrons containing only the “light” flavor quarks, u , d and s . Most of these hadrons are produced at low transverse momentum (p_T) and originate from soft QCD processes. In this work, the production of π^\pm , K^\pm , p and \bar{p} has been measured in Pb–Pb collisions at $\sqrt{s_{\text{NN}}} = 5.02$ TeV and in inelastic pp collisions at $\sqrt{s} = 5.02$ TeV. To this end, the excellent PID performance of the ALICE Time-Of-Flight detector (TOF) was exploited. The p_T spectra of pions, kaons and protons have been measured in a wide momentum range (from about 100 MeV/ c to 12 GeV/ c) and as a function of centrality. Based on these fundamental measurements, it was possible to characterize the medium formed in the collision. Particle production at low p_T exhibits features typical of the collective evolution of a strongly interacting medium. At this energy the largest radial flow velocity is observed. The thermal properties of the medium can be accessed by studying the relative particle abundances in the framework of Statistical Hadronization Models. The Nuclear Modification Factor was computed to quantify the effect of parton energy loss in the QGP on high- p_T particle production. The results are interpreted in comparison to predictions from state-of-the-art models and to similar measurements at the LHC.

Introduction

The subject of this thesis is the study of the production of $\pi^+ + \pi^-$, $K^+ + K^-$, p and \bar{p} in proton-proton (pp) and lead-lead (Pb–Pb) collisions at the Large Hadron Collider (LHC). This measurement is carried out with the detector of the A Large Ion Collider Experiment, especially designed to cope with the large number of particles created in a typical collision between heavy nuclei, accelerated at relativistic energies.

The ultimate goal of heavy-ion physics is the study of the properties of the Quark-Gluon Plasma (QGP), a de-confined state of matter made of (quasi-)free quark and gluons and in which chiral symmetry is restored. The presence of a de-confined phase manifests itself with typical signatures that can be quantified by studying particle production. In particular, the measurement of identified particles provides a unique way to gain insight into the physical properties of the medium and the underlying processes at play. In late 2015, the ALICE Collaboration recorded Pb–Pb collisions at the highest energy ever achieved in the laboratory ($\sqrt{s_{\text{NN}}} = 5.02$ TeV), allowing for the quantitative comparison with measurements performed at lower energies. The ALICE experiment, thanks to its excellent tracking performance coupled with extensive Particle IDentification (PID) capabilities, is particularly well suited for the study of identified hadron production over a wide range of transverse momentum. This is achieved by combining multiple techniques that allow one to perform hadron identification at mid-rapidity starting from transverse momentum $p_T = 100$ MeV/ c and up to $p_T = 12$ GeV/ c .

The first and second chapters of this work are dedicated to the physics of heavy-ion collisions and the observables that can be used to access the dynamic and thermal properties of the QGP. The second chapter is focused on the light flavor hadron production and motivates the study carried out in this thesis.

The ALICE detector and the sub-systems used for the measurements reported in this work are described in the third chapter. The studies reported in this thesis are based on the Particle IDentification with the ALICE Time-Of-Flight detector (TOF), of which a detailed description is given in the forth chapter.

The fifth chapter is dedicated to the study of the performance of TOF during the years 2015 to 2018. This chapter also includes a description of the calibration procedure, crucial

to guarantee optimal PID performance to be exploited for the measurement of light flavor hadrons. In addition, the chapter includes a concise report on the hardware and software developments carried out in view of the upgraded phase of the LHC (Run 3 and Run 4, from 2021 to 2029). In particular, the studies concerning the aging of the detector and the tolerance to the high interaction rate expected in Run 3 and Run 4 are discussed.

The last two chapters contain the analysis details and the results, including the estimation of the systematic uncertainties. The original measurement using TOF PID of the p_T spectra of pions, kaons and protons in Pb–Pb and pp collisions at $\sqrt{s_{NN}} = 5.02$ TeV, is presented in this thesis. The results of this analysis are combined with the ones obtained with other PID techniques and discussed in the seventh chapter. The evolution of the particle ratios as a function of collision energy and centrality is discussed. The ratio between p_T -integrated particle yields are measured and compared to different collision energies as well as proton-proton and proton-lead collisions. The nuclear modification factors (R_{AA}) are computed and compared with results obtained at lower energy to study how parton energy loss in the QGP medium is affected by the increase in collision energy. Ratios of particle yields and their energy (in)dependence are discussed in the framework of statistical hadronization models. The measured spectra are also compared with state-of-the-art predictions from models based on relativistic hydrodynamics (IP-Glasma, MUSIC) and using a transport model approach (UrQMD) to describe re-scattering in the hadronic phase. Moreover, results from a simultaneous fit with the Boltzmann-Gibbs Blast-Wave model to the pion, kaon and proton p_T distributions are compared with those obtained in Pb–Pb collisions at $\sqrt{s_{NN}} = 2.76$ TeV as well as in pp and p–Pb collisions, in order to quantify radial flow from small to large systems.

Table of contents

Abstract	ix
Introduction	xi
List of figures	xvii
List of tables	xxvii
Nomenclature	xxix
1 Nuclear physics at high energies	1
1.1 Quantum Chromodynamics	1
1.1.1 Running coupling constants	2
1.1.2 The phase diagram of the QCD	4
1.1.3 Colliding extended objects: the collision centrality	7
1.2 The Quark-Gluon Plasma	8
1.2.1 Time evolution of the QGP	15
2 Probing the QGP with light flavor particles	17
2.1 Thermal models of particle production	18
2.1.1 Strangeness enhancement	24
2.2 The collective flow	28
2.2.1 The Boltzmann-Gibbs Blast-Wave model	35
2.2.2 Anisotropic flow	38
2.3 pp collisions: more than a reference for heavy-ions	40
2.3.1 The Nuclear Modification Factor	41
2.3.2 From large to small systems: pp collisions vs multiplicity	45

3 A Large Ion Collider Experiment	51
3.1 The ALICE detector	52
3.1.1 The Inner Tracking System (ITS) detector	56
3.1.2 The Time Projection Chamber (TPC) detector	57
3.1.3 The Time-Of-Flight (TOF) detector	59
3.1.4 The High Momentum Particle IDentification (HMPID) detector . .	60
3.1.5 Forward detectors	60
3.2 Particle Identification in ALICE	62
3.2.1 Topological identification and decay reconstruction	66
3.3 Event characterization and selection in ALICE	69
3.3.1 Trigger selection	69
3.3.2 Centrality estimation	70
3.4 Data flow, reconstruction and simulation	72
4 The ALICE Time-Of-Flight detector	77
4.1 Timing resolution requirements for detector design	77
4.2 The Multigap Resistive Plate Chamber technology	81
4.3 Experimental setup	86
4.3.1 Detector readout	90
5 Performance of the ALICE Time-Of-Flight detector in Run 2 and preparation for Run 3	95
5.1 Reconstruction and calibration	95
5.1.1 Track matching	96
5.1.2 Time calibration procedure	98
5.1.3 Event time determination	101
5.2 PID performance of the TOF detector	106
5.2.1 TOF detector calibration in Run 2	107
5.2.2 Signal shape of the TOF detector	110
5.2.3 PID separation power	111
5.2.4 Standards for the Quality Assurance of data	111
5.3 Developments for Run 3	117
5.3.1 Detector stability during Run 1 and Run 2	118
5.3.2 Effects of the TPC calibration on the TOF performance	121
5.3.3 The new TOF geometry in the O ²	123

6 Description of the TOF analysis details	133
6.1 Data sample	134
6.1.1 Pb–Pb and pp data samples	135
6.1.2 Monte Carlo samples	135
6.1.3 Event selections	135
6.1.4 Track selection	139
6.2 Particle identification with TOF	142
6.2.1 TOF signal description	143
6.2.2 Mismatch parameterization	148
6.2.3 Yield extraction	148
6.2.4 Contamination from feed-down	157
6.3 Acceptance and efficiency corrections	161
6.3.1 Tracking efficiency	163
6.3.2 Matching efficiency	170
6.4 Systematic uncertainties	184
6.4.1 Data sample and track selection	185
6.4.2 Particle identification	188
6.4.3 Feed-down and fraction of primary particles	190
6.4.4 TPC-TOF matching	190
6.4.5 Material budget	190
6.4.6 Total systematic uncertainty	197
7 Results and discussion	199
7.1 Transverse momentum distributions of π , K and p measured with the TOF detector	199
7.2 Combined π , K and p spectra	200
7.2.1 Model comparison of the spectra	208
7.3 Nuclear modification factor	212
7.4 p_T -integrated yields, ratios and average p_T	215
7.4.1 Interpretation of the results in the SHM	218
8 Conclusions	223
References	225
Appendix A Entropy, partition functions and global observables	235
Appendix B Partition function for the Grand-Canonical ensemble	241

Appendix C The Cooper-Frye formula	245
Appendix D The TOF Quality Assurance	247
Appendix E Efficiency in pp collisions at $\sqrt{s} = 5.02$ TeV	259
Appendix F Cut variation in pp collisions	265
Appendix G PID variation in pp collisions	267
Appendix H Systematic uncertainties in pp	269

List of figures

1.1	Bosons and fermions of the Standard Model	2
1.2	α_s as a function of the energy scale	5
1.3	QCD phase diagram	6
1.4	Glauber Monte Carlo simulation of a Au–Au collision	8
1.5	Correlation between centrality and charged particle multiplicity	9
1.6	Charged-particle pseudorapidity density as measured for a large η range in centrality classes in Pb–Pb collisions at $\sqrt{s_{\text{NN}}} = 5.02$ TeV [1].	10
1.7	Energy density scaled to T^4 as obtained from lattice QCD calculations . . .	11
1.8	ε_{Bj} for different collision centrality classes as obtained in Au–Au collisions	12
1.9	$\frac{dE_T}{d\eta}/\frac{dN_{\text{ch}}}{d\eta}$ for different collision centrality classes as obtained in Au–Au collisions	13
1.10	$2 \langle dN_{\text{ch}}/d\eta \rangle / \langle N_{\text{Part}} \rangle$ as measured in Pb–Pb collisions at $\sqrt{s_{\text{NN}}} = 5.02$ TeV	14
1.11	QGP evolution in a Minkowski-like plane	16
2.1	Hadron yields (dN/dy) at mid-rapidity for different particle species as measured in central AA collisions	22
2.2	Hadron multiplicities as measured in central Pb–Pb collisions	23
2.3	K/π and p/π ratios as obtained from thermal model	24
2.4	QCD phase diagram with data points as obtained at different energies from the thermal model; Evolution of the temperature T_{Ch} and the μ_B as a function of the $\sqrt{s_{\text{NN}}}$	25
2.5	Strangeness suppression factor	26
2.6	Time evolution of the relative strange-quark to baryon-number abundances .	27
2.7	Enhancement of ϕ , Λ , Ξ , and Ω^- as measured in Pb–Pb collisions at $\sqrt{s_{\text{NN}}} = 2.76$ TeV with respect to the pp reference yields [2]. The enhancement of the ϕ meson is also shown as measured in Au–Au collisions at $\sqrt{s_{\text{NN}}} = 200$ GeV.	28

2.8	Yield enhancement factor per participating nucleon as measured in Pb–Pb 158 AGeV collisions	29
2.9	Calculation of the m_T spectra for different particle species with non zero flow	33
2.10	m_T spectra of π^- , K^- and \bar{p} as measured at $(\sqrt{s})\sqrt{s_{NN}} = 200$ GeV in pp and central Au–Au collisions	33
2.11	π^\pm , K^\pm , p , \bar{p} spectra $\langle p_T \rangle$ as measured in Pb–Pb collisions at $\sqrt{s_{NN}} =$ 2.76 TeV and Au–Au collisions at $\sqrt{s_{NN}} = 200$ GeV	34
2.12	p_T -dependent spectra of π^\pm , K^\pm , p and \bar{p} spectra as measured in different centrality classes in $\sqrt{s_{NN}} = 2.76$ TeV	36
2.13	Temperature of kinetic freeze-out and expansion velocity as obtained from the BGBW combined fit to the π^\pm , K^\pm , p and \bar{p} spectra measured in Pb–Pb collisions at $\sqrt{s_{NN}} = 2.76$ TeV and Au–Au collisions at $\sqrt{s_{NN}} = 200$ GeV	37
2.14	Comparison of the expansion velocity as obtained from the combined BGBW fit	38
2.15	Fireball that follows a peripheral collision represented in the collision Reaction Plane [3].	39
2.16	Characteristic shape related to each component of the anisotropic flow given in Eq. 2.16.	40
2.17	Centrality dependence of v_2 for π^\pm , K^\pm , p and \bar{p} , $\bar{\Lambda}$, K_S^0 , and the ϕ -meson [4].	41
2.18	Charged multiplicity multiplicity density $dN_{ch}/d\eta$ measured at mid-rapidity as a function of the collision energy	42
2.19	Nuclear modification factors measured by ALICE in central (0 – 5%) and peripheral (70 – 80%) Pb–Pb collisions and in p–Pb collisions at $\sqrt{s_{NN}} =$ 5.02 TeV [5].	44
2.20	Multiplicity distribution as measured in p–Pb collisions at $\sqrt{s_{NN}} = 5.02$ TeV compared to the distribution obtained in pp collisions at $\sqrt{s} = 7$ TeV [6]. The dashed lines mark the 80% and the 60% percentile of the p–Pb cross-section.	46
2.21	$\Delta\eta - \Delta\phi$ angular correlation	47
2.22	p_T -integrated yield ratios of strange and multi-strange hadrons to $\pi^+ + \pi^-$ and spectra of identified particles $\pi^+ + \pi^-$, $K^+ + K^-$, $p + \bar{p}$, K_S^0 , $\Lambda + \bar{\Lambda}$, $\Xi^- + \Xi^-$, $\Omega + \bar{\Omega}$, ϕ , K^* as measured in pp collisions at $\sqrt{s} = 7$ TeV	49
2.23	$p/(\pi^+ + \pi^-)$ and $(\Lambda^0 + \bar{\Lambda}^0)/(2K_S^0)$ ratios as a function of $\langle dN_{ch}/d\eta \rangle$ in pp collisions at $\sqrt{s} = 7$ TeV and double ratios $h/(\pi^+ + \pi^-)$ over $h/(\pi^+ + \pi^-)$ in MB collisions.	50
3.1	The LHC facility	53
3.2	Layout of the ALICE detector in Run 2	54

3.3	ITS	56
3.4	Schematics of the TPC detector	58
3.5	Schematics of the TOF detector	60
3.6	Schematics of the HMPID detector	61
3.7	Layout of the ZDC on the A side	61
3.8	Layout of the detectors located at forward rapidity close to the IP. The two arrays of the V0 detector are visible as grey disks. The two arrays forming the T0 detector are shown as blue cylinders around the beam pipe. V0A and T0A (V0C and T0C) are located on the left (right) side of the figure.	62
3.9	Performance of the ALICE detectors used in Particle IDentification	64
3.10	PID separation power measured in units of σ obtained by using different techniques available in ALICE	65
3.11	Example of statistical unfolding used for particle identification	66
3.12	Combined PID with signals from both TPC and TOF detectors	67
3.13	Representation of the secondary vertices reconstruction procedure	68
3.14	Invariant mass distribution of kink-decay daughters under the assumption of a decay in the muon and neutrino channel	68
3.15	Integrated and instantaneous luminosity collected during Run 2	71
3.16	Correlation between V0 amplitude (multiplicity at forward rapidity) and number of hits in SPD (multiplicity at mid-rapidity) as measured in p–Pb and Pb–Pb collision.	72
3.17	Distribution of the V0 amplitude	73
3.18	ZDC/ZEM signal correlation	73
3.19	Collection workflow of the running conditions of the ALICE detectors	74
4.1	Cross section of the ALICE apparatus	78
4.2	Particle separation in TOF	80
4.3	Gas gap for a RPC	81
4.4	Representation of the design of the ALICE TOF MRPC	82
4.5	Detail of the construction of a TOF MRPC	83
4.6	Avalanche footprint	84
4.7	Detector schematics of the double stack MRPC	85
4.8	Example of a module of the ALICE TOF detector	87
4.9	Layout of the ALICE TOF detector	88
4.10	Design blueprints [7] of the (a) central module and (b) region of interface between the intermediate and external TOF modules.	89

5.1	Data reconstruction workflow of the ALICE experiment	96
5.2	TPC-TOF matching efficiency as computed in Monte Carlo and real data . .	98
5.3	Global offset for TOF calibration	99
5.4	Time slewing effect	100
5.5	(a) Correlation between the ToT and the measured time for the single TOF channel 37833. Two parameterization of the behaviour are reported: the dashed line indicates a 5th-order polynomial (Run 1 situation), the solid line represents the point-by-point spline parameterization (Run 2 situation). (b) Distribution of the measured times before and after the time-slewing correction.	100
5.6	Calibration stability	102
5.7	Efficiencies of the different event time evaluation methods t_{ev}^{TOF} (circles), t_{ev}^{TOF} (squares) and t_{ev}^{Best} (diamond) [8]. (a) As a function of the charged particle multiplicity reaching TOF, measured in pp collisions at $\sqrt{s} = 7 \text{ TeV}$. (b) As a function of the Centrality class for Pb–Pb collisions $\sqrt{s_{\text{NN}}} = 2.76 \text{ TeV}$. .	105
5.8	TOF signal resolution for pion tracks with $0.95 < p < 1.05 \text{ GeV}/c$ as a function of the multiplicity of charged tracks matched as obtained from Run 1 p–Pb collisions during Run 1 [9]. The inset shows the TOF signal distribution for events with track multiplicity reaching TOF greater than 20. .	107
5.9	Resolution with standard and improved resolution	108
5.10	Event time resolution during Run 2 with the improved TOF time-slewing calibration.	109
5.11	Comparison between $\sigma_{t_{ev}^{\text{TOF}}}$ in Run 1 and Run 2	109
5.12	The impact of the improved resolution on the PID is depicted together with lines at 2 and 3 σ	110
5.13	Particle velocity as a function of the track momentum	112
5.14	Distribution of the particle velocity β as measured with the TOF detector .	113
5.15	Example of residual difference between the position of the extrapolated track and the position of the matched TOF cluster along the z direction as measured in 2015 in Pb–Pb collisions at $\sqrt{s_{\text{NN}}} = 5.02 \text{ TeV}$ (a) and pp collisions at $\sqrt{s} = 5.02 \text{ TeV}$ (b).	114
5.16	Mean resolution	115
5.17	TOF $n\sigma$ for pions, kaons and protons	116
5.18	New DRM2 board designed to replace the DRM in Run 3 [10].	118
5.19	TOF cosmic trigger rate	119
5.20	Total TOF current as a function of the charged particle load	120

5.21 TPC-TOF matching efficiency as a function of p_T , as measured in p–Pb collisions during Run 1 and Run 2. The agreement of the two matching efficiencies is crucial to reproduce the detector response.	120
5.22 Words per crate as a function of the interaction rate (IR) in pp collisions at $\sqrt{s} = 13$ TeV and compared to the equivalent IR in Pb–Pb collisions at $\sqrt{s_{\text{NN}}} = 5.5$ TeV.	122
5.23 Matching residuals between the TOF matched cluster and the position of the track in the z direction as a function of the strip index for (a) simulation in which the TPC v_{drift} is increased by 10%, (b) simulation in which the TPC v_{drift} is decreased by 10% and (c) TPC v_{drift} determined by the online calibration.	124
5.24 Distribution of the <i>time-of-flight</i> measured with t_{ev}^{Fill} (event time given by the bunch crossing time) as a function of the strip index for (a) +10% TPC v_{drift} , (b) -10% TPC v_{drift} and (c) TPC v_{drift} determined by the online calibration.	125
5.25 Full SM (a) and SM without the central module (b) of the TOF detector modelization implemented in the new O ² framework.	126
5.26 Full representation of the TOF detector in the O ² framework. In blue are represented the crates located at both ends of each SM.	126
5.27 Spatial distribution of the particle hits in a MC simulation using the new TOF geometry in the ALICE O ² framework. Three dimensional representation (a) and radial distribution (b).	127
5.28 Spatial distribution of the particle hits in a MC simulation using the new TOF geometry in the ALICE O ² framework.	128
5.29 Representation of the neural network used for the analysis of mismatched tracks. On the left side are located the input neurons, on the right side there is the response neuron used for the classification.	128
5.30 Value of the network response for correctly matched tracks (in blue) and mismatched tracks (in red).	129
5.31 (a) Efficiency and (b) residual contamination in the track sample tagged as correct match with different cuts on the value of the network response.	131
5.32 β distribution measured with the TOF detector as a function of the track momentum for unselected, correctly matched and mismatched tracks and for the tracks tagged as correct match and mismatch with the neural network, see text for details.	132

6.1 (a) Correlation between the sum and difference of signal times in V0A and V0C as measured in pp collisions at $\sqrt{s} = 7$ TeV [11]. Background events from Beam 1 and background events from Beam 2 can be seen at (-14.3 ns, -8.3 ns) and (14.3 ns, 8.3 ns) respectively. (b) Correlation between SPD clusters and reconstructed SPD tracklets [11]. Two bands are visible, they correspond to the genuine collisions and machine induced background. The dashed line represents the cut used in the offline selection: events lying in the region above the line are tagged as background and rejected.	137
6.2 Correlation between the sum and the difference of times recorded by the neutron ZDCs on either side (ZNA and ZNC) in Pb–Pb collisions at $\sqrt{s_{\text{NN}}} = 2.76$ TeV [11]. Genuine collisions between ions in the nominal bunch of both beams correspond to the large cluster centered at (0 ns, 760 ns). The small clusters distributed along the diagonals correspond to collisions in which one of the ions is displaced by one or more bunches.	138
6.3 Number of events analyzed in pp and Pb–Pb collisions	138
6.4 Events per centrality class	139
6.5 TPC readout segmentation	141
6.6 TOF signal parameterization	143
6.7 Variation of the TOF signal parameterization	144
6.8 (a) σ and (b) τ parameters as a function of p_{T} . The parameters are obtained by fitting the $t_{\text{TOF}} - t_{\text{exp},\pi} - t_{\text{ev}}$ distributions in every p_{T} interval with the TOF signal function described in Eq. 5.13.	146
6.9 Distribution of TOF signal under the pion mass hypothesis for different p_{T} intervals fitted with the Gaussian with exponential tail function described in Eq. 5.13. The parameters of the fit are reported for each transverse momentum interval in each figure. The limits of the fitting range are shown with blue lines. In figure (c) and (d) the peaks of kaons and protons are visible.	147
6.10 TOF times measured per channel	149
6.11 Extraction of the TOF signal parameters	151
6.12 Distribution of $t_{\text{MC}} - t_{\text{ev}} - t_{\text{exp},i}$ under the hypothesis of pion	154
6.13 $n\sigma$ separation in TOF, under the pion hypothesis	155
6.14 Example of yield extraction fit in central Pb–Pb	156
6.15 Combined TPC-TOF signals for π and p	158
6.16 DCA _{xy} distribution measured for π and for p	159
6.17 Primary fraction for π^+	160
6.18 Primary fraction for different centrality classes	161

6.19 Primary fraction for different centrality classes, ratio to MB	162
6.20 Tracking efficiency for both positive and negative π , K and p in MB Pb–Pb collisions	165
6.21 Tracking efficiency for both positive and negative π , K and p in MB pp collisions	166
6.22 Tracking efficiency of π in Pb–Pb collisions as a function of the centrality .	167
6.23 Tracking efficiency of K in Pb–Pb collisions as a function of the centrality .	168
6.24 Tracking efficiency of p in Pb–Pb collisions as a function of the centrality .	169
6.25 Matching efficiency for both positive and negative π , K and p in MB Pb–Pb collisions	171
6.26 Matching efficiency for both positive and negative π , K and p in MB pp collisions	172
6.27 Matching efficiency of π in Pb–Pb collisions as a function of the centrality .	174
6.28 Matching efficiency of K in Pb–Pb collisions as a function of the centrality .	175
6.29 Matching efficiency of p in Pb–Pb collisions as a function of the centrality .	176
6.30 Matching efficiency for unidentified positive and negative particles for real data and Monte Carlo	177
6.31 Matching efficiency for unidentified positive and negative particles for real data and Monte Carlo	178
6.32 Matching efficiency in Pb–Pb collisions at $\sqrt{s_{\text{NN}}} = 5.02$ TeV for identified π^\pm , K^\pm , p and \bar{p} in Monte Carlo and real Data as a function of p_T	180
6.33 Matching efficiency in pp collisions at $\sqrt{s} = 5.02$ TeV	181
6.34 GEANT3/GEANT4 correction for \bar{p} as a function of p_T	183
6.35 Signal loss for identified particles	184
6.36 Ratio between the spectra obtained with modified track selection criteria in Pb–Pb collisions	187
6.37 Ratio between the spectra obtained with modified TOF response parameters in Pb–Pb collisions	189
6.38 Ratio between the primary particle fraction obtained with the <i>TFractionFitter</i> (TFF) utility and the one obtained with <i>RooFit</i> in MB Pb–Pb collisions	191
6.39 Ratio between the primary particle fraction obtained with the <i>TFractionFitter</i> (TFF) utility and the one obtained with <i>RooFit</i> in MB pp collisions	192
6.40 Ratio to the default case of the tracking efficiency as obtained in simulations with modified material budget.	194
6.41 Ratio to the default case of the TPC-TOF matching efficiency as obtained in three simulations with modified material budget.	195

6.42 Maximum deviation from unity, obtained from the comparison of the tracking and matching efficiencies, evaluated in simulations with modified material budget.	196
6.43 Systematic uncertainty on the particle spectra in Pb–Pb collisions	198
7.1 Spectra for π^\pm, K^\pm, p and \bar{p} as obtained in pp and Pb–Pb collisions	201
7.2 $\pi^+/\pi^-, K^+/K^-$ and p/\bar{p} ratios for corrected spectra as obtained in Pb–Pb collisions	202
7.3 Comparison between the combined spectra for charged kaons and the single analyses.	203
7.4 Spectra for $\pi^+ + \pi^-, K^+ + K^-, p + \bar{p}$ as obtained in Pb–Pb collisions	205
7.5 Combined spectra in pp collisions at $\sqrt{s_{\text{NN}}} = 5.02$ TeV	206
7.6 Ratio of the spectra of kaons and protons to the ones of pions as a function of p_T as measured in Pb–Pb collisions at $\sqrt{s_{\text{NN}}} = 5.02$ TeV (this work) and at $\sqrt{s_{\text{NN}}} = 2.76$ TeV for several centrality classes.	207
7.7 Ratio of the spectra of kaons and protons to the ones of pions as a function of p_T as measured in pp collisions at $\sqrt{s} = 5.02$ TeV (this work), $\sqrt{s} = 2.76$ TeV [12], $\sqrt{s} = 7$ TeV [13] and $\sqrt{s} = 13$ TeV.	208
7.8 Ratio between the measured particle spectra and the result of the simultaneous BGBW fit to π, K and p as obtained in Pb–Pb collisions at $\sqrt{s_{\text{NN}}} = 5.02$ TeV for several centrality classes.	209
7.9 (a) Kinetic freeze-out temperature T_{Kin} , (b) expansion velocity $\langle \beta_T \rangle$ and (c) expansion velocity profile n parameters obtained from the simultaneous fit to the π, K and p spectra in several collision systems as a function of the pseudorapidity density of charged particles $\langle dN_{\text{ch}}/d\eta \rangle$	210
7.10 Correlation between the T_{Kin} and $\langle \beta_T \rangle$ parameters for different collision systems and different charged particle density. The color scale corresponds to the pseudorapidity density of charged particles $\langle dN_{\text{ch}}/d\eta \rangle$. The contour represents the 1σ interval defined by the fit procedure.	211
7.11 Identified particle spectra as a function of p_T as measured in three different centrality classes and compare to the prediction of theoretical models.	213
7.12 Particle spectra of kaons and protons scaled to the one of pions as a function of p_T as measured in three different centrality classes and compare to the prediction of theoretical models.	214
7.13 Nuclear Modification Factor of π, K and p measured as a function of p_T in several centrality intervals of Pb–Pb collisions at $\sqrt{s_{\text{NN}}} = 5.02$ TeV.	215

7.14 Nuclear Modification Factor of π , K and p measured in Pb–Pb collisions at $\sqrt{s_{\text{NN}}} = 5.02$ TeV and $\sqrt{s_{\text{NN}}} = 2.76$ TeV for several centrality intervals.	216
7.15 (a) Integrated particle yields normalized to $\langle N_{\text{Part}} \rangle$ as a function of $\langle N_{\text{Part}} \rangle$ as measured in pp and Pb–Pb collisions at $\sqrt{s_{\text{NN}}} = 5.02$ TeV. A fit with a logarithm function is added to guide the eye. (b) Ratio of $\langle dN/dy \rangle / \langle N_{\text{Part}} \rangle$ to the value measured in pp collisions.	217
7.16 $\langle dN/dy \rangle$ for kaons (a) and protons (b) relative to pion yields as a function of $\langle dN_{\text{ch}}/d\eta \rangle$ in Pb–Pb collisions at $\sqrt{s_{\text{NN}}} = 5.02$ TeV (this work) compared to several collision systems.	219
7.17 $\langle dN/dy \rangle$ for kaons and protons relative to pion yields measured as a function of the collision energy in MB pp collisions.	220
7.18 $\langle p_T \rangle$ for π , K and p in pp collisions at $\sqrt{s} = 5.02$ TeV, Pb–Pb collisions at $\sqrt{s_{\text{NN}}} = 2.76$ TeV and $\sqrt{s_{\text{NN}}} = 5.02$ TeV.	220
7.19 Grand canonical (GC) equilibrium and non equilibrium thermal fit to identified light hadron and (hyper-)nuclei yields measured in 0-10% central Pb–Pb collisions at $\sqrt{s_{\text{NN}}} = 5.02$ TeV. Three different implementations of the SHM are used. The yield of K^* is not included in the fit.	221
D.1 Track Properties	248
D.2 TOF time	248
D.3 TOF resolution	249
D.4 t_{ev} vs Multiplicity	249
D.5 T0 Detector	250
D.6 Start Time Resolution	251
D.7 Start Time Methods	251
D.8 Profile DZ vs Strip Number	252
D.9 PID sigmas Start Time	252
D.10 PID sigmas	253
D.11 PID	253
D.12 PID Expected Times	254
D.13 Matching Efficiency	254
D.14 Matching Efficiency Summary	255
D.15 Peak Difference Time Vs Run	255
D.16 Resolution	256
D.17 Resolution	256
D.18 Resolution	257

E.1	Tracking efficiency in pp collisions at $\sqrt{s} = 5.02$ TeV for identified π^\pm, K^\pm , p and \bar{p} as a function of p_T	260
E.2	Tracking efficiency in pp collisions at $\sqrt{s} = 5.02$ TeV for identified π^\pm, K^\pm , p and \bar{p} as a function of p_T	261
E.3	Matching efficiency in pp collisions at $\sqrt{s} = 5.02$ TeV for identified π^\pm, K^\pm , p and \bar{p} as a function of p_T	262
E.4	Matching efficiency in pp collisions at $\sqrt{s} = 5.02$ TeV for identified π^\pm, K^\pm , p and \bar{p} as a function of p_T	263
F.1	Ratio between the spectra obtained with modified track cuts in pp collisions	266
G.1	Ratio between the spectra obtained with modified TOF signal parameters in pp collisions	268
H.1	Systematic uncertainty on the particle spectra in pp collisions	270

List of tables

3.1	Collision energy and collision systems of Run 1 and Run 2	52
3.2	ITS layers	57
3.3	Gases used in the ALICE TPC	58
4.1	Characteristics of the TOF modules	88
4.2	Amount of components of the TOF	94
6.1	Summary of the cuts used to select the track sample. These include selection on the reconstruction quality, acceptance and TPC-TOF matching. See text for details.	140
6.2	Summary of the cut variation used to select the track sample.	186
7.1	π , K and p p_T -ranges in GeV/c used by the different analyses in Pb–Pb analysis.	203
7.2	π , K and p p_T -ranges in GeV/c used by the different analyses in pp analysis.	203

Nomenclature

Acronyms / Abbreviations

LS 1 Long Shutdown 1

LS 2 Long Shutdown 2

LS 3 Long Shutdown 3

ACM Auxiliary Control Module

AGS Alternating-Gradient Synchrotron

ALICE A Large Ion Collider Experiment

ASIC Application-specific integrated circuit

BES Beam Energy Scan

BGBW Boltzmann-Gibbs Blast-Wave

BNL Brookhaven National Laboratory

BP Beam Pipe

CERN European Organization for Nuclear Research

CMS Compact Muon Solenoid

CPDM Clock and Pulser Distribution Module

CTP Central Trigger Processor

CTTM Cosmic and Topology Trigger Module

DAQ Data Acquisition

DCA Distance of Closest Approach
DCS Detector Control System
DDL Detector Data Link
DQM Data Quality Monitor
DRM2 Data Readout Module 2
DRM Data Readout Module
FAIR Facility for Antiproton and Ion Research
FEAC Front End Analogue Control
FEA Front End Analogue
FEE Front End Electronics
FIFO First In First Out
FPGA Field-Programmable Gate Array
GSI Helmholtz Centre for Heavy Ion Research
HLT High Level Trigger
HMPID High Momentum Particle IDentification
HPTDC High Performance TDC
IP Interaction Point
IR Interaction Rate
ITS Inner Tracking System
ITSsa ITS stand-alone
LEP Large Electron Positron
LHC Large Hadron Collider
LINAC Linear Particle Accelerator
LSB Least Significant Bit

LS Long Shutdown

LTM Local Trigger Module

LVDS Low-Voltage Differential Signaling

MB Minimum Bias

MC Monte Carlo

ME Matching Efficiency

mip minimum ionizing particle

MRPC Multigap Resistive Plate Chamber

OCDB Offline Calibration Database

PCB Printed Circuit Board

PFP Past Future Protection

PID Particle IDentification

PPC Parallel Plate Chamber

PS Proton Synchrotron

QA Quality Assurance

QCD Quantum Chromodynamics

QED Quantum Electrodynamics

QGP Quark-Gluon Plasma

RAM Random Access Memory

RF RadioFrequency

RHIC Relativistic Heavy Ion Collider

RICH Ring Imaging Cherenkov

RMS Root Mean Square

RPC Resistive Plate Chamber

RP Reaction Plane

SDD Silicon Drift Detector

SHM Statistical Hadronization Model

SIS Heavy-Ion Synchrotron

SM Standard Model

SM Super Module

SPD Silicon Pixel Detector

SPS Super Proton Synchrotron

SSD Silicon Strip Detector

TDC Time to Digital Converter

TDR Technical Design Report

TFF TFractionFitter

TMLP TMultiLayerPerceptron

TOF Time-Of-Flight

ToT Time-Over-Threshold

TPC Time Projection Chamber

TRD Transition Radiation Detector

TRM TDC Readout Module

UPC Ultra Peripheral Collision

UrQMD Ultra-Relativistic Quantum Mechanics Dynamics

VME Versa Module Europa bus

ZDC Zero Degree Calorimeter

ZEM Zero Degree Electromagnetic Calorimeter

Chapter 1

Nuclear physics at high energies

Since the first discovery of radioactive processes, physicists had the possibility to investigate the fundamental laws that define the behaviour of matter. The curiosity of the scientists of the late 19th and early 20th centuries fueled the effort to extend the frontier of human knowledge. In those years the modern concept of nucleus was born. From that moment the number of developments in both experiments and theory has grown steadily with strong impact on technological advances and on the course of history. In February 2000 CERN announced [14] the observation of “compelling evidence for the existence of a new state of matter in which quarks, instead of being bound up into more complex particles such as protons and neutrons, are liberated to roam freely”. This announcement describes well the situation which is far from being ideal as no direct discovery was achieved. The arguments that led to these conclusions are nonetheless very striking when comparing the particle production in heavy-ion and simple pp collisions.

In this chapter the reader will be introduced to the concepts of the Quark-Gluon Plasma (QGP) and how it can be created in high energy heavy-ion collisions. A review of the most common QGP signatures is presented as well as the current state of the measurements performed in the field. As it will be shown later the QGP gives unique opportunities for the test the Quantum Chromodynamics under extreme conditions.

1.1 Quantum Chromodynamics

Quantum Chromodynamics (QCD) is defined within the Standard Model (SM) as a gauge theory based on the group $SU(3)c$. The eight generators of the group (the Gell-Mann matrices λ^a) determine the fundamental properties of the QCD interaction. The group is non-abelian, so interactions between gauge bosons are also permitted. The color interaction is mediated by eight mass-less exchange bosons which form the interaction gauge fields, these are the

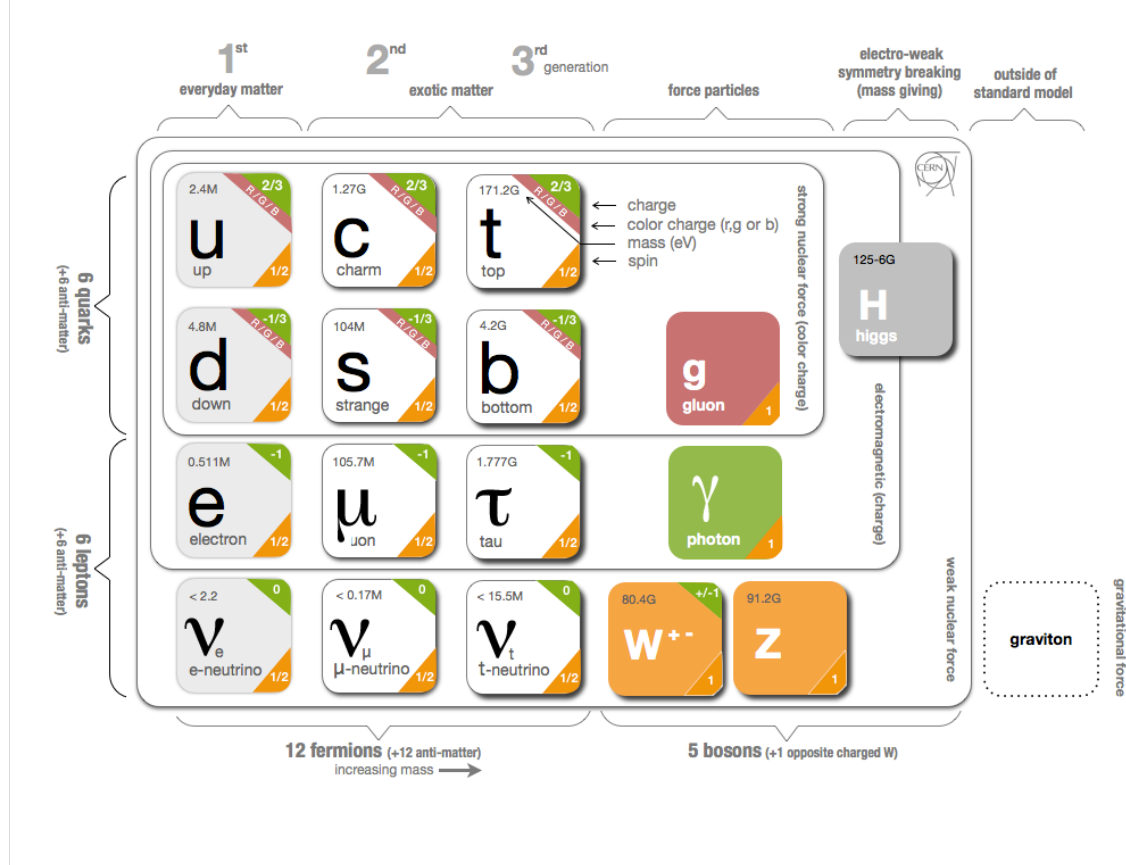


Fig. 1.1 Bosons and fermions that compose the Standard Model of particle physics [15].

eight gluons. In the SM only eight massive fermions have non zero color coupling, these are called quarks. Quarks and gluons complete the current representation of the SM depicted in Fig. 1.1. According to our knowledge, the whole visible world can be formed by these basic elements in a similar way to what happens for the case of atoms forming complex molecules. For this reason the properties of the fundamental particles of the SM (and their microscopic processes) give an imprinting to the measurable world and defines the way it is organized, even up to very large scales.

1.1.1 Running coupling constants

The coupling constant of QCD, α_s , is defined by the QCD renormalization scheme and depends on the energy scale. This dependence is due to the fact that the renormalization scheme of the adopted perturbative framework defines α_s .

In general, the evolution of the coupling constant α is described by the β -function obtained from its renormalization group equation (RGE) reported [16, 17]. The β -function

$\beta(\alpha)$ is defined as:

$$\beta(\alpha) = \frac{\partial \alpha}{\partial \ln \mu^2} \quad (1.1)$$

Following the calculations reported [16], the β function can be developed in perturbation theory as:

$$\beta(\alpha) = \pm b\alpha^2 [1 + b'\alpha + \dots] \quad (1.2)$$

Every new order in the sum of Eq. 1.2 is obtained by including an additional loop in perturbation theory. The coefficients of each term in the sum depend on the theory under study, but for simplicity, the overall sign is expressed explicitly, postulating $b > 0$. As stated by Eq. 1.1, $\beta(\alpha)$ describes the variation of the coupling constant with respect to its value at the reference scale $\mu(\alpha_\mu)$. The sign of Eq. 1.2 reflects the possible increase or decrease of α with the energy scale. The amplitude of the variation depends on the free parameters of the theory (the number of coupled quark flavors n_f , the color degeneracy N_C and the particle electric charge Q_i). Considering only 1-loop contributions, with $n_f = 6$ and color degeneracy $N_C = 1$ ($N_C = 3$) for leptons (quarks), yields two opposite behaviour for QED and QCD:

$$\begin{aligned} \text{QED} : & \begin{cases} \beta(\alpha) \sim +b\alpha^2 \\ b = \sum_i \frac{N_C Q_i^2}{3\pi} \end{cases} \\ \text{QCD} : & \begin{cases} \beta(\alpha) \sim -b\alpha^2 \\ b = \frac{11N_C - 2n_f}{12\pi} \end{cases} \end{aligned}$$

Defining Q as the transferred energy for a particular process, it is possible to introduce the dimensionless parameter $t = \log\left(\frac{Q^2}{\mu^2}\right)$ that quantifies the deviation from the reference scale μ . Combining Eq. 1.2 with Eq. 1.1 for the case of QCD we obtain, after an integration, the final expression for $\alpha_s(t)$:

$$\alpha_s(t) \sim \frac{\alpha_\mu}{1 - b\alpha_\mu t} \quad (1.3)$$

It is therefore natural to define an energy scale Λ_{QCD} as a limit to the effectiveness of the perturbative approach. At energies close to Λ_{QCD} the coupling, defined perturbatively, diverges and higher order terms cannot be neglected. The value of Λ_{QCD} depends on the reference scale μ but also on the renormalization scheme used and on the same parameters which define α_s .

$$\frac{1}{\alpha_\mu} = b \log \left(\frac{\mu^2}{\Lambda_{\text{QCD}}^2} \right) \quad (1.4)$$

By replacing $1/\alpha_\mu$ in Eq. 1.3 we can express the dependence of α_s only in terms of Λ_{QCD} and Q :

$$\alpha_s(t) \sim \frac{1}{\frac{1}{\alpha_\mu} - bt} = \frac{1}{b \log \left(\frac{\mu^2}{\Lambda_{\text{QCD}}^2} \right) - b \log \left(\frac{\mu^2}{Q^2} \right)} = \frac{1}{b \log \left(\frac{Q^2}{\Lambda_{\text{QCD}}^2} \right)} \quad (1.5)$$

In Fig. 1.2 are reported both measured and theoretical values of α_s as a function of the process transferred energy Q , α_s is found to be strongly dependent on the energy scale. It is therefore possible to distinguish two limits:

- For $\alpha_s \rightarrow 0$ at $Q \rightarrow \infty$: *asymptotic freedom*.

At this regime hadrons are loosely bound and perturbative QCD can be safely applied.

- For $\alpha_s \rightarrow \infty$ at $Q \rightarrow 0$: *quark confinement*.

Color charge is confined into ordinary hadronic matter and strong strong interactions are dominated by non perturbative processes.

1.1.2 The phase diagram of the QCD

In atoms the separation of the electrons from their nuclei can be achieved by increasing their energy. This can be performed by increasing the temperature of a gas or by applying strong electromagnetic fields. In principle a similar effect can be achieved for hadronic matter by reaching the *asymptotic freedom* regime.

Because of the confinement of the color charge, the only viable option to free the hadron constituents is to increase significantly the energy scale of the system by compression or by heating. At this high energy regime hadronic matter melts releasing its elementary degrees of freedom (quark and gluons) in a way which is analogous to a phase transition. A simple description of the phases of nuclear matter is given in Fig. 1.3. In order to gain insight into the dynamics of the QCD phase, many studies were performed by using lattice QCD calculations. Only recently the technical and theoretical advancements allowed to better constrain the characteristics of this phenomenon. Based on recent lattice QCD calculations [18] the phase transition is expected to happen when the energy density exceeds the critical value ε_c which is of the order of 1 GeV/fm^3 . The system temperature at the critical point (the critical temperature T_c) is estimated to be $154 \pm 9 \text{ MeV}$ [19]. The phase diagram shown in Fig. 1.3 can be interpreted as:

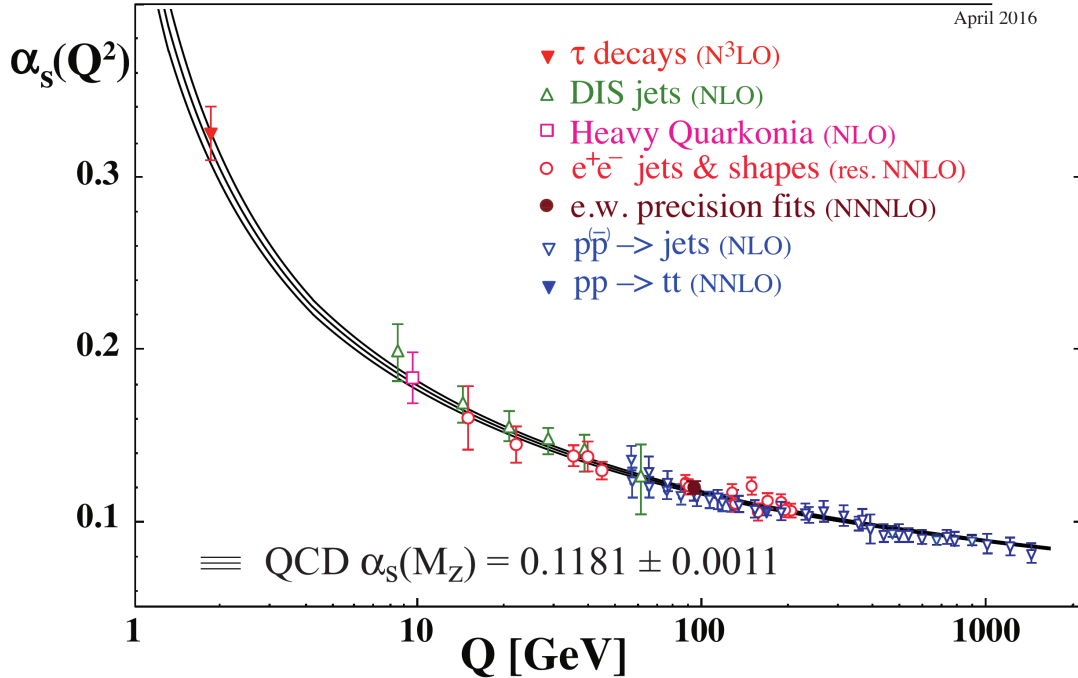


Fig. 1.2 Calculations and measurements of the α_s coupling constant as a function of the energy scale Q [17].

1. The phase transition can happen at low temperatures but extreme nuclear matter densities ($\mu_B \rightarrow \infty$) are required. This scenario can be obtained by compressing cold nuclear matter and reaching density values higher 3-10 times ρ_0 ($\rho_0 \sim 0.15/\text{fm}^3$ is the baryon density at equilibrium) [20].
2. At vanishing baryochemical potential ($\mu_B \rightarrow 0$) the phase transition can only be achieved by increasing the system temperature to values higher than T_c . In this case the transition is expected to be a “crossover”. The deconfined and confined phases would coexist close to the transition boundaries in such way that the entropy evolution as a function of the temperature ($S(T)$) is continuous.
3. At intermediate μ_B and at intermediate temperatures the transition is of the first order, implying that a discontinuity in the entropy $S(T)$ is located at temperature $T = T_c$. The first order transition requires the existence of a latent heat to keep the temperature constant during the completion of the phase transition.

It is thought that the conditions for the first case (low T , large μ_B) can be reached in the core of neutron stars where it is possible to increase significantly the matter density without raising the system temperature [21]. The other two situations can be reproduced in laboratory.

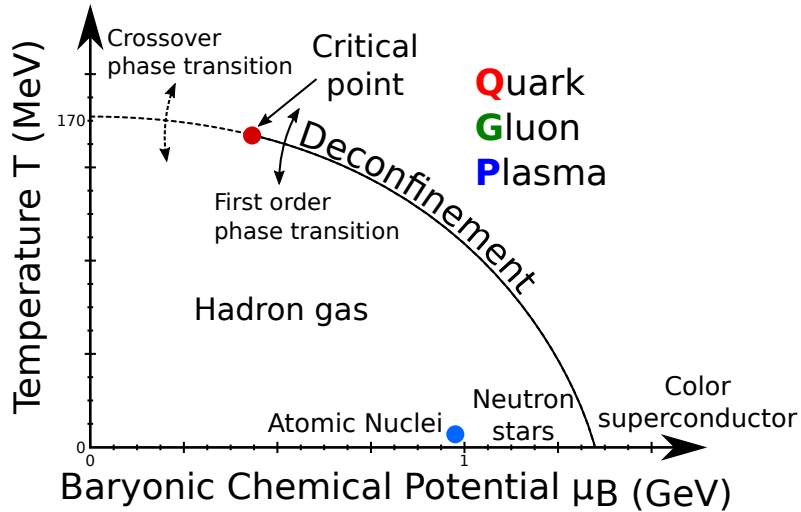


Fig. 1.3 Representation of the phase diagram for nuclear matter analogous to the famous “Clapeyron Diagram”. The baryon chemical potential represents the amount of net baryon charge available in the system.

High temperatures are reached when nuclei collide at ultra-relativistic energies thus allowing the energy density to exceed ϵ_c as it will be shown later. These kind of experiments have been and still are performed in both collider and fix target configuration at BNL, CERN, GSI and other facilities. The values of μ_B and T depend only on the type of nuclei that are used and on the collision energy itself. The latter, in particular, identifies different regimes: starting from the 1 AGeV scale (at the SIS facility) colliding nuclei are stopped resulting in a moderated compression and heating of the nuclear matter. As the collision energy increases the temperature rises and the baryon chemical potential of the system created at rest lowers. This is because the total stopping of the colliding nuclei is less likely to occur at higher energies. In recent years the physics program of the largest laboratories is focusing on the study of the QCD phase diagram, this is currently done by measuring collisions at the highest possible energies (LHC) or by investigating the phase transition by varying the collision energy (Beam Energy Scan at RHIC). This field of research will be critical for the development of science in the near future as more and more facilities dedicated to the nuclear physics are foreseen.

So far the highest energy per collision was reached at the Large Hadron Collider by using lead ions ($^{208}\text{Pb}^{82+}$) in 2015 [22] at \sqrt{s} of 5.02 TeV per nucleon pair ($\sqrt{s_{\text{NN}}} = 5.02$ TeV) i.e. an overall \sqrt{s} of ~ 2 PeV, which makes the LHC the first collider able to reach the PeV scale. At this energy scale the “fireball” created in the collision has no trace of the initial nuclei and is to good approximation constituted by a (net-)baryon-free hadronic matter, similar to the condition of our universe in its first moments.

1.1.3 Colliding extended objects: the collision centrality

One important difference between pp and heavy-ion collisions is based on geometrical considerations: the colliding ion is an extended object when compared to the single nucleon. In a proton-nucleus collision (pA) the maximum number of binary nucleon–nucleon collisions (N_{Coll}) can vary between a minimum of 0 (no collisions) up to A (atomic mass number). In this particular case, if N nucleon–nucleon collision occur, the total number of nucleons participating to the collisions will be $N_{\text{Part}} = N + 1$. The number of non-interacting nucleons (spectator nucleons, N_{Spect}) is given by $A - N_{\text{Part}}$. One can derive similar conclusions for AA collisions. Both A and the collision impact parameter b (depicted in Fig. 1.4) play a role in the determination of N_{Coll} . A is defined by the choice of ions used for the experiment while b is a free parameter that varies for each collision and is normally referred to as the “collision centrality”. Central collision happen when $b = 0$ while peripheral collisions have larger b ; the collision centrality is usually expressed in terms of fractions of the total cross section (in Pb–Pb collisions at $\sqrt{s_{\text{NN}}} = 2.76$ TeV $\sigma_{\text{Pb–Pb}} = 7.57 \pm 0.03$ barn and at $\sqrt{s_{\text{NN}}} = 5.5$ TeV $\sigma_{\text{Pb–Pb}} = 7.67 \pm 0.03$ barn [23])¹.

The probability for a collision to happen at a given impact parameter b can be computed as:

$$P(b) = \sigma_{\text{NN}} \times T_{\text{AA}}(b) \quad (1.6)$$

The T_{AA} is usually referred to as “nuclear overlap function” and accounts for the probability to have a nucleon at the same position in the transverse plane in both colliding nuclei. The nuclear overlap function is computed from the single nucleon distribution of the interacting nuclei.

A Glauber model [25] is typically used to relate parameters such as N_{Coll} , N_{Part} and b to the geometrical properties of the collision. An example of a collision simulated with such model showing participant and spectator nucleons is reported in Fig. 1.4.

The centrality of each collision has to be determined experimentally in order identify peculiar behaviour that can arise for very specific centrality classes. This can be done by obtaining the values of N_{Coll} and N_{Part} by measuring the products of the interactions available in the final state. Usually for a single collision the quantities that are used for the centrality determination are the number of charged particles produced and the number of nucleons which did not interact. The measured observables are compared with the predictions of the Glauber model so as to compute the average number of N_{Part} and N_{Coll} corresponding to

¹As an example, in Pb–Pb collisions at $\sqrt{s_{\text{NN}}} = 2.76$ TeV, the impact parameter of the most central collisions, corresponding to 5% of the total cross section, ranges within 0.0 and 3.5 fm [24].

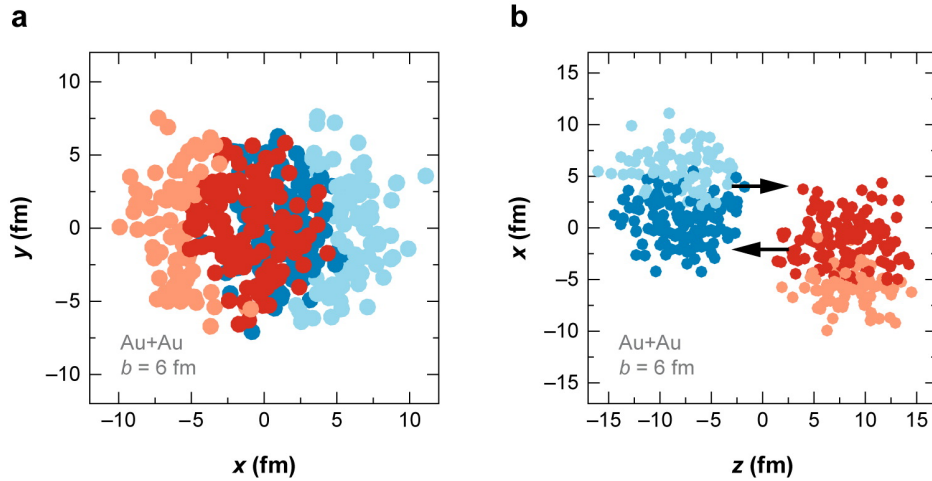


Fig. 1.4 A Glauber Monte Carlo [25] event of Au–Au at $\sqrt{s_{\text{NN}}} = 200$ GeV with impact parameter $b = 6$ fm. (a) transverse plane visualization (b) visualization along the beam axis. Darker circles represent participating nucleons.

each centrality class. An example of splitting collisions into centrality classes is shown in Fig. 1.5.

1.2 The Quark-Gluon Plasma

So far we discussed the possibility to reach a deconfined state of strongly interacting matter in heavy-ion collisions. The Quark-Gluon Plasma (QGP) inherits his name from its fundamental degrees of freedom i.e quarks and gluons. The use of heavy-ion collisions for the study of the QGP is due to the high energy density that can be reached in each collision. The energy density is the fundamental ingredient which is needed for the temperature to exceeds the critical value and create the QGP.

We can compute the energy density for colliding nuclei² as $\langle \varepsilon \rangle = 2 \times \rho_0 \gamma^2$ where ρ_0 indicates the energy density at rest of each nucleus and $\gamma = 1 / \sqrt{1 - \beta^2}$ is the Lorentz factor of the beam. The previous formula can be rewritten as $\langle \varepsilon \rangle = \frac{\sqrt{s}^2}{2 \times V mc^2}$ and values reached at the Relativistic Heavy Ion Collider (RHIC) are³ $\langle \varepsilon_{\text{RHIC}} \rangle \simeq 3 \times 10^3$ GeV/fm³ while at the Large Hadron Collider (LHC) the evaluation can be carried out as⁴ $\langle \varepsilon_{\text{LHC}} \rangle \simeq 2 \times 10^6$ GeV/fm³. The values obtained with this naive approach are much larger than the $\varepsilon_c \sim 1$ GeV/fm³ needed for the phase transition to occur but one has to take into account

²Under the assumption that the total momentum in the region is null.

³At $\sqrt{s_{\text{NN}}} = 200$ GeV and $R_{197\text{Au}^+} \sim 1.2 \times A^{1/3} \simeq 6.98$ fm.

⁴At $\sqrt{s_{\text{NN}}} = 5.02$ TeV and $R_{208\text{Pb}^+} \sim 1.2 \times A^{1/3} \simeq 7.11$ fm.

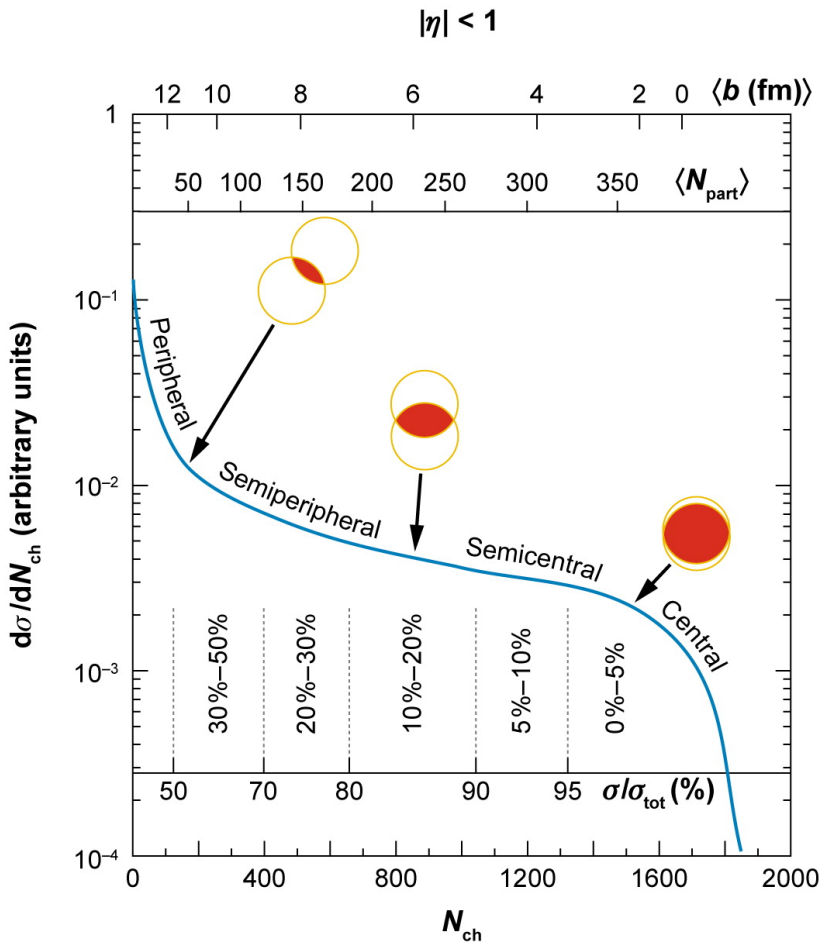


Fig. 1.5 Illustration of the correlation between the number of charged particle produced per event and the Glauber-calculated quantities (b , N_{Part}) [25]. It is possible to identify two extreme behaviour: peripheral collisions (where less particles are produced) and central collisions (where more particles are produced);

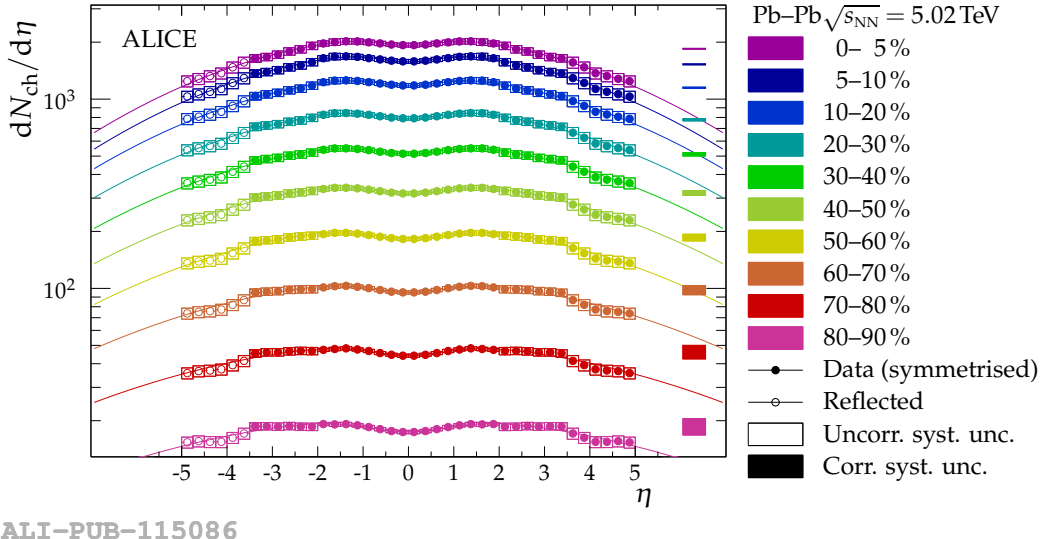


Fig. 1.6 Charged-particle pseudorapidity density as measured for a large η range in centrality classes in Pb–Pb collisions at $\sqrt{s_{\text{NN}}} = 5.02 \text{ TeV}$ [1].

that the energy densities are obtained for very short time duration i.e. only during the nuclei crossing times. A more precise formulation of the energy density was given by Bjorken [26]:

$$\langle \varepsilon_{\text{Bjorken}} \rangle \equiv \varepsilon_{Bj} = \frac{1}{\tau_f \cdot \pi R^2} \frac{d \langle E \rangle}{dy} \quad (1.7)$$

Where τ_f stands for the formation time of the fireball and R is the transverse radius of the participant volume and πR^2 is the nuclei overlap area. This formulation is valid as long as the particle production exhibits a “plateau” structure in the central rapidity region and the net baryon number at mid-rapidity is close to zero. The existence of the central plateau at $y \sim 0$ guarantees that the description of particle produced at large angles (in the system rest frame) do not depend on the particular choice for the reference frame. This condition was already verified the SPS energies [27] and continues to hold true up the the LHC as shown in Fig. 1.6. As a matter of fact the η distribution of the particle produced in heavy-ion collisions is shown to be flat for large η intervals.

Using the same argumentation of Bjorken as in [28–30] it is possible to obtain values of ε_{Bj} as a function of the collision energy⁵ under the assumption that $\tau_f \sim 1 \text{ fm}/c$:

- AGS: Au–Au, $\sqrt{s_{\text{NN}}} = 4.8 \text{ GeV} \rightarrow \varepsilon_{Bj} \sim 1.5 \text{ GeV/fm}^3$
- RHIC: Au–Au, $\sqrt{s_{\text{NN}}} = 19.6 \text{ GeV} \rightarrow \varepsilon_{Bj} \sim 2.2 \text{ GeV/fm}^3$
- SPS: Pb–Pb, 158 AGeV $\rightarrow \varepsilon_{Bj} \sim 3.2 \text{ GeV/fm}^3$

⁵For central collisions.

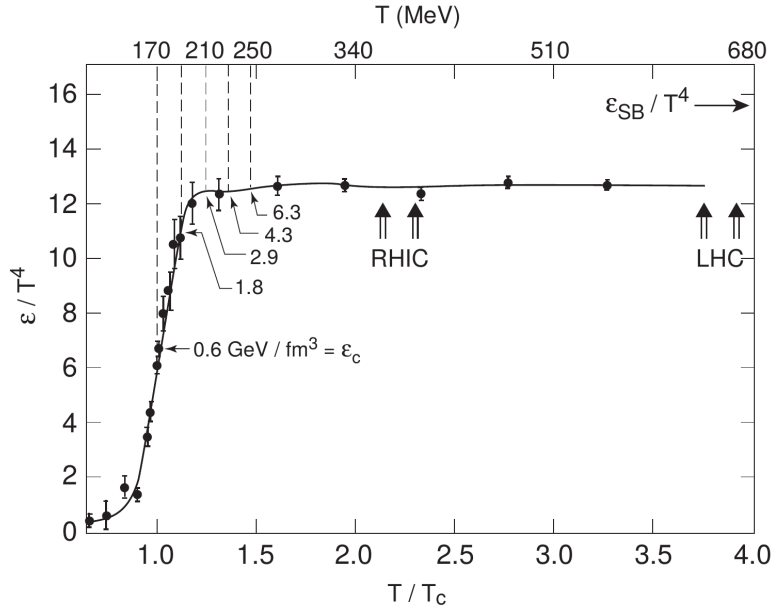


Fig. 1.7 Energy density scaled by T^4 as a function of the ratio T/T_c as obtained from lattice QCD with 3 quarks [20]. The values of energy density for $T_c = 170$ MeV are reported. It is important to highlight that the point at which $T/T_c \sim 1$ (deconfinement is expected) has energy density $\epsilon_c \sim 0.6$ GeV/fm 3 for $T_c = 170$ MeV.

- RHIC: Au–Au, $\sqrt{s_{\text{NN}}} = 130$ GeV $\rightarrow \epsilon_{Bj} \sim 4.7$ GeV/fm 3
- RHIC: Au–Au, $\sqrt{s_{\text{NN}}} = 200$ GeV $\rightarrow \epsilon_{Bj} \sim 5.4$ GeV/fm 3

The values for the Bjorken energy density are more reasonable and differ significantly (~ 3 order of magnitude) from the ones obtained naively before. It is now safe to compare the energy density ϵ_{Bj} to the lattice QCD calculations for the critical energy density shown in Fig. 1.7. The predicted value for $\epsilon_c \sim 1$ GeV/fm 3 is lower than ϵ_{Bj} , this shows that the conditions for a deconfined state are well within the reach of the heavy-ion accelerator facilities.

The definition of ϵ_{Bj} given in Eq. 1.7 clearly states the interconnection between the final state and the thermodynamic properties of the medium created in the collision. The measurement of particles production is to be considered as of primary importance if one wants to reconstruct the condition of the system few moments after the collision. Fundamental observables for this studies are the distribution of the particle transverse energy $\frac{dE_T}{d\eta}$ and the particle multiplicity $\frac{dN_{\text{ch}}}{d\eta}$. In particular using the $\frac{dE_T}{d\eta}$ to approximate $d\langle E \rangle / dy$ in Eq. 1.7 it is possible to derive ϵ_{Bj} from measured data. An example of such measurement performed by the PHENIX Collaboration at RHIC energies is reported in Fig. 1.8. As expected the

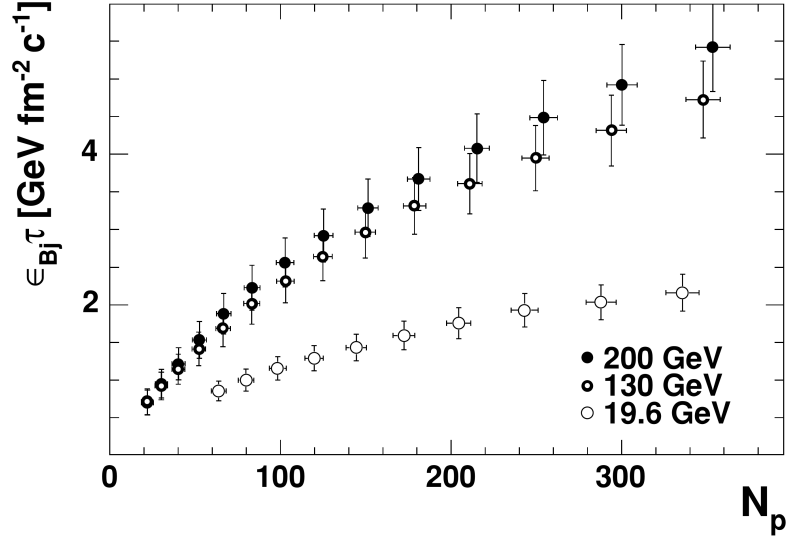


Fig. 1.8 ϵ_{Bj} as a function of the number of participant nucleons (N_p) as measured at RHIC energies in Au–Au [28].

energy density increases as a function of centrality and reaches values that are higher than the critical value ϵ_c already in most peripheral collisions.

We now have all the ingredients to verify the assumption of $\tau_f \sim 1 \text{ fm}/c$. Defining the particle transverse mass as $m_T \equiv \sqrt{m^2 + p_x^2 + p_y^2}$ and from basic considerations on the indetermination principle we obtain:

$$\Delta E \cdot \Delta t \geq \frac{\hbar}{2} \quad (1.8a)$$

$$\langle E \rangle = \langle m_T \rangle c^2 \cdot \cosh(y) \quad (1.8b)$$

$$\text{At mid-rapidity } y = 0: \& \langle E \rangle = \langle m_T \rangle c^2 \quad (1.8c)$$

$$\langle m_T \rangle c^2 \simeq \frac{dE_T}{d\eta} / \frac{dN}{d\eta} \quad (1.8d)$$

This allows us to give an estimate of the formation time of the system from simple measurements of $\langle m_T \rangle$:

$$\tau_f \simeq \frac{\hbar}{\langle m_T \rangle c^2} \quad (1.9)$$

Combining Eq. 1.9 with the measured values reported in Fig. 1.9 for central collisions at RHIC we can obtain $\frac{dE_T}{d\eta} / \frac{dN_{ch}}{d\eta} \simeq 0.85$, which converted gives $\frac{dE_T}{d\eta} / \frac{dN}{d\eta} = \frac{dE_T}{d\eta} / (\frac{dN_{ch}}{d\eta} \cdot \frac{3}{2})$. From Eq. 1.9 one gets $\tau_f \sim 0.34 \text{ fm}/c$ which is smaller than the assumed value of $1 \text{ fm}/c$.

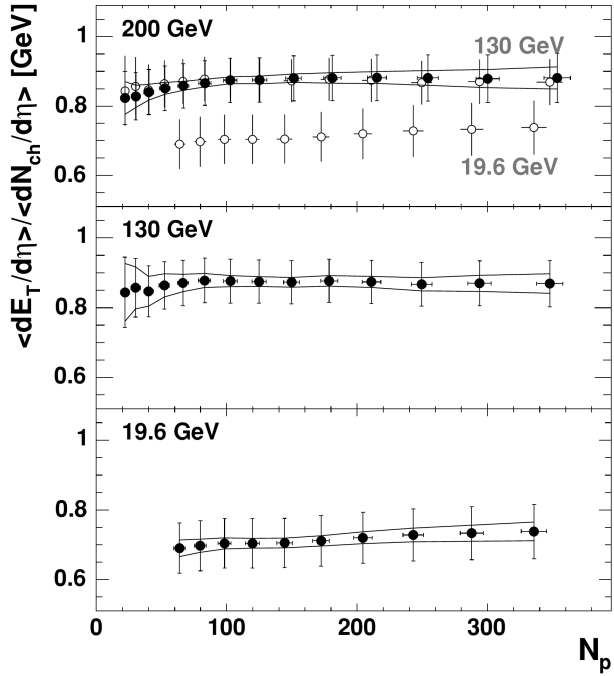


Fig. 1.9 Ratio of $dE_T/d\eta / dN_{ch}/d\eta$ as a function of the number of participant nucleons (N_p) as measured at RHIC energies in Au–Au collisions by the PHENIX Collaboration [28].

but is of the same order of magnitude and still larger than $2R/\gamma$. Considering the level of approximation used we can validate the assumption of short formation time.

The current state of the art for the measurements of the charged particle densities at the LHC energies can be found in [32, 31], an example is shown in Fig. 1.10. The values measured at the LHC energies (for the most central Pb–Pb collision $\frac{dN_{ch}}{d\eta} \sim 1584$ at $\sqrt{s_{NN}} = 2.76$ TeV, $\frac{dN_{ch}}{d\eta} \sim 1942$ at $\sqrt{s_{NN}} = 5.02$ TeV) are significantly larger than the ones obtained at RHIC (for the most central Au–Au collision at $\sqrt{s_{NN}} = 200$ GeV $\frac{dN_{ch}}{d\eta} \sim 687$ [28]) indicating that the system is created with significantly larger energy densities. As a matter of fact the Bjorken formula (Eq. 1.7) yields at these energies $\varepsilon_{Bj} > 15$ GeV/fm³ which is approximately 3 times larger than the one observed at RHIC. This is the reason why there is a rich heavy-ion program at the LHC as one would expect at these energies to observe the most significant signatures for the QGP. It is important to note that contrary to what happens for the heavy-ion case, in small collision systems the measured values of $\frac{dN_{ch}}{d\eta}$ (shown in Fig. 1.10 for pp and p–Pb collisions) are not expected to produce energy densities that are above the critical limit. In this case the system is not expected to reach a completely deconfined phase as for AA collisions.

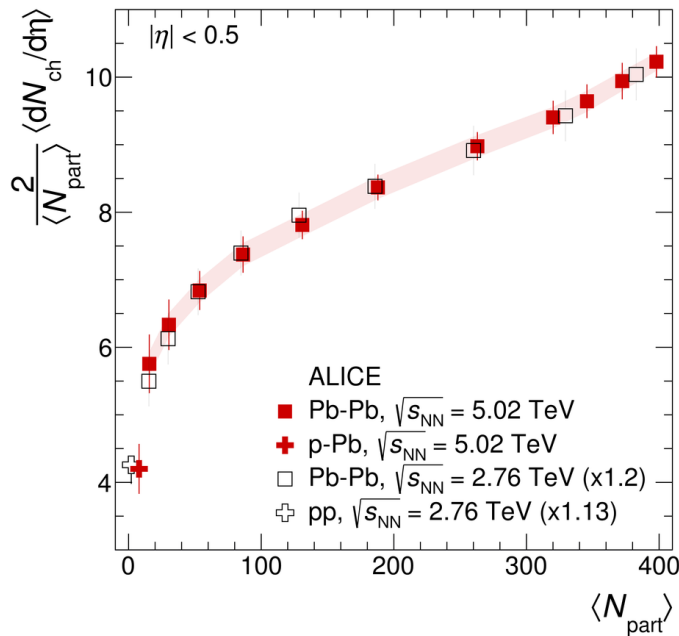


Fig. 1.10 The average number of charged particles produced at mid rapidity divided by the half of number of participant nucleons ($2 \left\langle \frac{dN_{\text{ch}}}{d\eta} \right\rangle / \langle N_{\text{Part}} \rangle$) as measured in Pb–Pb collisions at $\sqrt{s_{\text{NN}}} = 5.02 \text{ TeV}$ and $\sqrt{s_{\text{NN}}} = 2.76 \text{ TeV}$ and compared to pp and p–Pb collisions at $(\sqrt{s})\sqrt{s_{\text{NN}}} = 2.76 \text{ TeV}$ [31].

1.2.1 Time evolution of a heavy-ion collision

After the collision has occurred, the fireball evolves through a series of states as depicted in Fig. 1.11:

1. Pre-equilibrium ($t \lesssim 1 \text{ fm}/c$): the two nuclei just collided. The partons of every participating nucleon interact producing a large amount of quarks and gluons. At this stage the hard scatterings produce partons with high momentum that will later form massive “hard” hadrons or fragment into jets. Prompt photons are also produced. The system is now formed by a dense inhomogeneous droplet of strongly interacting QGP matter.
2. Thermalization ($t \sim 1 \div 10 \text{ fm}/c$): the medium reaches thermal equilibrium thanks to the many interactions of every newly-created parton. Inelastic scatterings occur as well and modify the “chemical” composition of the medium by changing the flavor of partons. The system, now in equilibrium, builds an internal pressure that finds no opposition by the void that surrounds it. This leads to a rapid expansion of the system together with a decrease in the temperature. As the temperature lowers, the system energy density is not able to keep partons separated and hadrons start to form.
3. Hadronization ($t \sim 20 \text{ fm}/c$): as the energy density crosses ϵ_c ($T \equiv T_c$) hadronization takes over. The system loses its degrees of freedom as all partons are confined into hadrons. The interactions between hadrons keep the system in thermal equilibrium.
4. Chemical freeze-out: the temperature decreases down to $T \equiv T_{\text{Ch}}$, at this point all inelastic interactions among hadrons have completely stopped. The system is now formed by a gas of hadrons that interact only (pseudo-)elastically.
5. Kinetic freeze-out: at this stage the hadrons start to decouple from the medium as the temperature lowers and the mean free path becomes larger than the mean distance between hadrons. This results in a complete stop of all interactions, the temperature is $T \equiv T_{\text{Kin}}$; Now the repartition of the kinetic energy among all hadrons has stopped and the momentum spectrum of each particle is fixed.

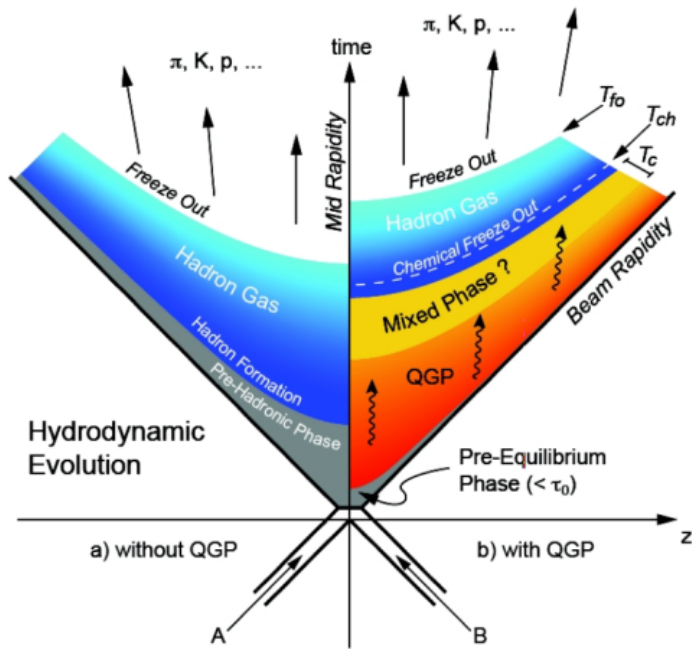


Fig. 1.11 Evolution of the system created in the collision in a Minkowski-like plane [33]. Two scenarios are given: one with (left) and one without (right) QGP formation. The two freeze-out temperatures T_{Ch} (chemical freeze-out) and T_{Kin} (Kinetic freeze-out) are reported together with the critical temperature T_c .

Chapter 2

Probing the QGP with light flavor particles

Experimentalists can access only the information available in the final state. Of course much importance is given to “early probes” such as prompt photons, hard scatterings or hadrons with heavy flavor (c, b, t) as they can give detailed information regarding the medium at the instant when they are created. The partonic energy loss due to gluon radiation in the medium can also be investigated through these hard probes. Nonetheless observables coming from the measurement of light flavor hadrons opens the way to the measurement of the thermodynamic properties of the system. This chapter is dedicated to the description of how the dynamics of the particle production is determined by the thermodynamic properties of the medium created in the collision. These will be the subject of the investigation carried out for this thesis, as it will be discussed in Chapter 7. We can identify different type of probes of the QGP that are accessible in the final state:

- Electromagnetic probes (prompt photons): consist of photons emitted before and after the thermalization (black body radiation) in both virtual and real form. In principle they could easily be identified by measuring the opposite sign lepton pairs in the final state but it is challenging to isolate the early photons from the background coming from successive stages of the evolution.
- Hard probes: are obtained in high Q^2 (momentum transfer) scatterings that occur at the early stage of the collision. These reactions can be described in terms of perturbative QCD thanks to the large energy scales at play. This category includes jets and production of particles containing heavy flavor quarks (c, t, b) in both open charm/beauty (in both mesons and baryons) and quarkonia ($q\bar{q}$).

- Soft probes: this category is densely populated as most of the particles are produced in soft processes (non-perturbative QCD). These probes come from the last stages of the fireball evolution. Among these we count the mean particle multiplicity, the mean transverse energy, the correlations in particle productions, the light flavor particle spectra and the collective evolution of particles (flow). All these are usually measured from hadrons with light quarks (u, d, s). Soft probes represent the “bulk” of the particle produced in heavy-ion collisions as more than $\sim 98\%$ have momenta below $2 \text{ GeV}/c$.

The majority of particles present in the final state fall in the “soft probes” category. An example of the possibilities to characterize the energetic properties of the medium created was already given in Section 1.1.2. As initially proposed by Fermi and Hagedorn the thermal production of particles can be described with a statistical approach [34]. This is the only practical solution to deal with such non-perturbative problem that involves every particle created in the collision. One of the greater successes of statistical models is to be found in the analysis of the particle abundances i.e. hadrons generated from the initial free partons at the time of the chemical freeze-out. Here we will summarize how this type of analyses can be used to extract information on the QCD phase diagram.

2.1 Thermal models of particle production

The statistical treatment starts by defining the entropy of the system S and its partition function Z . A detailed description of the procedure is given in Appendix A, here are just reported its main results.

The thermodynamic properties of the system at equilibrium such as the mean particle multiplicity $\langle N \rangle$, the mean energy $\langle E \rangle$, the mean entropy $\langle S \rangle$ can be derived from the partition function:

$$\langle N \rangle = \frac{1}{\beta} \left(\frac{\partial \ln Z}{\partial \mu_B} \right) \quad (2.1)$$

$$\langle E \rangle = - \left(\frac{\partial \ln Z}{\partial \beta} \right) + \mu_B \langle N \rangle \quad (2.2)$$

$$\langle S \rangle = k_B \frac{\partial (T \cdot \ln Z)}{\partial T} \quad (2.3)$$

$$P = \frac{1}{\beta} \frac{d \ln Z}{d V} \quad (2.4)$$

Where k_B is Boltzmann constant and $\beta = 1/(k_B \cdot T)$. The volume of the system created in heavy-ion collisions is considerably larger than the partonic scale, this justifies the usage of a grand-canonical ensemble. Under these conditions the elementary volume under study (ΔV) can exchange both particles and energy with its surroundings meaning that the quantum numbers are conserved only by averaging over the whole volume of the system. In addition one has to consider the quantum behaviour of both fermionic and bosonic degrees of freedom that form the system. From these considerations it is possible to obtain the grand-canonical partition function for the species s as:

$$\ln Z_s(T, V, \mu_s) \equiv \frac{\Delta V g_s}{2\pi^2 \hbar^3} \int_0^\infty \theta_s p^2 dp \ln(1 + \theta_s \lambda_s e^{-\beta \cdot E}) \quad (2.5)$$

Where $\lambda_s = e^{\beta \mu_s}$ is the fugacity for the particles species s defined trough the chemical potential μ_s and θ_s is $+1$ for fermions and -1 for bosons. Global observables such as the particle mean multiplicities can be derived:

$$\langle N_s \rangle = \frac{\Delta V g_s}{2\pi^2 \hbar^3} \int_0^\infty dp \frac{p^2}{e^{\beta \cdot E / \lambda_s} + \theta_s} \quad (2.6)$$

With these assumption on the type of ensemble the phase space distribution for particles of type s is:

$$f_s(x, p) = \frac{g_s}{e^{\beta \cdot p \cdot u / \lambda_s} + \theta_s} \quad (2.7)$$

The formulation given in Eq. 2.5 can be further developed by considering the Taylor expansion of the logarithmic part, the full derivation is given in Appendix B. The final form of the partition function for the grand-canonical ensemble can be obtained as:

$$\ln Z_s(T, V, \mu_s) = \frac{\Delta V g_s}{\beta 2\pi^2 \hbar^3} \sum_{k=1}^{\infty} \frac{(\theta_s \lambda_s)^k}{k^2} m_s^2 K_2(k \beta m_s) \quad (2.8)$$

Where K_2 indicates the modified Bessel function of the second kind [35].

The definition of the chemical potential μ_s is strictly related to the processes at play and to the type of chosen ensemble. The chemical potential μ_s is necessary in order to give the possibility to have fluctuations of the number of particles of species s inside the volume ΔV . This can happen because the volume ΔV can exchange particles with its surroundings, incrementing or decrementing the components of each species.

This formulation corresponds to the grand-canonical ensemble which is the most commonly used in the description of heavy-ion collisions [36] and enforces the average conservation of additive quantum numbers via the chemical potentials. In general the potential

for a given species i can be split into each conserved quantity: $\mu_i = B_i \mu_B + S_i \mu_S + Q_i \mu_Q$, where B_i , S_i and Q_i are respectively the baryon number, strangeness and electric charge while μ_B , μ_S and μ_Q are the corresponding chemical potentials. For smaller systems (e^+e^- , pp and p–Pb) the grand-canonical ensemble is no longer a good description of the system. In this case the volume created after the collision is considerably smaller and it is better to require the local conservation of quantum numbers (at least for the strangeness quantum number) and allow only energy exchanges among volumes (canonical formulation). A detailed description of the partition function for the canonical ensemble can be found in [36]. Nonetheless the grand-canonical approach is commonly used to treat central heavy-ion collisions where the system created has large spacial extension.

Different statistical hadronization (thermal) models (SHM) implement the basic formula in Eq. 2.6 [36–38]. These models differ from each other in the number of free parameters, the corrections applied and on the type of ensemble used. Some include a hadronic phase with residual chemical activity based on the Ultra-Relativistic Quantum Mechanics Dynamics model (UrQMD)¹. Other models make use of a flavor-dependent chemical decoupling by introducing γ_s as the strangeness suppression factor. In this case γ_s takes into account the possibility to have partial thermalization for strange quarks, as it will be explained later, it is expected to have $\gamma_s < 1$ in small collision systems (where the canonical ensemble i.e. local conservation of quantum number is imposed) while in heavy-ion collisions the s quarks can be fully thermalized and γ_s can reach values of 1. The common aim among all these models is to predict global properties of the medium by using the “soft probes” (or light flavor) which are thermal produced. These observables have the advantage of being commonly produced in each collisions and form a basic measurement for every experimental setup.

Starting from measurements of the identified particle yields (dN/dy) in the light flavor sector by using the SHM approach one gains the access to the thermodynamic properties of the system created in the collision. In principle the more particle species are measured the better, in fact all particle that are produced at equilibrium can be used for this purpose. An example of such measurement for different particle species (π^\pm , K^\pm , p , \bar{p} , Λ and $\bar{\Lambda}$) is given in Fig. 2.1 as a function of the $\sqrt{s_{NN}}$ for central collisions. At first glance it is possible to see the large evolution in particle production and identify some key features:

1. All particles and their corresponding anti-particles tend to be equally produced if the collision energy is high enough. This is especially true at LHC energies [39, 40].
2. Baryons (p and Λ) and mesons (π and K) follow different behaviour with significant baryon/anti-baryon discrepancies at lower energies.

¹ From the time evolution picture of the QGP given in Section 1.2.1 it is not forbidden to have distinct hadronization and chemical freeze-out i.e. $T_{\text{Ch}} < T_c$.

- The yields of p lowers while \bar{p} increase with $\sqrt{s_{\text{NN}}}$, in relation to the decrease of μ_B . When μ_B is larger than 0 the baryonic number of the colliding nuclei is to be found in the products of the collision. At low energies, an important fraction of the initial colliding nucleons are found in the final state (large stopping power). For larger beam energies the colliding nuclei become almost transparent to each other (no baryon stopping). At this energy regime the products of the primordial nucleons are less likely to be found in the final states.
- The production of Λ , similar to p , is affected by the non-zero μ_B at low energies but the effect is reduced since it contains an s quark. At intermediate energies Λ exhibits a decrease similar to that of p .

3. At high energies, pions are the most abundant particle species produced
4. Particles containing s quarks are subject to a significant increase in their abundances above the SPS energies. This effect known as “strangeness enhancement” was historically identified as a signature typical of the QGP. This topic will be the subject of Section 2.1.1.
5. At high energies the production of particles with same mass but different quark content tends to be similar (e.g. p and Λ).

The SHM can be used to fit the measured dN/dy to fix its parameters. This is done by using only a limited number of parameters (T , V , γ_s , μ) and carrying out the calculation with the best ensemble for the collision system. This allows to obtain quantities such as the chemical freeze-out temperature T_{Ch} , the system volume V and the chemical potential μ_B . Results from [41] (Fig. 2.2) show how the best fit parameters to describe the data from Pb–Pb central collisions collected by the ALICE experiment at $\sqrt{s_{\text{NN}}} = 2.76$ TeV are: $T = 156.5 \pm 1.5$ MeV, $\mu_B = 0.7 \pm 3.8$ MeV, $V = 5280 \pm 410$ fm 3 . The model is able to describe reasonably well measurements of yields which span over 9 order of magnitudes with a $\chi^2/\text{NDF} = 1.61$ with a low number of free parameters. The largest tension is observed for p and \bar{p} , reaching almost a 3σ deviation.

The effectiveness of the thermal model predictions is not only limited to the high energy of the LHC but covers lower collision energies as shown in Fig. 2.3. In this case both K/π and p/π are well reproduced by the model over a wide range of energies. The advantage of comparing the model to yield ratios instead of simple yields lays in cancelling out the dependence on the source volume V (Eq. 2.6).

The thermal model consists in a useful tool to investigate the phase diagram of QCD. Taking the values of T and μ_B obtained from the fit we can reconstruct a diagram similar

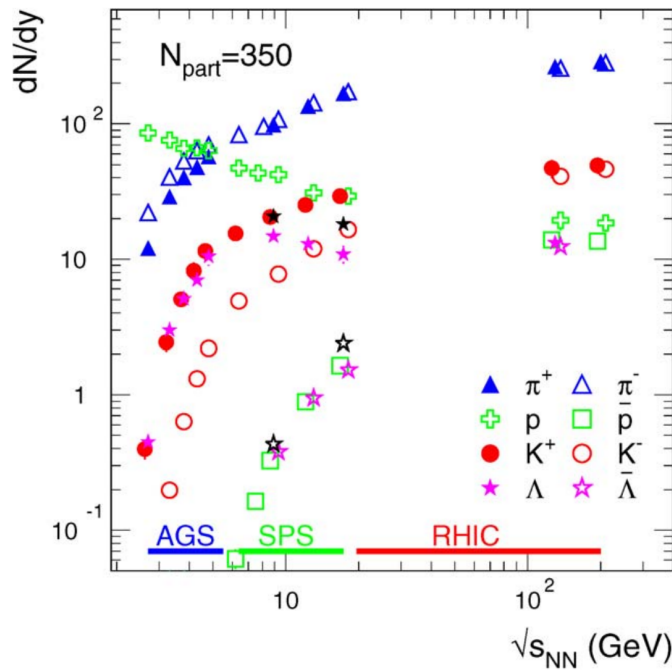


Fig. 2.1 Measured hadron yields (dN/dy) at mid-rapidity for different particle species as measured in central AA collisions by different experiments as a function of the $\sqrt{s_{NN}}$ [37]. The physics message of this plot could profit from the inclusion of the result from the Beam Energy Scan performed at RHIC and of the results at high energy coming from the LHC.

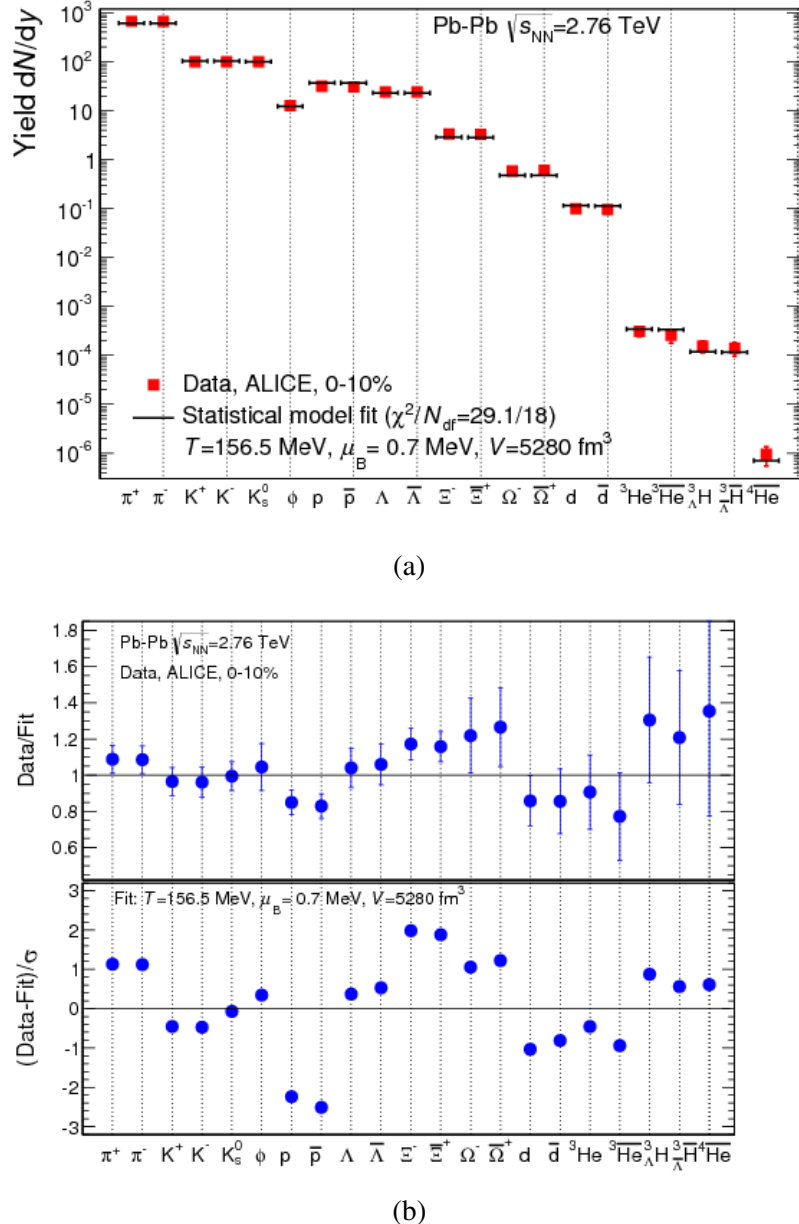


Fig. 2.2 (a) Hadron multiplicities (π^\pm , K^\pm , ϕ , p , \bar{p} , Λ , $\bar{\Lambda}$, Ξ^- , Ξ^+ , Ω , $\bar{\Omega}^+$, ${}^3\text{He}$, ${}^3\bar{\text{He}}$, ${}^4\text{He}$, ${}^4\bar{\text{He}}$) as measured in central Pb–Pb collisions (0–10%) at the LHC by the ALICE experiment [42, 40, 43–47] and relative fit. The best fit values from [41] are shown as well and the ratios of the measured values to the model are reported in the upper panel of (b) and divide by the experimental uncertainty in the lower panel.

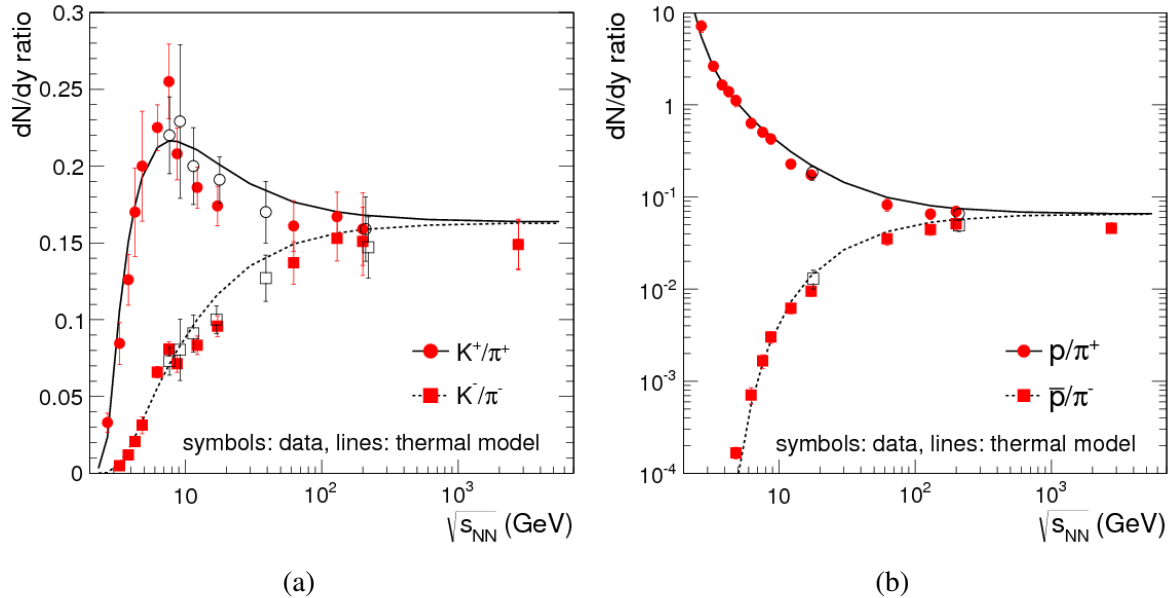


Fig. 2.3 K^+/π^+ and K^-/π^- (a), p/π^+ and \bar{p}/π^- (b) yield ratios as obtained from thermal model predictions compared to results at different collision energies [41]. The values of the temperature T and μ_B are obtained for each $\sqrt{s_{NN}}$ from the parameterization described in Fig. 2.4

to the one sketched in Fig. 1.3. In addition these results allow for a direct comparison with predictions from lattice QCD. The T_{Ch} temperature obtained from thermal model fits can be compared with the predictions for the critical temperature of the phase transition T_c obtained from lattice QCD calculations at vanishing μ_B [41]. Such comparison is shown in Fig. 2.4a. It is worth to note that the chemical decoupling happens at T_{Ch} which is fully consistent with the values of T_c (154 ± 9 MeV [19]) predicted by lattice QCD. This indicates that the hadronization occurs few instants before the chemical freeze-out.

The SHM is not only limited to heavy-ion collisions as it can also be applied to small systems such as pp and e^+e^- collisions. In this case [49] it is necessary to perform the computations in the canonical ensemble (at least requiring local strangeness conservation).

2.1.1 Strangeness enhancement

When considering the production of particles with strangeness content one would expect a suppression (with respect to other light quarks u and d) due to the conservation of quantum numbers (no strangeness is present in the initial state) and because of the larger constituent mass of s ($m_s = 1.4 \cdot m_u$). This is related to the fact that strong interactions conserve the strangeness number exactly, thus for the whole system $\sum S = 0$. This consideration has little

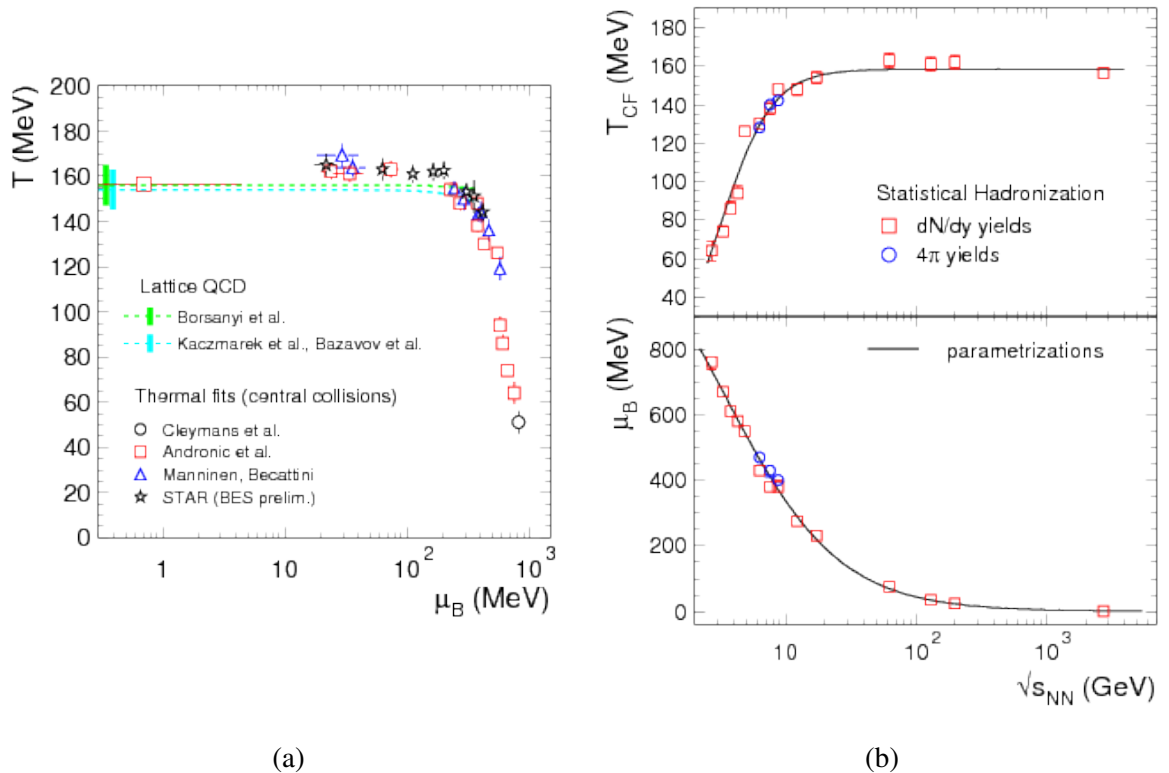


Fig. 2.4 (a) Phase diagram of QCD with data points as obtained at different energies from the thermal model fits from SIS up to LHC data [41] and compared to predictions of T_c from lattice QCD. Colored bands at low μ_B indicate the T values in the crossover regime. (b) Evolution of the temperature T_{Ch} and the μ_B as a function of the $\sqrt{s_{\text{NN}}}$ together with parameterization [48]. $T_{\text{Ch}} = T_{\text{Ch}}^{\text{lim}} / (1 + e^{2.6 - \ln \sqrt{s_{\text{NN}}} / 0.45})$, $\mu_B = a / 1 + 0.288 \sqrt{s_{\text{NN}}}$ with the temperature at the plateau $T_{\text{Ch}}^{\text{lim}} = 158.4$ MeV and $a = 1307.5$ MeV.

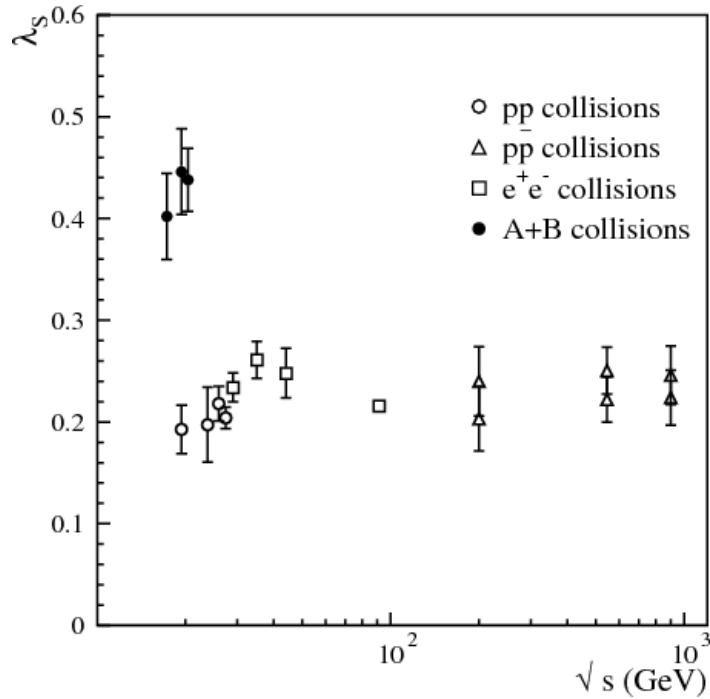


Fig. 2.5 Strangeness suppression factor measured by scaling the net strange content to the non strange one: $\lambda_s = 2 \langle s\bar{s} \rangle / \langle u\bar{u} + d\bar{d} \rangle$ [50]. Different collision systems are shown (pp, $p\bar{p}$, e^+e^- and AA).

effect if the volume of the source is large as the strangeness conservation has to be fulfilled on average over the whole system. Instead, the canonical ensemble needed to describe smaller systems such as as pp or e^+e^- , implies that strange hadrons are always produced in pairs (local strangeness conservation), resulting in a large energetic threshold that the system has to overcome (canonical suppression). As a consequence these processes are unlikely to happen in small source volumes [34]. The grand-canonical formulation instead assumes the average conservation of the strangeness quantum number, a condition that is easily reproduced in heavy-ion collisions. As expected, the strangeness suppression is observed in small collision systems such as pp, $p\bar{p}$ and e^+e^- , as shown in Fig. 2.5.

In heavy-ion collisions, thanks to the large energy densities, strange quarks can be produced thermally [51]. In the deconfined phase the large gluon density can lead to an increase in the production of $s\bar{s}$ pairs by gluon fusion processes. In addition, the restoration of the chiral symmetry in proximity to the temperature of deconfined transition lowers the constituent mass below ~ 150 MeV [52] thus decreasing the energetic threshold for its production. These two effects combined allow to significantly reduce the time scale for strangeness saturation and chemical equilibration [20]. As such, with respect to small systems, the enhancement in the strangeness production was proposed as a signature of the

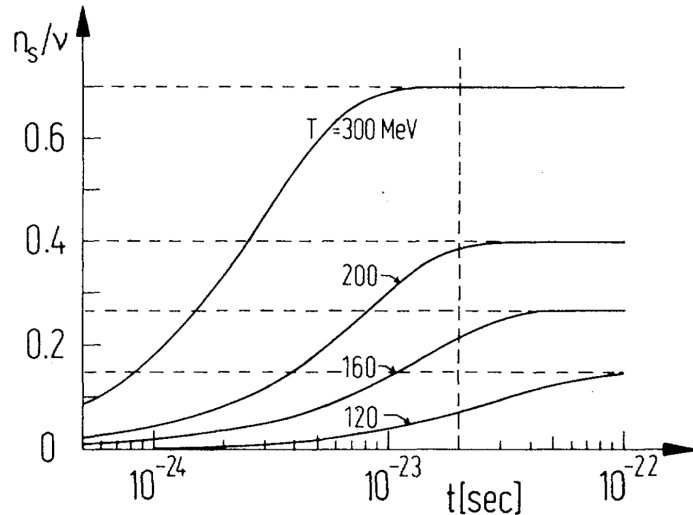


Fig. 2.6 Time evolution of the relative strange-quark to baryon-number abundance in the plasma for various temperatures [51].

presence of the QGP [51]. The time evolution of the net strange quark content (strange quark density relative to the baryon number) of the plasma state is shown for different temperature scenarios is given in Fig. 2.6. The net strange quark abundance is starting to saturate for temperatures above 160 MeV, this temperature is close to the one of the chemical freeze-out (T_{Ch}) where the relative particle abundances are fixed. As a consequence of the larger amount of strange quarks available before the hadronization it is expected that strange hadrons will be found more abundantly in the final state. The production of strange content in the plasma is predominant with respect to the one formed in interactions occurring after the hadronization phase. In this case the creation of $s\bar{s}$ pairs is kinematically suppressed. From considerations on the energy density the QGP is expected to form in heavy-ion collisions and not in small systems. The strangeness production is therefore expected to be enhanced exclusively in AA collisions and be suppressed in smaller systems. This is shown in Fig. 2.5 where the total amount of produced strangeness is doubled in AA with respect to pp.

A quantitative comparison between the production of strange hadrons in small and large systems is shown in Fig. 2.7. The yields of baryons and mesons with strangeness content ($\phi, \Lambda, \Xi, \Omega^-$) are measured for different in different centrality classes of AA collisions and compared to the pp results. In measurement in AA collisions shows a significant increase in the yield of strange particles with respect to the pp reference. The enhancement (the steepness of the rise) is greater for particles with larger strangeness content (such as $\Omega + \Omega$, $S = 3$), similar results are obtained from previous experiments at lower energies [53].

The strangeness enhancement is more evident if we compare the production of strange and non-strange hadrons. The yield enhancement with respect to the p-Pb values is shown as

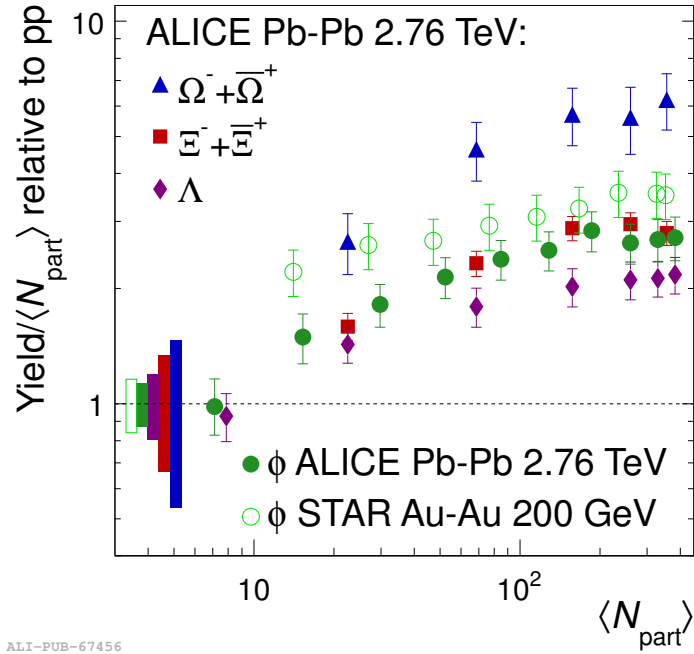


Fig. 2.7 Enhancement of ϕ , Λ , Ξ , and Ω^- as measured in Pb–Pb collisions at $\sqrt{s_{\text{NN}}} = 2.76$ TeV with respect to the pp reference yields [2]. The enhancement of the ϕ meson is also shown as measured in Au–Au collisions at $\sqrt{s_{\text{NN}}} = 200$ GeV.

a function of the particle net strangeness content in Fig. 2.8. While the yield increase is not much pronounced for the unidentified hadrons (h^-) it is shown that it is well correlated with the strangeness content for both mesons and baryons. This enhanced production of strange hadrons cannot originate from the hadronic phase and has to be present before chemical freeze-out. These observations are in agreement with the presence of thermalized gluons forming $s\bar{s}$ pairs.

2.2 The collective flow

The success of the SHM in describing particle production in both pp and AA collisions confirms the picture where the fireball can be thought as a thermalized gas of strongly interacting particles with quark and gluons as degrees of freedom. After being created in the collision the fireball expands while cooling down. The internal pressure of the fireball pushes the system from the inside forcing it to expand. The pressure is a thermodynamic property of the system and can be derived from the partition function as reported in Eq. 2.4. The particles velocities in the fireball are under the effect of pressure gradients and are not independent. The fireball starts behaving like a fluid as particles show correlated velocities that depend on their position. A direct consequence of this is that in the final state particle

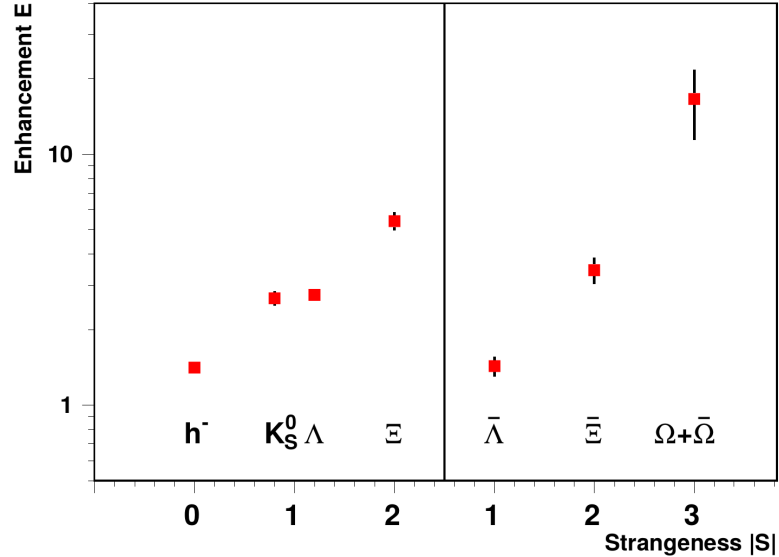


Fig. 2.8 Yield enhancement factor per participating nucleon as measured in Pb–Pb 158 AGeV collisions relative to the one measured in p–Pb collisions [34]. Both strange and non-strange hadron species are shown.

velocities will not be distributed according to random thermal motion, but instead will keep a collective motion imprinted by their common source. This means that the presence of a thermalized medium has an effect on the momentum distribution of particles, as it would happen in an expanding volume of gas. This feature is commonly called “collective flow” as opposed to the “non-collective flow” in which particles show uncorrelated velocities. The presence of collective flow in heavy-ion collisions can be explained as due to the presence of a strongly interacting QGP characterized by hydrodynamic evolution.

Collective flow can be defined more rigorously by considering in the fireball the volume ΔV located at x and the sum of the momenta of all particles inside ΔV ($\vec{p} = \sum_i \vec{p}_i$) the collectivity manifests if the flow velocity $\vec{v}(x) = \vec{p}/p^0$, with $p^0 = \sum_i p_i^0$ being the total energy inside ΔV . From this perspective, collectivity is equivalent to having momentum and space correlated to each other. The flow velocity can be separated into the component perpendicular to the reaction plane (“transverse flow” velocity v_T) and the one along the beam axis (“longitudinal flow” velocity v_L)

In order to quantify this effect one has first to understand how momenta are distributed among the particles in the fireball. This was first described in [54] by what is called now the “Cooper-Frye formalism”. By introducing kinematic variables such as the rapidity y , the

pseudo-rapidity η , the transverse and longitudinal (to the beam axis) momentum p_T and p_L , the transverse mass m_T :

$$y = \frac{1}{2} \cdot \ln \frac{E + p_L}{E - p_L} \quad (2.9a)$$

$$\eta = \frac{1}{2} \cdot \ln \frac{E + u_L}{E - u_L} \quad (2.9b)$$

$$p_T = \sqrt{p_x^2 + p_y^2}, \text{ being } p_z \text{ along the beam direction} \quad (2.9c)$$

$$m_T = \sqrt{m^2 + p_T^2} \equiv \sqrt{m^2 + p_x^2 + p_y^2} \quad (2.9d)$$

The expression of the Cooper-Frye formulation, derived in more detail in Appendix C, can be written as:

$$E \frac{d\langle N_s \rangle}{d^3 p} = \frac{1}{(2\pi\hbar)^3} \int_{\Sigma} d^3 \sigma(x) p f_s(x, p) \quad (2.10)$$

With φ indicating the polar angle in the xy plane perpendicular to the beam axis and $f_s(x, p)$ is the phase-space distribution defined in Eq. 2.7. From the expression of the Cooper-Frye formulation given in Eq. 2.10 we can summarize the following:

- Eq. 2.10 give the number of particles present inside of a hyper-surface in the $\Sigma(\vec{x}, t)$ containing the fireball. There are no particular requirements for Σ , for example the surface can coincide with the one covered by an experimental setup.
- The number of particles available within the surface Σ does not change as long as f_s is a solution of the collision-less Boltzmann equation $p^\mu \partial_\mu f_s(x, p) = 0$ i.e. the chemical freeze-out has already occurred.
- The momentum distribution of the particles within the surface Σ remains unchanged as long as the hadrons are evolving in the free-streaming regime i.e. the kinetic freeze-out already took place.
- In case the last two conditions are met it is useless to use a large surrounding surface as for $t \rightarrow \infty$ the result is expected to be the same, independently on the surface. There is no upper limit of applicability for the dimension of the surface. Instead, the presence of a fireball evolution in the early phase defines a limit where both particle relative abundances and their momentum distributions depend on the surface size.

The smallest Σ with fixed abundances and momenta distributions identifies the surface of last scattering Σ_f which corresponds to the surface of kinematic freeze-out. In order to be

able to compute the momentum spectra of single particle species one has to know the particle phase-space distribution at the time they reach Σ_f . It is generally assumed that such quantities cannot evolve wildly near the surface of last scattering. In models it is postulated that the end of the thermal equilibrium (mean free path ~ 0) is marked by an abrupt decoupling from the medium followed by a free-streaming regime (mean free path $\sim \infty$). This is known as the “Cooper-Frye” prescription. Following the same arguments as in [34, 55, 56], assuming angular symmetry (which is easily verified in central collisions) one can integrate over the angle φ and use the global properties at the time of the decoupling to obtain:

$$\frac{dN_s}{dy m_T dm_T} = \frac{g_s}{\pi^2 \hbar^3} \int_0^\infty r_T dr_T n_s(r_T) [m_T \cdot K_1 \left(\frac{m_T \cosh \rho(r_T)}{T} \right) \cdot I_0 \left(\frac{p_T \sinh \rho(r_T)}{T} \right) - p_T \frac{\partial \tau_f}{\partial r_T} K_0 \left(\frac{m_T \cosh \rho(r_T)}{T} \right) \cdot I_1 \left(\frac{p_T \sinh \rho(r_T)}{T} \right)] \quad (2.11)$$

Eq. 2.11 is valid for the generic case of non-instantaneous freeze-out on the surface.

- r_T indicates the position in the transverse plane.
- τ_f is the proper time corresponding to the freeze-out surface.
- $n_s(r_T) \equiv \tau_f e^{\mu_s/T}$ quantifies the radial density of the particle species s .
- u_T is the transverse flow velocity
- $\rho = \tanh^{-1}(u_T)$ is the “transverse flow rapidity”

Eq. 2.11 allows us to understand what are the effects of the medium on particle production and therefore determine the characteristics of the final state. From that we can derive global properties of the particle source. For example if we fix $\rho = 0$ (no flow condition) and the temperature $T = T_f$ for species s we get a simpler expression as $I_0(0) = 1$ and $I_1(0) = 0$:

$$\frac{dN_s}{dy m_T dm_T} \propto m_T K_1 \left(\frac{m_T}{T_f} \right) \sim m_T e^{-m_T/T_f} \quad (2.12)$$

Here the only explicit dependence of the particle distribution is on T_f and m_T , while first one does not depend on the particle species, the latter does. This property is known as “ m_T -scaling” and implies that all hadron have similar m_T -spectra. On the contrary, the presence of collective flow affects all particle species differently as heavier masses are shifted towards higher m_T . This effect is shown in Fig. 2.9 for different masses for two flow velocities

($\beta = 0.4$ and $\beta = 0.9$). As a consequence of the presence of flow, the m_T -scaling is expected to be broken. This is especially visible at low m_T while the effect weakens at larger m_T where all spectra have similar slopes. As expected, the freeze-out temperature has an important role as it determines the slope of the spectral shape. As derived in [57] in the flow regime the general T_{slope} that replaces T_f in Eq. 2.12 for the spectrum of particle s is defined as $T_{s, \text{slope}} = T_f + \frac{m_s}{2} \langle v_T \rangle^2$, which yields to these limits:

$$T_{s, \text{slope}} \simeq T_f + \frac{m_s}{2} \langle v_T \rangle^2, \text{ for } p_T \ll m_s \quad (2.13)$$

$$T_{s, \text{slope}} \simeq T_f + \sqrt{\frac{1+v_T}{1-v_T}}, \text{ for } p_T \gg m_s \quad (2.14)$$

A low p_T the formulation given in Eq. 2.13 allows to separate between the effect due to thermal motion (T_f) and the one caused by the radial flow. The latter appears to be coupled to the particle mass, yielding different slopes for different particle species (breaking the m_T -scaling). In general spectra are shown to have a steeper decrease at large p_T while flattening at low momenta. These formulations have of course their practical limitations: pions for instance (the lightest hadrons) are quickly falling into the relativistic case and are challenging to measure at extremely low momenta (especially in collider experiments). In addition, non-relativistic pions are affected by both Bose-Einstein statistics and contribution from resonance decays. The effect of the inclusion of resonance decays in computations can be seen in the solid black line of Fig. 2.9. This correction cannot be neglected for the description of the data.

The radial flow can be measured experimentally from the m_T or momentum distribution of identified particles. An example is give in Fig. 2.10 where the spectra of identified π^- , K^- and \bar{p} are shown for central Au–Au collisions and pp collisions. It is rather evident that for the pp case the three spectra have the same slope (m_T -scaling at work) while for the heavy-ion case the presence of the radial flow breaks the m_T -scaling. As expected, radial flow causes a mass-dependent flattening of the spectra in the low p_T region, while all spectra start to assume the same slope ad higher momenta.

The modification of the spectral shape affects also the mean of the distribution in a mass-dependent way, resulting in an increase of the $\langle p_T \rangle$ with the particle mass. This is observed from results at the RHIC and LHC energies reported in Fig. 2.11 as a function of charged particle density at mid-rapidity for different collision energies. The increase in the $\langle p_T \rangle$ is expected to be more evident when flow is stronger i.e. when energy densities are larger.

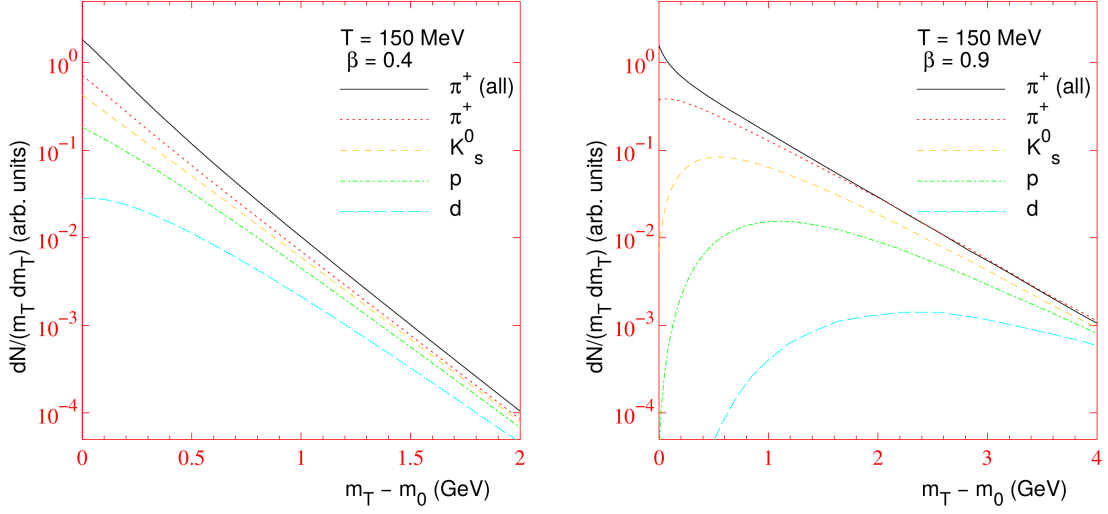


Fig. 2.9 Calculation of the m_T spectra for different particle species with non zero flow [34]. The effect on the spectral shape is more evident for heavier particles as the flow velocity increases. The contribution of resonance decays to the spectrum of pions is reported as π^+ (all), this inclusions have important effects on the spectral shape, especially for low m_T .

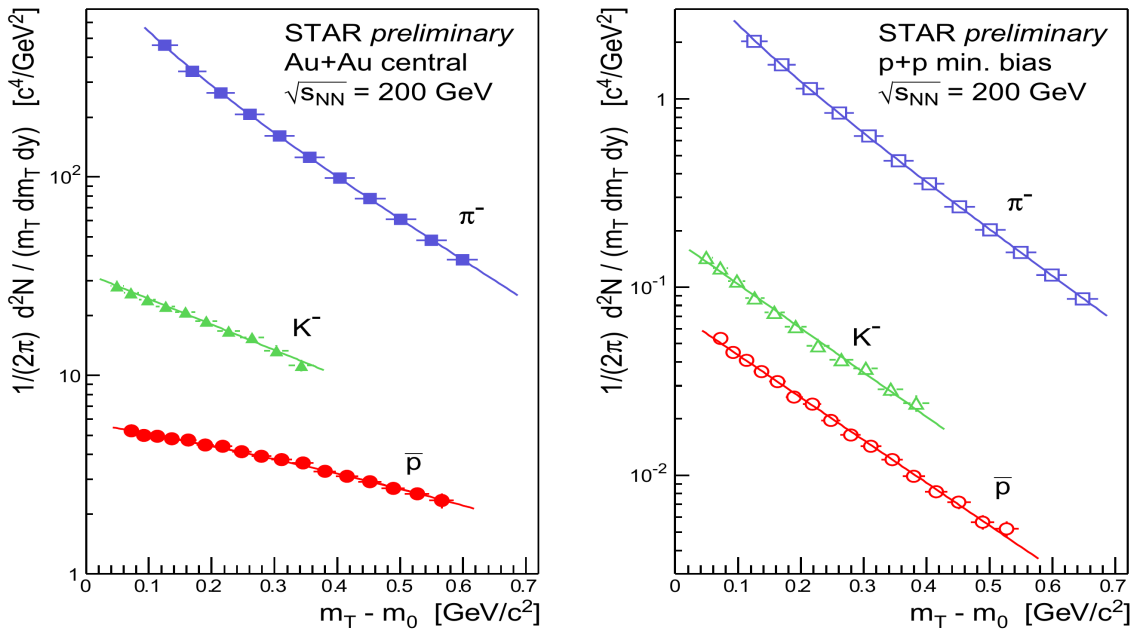


Fig. 2.10 m_T spectra of π^- , K^- and \bar{p} as measured at $(\sqrt{s})\sqrt{s_{NN}} = 200$ GeV in central Au–Au collisions (left) and pp collisions (right) by the STAR Collaboration [58, 34].

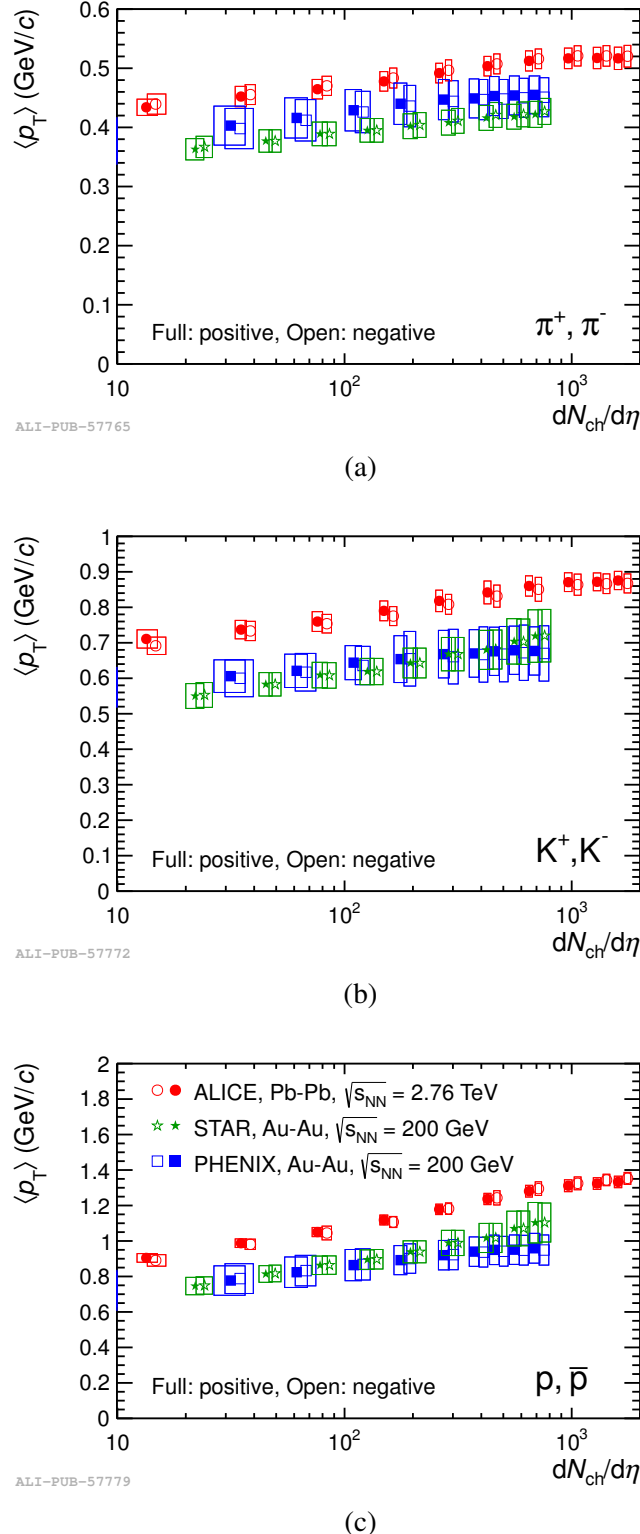


Fig. 2.11 (a) π^\pm , (b) K^\pm , (c) p, \bar{p} spectra $\langle p_T \rangle$ as measured in Pb–Pb collisions at $\sqrt{s_{NN}} = 2.76$ TeV and Au–Au collisions at $\sqrt{s_{NN}} = 200$ GeV [40]. A clear increase in the $\langle p_T \rangle$ is visible in central collisions.

The increasing trend of $\langle p_T \rangle$ with $dN_{\text{ch}}/d\eta$ is expected as in central collision the energy density of the fireball is larger and so is the radial flow. For the same reason, when going from $\sqrt{s_{\text{NN}}} = 200$ GeV to $\sqrt{s_{\text{NN}}} = 2.76$ TeV the $\langle p_T \rangle$ is significantly higher. The mass dependence manifests when comparing data in the most central collisions for different particle species: the $\langle p_T \rangle$ is found to be consistent between particle and anti-particle while assuming a hierarchical mass ordering ($\langle p_T \rangle_{\pi^\pm} < \langle p_T \rangle_{K^\pm} < \langle p_T \rangle_p$).

2.2.1 The Boltzmann-Gibbs Blast-Wave model

Eq. 2.11 can be simplified by assuming instantaneous freeze-out at $r_T = R$. In this case there is no dependence of the proper time at the freeze-out surface τ_f therefore $\frac{\partial \tau_f}{\partial r_T} = 0$. Only the first part of the expression survives yielding to:

$$\frac{dN_s}{dy m_T dm_T} \propto g_s m_T \int_0^R r_T dr_T K_1 \left(\frac{m_T \cosh \rho(r_T)}{T} \right) \cdot I_0 \left(\frac{p_T \sinh \rho(r_T)}{T} \right) \quad (2.15)$$

which is commonly known as the Boltzmann-Gibbs Blast-Wave model (BGBW) [56]. $\rho = \tanh^{-1}(u_T) \equiv \tanh^{-1}(\beta_r)$ is the flow rapidity while the velocity profile β_r is defined by the surface velocity β_s : $u_T(r_T) \equiv \beta_r(r_T) \equiv \beta_T(r_T) = \beta_s \cdot \left(\frac{r}{R}\right)^n$ defined by the profile shape parameter n and the maximum radius reached by the fluid at the freeze-out R .

The model can be used to perform a simultaneous combined fit to the different particle species in order to extract the properties of the common source such as the temperature T_f , the profile n and the velocity β . Alternatively it can be used to fit the single particle spectra. This approach is commonly used to extrapolate the spectra in the unmeasured regions of p_T .

The parameter T in the model corresponds to the kinetic freeze-out temperature described in Section 1.2.1. At this temperature all interactions cease and hadrons enter the free-streaming regime. While the BGBW model can be used to derive T_{Kin} , the SHM gives T_{Ch} .

An example of both single particle spectra and combined fit is shown in Fig. 2.12 for π , K and p measured by the ALICE Collaboration at $\sqrt{s_{\text{NN}}} = 2.76$ TeV. The agreement of the BGBW model with the spectra is quite remarkable, it is important to note that the single spectra fit and the combined one tend to agree more in central events where the thermal description is expected to work better. Conversely, for peripheral collisions the two fits give quite different results.

The values of the parameters obtained from the combined BGBW fit are reported for two collision energies as a function of the charged particle density at mid-rapidity in Fig. 2.13. As expected, the increased energy density available at higher collision energies is reflected

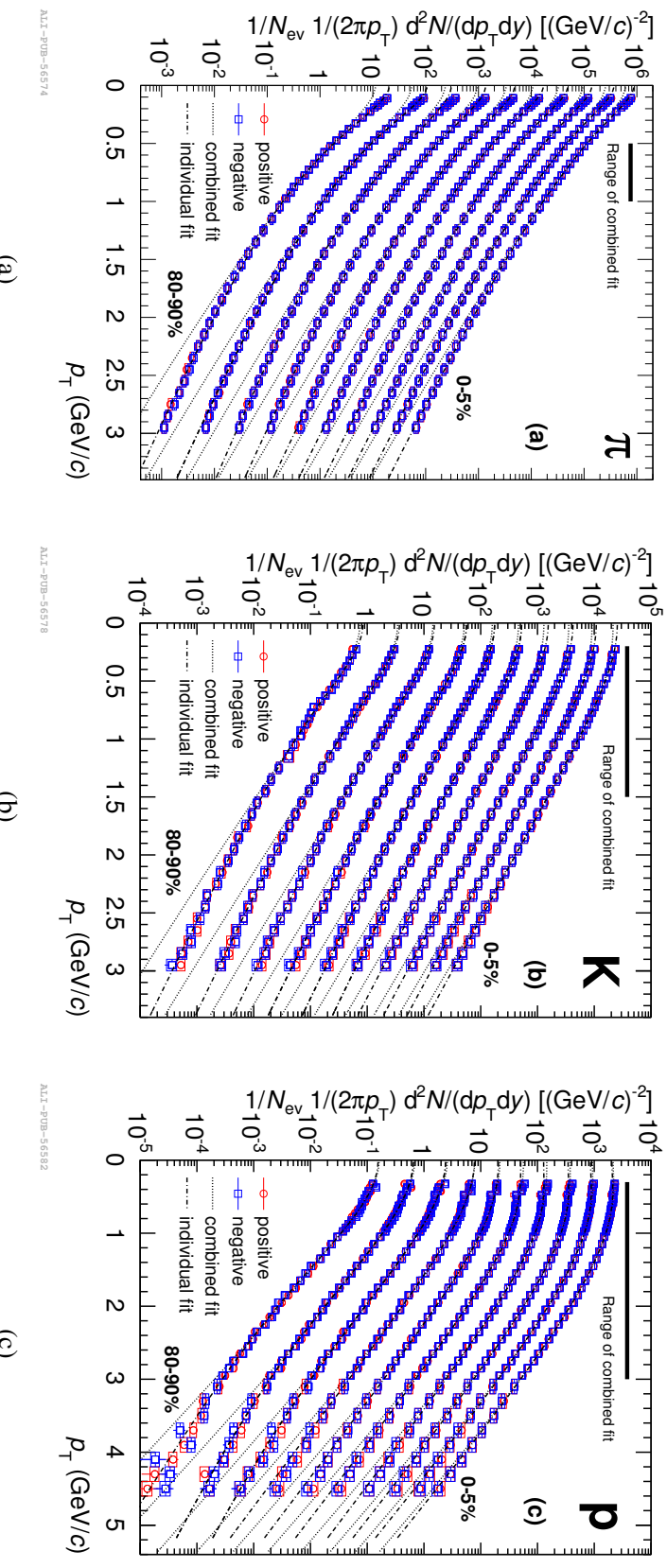


Fig. 2.12 p_T -dependent spectra of (a) π^\pm , (b) K^\pm , (c) p and \bar{p} spectra as measured in different centrality classes in $\sqrt{s_{NN}} = 2.76$ TeV [40]. Both single spectra and combined BGBW fit are shown.

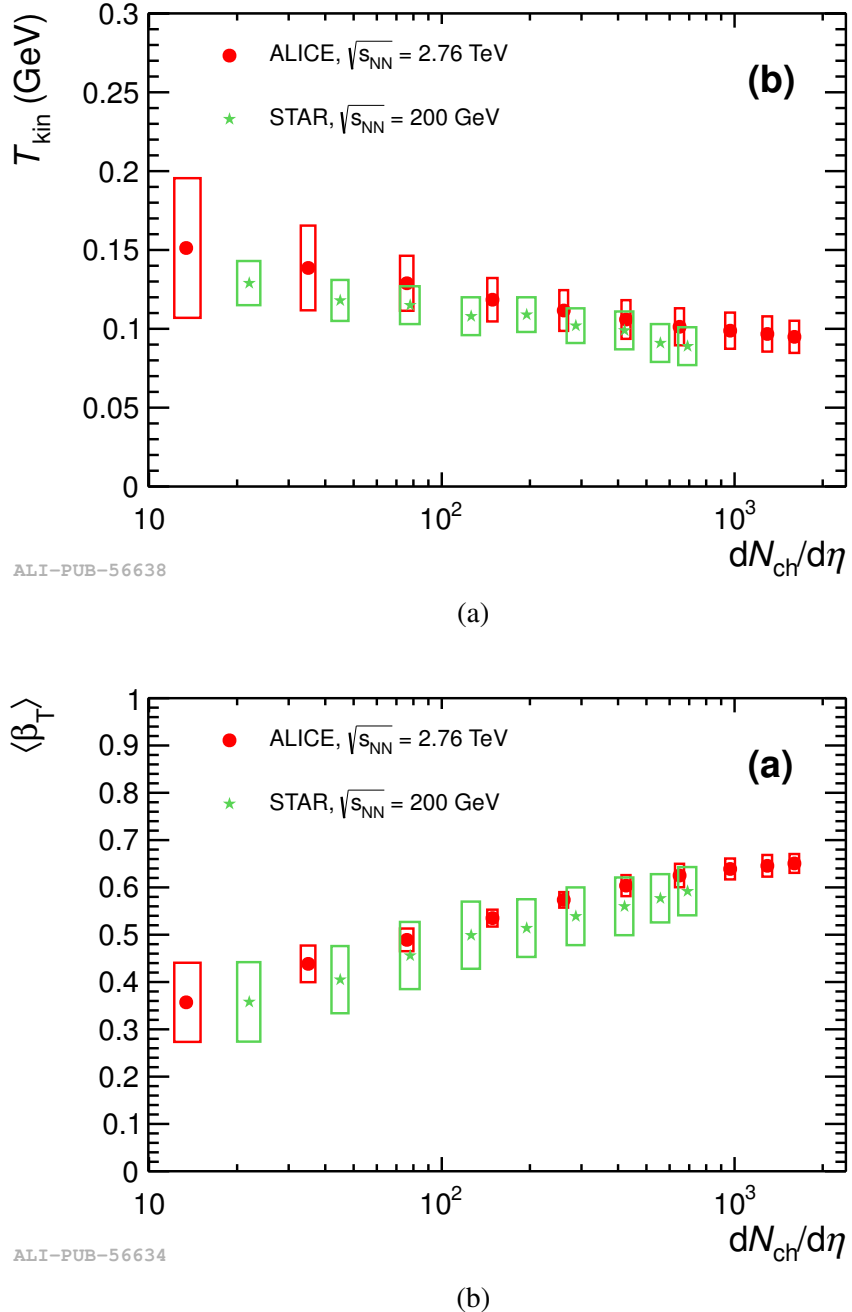


Fig. 2.13 (a) Temperature of kinetic freeze-out and (b) expansion velocity as obtained from the BGBW combined fit to the π^\pm , K^\pm , p and \bar{p} spectra measured in Pb–Pb collisions at $\sqrt{s_{NN}} = 2.76$ TeV and Au–Au collisions at $\sqrt{s_{NN}} = 200$ GeV [40].

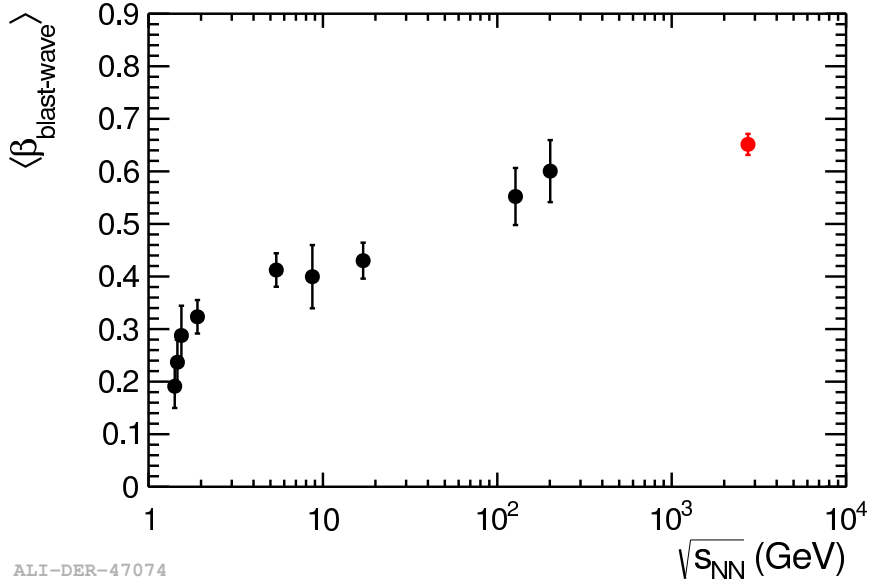


Fig. 2.14 Comparison of the expansion velocity as obtained from the combined BGBW fit to the spectra of π^\pm , K^\pm , p and \bar{p} in 0 – 5% centrality class as a function of the $\sqrt{s_{\text{NN}}}$ [40].

in larger expansion velocities. The centrality dependence of $\langle \beta_T \rangle$ can be understood in terms of a more rapid expansion for central collisions ($\langle \beta_T \rangle$ increasing with centrality). The temperature T_{Kin} is larger in peripheral collisions. This can be interpreted as due to the shortening of the fireball lifetime implying a quick decoupling of the particles from the medium.

The dependence on the collision $\sqrt{s_{\text{NN}}}$ can be better appreciated in Fig. 2.14, here the BGBW analysis is repeated for the most central collisions (0 – 5%) in different systems. The fact that the expansion velocity is only mildly rising in front of an increase of more than one order of magnitude in the collision energy between RHIC and LHC is quite striking. The radial flow seems to be saturating and the increased amount of energy available is spent in producing a large number of particles rather than in increasing the fireball pressure (Fig. 2.18). This could hint at the fact that beyond a certain energy threshold all systems are produced with similar characteristics.

2.2.2 Anisotropic flow

The manifestation of the liquid-like behaviour of the fireball is not to be found exclusively in the breaking of m_T -scaling. As a matter of fact radial flow is not the only type of collective effect that can characterize the evolution of the fireball.

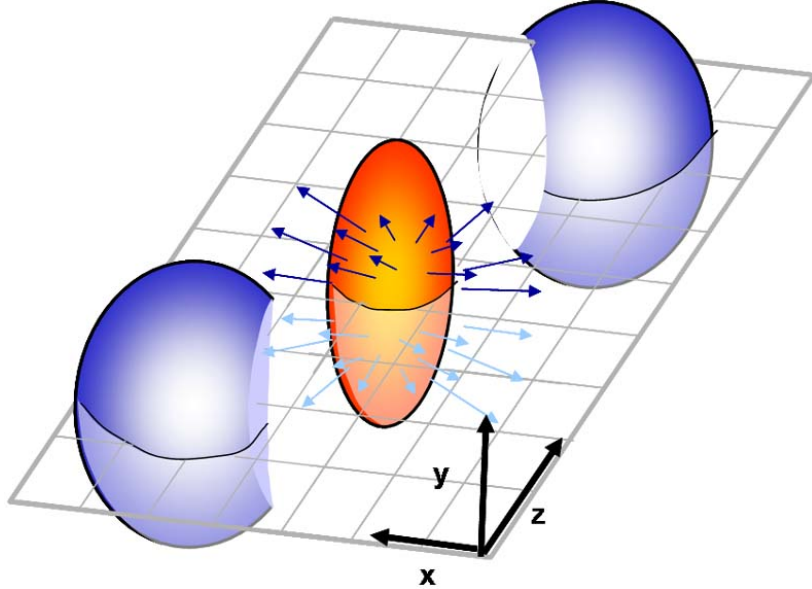


Fig. 2.15 Fireball that follows a peripheral collision represented in the collision Reaction Plane [3].

Particle production can be affected by the geometrical properties of an extended and strongly interacting medium. The spacial anisotropy of a highly asymmetric fireballs reflect in the pressure gradients that develop. This is the case, for instance, of non-central collisions. The system created in collisions with large impact parameter b is expected to extend more in the direction perpendicular to the Reaction Plane (RP). The anisotropic fireball created in peripheral collisions is depicted in Fig. 2.15.

The initial spacial anisotropy quickly turns into anisotropic pressure gradients that identify the RP as the preferred direction for particle emission. In such strongly interacting medium, pressure gradients are stronger when close to the reaction plane. This effect, known as elliptic flow (or anisotropic flow), introduces position dependent correlations in the momentum distributions of partons. Such anisotropies can be quantified by using a Fourier expansion:

$$E \frac{d^3N}{dp^3} = \frac{1}{2\pi} \frac{d^2N}{p_T dp_T dy} \left(1 + 2 \sum_{n=1}^{\infty} v_n \cos(n[\varphi - \Psi_{RP}]) \right) \quad (2.16)$$

The flow coefficients v_n take into account the amount of anisotropy in the particle production. Large v_n correspond to a strong anisotropic component while if v_n is null the emission is totally isotropic. The characteristic shape of each flow coefficient is show for different magnitudes in Fig. 2.16. The elliptic flow is represented by v_2 (elliptic shape), higher flow harmonics are the v_3 (triangular flow) and v_4 . A review of the several methods

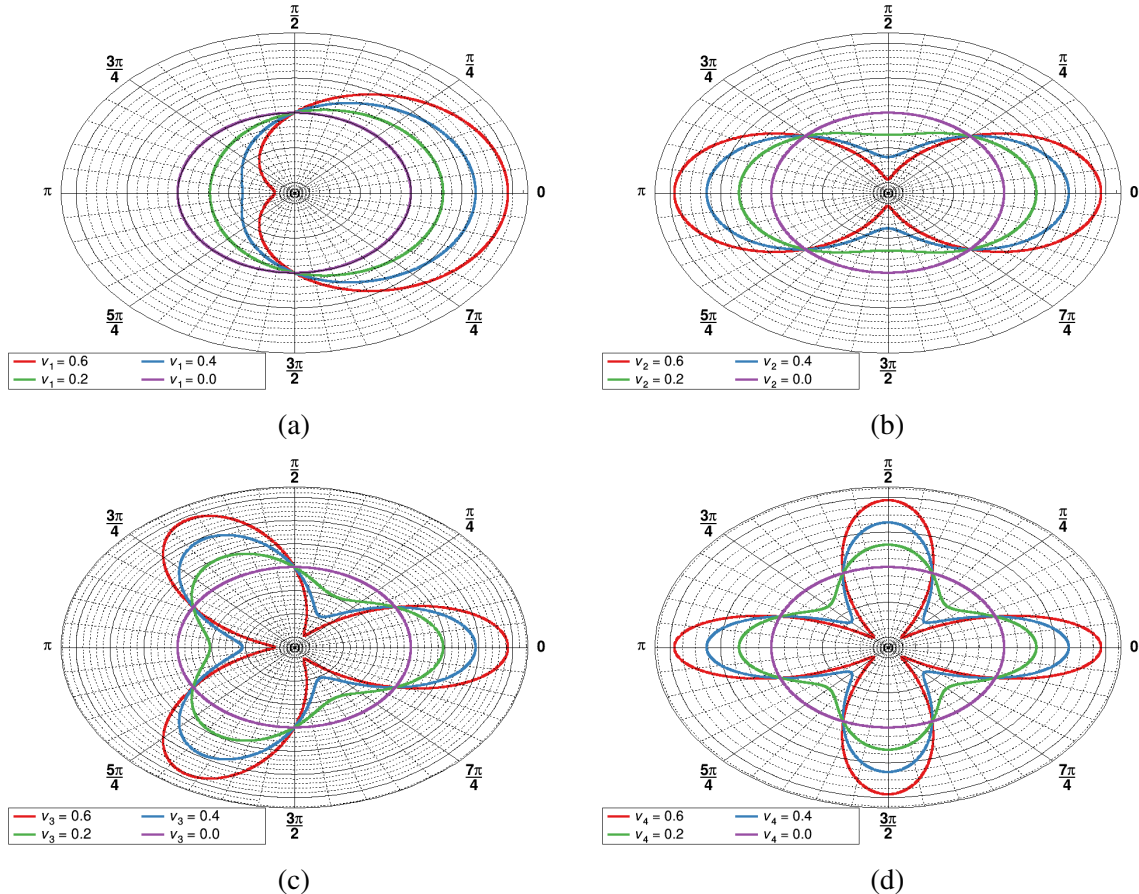


Fig. 2.16 Characteristic shape related to each component of the anisotropic flow given in Eq. 2.16.

available to obtain experimentally the coefficients of the anisotropic flow can be found in [59].

Recent results on the anisotropic flow of identified particle as measured in Pb–Pb collisions at $\sqrt{s_{\text{NN}}} = 5.02$ TeV by the ALICE Collaboration [4] are shown in Fig. 2.17. The amount of v_2 is shown to be increasing for all particle species in peripheral collisions indicating a strong effect of anisotropic flow.

2.3 pp collisions: more than a reference for heavy-ions

The importance of pp collisions as a reference for the heavy-ion case is discussed in this section together with most recent developments.

The number of particles produced in pp and pA collisions is considerably smaller than the one reached in AA. For this reason and considering the mere size of the projectiles involved,

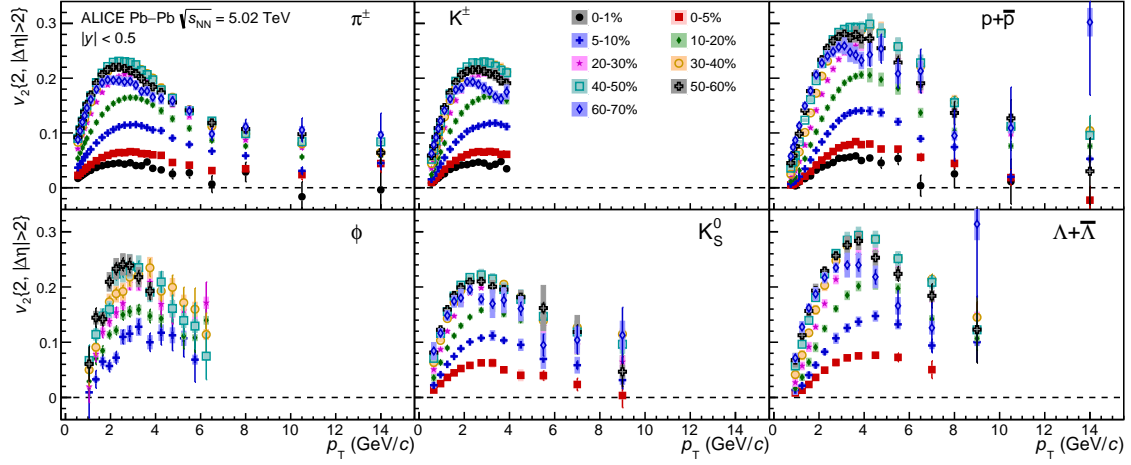


Fig. 2.17 Centrality dependence of v_2 for π^\pm , K^\pm , p and \bar{p} , $\bar{\Lambda}$, K_S^0 , and the ϕ -meson [4].

these collisions are commonly labeled as “small systems” when compared to AA. In this case the energy densities are much lower than the one reached in AA, meaning that both pp and pA collisions can be used as reference as no deconfined phase is expected to occur. The particle production in AA is often compared to the one in pp (pA) to highlight behaviour specific to presence of the deconfined phase. For example significant differences already appear when considering a global observable such as the inclusive charged particle multiplicity at mid-rapidity shown in Fig. 2.18. It is clearly visible that the particle multiplicities follow different trends (identified by different parameterization of the curve): for the heavy-ion case the rise is considerably steeper than for simple pp collisions. This behaviour seems to consistently differentiate between large and small systems independently on the collision energy.

The breaking of the m_T -scaling shown in Fig. 2.10 can be considered another characteristic of Au–Au collisions as it is not seen in pp. Before comparing different collision systems, it is important to distinguish between the mere effects of the presence of the nuclei in the reaction (cold nuclear-matter effects) from the ones originating during the QGP formation (hot nuclear-matter effects).

2.3.1 The Nuclear Modification Factor

The Nuclear Modification Factor (R_{AA}) is commonly used to compare particle production in pp and heavy-ion collisions and quantify the modification due to the QGP formation. The R_{AA} can be defined as:

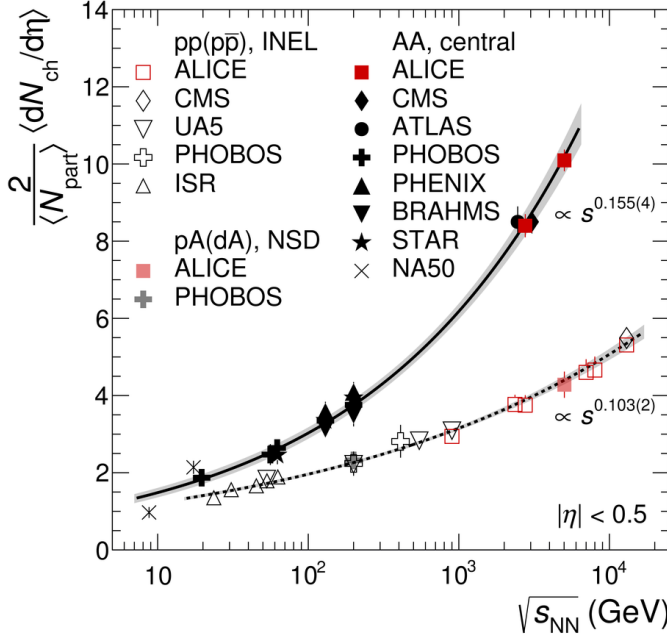


Fig. 2.18 Charged multiplicity multiplicity density $dN_{ch}/d\eta$ measured at mid-rapidity as a function of the collision energy in pp, pA and AA [31].

$$R_{AA}(p_T) = \frac{1}{\langle N_{Coll} \rangle} \cdot \frac{d^2N_{AA}/dydp_T}{d^2N_{pp}/dydp_T} \equiv \frac{1}{\langle T_{AA} \rangle} \cdot \frac{d^2N_{AA}/dydp_T}{d^2\sigma_{pp}/dydp_T} \quad (2.17)$$

Or integrating over p_T :

$$R_{AA} = \frac{1}{\langle N_{Coll} \rangle} \cdot \frac{dN_{AA}/dy}{dN_{pp}/dy} \quad (2.18)$$

This observable quantifies the discrepancy of a heavy-ion collisions from a sum of $\langle N_{Coll} \rangle$ incoherent nucleon–nucleon collisions. Therefore it is very sensitive to the QGP formation. A definition similar to the one of the R_{AA} is used for pA collisions, in this case we use the notation R_{pA} (R_{pPb} for p–Pb collisions). From the Nuclear Modification Factor measured in Pb–Pb and p–Pb collisions by ALICE one can identify three general behaviour:

- $R_{AA} > 1$: particle production in heavy-ion collisions is enhanced with respect to pp. This manifests as the Cronin effect in the low p_T region and can be explained through k_T broadening [60].
- $R_{AA} = 1$: there is no significant difference between pp and heavy-ion collisions. In this case the presence of the medium has no effect on the particle production as it can be described by a sum of uncorrelated $\langle N_{Coll} \rangle$ collisions. This condition is expected to

be verified when the system size is small i.e. in peripheral collisions or smaller systems (pA).

- $R_{AA} < 1$: particle production in heavy-ion is suppressed with respect to pp. Hard partons lose their energy in the strongly interacting medium of the thermalized phase by gluon radiation. The partonic energy loss is purely due to presence in the plasma of free color charge as degrees of freedom. This effect can reduce the amount of hard partons with large momenta resulting in less hadrons at high p_T and apparently unbalanced jets (jet quenching).

It is worth to note that despite the effect of the radial flow increasing the $\langle p_T \rangle$ of particle in the heavy-ion case, a strong suppression of the R_{AA} is observed at large momenta (for $p_T > 8 \text{ GeV}/c$) in central collisions. This effect has to be interpreted with the increasing steepness in the number of particle produced in AA collisions shown in Fig. 2.18. In the thermalized medium the energy of hard partons is absorbed and spent in the creation of a large number of soft particles. As a result of this, the QGP absorbs hard partons thus decreasing the number of particles at large momenta and suppressing the R_{AA} . The discrepancy between pp and pA is reduced when considering peripheral events, in this case the energy density of the fireball is smaller and the nuclear collision becomes closer to an incoherent sum of nucleonic scatterings.

It is possible to compute the R_{AA} for every particle species, each one accessing different stages of the QGP evolution. As an example the R_{AA} of charmonium states are particularly interesting as they give access to the very early moments after the collision. As described in Section 1.2.1 heavier quarks are predominantly produced in early hard scatterings, since the creation of the medium they interact with it for the whole duration of its evolution. The color analogue of the Debye screening for c quarks in a deconfined QCD dominated state is expected to result in a J/ψ suppression [61]: a typical signature of QGP formation. The color screening expected in heavy-ion collisions is of course not the only mechanism capable of modifying the J/ψ yield. Other processes, such as thermal production of c quarks, can occur at high temperatures. Any effect of the QGP presence on the J/ψ production would be visible in the R_{AA} : observing values lower (higher) than 1 following a suppression (enhancement). This could be useful to check whether the production mechanism of light particles is applicable also to the case of heavier quarks (c and b). The masses of these quarks are significantly larger than the one u , d , s quarks and of the system temperature before hadronization. For this reason their thermal production is heavily Boltzmann-suppressed (by $E/k_B T$). The thermal emission would also combine with the prompt production from hard scatterings, giving many concurrent channels to obtain the measured final state production.

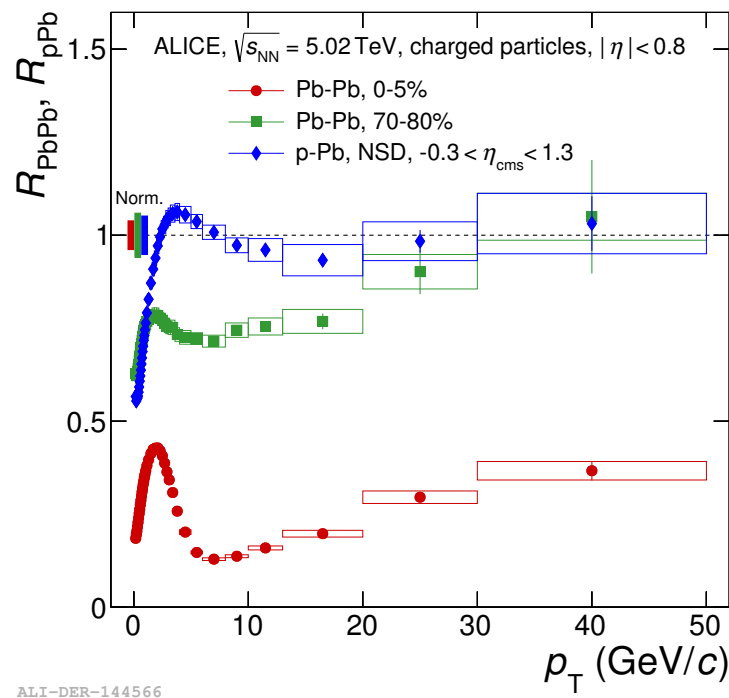


Fig. 2.19 Nuclear modification factors measured by ALICE in central (0 – 5%) and peripheral (70 – 80%) Pb–Pb collisions and in p–Pb collisions at $\sqrt{s_{\text{NN}}} = 5.02 \text{ TeV}$ [5].

Nonetheless the SHM can be extended to describe the hadrons containing heavy quarks so as to disentangle the different production mechanisms. Recent results [41, 48] show the suppression of the J/ψ in heavy-ion collisions but suggest that at LHC energies the thermal production of charm is enhanced.

In summary, the phases of the fireball evolution and its fundamental properties can be characterized in detail by combining theoretical models to experimental measurements in the light flavor sector. This motivates the detailed study of identified particle production in Pb–Pb collisions at $\sqrt{s_{\text{NN}}} = 5.02$ TeV that is the argument of this thesis.

2.3.2 From large to small systems: pp collisions vs multiplicity

The reference used for the comparison of particle production heavy-ion collisions is obtained from Minimum Bias (MB) collisions. These events are selected with basic cuts (e.g. by requiring at least one hit at mid-rapidity) in order to reduce any possible bias source (both from physical or detector reasons).

Nonetheless small systems are interesting per se to test QCD at extreme energies. For this purpose differential analyses can be carried out by collecting rare events where large number of particles are produced. Fig. 2.20 shows the multiplicity distributions as measured by ALICE in pp and p–Pb collisions at LHC energies [6]. At the LHC energies the measured distribution of charged particle multiplicities is considerably wide. Events of pp (pA) collisions can be classified according to the charged particle multiplicity produced. In some rare cases the produced multiplicity reaches ~ 10 times the one obtained on average. For these events the charged particle multiplicity becomes close (or even larger for pA) than the one measured in peripheral collisions. By probing the fraction of the cross section where multiplicities are the highest, one can highlight exotic processes of QCD that occur rarely in MB collisions.

In recent years the number of studies going in this direction increased significantly revealing unexpected features. The first significant results are shown in Fig. 2.21b for pp collisions. Here the two-particle angular correlations ($\Delta\eta = \eta_1 - \eta_2$, $\Delta\phi = \phi_1 - \phi_2$) are shown as measured in events with high multiplicity. The same type of correlation is reported as measured in p–Pb collisions in Fig. 2.21c. In this case the correlation obtained from low multiplicity events is subtracted to highlight the one specific to the high multiplicity events.

From the two-particle correlation measured in Pb–Pb collisions at $\sqrt{s_{\text{NN}}} = 2.76$ TeV is shown in Fig. 2.21d one can identify three main structures: the central peak at $(\Delta\eta; \Delta\phi) = (0; 0)$ originates from particles produced in the same jet; there is a long range (extending over a wide $\Delta\eta$ interval) correlation in particle emission in the “near side” ($\Delta\phi \sim 0$) due to the

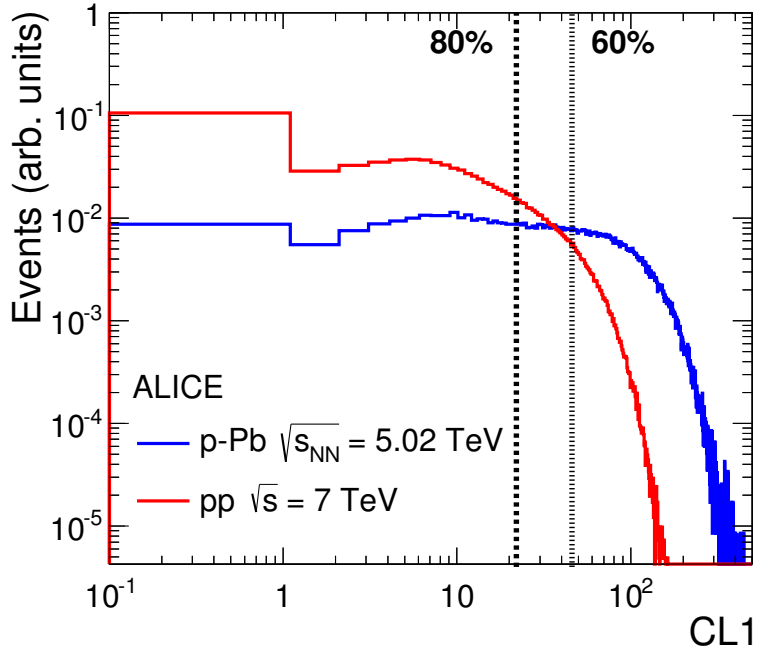


Fig. 2.20 Multiplicity distribution as measured in p–Pb collisions at $\sqrt{s_{\text{NN}}} = 5.02$ TeV compared to the distribution obtained in pp collisions at $\sqrt{s} = 7$ TeV [6]. The dashed lines mark the 80% and the 60% percentile of the p–Pb cross-section.

presence of collective flow; the “away side” ($\Delta\phi \sim \pi$) is characterized by a broad correlation (jet quenching).

Similar considerations can be drawn from Fig. 2.21b and Fig. 2.21c. The presence of a long range ridge in the near side close to the central peak at $(\Delta\eta; \Delta\phi) = (0; 0)$ is not visible in small collision systems unless one selects events with large multiplicities (~ 8 times larger than the MB for [62]). Nonetheless the similarities are limited to the near side as in the away side the ridge is greatly reduced only for Pb–Pb collisions (in Fig. 2.21d).

The fact that the near side ridge is observed independently on the collision system (if the multiplicity density is sufficiently high) suggests the presence of common mechanism of particle production rather than three separate regimes. The near side ridge in small systems could mean that a primordial collective evolution is already present at this stage and the charged particle multiplicity seems to be the correct scaling variable to describe these phenomena.

Several mechanisms were proposed to explain the origin of these ridge-like correlations, these among these the colour re-connection [65, 66], the jet-medium [67] and multi-parton induced [68, 69] interactions, or the possibility to form a high-density system in these collisions which could cause collective effects [70, 71]. These discoveries started a very rich

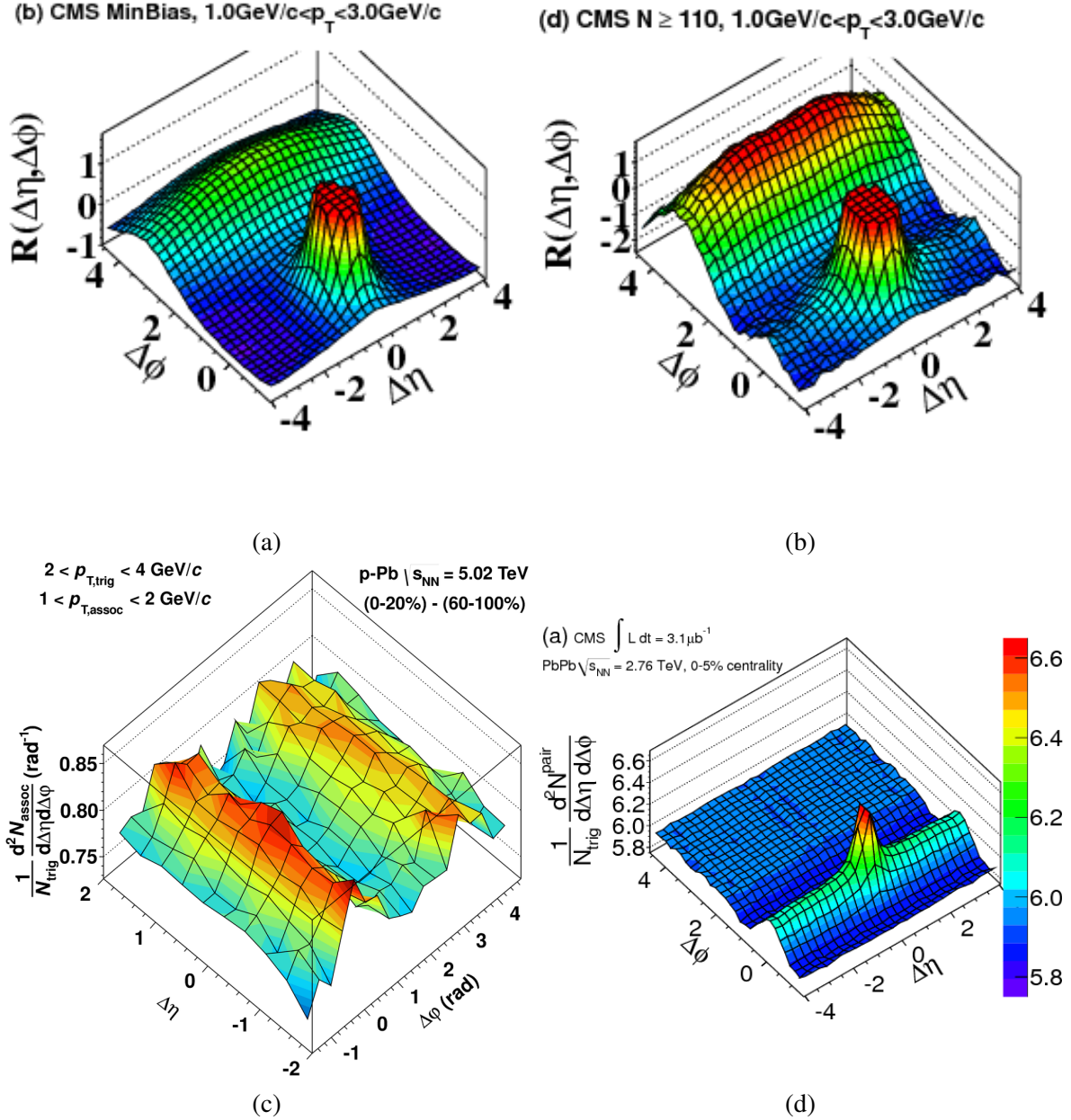


Fig. 2.21 $\Delta\eta - \Delta\phi$ angular correlation as measured (a) and (b) in pp collisions at $\sqrt{s} = 7 \text{ TeV}$ [62] for different reconstructed charged particle multiplicities (c) in p-Pb collisions at $\sqrt{s} = 5.02 \text{ TeV}$ [63] for the 0 – 20% multiplicity class (the correlation of 60 – 100% was subtracted) and (d) in most central Pb–Pb collisions at $\sqrt{s_{NN}} = 2.76 \text{ TeV}$ [64]. One can clearly see the long range ridge at $\Delta\phi \sim 0$ and extending along $\Delta\eta$ for the events where large charged particle densities are produced.

research field which is finding more and more similarities between small and large systems even connecting observables specific to the QGP such as the particle composition, collective phenomena and the strangeness enhancement.

In Fig. 2.22a are reported the ratios of strange particles (K_S^0 , $\Lambda + \bar{\Lambda}$, $\Xi^- + \Xi^+$, $\Omega + \bar{\Omega}$) to pion yields as a function of the charged particle multiplicity density $\langle dN_{ch}/d\eta \rangle$ for different collision systems [72] (pp, p–Pb and Pb–Pb). The lowest concentration of particles containing strangeness is observed in low multiplicity pp events (as expected from the canonical suppression). As the multiplicity increases the particle production seems to evolve without any evident discontinuity, independently on the collision system. The enhancement of strangeness is clearly visible as a function of $\langle dN_{ch}/d\eta \rangle$ as particles with larger strangeness content are relatively more enhanced (e.g. $\Omega + \bar{\Omega}$ with respect to K_S^0). This increase is evident from Fig. 2.23, where the hadron-to-pion ratio is shown scaled to the one measured in the MB pp events. This effect is purely due to the chemical composition of the hadrons under consideration as mesons and baryons with equal strangeness content show the same increase (e.g. K_S^0 and Λ in Fig. 2.23a). Standard event generators such as PYTHIA [73], DIPSY [74] and EPOS LHC [75] are in tension with the measured data. Modification to the usual mechanisms of particle production (such as color re-connection [65, 66], color ropes [76], string shoving [77]) were proposed to explain such behaviour. These mechanism show better agreement with the experimental data even In Fig. 2.22b are reported the spectra of identified particles as measured in high multiplicity pp collisions at $\sqrt{s} = 7$ TeV [78–81]. The parameters obtained from a combined fit to the $\pi^+ + \pi^-$, $K^+ + K^-$, $p + \bar{p}$ with the BGBW model are used to predict the spectral shape of other particle species. The BGBW model is found to describe the data relatively well and qualitatively manages to predict the shape for other particles.

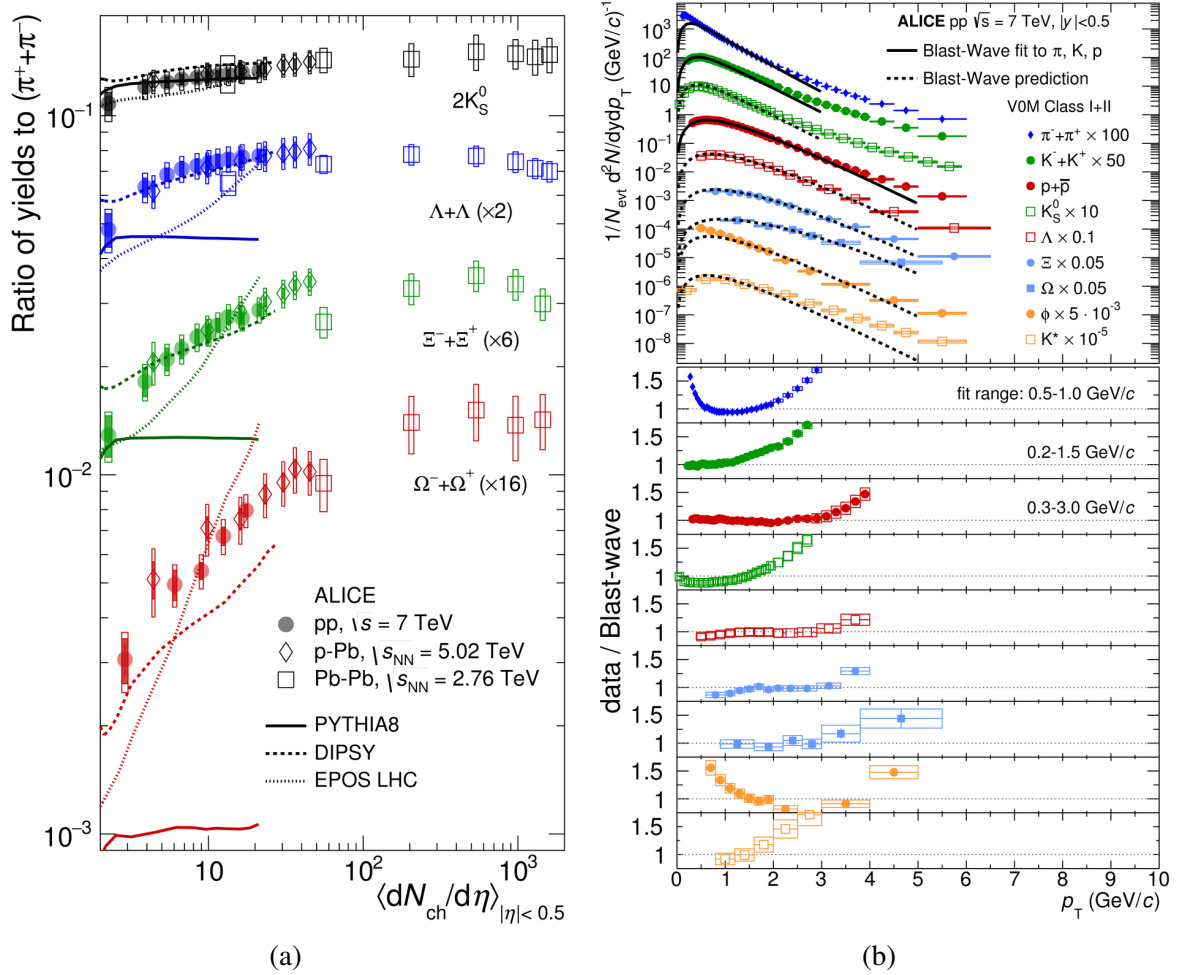


Fig. 2.22 (a) p_T -integrated yield ratios of strange and multi-strange hadrons to $\pi^+ + \pi^-$ as a function of $\langle dN_{ch}/d\eta \rangle$ measured in the rapidity interval $|y| < 0.5$ as measured in pp, p–Pb and Pb–Pb collisions [72]. (b) spectra of identified particles $\pi^+ + \pi^-$, $K^+ + K^-$, $p + \bar{p}$, K_S^0 , $\Lambda + \bar{\Lambda}$, $\Xi^- + \Xi^+$, $\Omega + \Omega$, ϕ , K^* as measured in pp collisions at $\sqrt{s} = 7$ TeV in high multiplicity events [78].

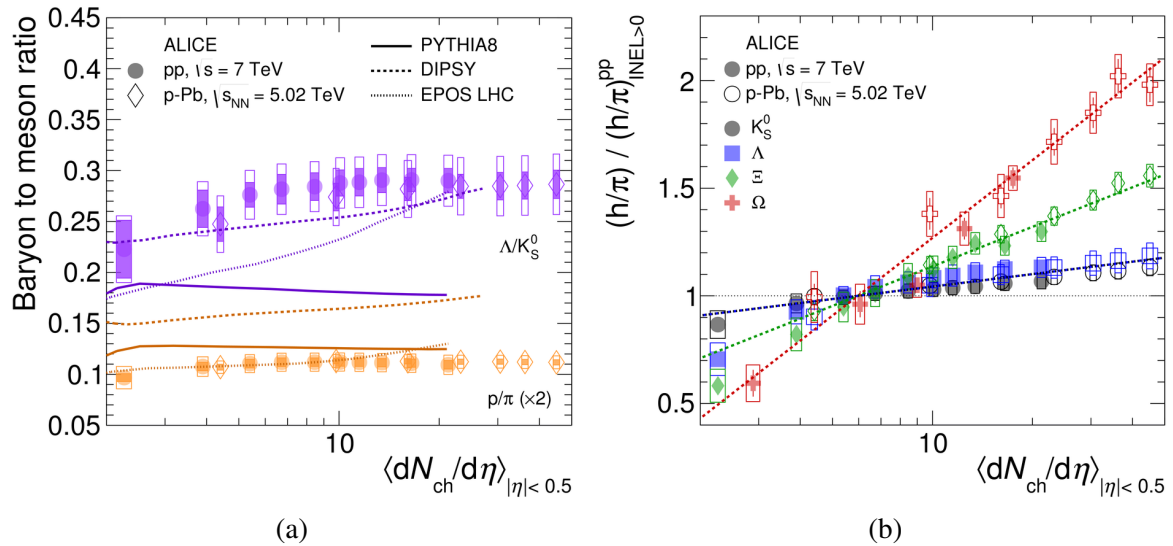


Fig. 2.23 (a) $p/(\pi^+ + \pi^-)$ and $(\Lambda^0 + \bar{\Lambda}^0)/(2K_S^0)$ ratios as a function of $\langle dN_{ch}/d\eta \rangle$ as measured in pp collisions at $\sqrt{s} = 7 \text{ TeV}$ [72]. Baryon to meson ratios of hadrons with same strangeness show no significant increase. (b) Double ratios $h/(\pi^+ + \pi^-)$ over $h/(\pi^+ + \pi^-)$ in MB collisions.

Chapter 3

A Large Ion Collider Experiment

In this chapter we discuss the experimental setup of the A Large Ion Collider Experiment (ALICE) which is used for all the new measurements that will be reported in this thesis. The main subsystems of the ALICE apparatus that were used for the analysis are described here.

The European Organization for Nuclear Research (CERN) was founded in 1954; its laboratories are located along the Franco-Swiss border near the city of Geneva. Since then the CERN complex has been growing with the addition of many new elements. The last one is the the Large Hadron Collider (LHC), so far it's the largest and most powerful particle accelerator in the world [15]. The operations of the accelerator are separated into periods covering several years (Runs). Two runs of data taking with collisions were performed so far (Run 1 2009-2013 and Run 2 2015-2018). The data taking periods alternate with Long Shutdown phases (LS) during which no beam is accelerated. During this time period, the accelerator equipment and the detectors maintained are upgraded.

The first LS (LS 1) was performed during the years 2013-2015. The next Long Shutdown phase (LS 2) is planned for the next years (2019-2020). During this period several subsystems of the ALICE detector will be upgraded, to improve the reconstruction performance and record data at high rates¹. After this phase of upgrade Run 3 will take place in 2021-2023. Another major upgrade phase will be starting at the end of Run 3 in preparation of Run 4 (2027-2029).

The LHC is capable of accelerating both pp and heavy ions at ultra-relativistic energies. This versatility allows the extension of the physics program of the machine to study nuclear interactions at extreme energies, these are the main subjects studied by the ALICE experiment. All collision systems and their energy used in the LHC during Run 1 and Run 2 are shown in Table 3.1.

¹At the highest interaction rate ALICE will record Pb–Pb collisions at 50 kHz.

Collision system	Energies (\sqrt{s} , $\sqrt{s_{\text{NN}}}$)
pp	900 GeV, 2.76, 5.02, 8.16, 13 TeV
p–Pb	5.02, 8.16 TeV
Pb–Pb	2.76, 5.02 TeV
Xe–Xe	5.44 TeV

Table 3.1 Collision energy and collision systems of Run 1 and Run 2

It is worth to note that it is generally preferred to collect pp collisions at the same energy of the heavy-ion case so as to give a reference for the computation of significant quantities such as the Nuclear Modification Factor.

In the LHC, the charged particles are accelerated via radio-frequency cavities (RF cavities) located on the circumference of the accelerator and oscillating with frequency ~ 400 MHz. In order to be accelerated, particles have to be synchronized with the frequency of the RF cavities (synchronous particle). All particles in the accelerator oscillate around the position of the synchronous particle. For this reason particles are concentrated in bunches, distributed along the LHC circumference. In the LHC, the bunch separation is about 7.5 m or 25 ns, this separation corresponds to ten times the period of the RF cavities [82]. During fills, the bunches are injected in the LHC with the correct bunch spacing. The separation of particles into bunches is performed earlier in the acceleration chain by the PS synchrotron.

Four main points of interaction are arranged along the LHC circumference (Fig. 3.1), each site is occupied by an experiment: ALICE, ATLAS, CMS, LHCb. These experiments all differ in their design and are focused on complementary sectors of the Standard Model [83].

3.1 The ALICE detector

The ALICE detector is located at the interaction point IP2 (Point 2) on the LHC ring. The ALICE apparatus was built to study the QGP by covering the physics cases described in Chapter 1. High energy heavy-ion collisions are the only known way to produce QGP in laboratory. As a high energy heavy-ion experiment, the ALICE detector has to fulfill tight operational requirements to allow the detailed study of the deconfined phase.

To cope with the high charged particle densities (up to 8000 charged particles per rapidity unit at mid-rapidity were expected at the time of the experiment design) the ALICE subsystems were built with very fine granularity so as to minimize the probability of having multiple hits in the same sensitive region.

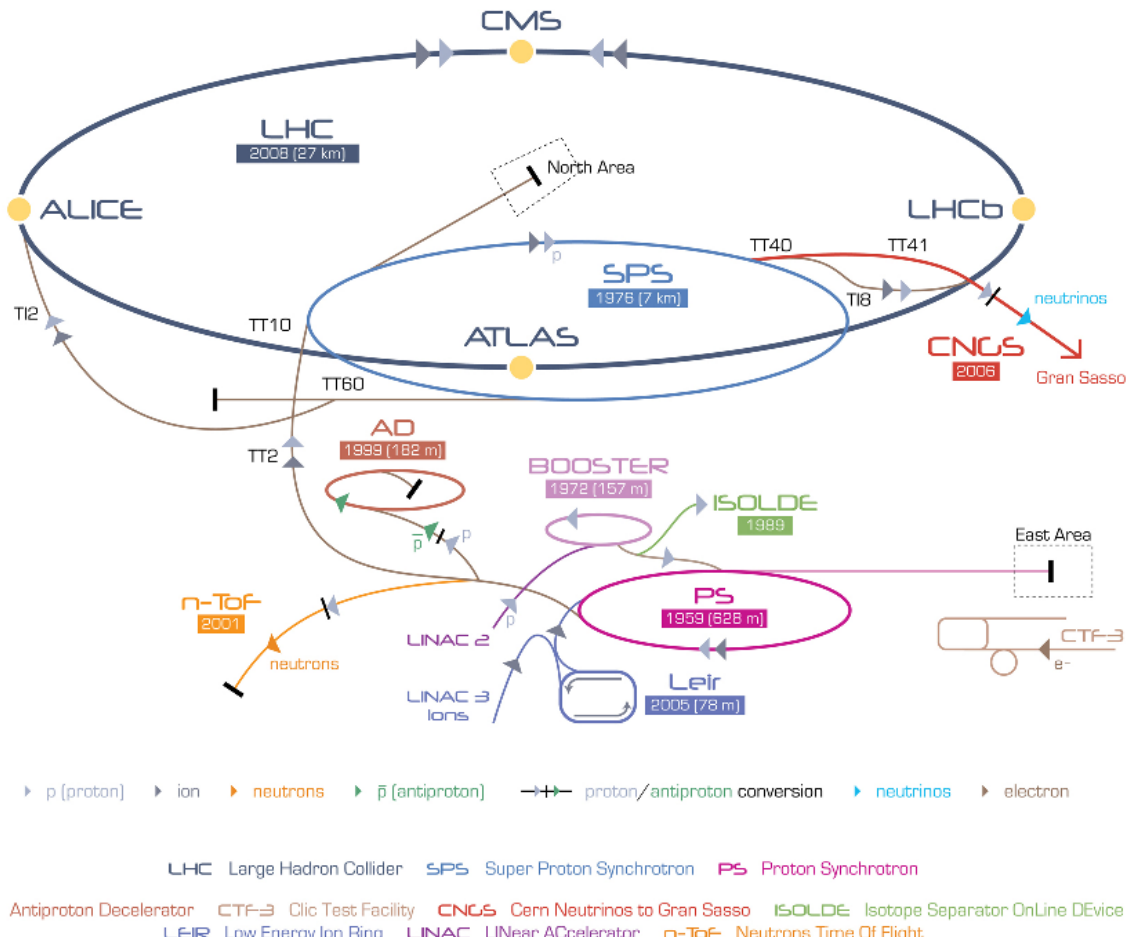


Fig. 3.1 Scheme of the CERN accelerator facility with the main experiments that take place at the LHC, the ALICE experiment is one of them. The many steps that precede the injection of the beam in the LHC ring are visible following the lines starting from LINAC 2 and LINAC 3.

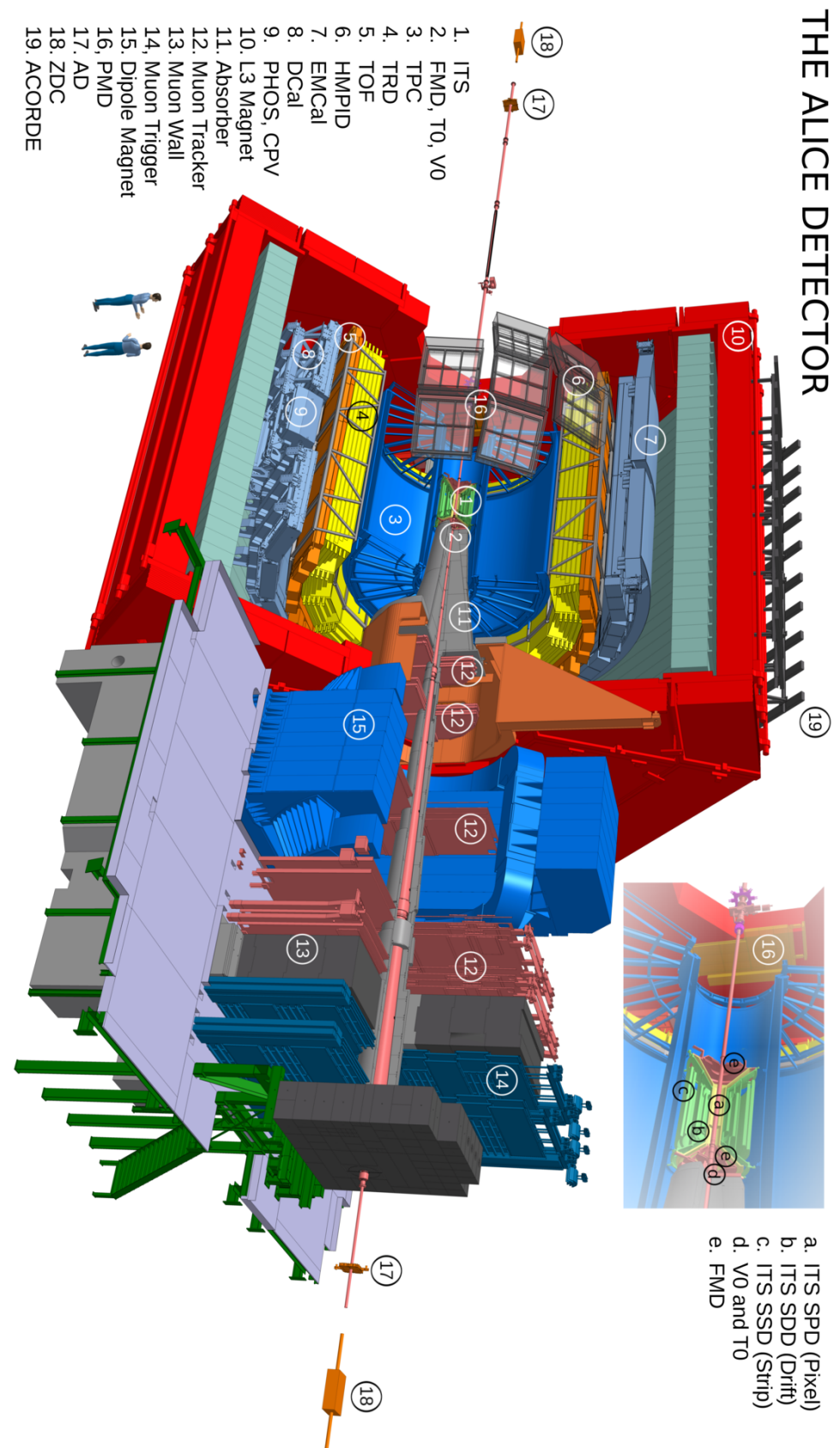


Fig. 3.2 Layout of the ALICE detector in Run 2.

As discussed in Chapter 1, the detector has to be able to measure particles down to very low p_T to access the “soft” probes. Hard probes are important to give a complete picture of the QGP, these can be accessed by reconstructing jets, open heavy flavor and quarkonia. In order to cover these topics the ALICE detector can provide high precision tracking for particles in a wide p_T range ($100 \text{ MeV}/c - 100 \text{ GeV}/c$). In addition the detector is provided with Particle IDentification (PID) capabilities obtained by combining different technologies in several sub-detectors.

On top of that, quarkonia states can be accessed in the forward rapidity region by measuring their muonic decay channels. The ALICE apparatus is divided into two parts: one at mid-rapidity ($|\eta| < 1$ “central barrel”) and one at forward rapidity $-4 < \eta < -2.5$ (“muon spectrometer”). Two magnets are used to bend particle trajectories in the two pseudorapidity intervals, they are shown in the detector representation of Fig. 3.2. All detectors in the central barrel are embedded in a magnetic field provided by a room-temperature solenoid magnet used previously in the L3 experiment at the Large Electron Positron (LEP) collider. The solenoid magnet is operated at nominal intensity of 0.5 T. In addition, during Run 2, a low B-field configuration with $B = 0.2$ T was used for short periods of time. In the configuration with low magnetic field both detection efficiency of soft particles and momentum resolution are increased. The magnet completely surrounds the Interaction Point (IP) with full azimuthal coverage. The L3 magnet provides a solenoidal field parallel to its axis, along the Beam Pipe (BP).

Surrounding the BP at forward rapidity, outside the L3 magnet, there is a large warm dipole magnet capable of producing a 3 Tm field integral. Hadrons and photons coming from the interaction vertex are stopped by a passive absorber located in front of the dipole magnet with respect to the interaction point. This filter provides a cleaner environment at forward rapidity for the detection of muons. By design only muons of $p > 4 \text{ GeV}/c$ are allowed to reach the high-granularity tracking system made of 10 detection planes shown in Fig. 3.2 [84].

This chapter is dedicated to the detectors located at mid-rapidity that are used for the analysis presented in this work. These detectors allow the tracking and the PID by measuring specific quantities that depend on the particle species:

- The Inner Tracking System (ITS) described in Section 3.1.1:
A six layer silicon detector based on three different technologies: Silicon Pixel Detector (SPD), Silicon Drift Detector (SDD) and Silicon Strip Detector (SSD). Used for mostly for vertexing and tracking it can also perform PID via analogue measurement of the dE/dx in the SDD and SSD.

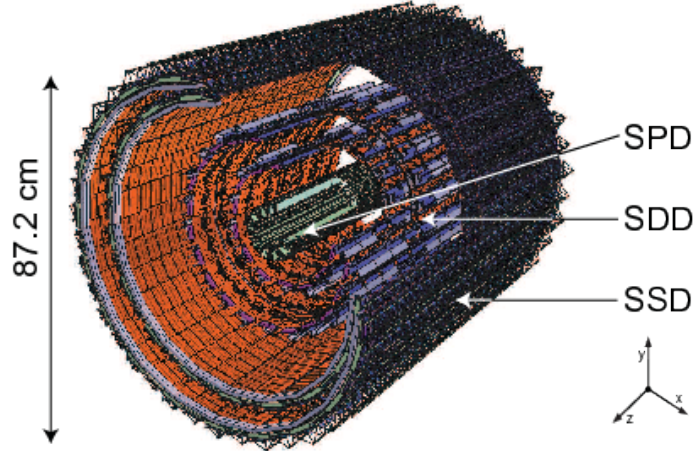


Fig. 3.3 Schematics of the ITS detector.

- The Time Projection Chamber (TPC) described in Section 3.1.2:
A $\sim 90 \text{ m}^3$ cylindrical detector built around the BP with 2π azimuthal coverage in $|\eta| < 1$. It is used for tracking of charged particles and PID via the measurement of the specific particle energy loss (dE/dx) by ionization.
- The Time-Of-Flight (TOF) described in Section 3.1.3:
A large area ($\sim 140 \text{ m}^2$) gaseous detector that provides particle identification in the intermediate p_T range and a dedicated trigger for cosmic ray events and Ultra Peripheral Collision collisions (UPC).
- The High Momentum Particle IDentification (HMPID) described in Section 3.1.4:
An array of Ring Imaging Cherenkov (RICH) detectors located in the outer region of the “central barrel” designed for the identification of high p_T hadrons.
- The detectors at forward rapidities, used for the characterization of the collision, are described in Section 3.1.5.

A brief description of these subsystems will be given in the next sections, more information on the detector design and performance can be found in [11, 85, 86].

3.1.1 The Inner Tracking System (ITS) detector

The ITS detector [87], the innermost part of the central barrel, is sketched in Fig. 3.3, its six concentric layers of silicon detectors are shown. The ITS is disposed all around the BP (a $800 \mu\text{m}$ thick beryllium cylinder of 3 cm of radius that contains the crossing beams) and

Layer	Type	r (cm)	$\pm z$ (cm)	Area (m^2)
N°1	pixel	3.9	14.1	0.07
N°2	pixel	7.6	14.1	0.14
N°3	drift	15.0	22.2	0.42
N°4	drift	23.9	29.7	0.89
N°5	strip	38.0	43.1	2.20
N°6	strip	43.0	48.9	2.80
Total area				6.28

Table 3.2 ITS layer dimensions.

covers the pseudorapidity interval $|\eta| < 0.9$ for interactions occurring within 10 cm from the detector center (along the beam axis z). The geometrical dimensions of the layers are reported in Table 3.2. For the operational point of view, each layer can be considered as independent detectors. The construction was carried out by using different technologies depending on the role of each one of them. For instance the two innermost layers of Silicon Pixel Detector (SPD) are used to locate the primary vertex with a resolution better than $100 \mu\text{m}$ and isolate events coming from pileup. The other four layers allow particle identification by measuring the particle dE/dx . The interaction vertex position determined with two SPD layers provides the information needed for the tracking of charged particles in the whole experiment. All-together the six layers of the ITS are used to propagate to the primary vertex the tracks reconstructed in outer detectors. In addition the ITS provides a “stand-alone” tracking that reconstructs charged particles in the low p_T region by using exclusively the information from its six planes. Thanks to this feature the ITS can be used for the measurement and identification of low p_T particles (e.g. pions with $p_T < 80 \text{ MeV}/c$). The tracking system has to meet the requirements of the heavy-ion program by measuring several thousands of particles produced per event. The high granularity of ITS allows to keep the detector occupancy below a safe level. The good resolution of the detector allows to separate primary and secondary vertices from the weak decays, hyperons, D and B mesons. The analogue readout in the four outer layers (Silicon Drift Detector and Silicon Strip Detector) samples the particle energy loss in the material, this information is sufficient to perform PID below $700 \text{ MeV}/c$.

3.1.2 The Time Projection Chamber (TPC) detector

The TPC [88, 89] is the main tracking detector in the central barrel. As sketched in Fig. 3.4, the detector has cylindrical symmetry: at the center, perpendicular to the cylinder axis, there

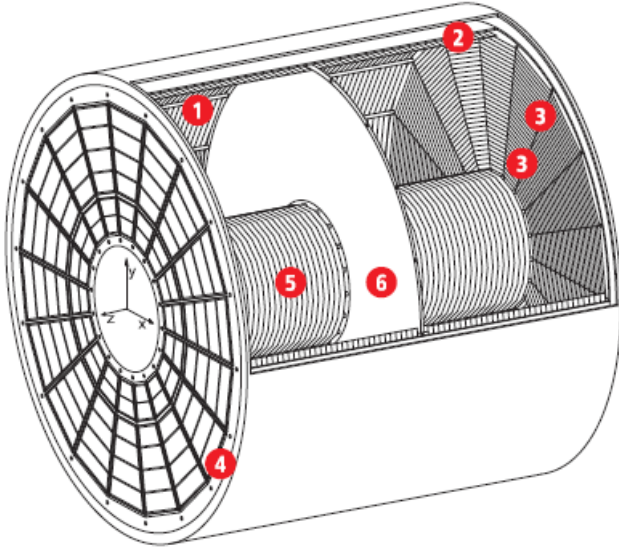


Fig. 3.4 Schematics of the TPC detector: 1) Field cage 2) Outer containment volume 3) Readout chambers 4) End plate 5) Inner containment volume 6) Central electrode.

Period	Gas mixture	Gas percentage
TDR	Ne-CO ₂	(90-10)
2010	Ne-CO ₂ -N ₂	(90-10-5)
2011	Ne-CO ₂	(90-10)
2015	Ar-CO ₂	(88-12)
2017	Ne-CO ₂ -N ₂	(90-10-5)

Table 3.3 Gases used so far inside the ALICE TPC.

is the high voltage electrode; the walls of the cylinder form the field cage. The active volume starts at an inner radius of ~ 85 cm, with an outer radius of ~ 250 cm, the grand-total span along the beam direction is of 500 cm. The total volume of TPC (~ 90 m³) can be filled with different gases depending on the running conditions, the list of gases used so fare in both Run 1 and Run 2 is listed in Table 3.3. The pseudorapidity range covered by the TPC is $|\eta| < 0.9$ for tracks with full radial length. Thanks to its large radial coverage, it has a wider pseudorapidity acceptance for tracks with incomplete length. TPC provides a charged-particle momentum measurement coupled with good two-track separation. TPC is also used, together with the ITS, to determine the primary vertex of the collision by extrapolating the reconstructed tracks to the interaction point. It allows also to identify particle by sampling their specific energy loss, dE/dx .

The primary electrons produced by the ionizing particles are transported over distances up to 2.5 m (half of the length of the TPC at most) on either side of the central electrode and collected by the end plates. The readout is done by using multi-wire proportional chambers positioned at each end-plate. The position resolution for the inner/outer radii ranges from 800 to 1100 μm in the transverse plane ($r\phi$) and from 1100 to 1250 μm along the beam axis (z). The total charge collected at the end plates for each track is proportional to the particle energy loss in the gas. This allows a sampling of the dE/dx and therefore perform PID below 1 GeV/c and above 3 GeV/c (relativistic rise of the dE/dx). The resolution on the dE/dx is 5% for isolated tracks (low multiplicity collisions), while in a high-occupancy environment such as Pb–Pb collisions, the resolution is 7%. This is due to the increased probability to have hits close in space. In addition, the contribution of positive ions to the signal shape increases with the particle occupancy. An other effect is due to the formation of large amount of charged particles (both electrons and ions) in the ionization volume can induce local modifications to the electric field. The presence of field distortions has an impact on the track reconstruction. This effect depends on both particle flux and on the type of gas used for the electron multiplication. As a consequence, the drift velocity is modified resulting in displaced reconstructed clusters. Offline corrections are applied with dedicated procedures that realign the reconstructed tracks by combining the information of the TPC with the other detectors in the central barrel. An example of the particle specific dE/dx as a function of momentum is shown in Fig. 3.9b.

3.1.3 The Time-Of-Flight (TOF) detector

The TOF detector [90, 7, 9] consists in a large-area array of Multigap Resistive Plate Chambers (MRPC), covering the central pseudorapidity range ($|\eta| < 0.9$). It is mainly used for the identification of particles in the intermediate momentum range (0.6-5 GeV/c). In addition TOF has been used to provide a trigger specific for cosmic ray and Ultra Peripheral Collision (UPC) events. The TOF detector has a modular structure divided along the azimuthal direction into 18 super modules (the 18 sectors in ϕ are shown in orange in Fig. 3.5) each one segmented into 5 modules along the beam axis (z). The detector is arranged in a cylindrical structure with internal (external) radius of 370 (399) cm for a material thickness of $\sim 30\%$ of a radiation length. The particle identification is based on the *time-of-flight* measured between the time at the point of the collision (t_{ev}) and the time of arrival at the sensitive volume in TOF detector (t_{TOF}). More details on the TOF detector are presented in Chapter 4.

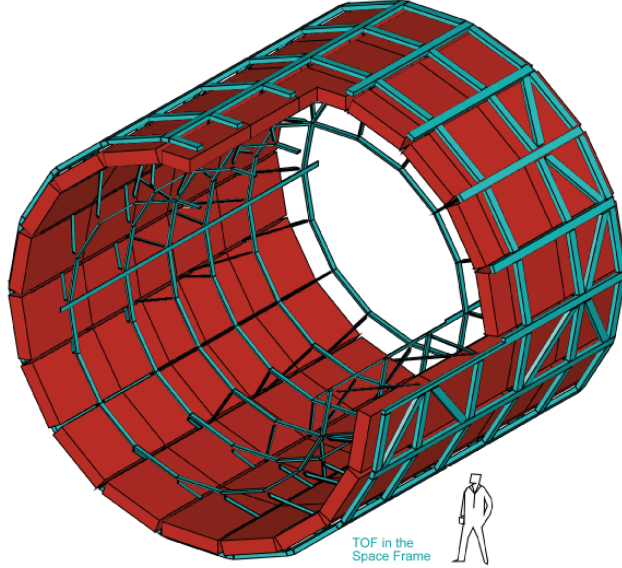


Fig. 3.5 Schematics of the TOF detector.

3.1.4 The High Momentum Particle IDentification (HMPID) detector

The HMPID [91–93] is dedicated to the identification of charged hadrons with $p_T > 1$ GeV/ c , thus extending the PID capabilities of the ITS, TPC and TOF at high momentum. The HMPID detector was designed as a single-arm array, it covers ~ 11 m 2 corresponding to 5% of the total central barrel acceptance. The coverage is $|\eta| < 0.6$ and $1.2^\circ < \varphi < 58.8^\circ$. This small acceptance is somehow a downside of the system as it usually needs larger statistics with respect to detectors with full azimuthal coverage, nonetheless HMPID saw extensive usage for the identification of particles at large momenta. The detector is based on proximity-focusing Ring Imaging Cherenkov (RICH) counters and is composed of seven modules, as shown in Fig. 3.6. The Cherenkov ring identification is done offline via pattern recognition algorithms.

3.1.5 Forward detectors

Additional detectors are used for the determination of the global properties of the events such as the collision centrality. These detectors are located at forward rapidities with respect to the IP.

Zero Degree Calorimeter The Zero Degree Calorimeter (ZDC) [94] consists of two tungsten-quartz neutron (ZN) and two brass-quartz proton (ZP) calorimeters located along the

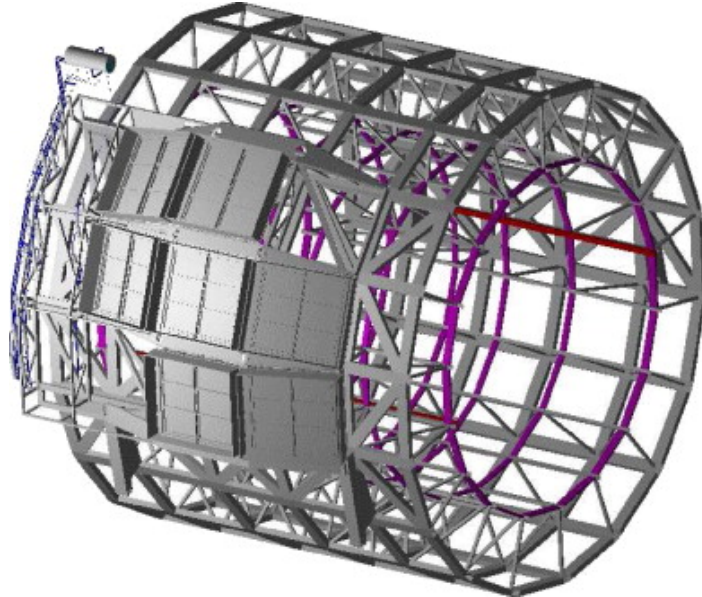


Fig. 3.6 Schematics of the HMPID detector.

Beam Pipe in two stations (ZDCA and ZDCC) ~ 112.5 m away from the Interaction Point, symmetrically in both directions. These calorimeters are used to count the number of spectators nucleons, they are shown in Fig. 3.7.

V0 detector The V0 detector [96, 97] consists of two circular arrays of scintillator counters (named V0A and V0C) one per side with respect to the interaction point. The V0A array is located 340 cm away from the IP, opposite to the muon spectrometer and covers the pseudorapidity range $2.8 < \eta < 5.1$. The V0C is placed before the hadronic absorber, it covers the range $-3.7 < \eta < -1.7$. Both V0A and V0C are segmented into 32 individual

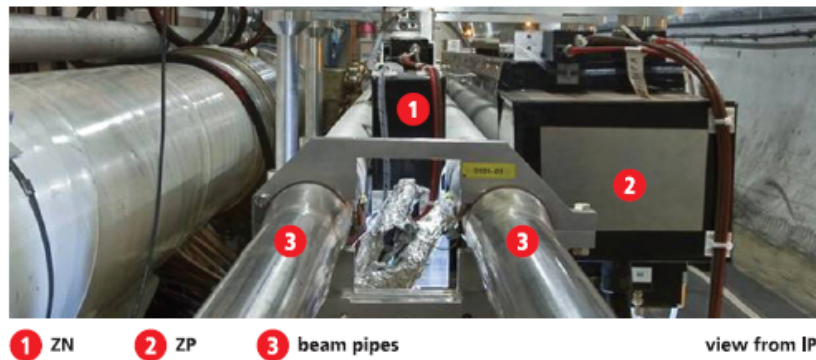


Fig. 3.7 Picture representing the layout of the ZDC on the A side [95].

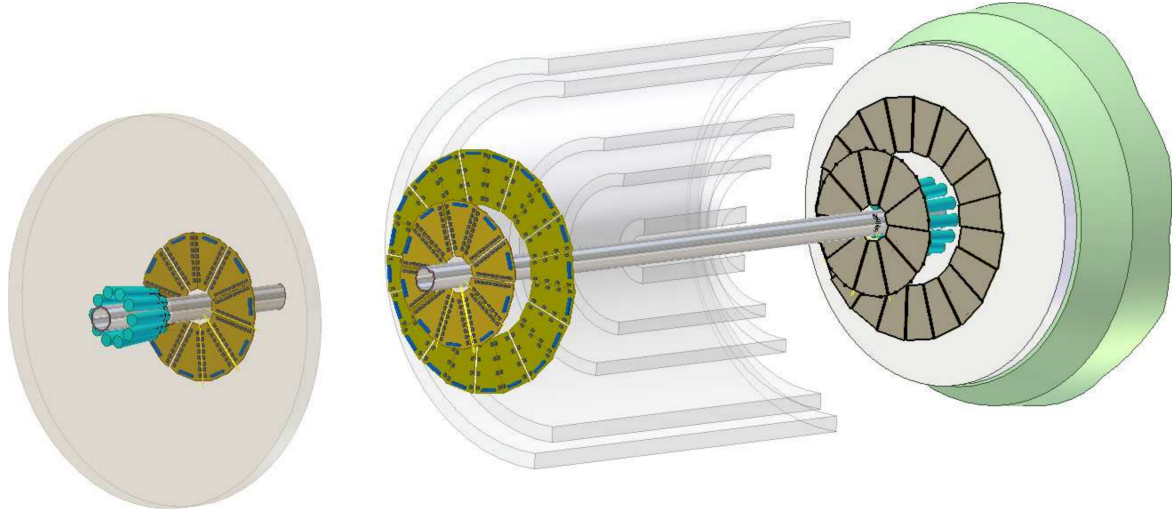


Fig. 3.8 Layout of the detectors located at forward rapidity close to the IP. The two arrays of the V0 detector are visible as grey disks. The two arrays forming the T0 detector are shown as blue cylinders around the beam pipe. V0A and T0A (V0C and T0C) are located on the left (right) side of the figure.

counters distributed in four rings. The signal given by the V0 detector is proportional to the number of particles traversing it, therefore it can be used for the multiplicity/centrality determination. The timing information of the detector can also be used to reduce accelerator induced background.

T0 detector The T0 detector [96] consists of two arrays, T0A and T0C, of Cherenkov counters placed along the BP on each side of the IP, respectively at -72.7 cm and 375 cm. The layout of the T0 detector is shown in Fig. 3.8. The pseudorapidity coverage are $4.61 < \eta < 4.92$ (T0A) and $-3.28 < \eta < -2.97$ (T0C). The main purpose of the T0 detector is to provide a precise measurement of the event collision time (t_{ev}) that can be used as a start time for *time-of-flight* measurements. The T0 can be used for an independent determination of the vertex position along the beam axis (with a precision of ± 1.5 cm) and to provide a low level trigger when the vertex position is within the expected values.

3.2 Particle Identification in ALICE

The goal of Particle IDentification (PID) is to determine the mass of each reconstructed track and therefore to identify the particle itself. PID is an essential tool to access the observables of the Quark-Gluon Plasma as it allows the investigation of the chemical properties of the medium created in the collision. The PID in ALICE is performed by using direct

measurements (such as direct identification of long lived particles by measuring of the particle energy loss or the *time-of-flight*) or by reconstructing the particle decay chains. This gives access also to hard probes that undergo strong decays. The several sub-detectors that are used in ALICE provide useful information for both of these methods. A review on the usage of the PID techniques can be found in [11, 98].

The basic approach to perform the PID makes use of the single detector raw signal S and the knowledge of its physical properties. These characteristics define the detector response R that depends on the track kinematic variables and on the particle species. As in all pattern recognition algorithms, the particle identity is chosen based on a discriminating quantity. The discriminating quantity for the particle species i can be evaluated using detectors with Gaussian response (mean value R_i and resolution σ_i) in units of σ ($n\sigma$) as:

$$n\sigma_i \equiv \frac{S_i - R_i}{\sigma_i} \quad (3.1)$$

The resolution is usually given by an intricate convolution of track parameters and detector characteristics. Single tracks can be identified without significant ambiguity if the separation of the detector response for different species is sufficient.

The ALICE PID separation power, for Run 1 conditions (2010-2011) [11, 99], obtained with different detectors is shown as a function of transverse momentum in Fig. 3.10. In the figure, the separation is expressed as a function of p_T because it is the scaling variable that drives the physical processes. The separation power however, is determined as a function of the track momentum before it is expressed in terms of p_T . By combining the information of the four detectors described above, one can identify π , K and p by assuring at least a 2σ π - K separation and a 1σ K - p separation over the whole momentum interval. This feature, combined with a high precision tracking down to low momenta (below 100 MeV/ c), makes ALICE the ideal setup for the measurement of identified particle spectra.

Long-lived particles can be identified by using a track-by-track approach (single track identification) if there is sufficient separation of the signals. In case of a reduced separation power (e.g. for separations smaller than 2σ as for K/p in TPC above 4 GeV/ c) the identification can still be done by using a statistical approach. As shown in Fig. 3.11, by splitting the track-integrated signals in single components for every species, one can measure integrated particle yields with high purity.

In the low p_T region the identification of hadrons is usually performed with the ITS alone. This is due essentially to two reasons. Firstly, the efficiency with the ITS stand-alone algorithm is the higher at low momentum with respect to algorithms that require the TPC. This is because of less detector material is needed to be crossed by the particles. Secondly, slower particles do not reach the regime of the minimum ionizing particle and deposit in the

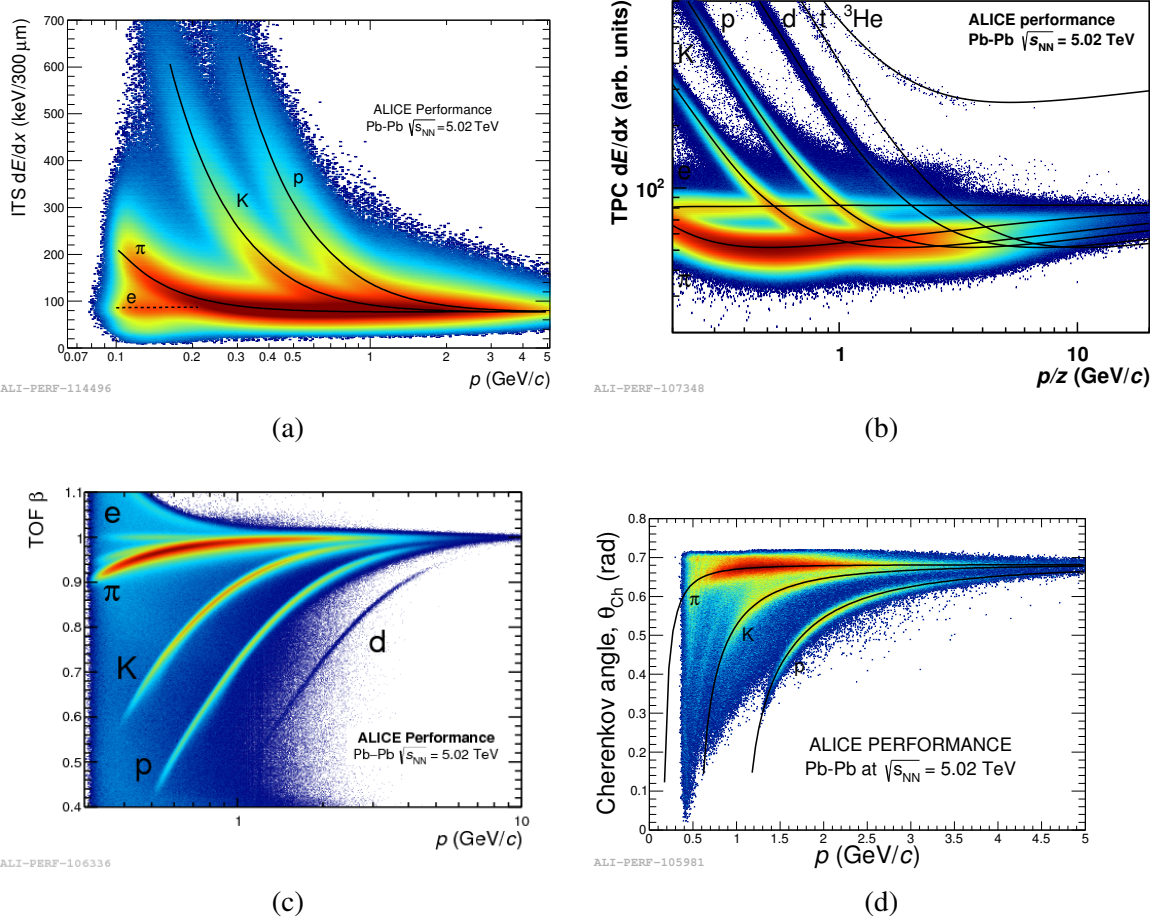


Fig. 3.9 (a) Distribution of the dE/dx as measured in the four outer layers (SDD and SSD) of the ITS as a function of the reconstructed track momentum. In this case the reconstruction uses only the 6 layers of the ITS to extend the efficiency at low momenta. The dE/dx is averaged over the available samples (from 3 to 4) with the truncated-mean method as in [79]. The expected mean values for the dE/dx obtained with the Phobos parameterization are shown for each particle species. (b) Distribution of the dE/dx as measured by the TPC as a function of the reconstructed rigidity (momentum/charge). The tracks used for this plot are reconstructed using ITS and TPC information. The parameterization of the dE/dx specific to each particle species are shown. (c) β distribution as measured by the TOF detector as a function of the reconstructed track momentum. The bands corresponding to each particle species are clearly visible. (d) Cherenkov angle measured by the HMPID detector as a function of the reconstructed track momentum. The expected amplitude of the Cherenkov angle for each particle species is shown.

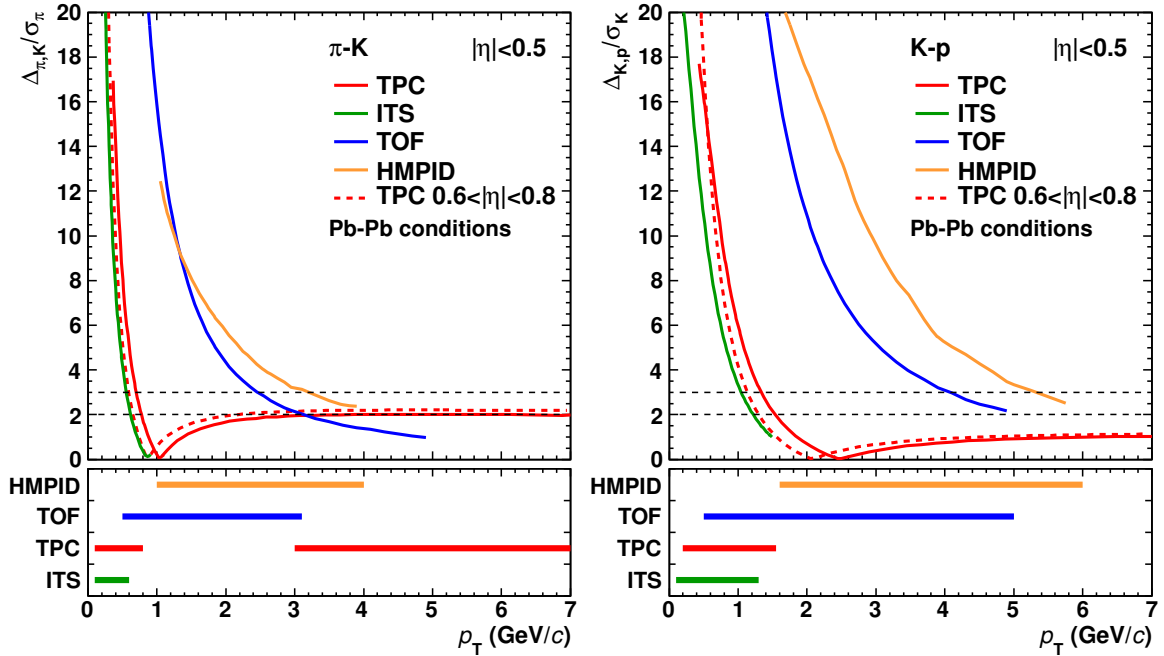


Fig. 3.10 PID separation power measured in units of σ obtained by using the different techniques available in ALICE for the identification of π , K and p [11].

material significantly different amounts of energy depending on their mass. Requiring three or four samples of dE/dx in the ITS gives the possibility to suppress the Landau tails of the energy loss distributions by considering the average of the measurements. An example of the ITS PID performance is shown in Fig. 3.9a.

From the dE/dx measurements of tracks reaching the TPC one can identify the different particles species at larger momenta. As shown in Fig. 3.9b the TPC allows to identify hadrons and light (anti-)nuclei over a wide momentum interval. The identification is usually carried out at low momenta in the 0.1-0.8 GeV/ c interval for π/K and 0.2-1.6 GeV/ c for K/p . At low momenta the detection efficiency is lower with respect to one of the ITS but the momentum coverage is wider. Particle identification can be performed also at high momentum ($p > 4$ GeV/ c) by exploiting the region of relativistic rise of the dE/dx in the TPC gas.

At intermediate p_T (~ 600 MeV – 5 GeV/ c) the tracks that reach the TOF detector can be well separated by measuring their *time-of-flight*. The particle velocity can be obtained by reconstructing the track length and momentum measured with tracking in ITS and TPC. The detector good timing precision (better than 100 ps) allows to separate also electrons and muons at very low momenta. The particle velocity β is shown in Fig. 3.9c as a function of the track momentum for Pb-Pb collisions at $\sqrt{s_{NN}} = 5.02$ TeV.

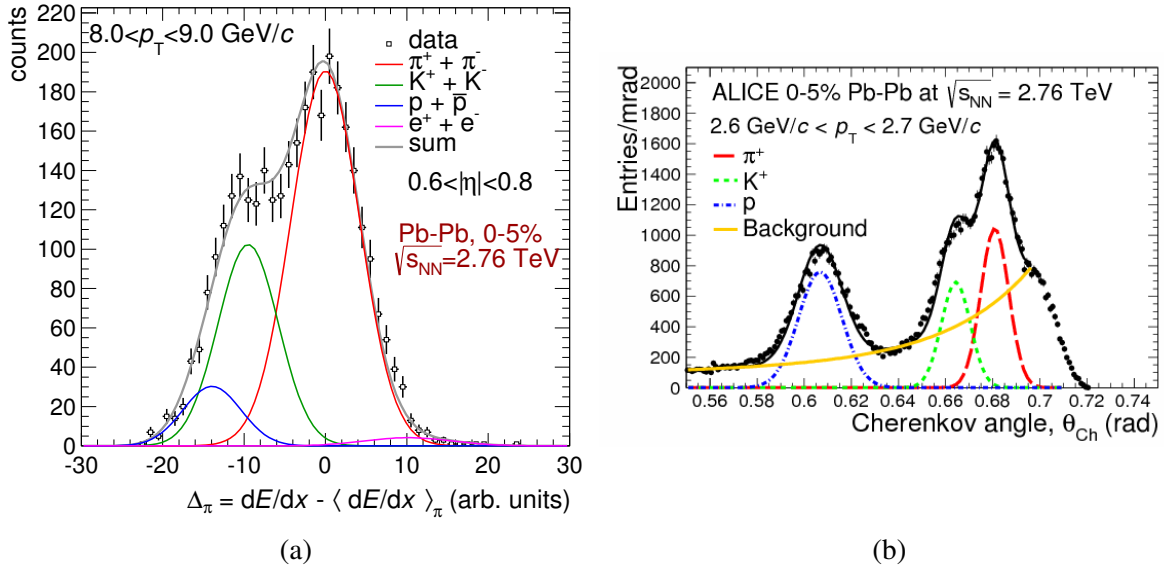


Fig. 3.11 (a) Statistical deconvolution of the signals measured with the TPC detector in Pb–Pb collisions at $\sqrt{s_{NN}} = 2.76$ TeV for tracks with p_T ranging between 8.0 and 9.0 GeV/c [11]. (b) Example of the statistical unfolding of the signals measured with the HMPID detector in Pb–Pb collisions at $\sqrt{s_{NN}} = 2.76$ TeV for tracks with p_T ranging between 2.6 and 2.7 GeV/c [12].

The HMPID detector is dedicated to the identification of high momentum particles. As shown in orange in Fig. 3.10 the separation power is larger than 2σ up to $p_T \sim 4 \text{ GeV}/c$ for π - K and up to $p_T > 6 \text{ GeV}/c$ for K - p . In this case the identification is usually performed via statistical unfolding (Fig. 3.11b). The Cherenkov angle measured in Pb–Pb collisions at $\sqrt{s_{NN}} = 5.02$ TeV is shown as a function of momentum for various species in Fig. 3.9d.

The information of several detectors can be combined to obtain track samples with extremely low contamination. The simplest way to proceed is to define N-dimensional cuts such as as the one obtained by combining the TPC and TOF information shown in Fig. 3.12:

$$n\sigma_{\text{TPC-TOF}} = \sqrt{(n\sigma_{\text{TPC}})^2 + (n\sigma_{\text{TOF}})^2} \quad (3.2)$$

The combination of the detector information can also be done by using Bayesian techniques, as extensively discussed in [98].

3.2.1 Topological identification and decay reconstruction

The direct identification of long-lived particles that reach the detectors located further away from the interaction point is not the only viable option. Secondary vertices can be reconstructed thanks to high precision tracking in the inner layers of the ITS thus allowing the

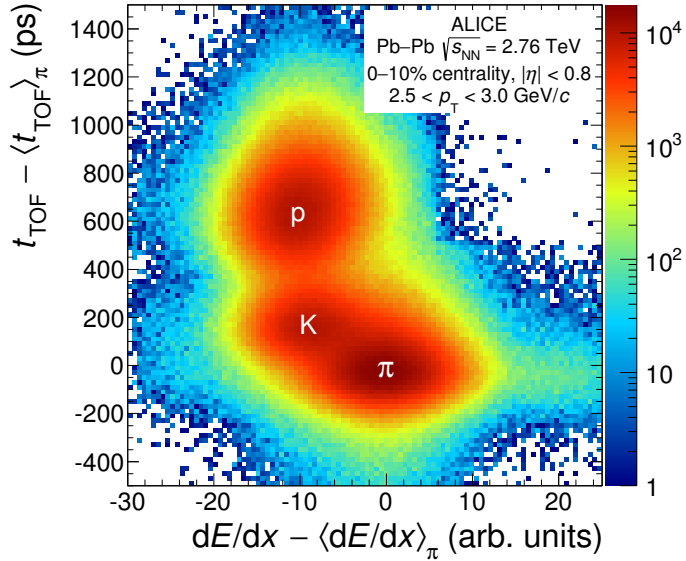


Fig. 3.12 Combined PID using signals from both TPC and TOF detectors in central Pb–Pb collisions at $\sqrt{s_{\text{NN}}} = 2.76$ TeV.

identification of unstable hadrons from their weak decay topology. This technique extends significantly the number of particle species that can be detected, including strange and multi-strange particles such as K_S^0 , Λ , Ξ and Ω^- . Charmed hadrons are also reconstructed via their decay topology. A representation of the weak decay topology of strange and multi-strange particles is given in Fig. 3.13. A detailed description of the procedures can be found in [11].

In addition to measuring neutral or short lived-particles, the full kinematic reconstruction of the decay is useful also for hadrons which can be detected directly. In Fig. 3.14 the reconstructed invariant mass of the charged kaon is obtained from the processes $K^\pm \rightarrow \pi^\pm + \pi^0$ or $K^\pm \rightarrow \mu^\pm + \nu$ for both real and simulated data. The same can be done with the reconstruction of charged pions exploiting the process $\pi^\pm \rightarrow \mu^\pm + \nu$. In these decays the reconstructed track appears to be continuous but with a sudden change of direction in the point of the decay (the so-called “kink”). The momentum of the neutrino is obtained by taking the difference of the track momentum before and after the kink. This approach to PID has several advantages. For instance, the particle purity is significantly larger with respect to the one achieved with a single detector. Kink decays are also reproduced with great precision in the simulation thus keeping the efficiencies under control. The contamination from single tracks with small angle deviations due to scattering in the material is usually below few percent.

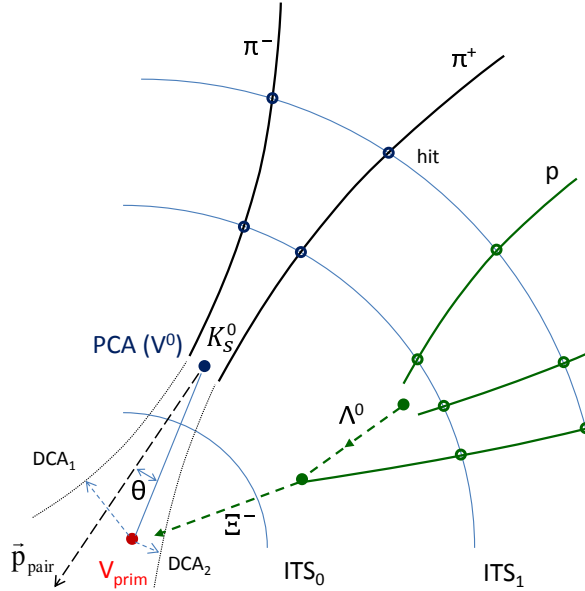


Fig. 3.13 Representation of the secondary vertices reconstruction procedure [11] for K_S^0 , Ξ and Λ decays. Long-lived particles such as pions and protons are detected, neutral vertices (V^0) are reconstructed by back-propagating charged particles. The Distance of Closest Approach (DCA) of tracks to the primary vertex, the total reconstructed momentum and its orientation constitute useful quantities for background rejection.

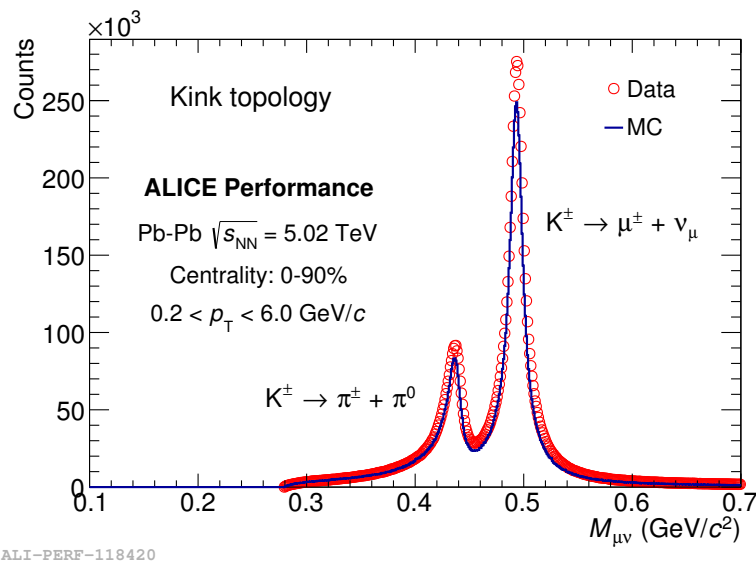


Fig. 3.14 Invariant mass distribution of kink-decay daughters under the assumption of a decay in the muon and neutrino channel.

3.3 Event characterization and selection in ALICE

An important ingredient for the study of heavy-ion collisions is the characterization of the recorded events based on their centrality. As introduced in Chapter 1 the particle production phenomenology might change significantly for collisions with different impact parameter because of the different energy density available and anisotropies in the created fireball.

3.3.1 Trigger selection

The choice on whether to record the data generated by the collision form the detector “trigger”. In ALICE all trigger decisions are generated by a dedicated system called Central Trigger Processor (CTP) [100]. These are based on the information on the LHC beam filling scheme and on the signals of the detectors capable to generate a trigger response (trigger detectors). To this purpose, the CTP checks the trigger inputs received from all trigger detectors every machine clock cycle (~ 25 ns).

The outcome of the CTP forms the Level 0 trigger decision (L0), this is taken ~ 0.9 μ s after every collision. The events that survive the L0 selection are propagated trough the decision chain and compared to the Level 1 (L1) trigger algorithm in the CTP. The L1 trigger decision is taken 260 LHC clock cycles (~ 6.5 μ s) after L0. This latency is due to the computation time and to the signal propagation from far detectors (such as the ZDC). The L0 and L1 trigger decisions are sent to the readout detectors with a latency of ~ 300 ns. The arrival of the trigger signal starts the buffering process of the data in the detector front-end electronics. If both L0 and L1 conditions are met, a Level 2 (L2) decision is issued after ~ 100 μ s. This time gap is necessary to allow the complete drift of ionization charges in the TPC. Events with a positive L2 response are accepted, at this point the Data Acquisition (DAQ) system collects the measured data. During Run 1 and Run 2 all events with a L1 decision were also accepted by L2. nonetheless the L2 decision is important as it gives the possibility to collect Minimum Bias triggered events in parallel to rare events (e.g. high multiplicity events in pp collisions). In addition it can help in the removal of piled-up events coming from subsequent bunch crossings (past-future protection). The beam-gas interactions and other sources of background can be discarded by analyzing the timing information of the signals in forward detectors.

The design of the detector, optimized for the study of heavy-ion collision, requires a reduced luminosity (when recording pp collisions) with respect to the one deliverable by the accelerator machine [11]. In standard data taking operations² the usual interaction rate of pp collisions is around ~ 1 MHz. The peak luminosity (\mathcal{L}) for the whole Run 2 is shown

²Higher rates can be achieved for testing purposes.

in Fig. 3.15a. Usual values of the luminosity for pp collisions are at $0.1 - 1 \text{ s}^{-1} \text{cm}^{-2}$ and roughly a factor 100 lower for heavy-ion collisions (due to the larger number of charged particle produced on average per single collision). The average number of interactions per bunch crossing (μ) in pp collisions varies from 0.05 to 0.3 meaning that the pile-up coming from collisions happening the same bunch crossing is under control. During Run 2 several high rate tests were performed to study the detector behavior at higher interaction rates in view of Run 3, these are visible as the spikes in the peak delivered luminosity in Fig. 3.15a.

3.3.2 Centrality estimation

As discussed in Section 1.1.3 centrality is expressed in terms of the fraction of the total nuclear hadronic cross section, σ_{AA} . The centrality percentile of collisions with impact parameter ranging in the interval $[b_1, b_2]$ can be defined as in Eq. 3.3:

$$\text{Centrality}(b_1, b_2) = \frac{\int_{b_1}^{b_2} db \frac{d\sigma}{db}}{\int_0^\infty db \frac{d\sigma}{db}} \equiv \frac{1}{\sigma_{\text{AA}}} \cdot \int_{b_1}^{b_2} db \frac{d\sigma}{db} \quad (3.3)$$

This quantity is accessible experimentally by measuring the charged particle multiplicity at mid-rapidity or by counting the number of spectator nucleons in the projectiles at forward rapidity, along the BP:

$$\text{Centrality}(b_1, b_2) \approx \frac{1}{N_{\text{Ev}}} \cdot \int_{N_{\text{ch}}=1}^{N_{\text{ch}}=2} dN_{\text{ch}} \frac{dN_{\text{Ev}}}{dN_{\text{ch}}} \approx \frac{1}{N_{\text{Ev}}} \cdot \int_{E_{\text{ZDC}}=1}^{E_{\text{ZDC}}=2} dE_{\text{ZDC}} \frac{dN_{\text{Ev}}}{dE_{\text{ZDC}}} \quad (3.4)$$

In order to have the correct normalization the hadronic cross section σ_{AA} in Eq. 3.3 can be replaced by the number of measured events as long as they are corrected for the trigger efficiencies and non hadronic interactions. In ALICE the centrality determination is usually determined by using the sum of the signals amplitudes in the V0 detector (V0A and V0C) or in the ZDC. The correlation between the charged particle density in the region at forward rapidity and at mid-rapidity is shown in Fig. 3.16. It is worth to note that the two quantities are well correlated, without any sign of saturation. This characteristics confirms the V0 amplitude as a good estimator for the centrality/multiplicity.

The summed signal of the two V0 arrays is shown as measured in Pb–Pb collisions at $\sqrt{s_{\text{NN}}} = 5.02 \text{ TeV}$ in Fig. 3.17. The fit with the Glauber model (discussed in Section 1.1.3) is shown to describe correctly the data and can be used to extract the microscopic characteristics of each centrality class ($N_{\text{Part}}, N_{\text{Coll}}, b$).

The centrality can also be estimated by the ZDC with a procedure similar to the one of the V0. It is worth to note that a possible ambiguity can arise between most central

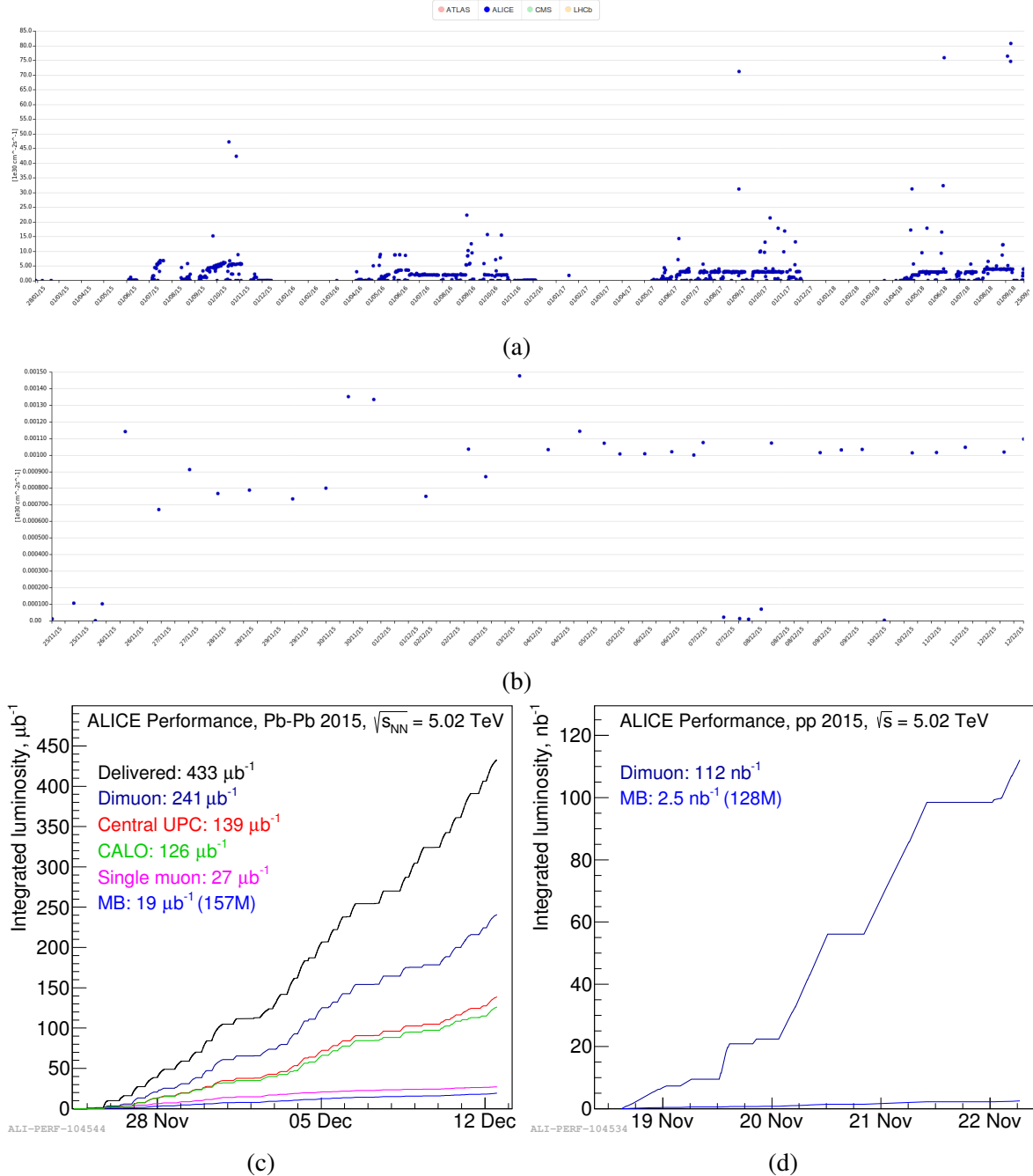


Fig. 3.15 (a) Peak luminosity delivered to ALICE during the whole Run 2 (so far) for both pp and Pb–Pb running conditions [101]. The visible spikes in the peak delivered luminosity correspond to the several high rate tests performed during Run 2 to study the detector behavior at higher interaction rates in view of Run 3. (b) Peak luminosity delivered to ALICE during the Pb–Pb period of data taking during 2015 [101]. (c) Total integrated luminosity for various triggers in Pb–Pb at $\sqrt{s_{\text{NN}}} = 5.02 \text{ TeV}$ taken in 2015. (d) Total integrated luminosity for the Minimum Bias and dimuon triggers in pp at $\sqrt{s} = 5.02 \text{ TeV}$ taken in 2015.

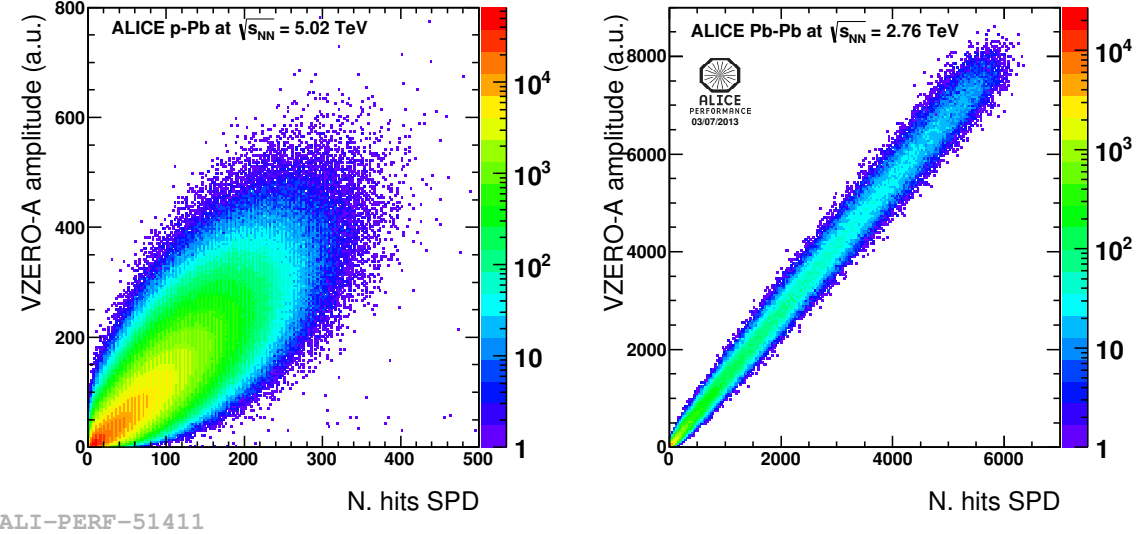


Fig. 3.16 Correlation between V0 amplitude (multiplicity at forward rapidity) and number of hits in SPD (multiplicity at mid-rapidity) as measured in p–Pb and Pb–Pb collision.

and most peripheral events. The expected energy deposited in the ZDC for central Pb–Pb collisions is close to zero as all nucleons participated to the collision. This scenario can be mimicked in peripheral events when spectator nucleons stay bound in few nuclear fragments yielding a low signal in the ZDC. To resolve this issue ALICE is equipped with Zero Degree Electromagnetic Calorimeter (ZEM) detectors located at $\sim 7.35 \text{ m}$ from the interaction point (on both sides), covering the pseudorapidity interval $4.8 < \eta < 5.7$. The ZEM is useful to resolve the ambiguity as it yields a signal proportional to the total charge of trough-going particles. The correlation between the signals of the ZDC and the ZEM is shown in Fig. 3.18 together with the division into centrality classes.

3.4 Data flow, reconstruction and simulation

In ALICE, data are recorded in data taking intervals (“runs”) during which the conditions of the detector (e.g. the magnetic field) are stable. Recorded raw data cannot be directly used for analysis purposes. Online detector calibrations and running conditions are needed as well, in ALICE these parameters are constantly monitored by the Detector Control System (DCS). After the data-taking is complete the data containing information on the running conditions are sent from the detector site (Point 2) to the CERN storage facility via the SHUTTLE frameworks [102] to a central catalogue: the Offline Calibration Database (OCDB). The workflow from detector level to the OCDB is shown in Fig. 3.19. From this catalogue, all

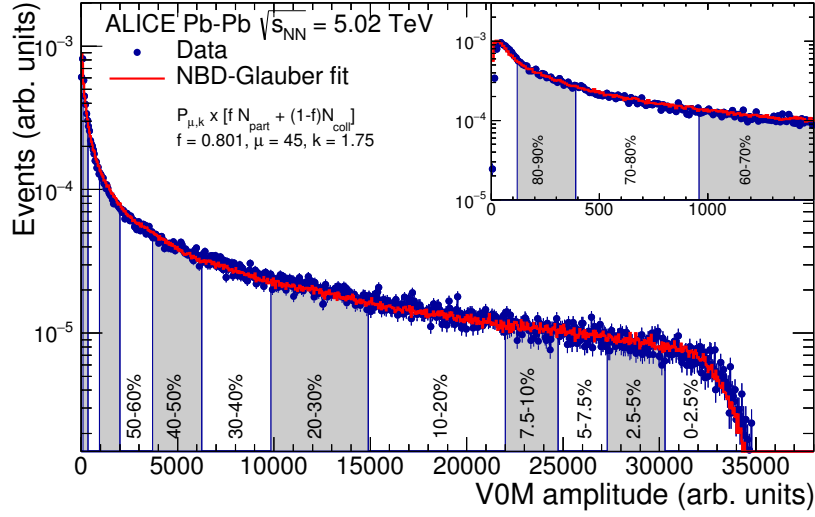


Fig. 3.17 Distribution of the V0 amplitude (sum of V0A and V0C) as measured in Pb–Pb collisions at $\sqrt{s_{NN}} = 5.02$ TeV [31]. The centrality classes are defined by integrating from right to left following Eq. 3.4. The absolute scale is determined by fitting the data with a Glauber model [25] (red line). The inset shows a magnified version of the most peripheral region.

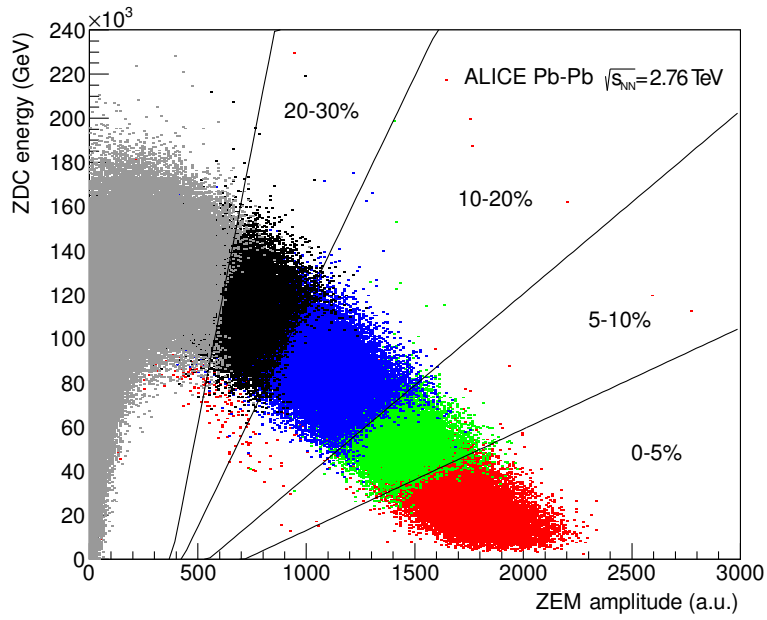


Fig. 3.18 Correlation between the total energy deposited in the ZDC and the ZEM amplitude. The central/peripheral ambiguity is resolved (see text). The centrality bins defined based on this distribution (lines) are compared to the centrality from V0 (colored dots) [11].

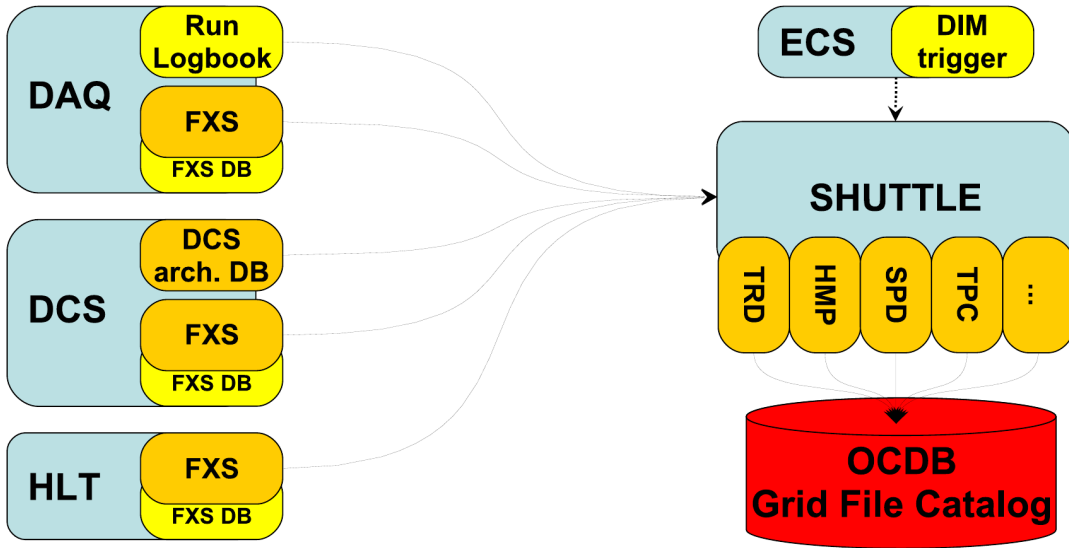


Fig. 3.19 Workflow for the measurement and record of the running conditions of the ALICE subsystems [102].

detector running conditions (e.g. instantaneous luminosity, number of active channels in readout per detector, online calibration constants, high-voltage setup, measured drift velocity in the sensitive area, et cetera) are kept and used during the reconstruction phase. The successful completion of the SHUTTLE migration triggers the first data reconstruction.

The OCDB also contains calibration corrections that are not obtained during the data-taking but rather are generated afterwards (offline) in an iterative reconstruction and calibration procedure. The output of each reconstruction and calibration step is validated manually by several teams of detector experts (checking the behavior of the single detector) and by dedicated task forces that perform user case analyses and check the consistency of the reconstructed data. This quality assurance procedure of the reconstructed data takes place offline and is separated with respect to the one performed concurrently to the data-taking by the Data Quality Monitoring (DQM) system. The stages of reconstruction are done before the data is available for the analysis:

1. The SHUTTLE transmission is successfully completed and the reconstruction starts.
2. The first reconstruction phase (pass) is used for the calibration of TPC, TRD, TOF, T0. At this point the collision centrality is defined for each event.
3. Raw data are reconstructed again with the updated calibration obtained from step 2. The outcome of the reconstruction procedure is validated by the Quality Assurance

(QA) analysis and potential flaws are spotted. Manual calibration algorithms can be used to improve detector response or fix issues.

4. The most updated calibration constants and reconstruction algorithms are used in the final reconstruction. Another round of QA analysis is carried out by experts before delivering the data to analyzers.

This workflow can result in a large computing time per event coupled with large data flow in I/O. The only viable option to tackle the reconstruction problem is the parallel processing.

Reconstruction takes place on the ALICE computing Grid [103], a distributed facility with large storage and computing resources coupled with high-speed interconnections links. This allows to reconstruct data samples that on a single core would take more than one year (including the reconstruction and the I/O). The Grid is also used for analysis purpose. The reconstructed data is accessed and processed in parallel to reduce the user running time.

Chapter 4

The ALICE Time-Of-Flight detector

The ALICE Time-Of-Flight (TOF) detector is a large area, high precision gaseous detector used for Particle IDentification (PID) at intermediate momenta ($\sim 600 \text{ MeV}/c$ to $\sim 5 \text{ GeV}/c$). In this momentum range particles can be distinguished by measuring their velocity. For this purpose it is important to reach a good experimental resolution on both length and *time-of-flight* of the particle trajectory. The TOF detector is located at 370 cm from the interaction point, in the outer part of the ALICE frame (Fig. 4.1), to guarantee the best particle separation capabilities by keeping a large distance between the particle production and the detection points, thus increasing the overall track length. The TOF detector covers $\sim 170 \text{ m}^2$ in the “central barrel” region, with a 2π coverage of the $|\eta| < 0.9$ interval. The active area of the ALICE Time-Of-Flight detector is based on the Multigap Resistive Plate Chamber (MRPC) technology, a design of Parallel Plate Chamber (PPC) with good intrinsic timing precision ($\sim 50 \text{ ps}$), high detection efficiency (eff. $> 99\%$) and good tolerance to high charged particle fluxes. The working principle of the MRPC will be given below.

This chapter will describe the technology developments, the experimental setup, and the operations (from the data taking to reconstruction and Quality Assurance of the recorded data) of the ALICE Time-Of-Flight detector. In the last part of the chapter, the studies performed in the context of the upgrade of the TOF detector will be presented.

4.1 Timing resolution requirements for detector design

Particle identification is performed by combining the information provided by tracking detectors (momentum p and track length l) with the measurement of the *time-of-flight* (t) in TOF. The mass (m) corresponding to the one of the detected particle can be obtained.

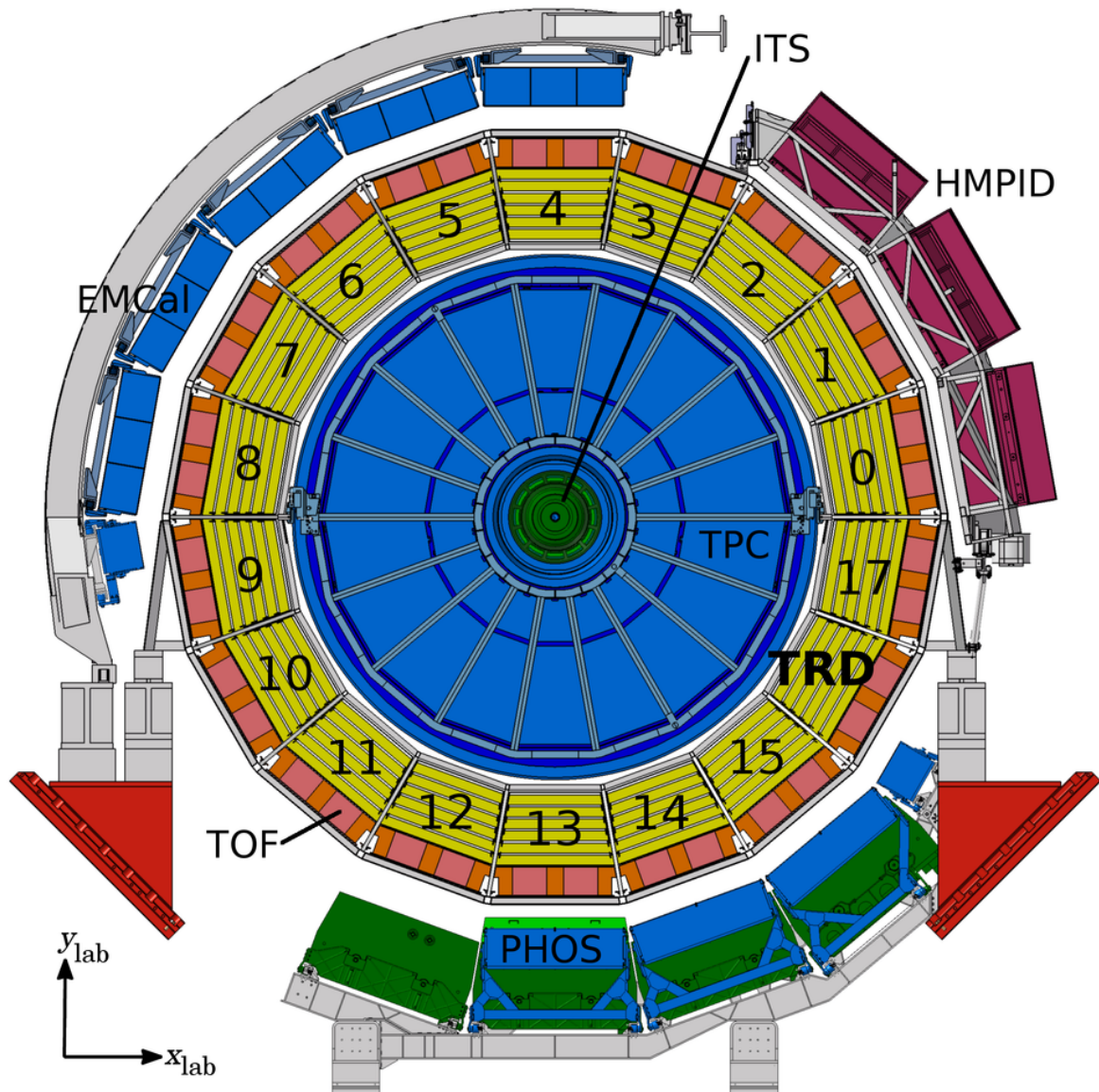


Fig. 4.1 Cross section of the “central barrel ” of the ALICE apparatus. The 18 sectors surrounding the inner detectors are shown.

$$m = \frac{|\vec{p}|}{c} \cdot \sqrt{(1/\beta)^2 - 1} \quad (4.1)$$

The particle velocity β is measured experimentally.

$$\beta = l/(t \cdot c) \quad (4.2)$$

The mass measurement can be expressed using natural units ($c \equiv 1$).

$$m = |\vec{p}| \cdot \sqrt{\left(\frac{t}{l}\right)^2 - 1} \quad (4.3)$$

From Eq. 4.3 one is able to estimate the mass resolution.

$$\sigma_m = \sqrt{\left(\frac{\partial m}{\partial p}\right)^2 \cdot \sigma_p^2 + \left(\frac{\partial m}{\partial t}\right)^2 \cdot \sigma_t^2 + \left(\frac{\partial m}{\partial l}\right)^2 \cdot \sigma_l^2} \quad (4.4)$$

The relative uncertainty on the mass measurement can be derived as

$$\frac{\sigma_m}{m} = \sqrt{\left(\frac{\sigma_p}{p}\right)^2 + \left(\frac{E}{m}\right)^4 \left(\left(\frac{\sigma_t}{t}\right)^2 + \left(\frac{\sigma_l}{l}\right)^2\right)} \quad (4.5)$$

From Eq. 4.5 one notices that the three terms contributing to the uncertainty have different weights. In particular, at large momenta the resolution on the track momentum (σ_p) becomes negligible and the total uncertainty is driven by precision on the timing (σ_t) and track length (σ_l). The TOF performance affects exclusively the uncertainty on t , σ_t . To perform PID in the momentum range needed to meet the ALICE requirements [85, 86], the TOF detector was designed to achieve a timing resolution better than 90 ps. The effect of the detector precision on the PID can be evaluated in terms of momentum reach in Fig. 4.2. Three different scenarios with different timing resolutions are given with the corresponding particle separation power. The scenario with the worst resolution (150 ps) allows to separate (at a 3 σ level) π from K up to ~ 2 GeV/c and K from p up to ~ 3 GeV/c. This separation power is not optimal when considering the separation ranges of other detectors. Having such timing resolution would constitute a potential problem for the measurement of particle spectra in a continuous range of momenta. The situation is considerably improved with a detector resolution of 80 ps, in this case π are separated from K up to ~ 2.5 GeV/c and K from p up to ~ 4 GeV/c (at a 3 σ level).

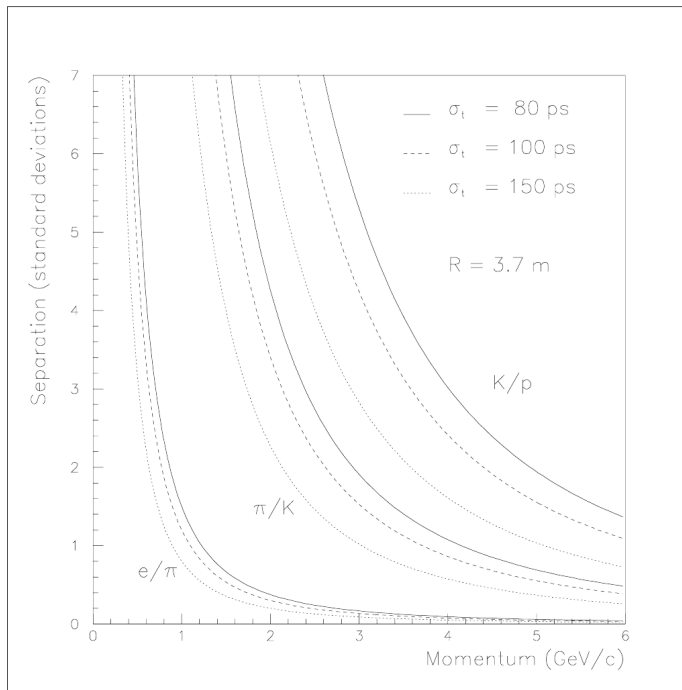


Fig. 4.2 Separation power (π/K and K/p) with the TOF detector measured in $n\sigma$ [90]. Three scenarios are given with different timing resolutions: $\sigma_t = 150, 100, 80 \text{ ps}$. As expected, the largest range with more than 3σ separation is obtained when having the best detector resolution.

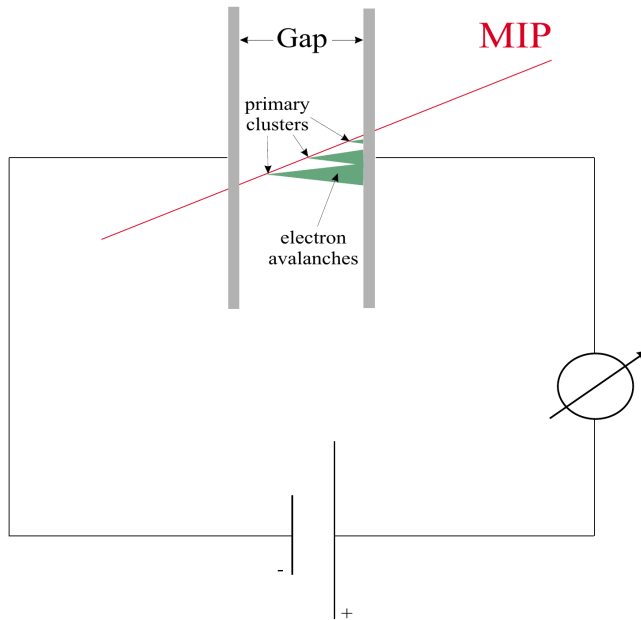


Fig. 4.3 Representation of the gas gap of a Resistive Plate Chamber [90].

4.2 The Multigap Resistive Plate Chamber technology

The active area of the Time-Of-Flight detector is based on the Multigap Resistive Plate Chamber (MRPC) technology developed specifically for requirements of the ALICE experiment. The Parallel Plate Chamber (PPC) design of the MRPC ensures a high and uniform electric field over the whole sensitive region. This feature allows for the immediate collection of all charges produced by ionization by the pick-up electrodes with no associated drift time. This suppresses the time jitter caused by variations in the position of the initial clusters of primary ionization. A detailed description of the R&D process that led to the design of the ALICE MRPC can be found in [90, 7]. In this thesis the description will be focused to the final MRPC design.

The design of a Resistive Plate Chamber (RPC) is similar to the one of a PPC if one exchanges the metallic plates used in PPC detectors with resistive electrodes. This choice quenches the charge streamers thus reducing the chance to have sparks (and the consequent breakdown of the electric field) in the chamber. As a consequence, RPC detectors can be operated at much higher gains in avalanche mode and without the risk of damaging the pick-up electrodes. The RPC design allows also to work in the streamer regime.

The active part of the detector is where the electron multiplication takes place, and is the so called “gas gap”, as represented in Fig. 4.3. The signal gain and the particle rate tolerance are defined by the dimensions of the gap. The choice of the gas used in the active area also

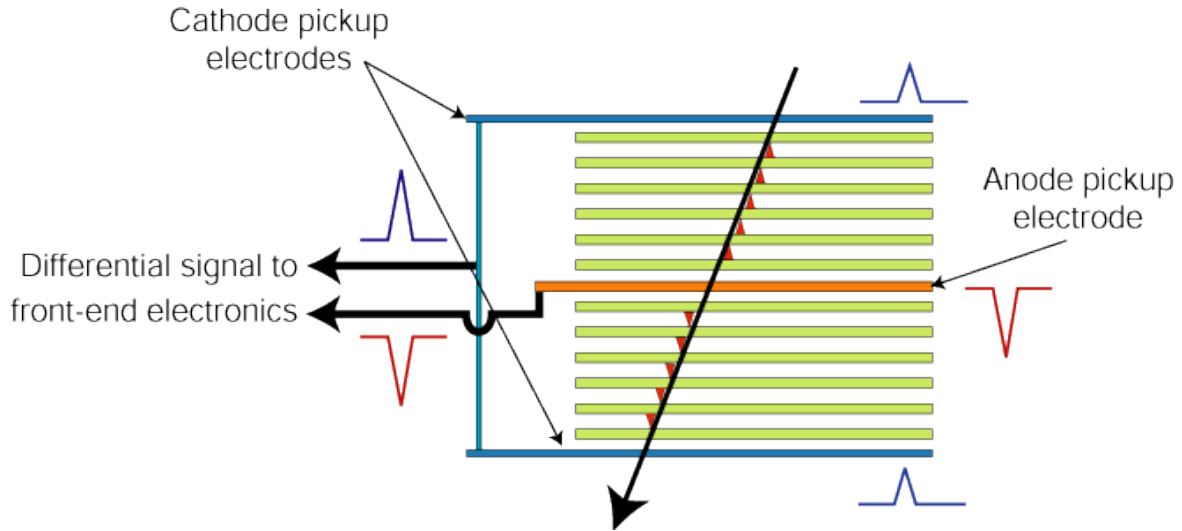


Fig. 4.4 Representation of the design of the ALICE TOF MRPC. The charge deposited by a ionizing particle is shown together with the corresponding signals on the pick-up electrodes.

affects the detector response. Before the R&D for the ALICE TOF detector, RPC were built using glass [104] and Bakelite [105] electrodes. Two configuration were implemented: the “small gap” (~ 2 mm) and the “wide gap” (~ 8 mm) RPC. While the former allows to reach the best timing resolution, it cannot handle large particle fluxes. Instead, the “wide gap” RPC improves the rate tolerance at the expense of the time precision (due to time jitter). The two designs converged into the MRPC, where a large gas gap is divided into several smaller gaps thus allowing to achieve good timing resolution and high detection rate at the same time. The intrinsic MRPC efficiency is more than 99% and its time resolution is ~ 50 ps [7, 9].

The design of the ALICE TOF MRPC is represented in Fig. 4.4. The schematics shows a double stack of five gas gaps (ten gaps in total). The cathode pick-up electrodes are located at the top and bottom of the chamber, the anode is placed in the middle and is shared between the two stacks. The inner plates are made of glass and are electrically floating. These are kept to the correct voltage with the charge induced by electrostatic effect and by the flux of charges (both electrons and ions) created by avalanches in the gaps. This electrical coupling forces all gaps to have the same gain. The separation of the single glass sheets is achieved by stretching a Nylon fishing line between the planes as shown in Fig. 4.5. The fishing line is connected to nylon screws, this characteristics is fundamental as it keeps the glass sheets electrically floating.

Ionizing particle can create independent avalanches in each gap, as sketched in Fig. 4.4. Each resistive plate is transparent to the fast signal generated by the avalanches. The total signal induced on the pick-up electrodes is given by the sum of all the avalanches that are created in the single gaps. The collected signal has the shape of a Landau distribution with

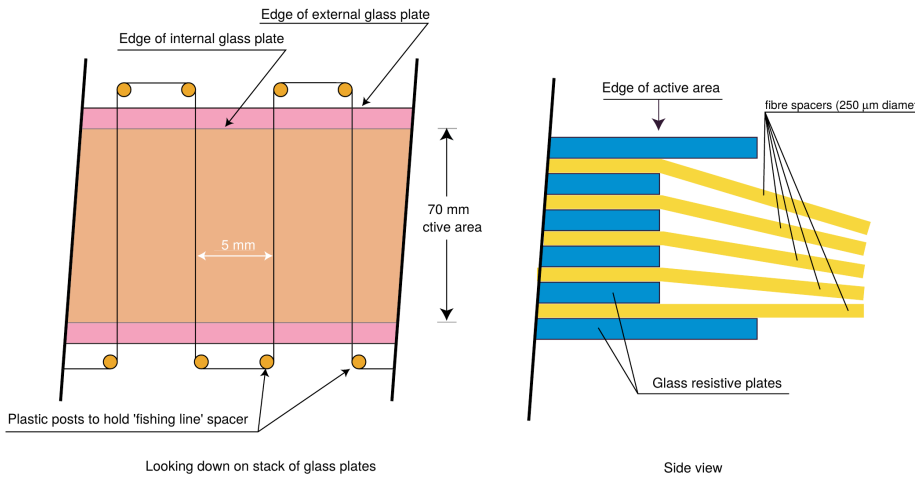


Fig. 4.5 Detail of the plates in the ALICE TOF MRPC and their mechanical separation [7].

a peak well separated from zero. This feature increases the rate tolerance with respect to single gap chambers. In addition, the presence of several independent gas gaps increases the probability of particle detection with respect to the single gap configuration, thus increasing the overall detector efficiency.

For the ALICE TOF detector, the double stack MRPC was chosen for its features:

- Large range of operating voltages.
- High detection efficiency.
- The double stack design has twice the gain (and therefore the signal) of the single stack with same characteristics and operating with the same voltage. The double stack configuration requires half of the voltage of the single stack in order to achieve the same efficiency.
- The separation between cathode and anode is smaller in the double stack configuration, yielding a smaller avalanche footprint (less diffusion in the plane parallel to the plates). The avalanche footprint is represented in Fig. 4.6.
- As the operating voltage can be kept lower with respect to the single stack, the double stack design increases the number of gaps that can be used per detector element.
- The total gas gap width of the chamber is large enough to allow large rate tolerance. Tests showed that working conditions are stable for particle flux exceeding $1 \text{ kHz}/\text{cm}^2$ [7], this is satisfactory for the requirements of the design of ALICE. This is achieved thanks to the small charge produced per trough-going ionizing particle.

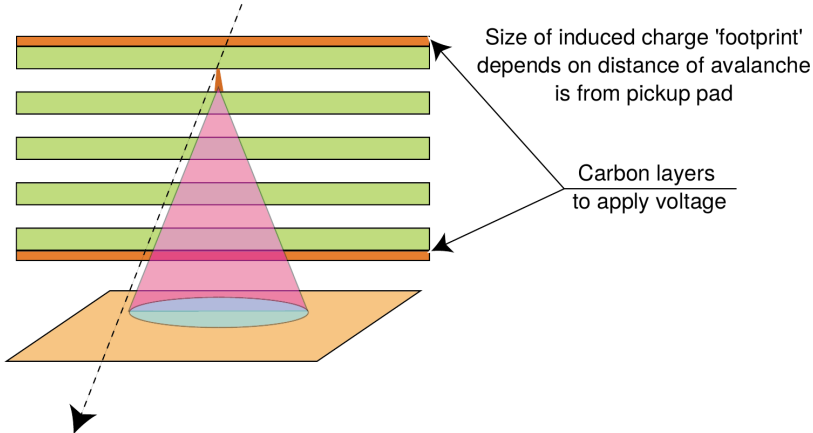


Fig. 4.6 Diagram of the avalanche footprint [7].

- The resistance of the the detector to the aging effects was tested extensively before the installation in the ALICE detector frame and during Run 1 and Run 2. This detector design proved to be very stable, well behaving also in high particle flux environments (2.5 kHz/cm^2 minimum ionizing muons equivalent) and after exposure for long periods of time (six months) [106]. For this reason the TOF detector will be able to take data also during Run 3 without any major modification to its design.

Fig. 4.7 shows the cross section of a “strip” i.e. the sensitive volume of the detector. The two double stacks, each one consisting of five gaps, are visible in the figure. The total area covered per strip is $7 \times 120 \text{ cm}^2$. The plane separation is of $250 \mu\text{m}$. The glass thickness is $400 \mu\text{m}$ for the inner plates and $550 \mu\text{m}$ for the outer ones. The bulk resistivity of the glass plates is about $10^{13} \Omega \cdot \text{cm}$. The outer surface of the external plates is painted with a special coating with high resistivity (acrylic paint loaded with metal oxides, reaching $5 \text{ M}\Omega/\square$), serving as a high-voltage electrode. The readout Printed Circuit Board (PCB) for both anodes and cathodes is 0.8 mm thick, with a total surface of $2.5 \times 3.5 = 8.75 \text{ cm}^2$ and a 3 mm margin in all four boundaries, this defines the smallest cell of the detector. The total sensitive area of the strip ($7 \text{ cm} \times 120 \text{ cm} = 840 \text{ cm}^2$) is segmented into readout cells of 8.75 cm^2 . In total 96 pads are needed to read the whole strip. In order to ensure mechanical rigidity and sustain the glass planes against bending, the double stack MRPC is contained within two layers of cardboard honeycomb.

In order to have electron multiplication the gaps between the resistive planes have to be filled with a gas mixture that maximizes the detector performance. Several tests were done during the R&D phase [90, 7]. The final adopted solution was to fill the active area of the MRPC with a non-flammable freon-rich gas mixture containing $\text{C}_2\text{H}_2\text{F}_4$ (tetrafluoroethane or freon) and SF_6 (sulfur hexafluoride) in the concentration of 93% and 7% respectively.

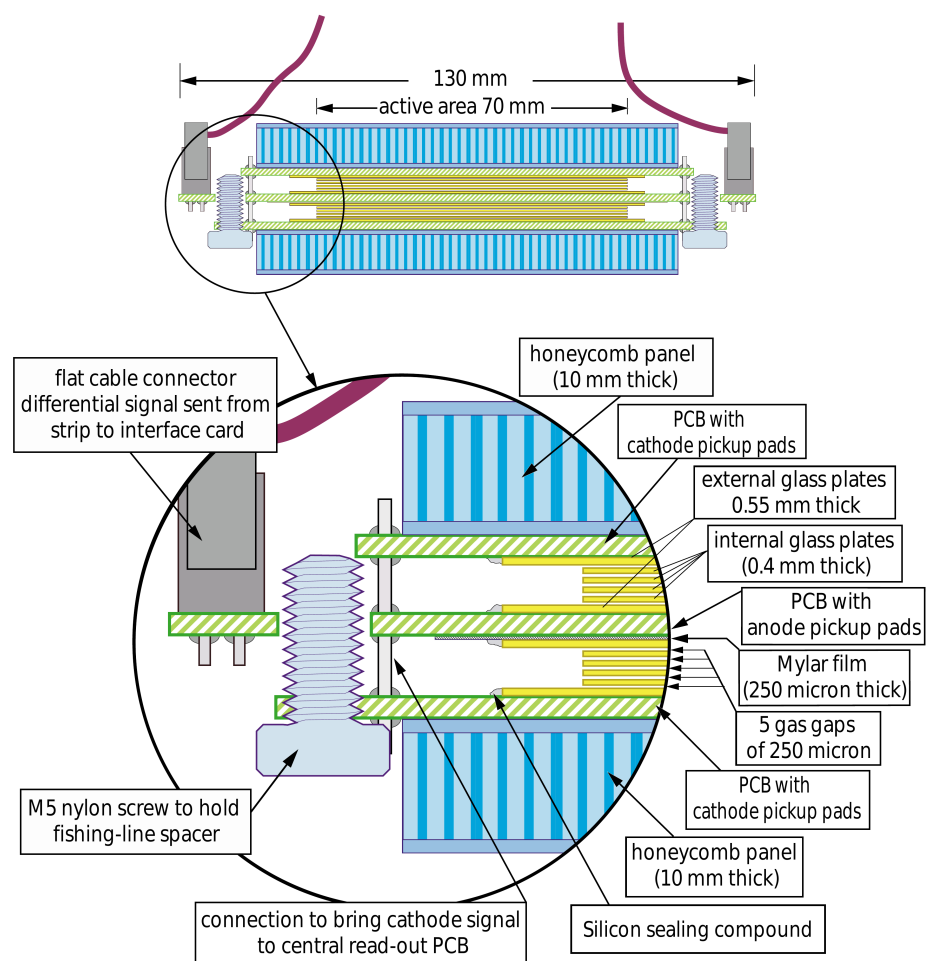


Fig. 4.7 Detector schematics of the double stack ALICE TOF MRPC [7].

The non flammability of the gas mixture was a key feature taken into account during the development phase as unnecessary risks had to be taken otherwise (considering also the remote possibility to have sparks in the chamber). The usage of freon based gas detectors constitute a non trivial problem as those gases are known to affect the earth atmosphere. For this reason since several years a research for alternative solutions is ongoing.

All planes of the MRPC strip are electrically floating but are not sealed and exchange gas with their surroundings. For this reason, strips are located in a gas-tight volume filled with the gas mixture. After several flushing iterations (~ 10 volumes), the amount of contaminants is negligible and the operating conditions are met. Several MRPC strips are placed inside a gas tight box made of fiberglass (3 mm thick) and aluminum (0.3 mm thick), the latter to ensure electrical shielding. The gas box is then equipped with an aluminum honeycomb layer to give mechanical support and provide a basis for the positioning of the front-end electronics (FEA in Fig. 4.8). A large PCB interface card is glued on top of the honeycomb to form a basis for all needed electrical connections.

This complex component (strips + gas box + front-end electronics) is the working element of the TOF detector. This part of the detector is referred to as “module” or “plate”, an example of a TOF module is depicted in Fig. 4.8. As it will be discussed in the next section, each TOF “Super Module” (SM) is built from four or five single modules, each one having different characteristics, and containing different number of strips depending on its position along z .

4.3 Experimental setup

The experimental setup of the TOF detector in the ALICE frame is shown in Fig. 4.9. The structural frame containing the detector completely surrounds the beam axis giving a total 2π coverage. The detector unit contained in the frame is the Super Module (SM). This unit is completely self sufficient as it contains the modules with MRPC strips and the readout electronics (including front-end electronics). The TOF frame is divided into 18 identical sectors shown in Fig. 4.1, each one occupied by a SM.

The MRPC strips, described in Section 4.2, are arranged in the SM so that they are parallel to its short side, with the glass planes facing the beam axis. This choice allows to keep a perpendicular angle between the strip and the direction of particles coming from the interaction point. The configuration of each module depends on its position along z or its tilting angle with respect to the beam axis θ . Using symmetry considerations with respect to the Interaction Point (IP), one can consider only half of the TOF cylinder and identify three different types of modules: the central module ($\theta \sim \pi/2$), the intermediate module and the outer module ($\theta \sim \pi/4$). The strips of each module are specially positioned to

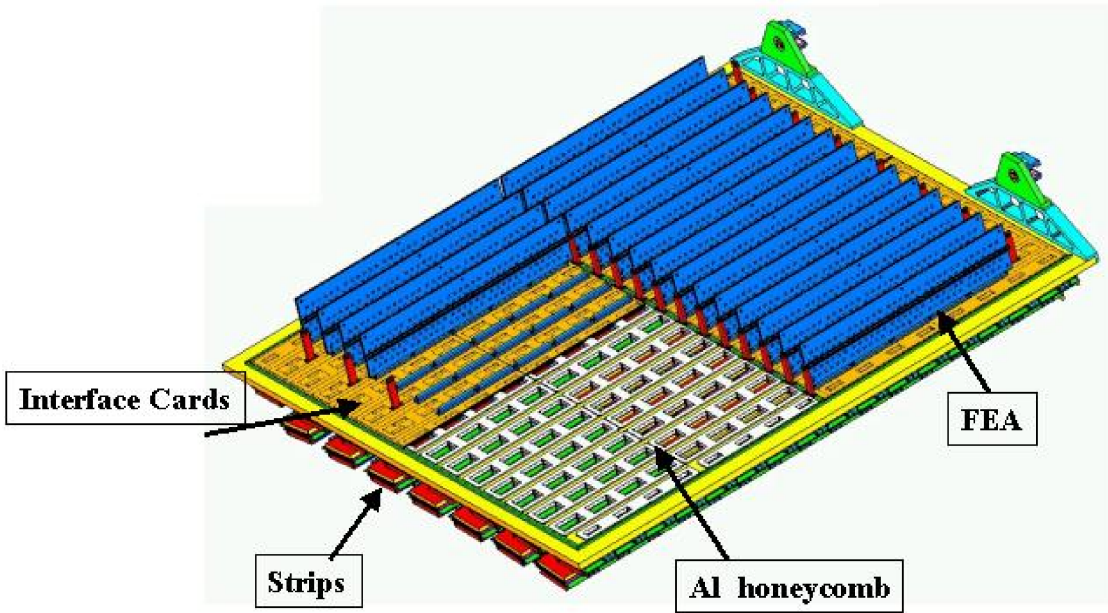


Fig. 4.8 Example of a module of the ALICE TOF detector.

minimize the particle oblique traversal path in the sensitive region. The strip tilting angle with respect to the axis of the TOF cylinder is progressively increased from 0° in the most central strip of the central modules (located at $\theta = \pi/2$ with respect to the IP) to 45° in the external strip of the outer module (located at $\theta = \pi/4$ with respect to the IP). Thanks to their mechanical rigidity, strips can be positioned close in space, allowing for partial coverage overlap of adjacent strips inside each modules (~ 4 mm at the edge of the sensitive area). This maximizes particle detection efficiency and minimizes losses of the sensitive area along the z axis of the experiment. An example of the strip positioning for the central, intermediate and outer module is shown in Fig. 4.10a and Fig. 4.10b. The whole SM (see Fig. 4.9) is constructed by stacking five single modules in a row (two outer modules, two intermediate modules and one inner one), symmetrically placed with respect to the center of the detector.

Each type of TOF module has a different number of strips, positioned with different tilting angles. In Table 4.1 the characteristics of the three types of TOF modules are reported.

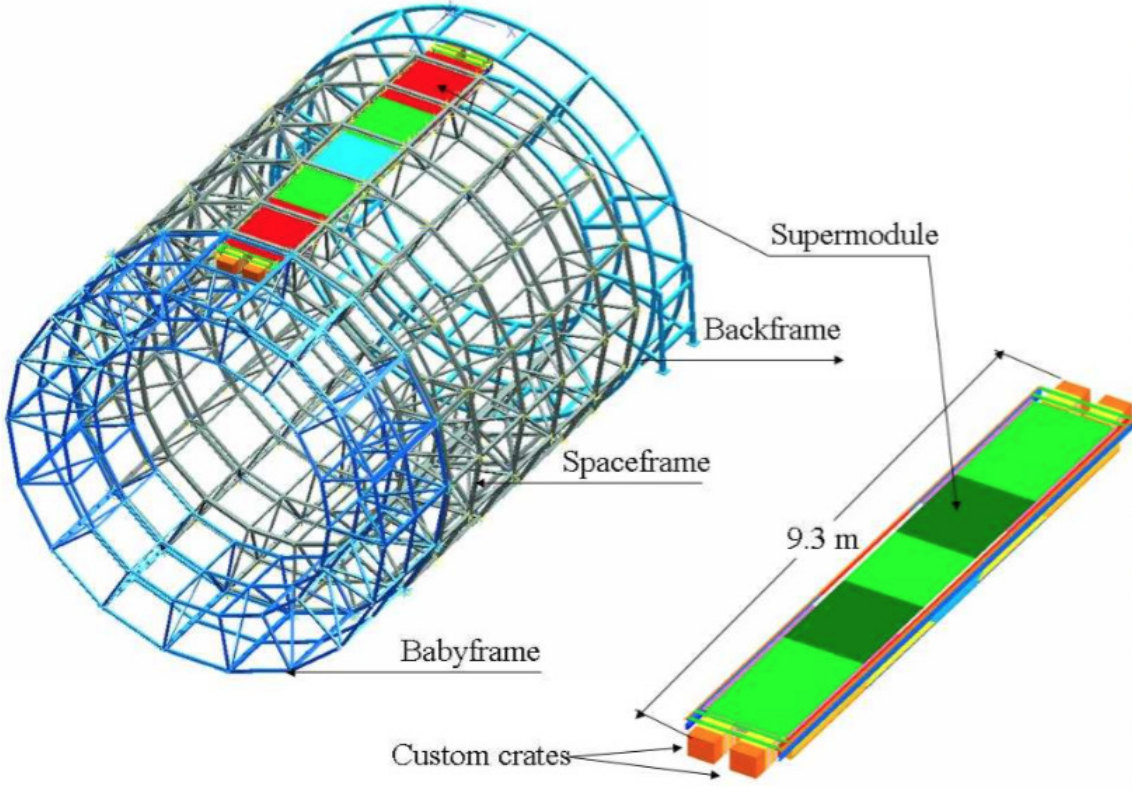


Fig. 4.9 Layout of the TOF detector in the ALICE frame with one of the 18 Super Module inserted [7]. The Super Module is also shown divided into five modules and with its four custom crates used for readout purposes.

Module type	Central	Intermediate	External
Number of strips	15	19	19
Number of pads	$96 \times 15 = 1440$	$96 \times 19 = 1824$	$96 \times 19 = 1824$
Total sensitive area	1.26 m^2	1.6 m^2	1.6 m^2
MRPC tilt angles in degrees	$(-7.43^\circ, +7.43^\circ)$	$\pm (8.73^\circ, 27.8^\circ)$	$\pm (28.7^\circ, 43.9^\circ)$

Table 4.1 Characteristics of the different type of TOF modules [7].

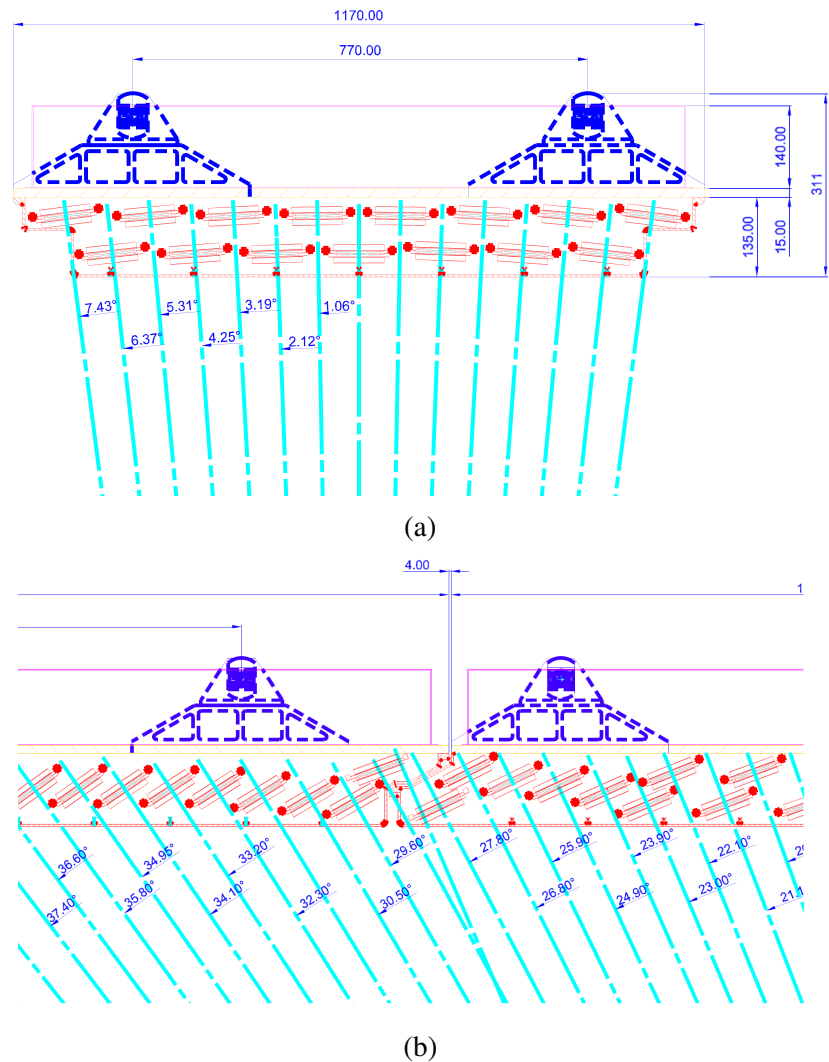


Fig. 4.10 Design blueprints [7] of the (a) central module and (b) region of interface between the intermediate and external TOF modules.

We can now summarize the dimensions of the TOF array:

- The total sensitive area per SM is 7.65 m^2 . This surface is obtained with 91 strips per SM, each one read by 96 pads for a grand total of 8736 readout channels per SM.
- 18 SM are located in the 18 sectors of the ALICE frame, each SM is divided into five modules (90 modules in total). The total sensitive area is therefore $\sim 137.7 \text{ m}^2$, with 157248 readout channels.
- Due to requirements of the Photon Spectrometer detector (PHOS) [107] to have the reduced material budget in the region at mid-rapidity, the central modules of SM of sector 12, 13 and 14 are not installed. This corresponds to $1440 \times 3 = 4320$ readout channels and to 3.78 m^2 of sensitive surface at $\theta \sim 0$ and $\varphi \sim 270^\circ$.
- The final TOF array consists of 1593 strips placed into 87 modules divided into 18 SMs, for a total of 152928 readout channels.

4.3.1 Detector readout

The readout of the ALICE TOF detector interfaces directly with the ALICE central Detector Control System (DCS) which has control over each one of its components. This section is dedicated to the description of the readout chain of the ALICE TOF detector. The readout is carried out by custom made electronics located close to the MRPCs (front-end readout) and at the edges of each SM in four custom crates (two per side). From the point of view of the readout, each SM is segmented into four independent sectors.

The strategy used to collect and record the signals from every strip is the following:

- The signal from each pad is first amplified and discriminated by a Front End Analogue card (FEA) mounted on every TOF module, as shown in Fig. 4.8. All FEAs are located very close to the source of the signal and are directly connected to the anode PCB by means of flat cables. FEA cards are positioned on the PCB located on top of the aluminum honeycomb and are controlled through the Front End Analogue Control (FEAC) cards. This allows for sorting each connection between the card and the pads on the strip. At this stage, the discriminated signal is shaped to provide a Time-Over-Threshold (ToT) information. The information on the time of the hit (the signal leading edge) and signal amplitude (approximated in the Time-Over-Threshold approach by measuring the width of the signal) are recorded. This technique requires the evaluation of time-slewing corrections to take into account the finite rise time of the signals.

- The ToT signal provided by FEAs is transmitted through special shielded cables (optimized to preserve the signals) to dedicated boards located at the ends of the SM: the TDC Readout Module (TRM). Every TRM is equipped with High Performance TDCs (HPTDC) capable of very high timing resolution ($\sigma_{\text{HPTDC}} \sim 25 \text{ ps}$).
- For the synchronization of all readout modules the common LHC clock is distributed to HPTDCs through the Clock and Pulser Distribution Module (CPDM) which also generates the pulse signals to test MRPCs.
- All TRMs are read by Data Readout Module (DRM) boards that collect and process the data that are sent to the central DAQ via dedicated optical links (Detector Data Link or DDL).
- The information for the trigger is collected via a Local Trigger Module (LTM) board coupled to a dedicated TRM.

The Front End Analogue: FEA

The Front End Analogue cards (FEA) are located close to the strips. This solution was adopted to avoid any possible degradation of the fast signals coming from the MRPCs and to achieve the best detector resolution. They collect the signals from the PCB anodes/cathodes and are the first layer of readout. FEAs process the input signals received from the strip by performing both amplification and discrimination.

The outcome of the detector R&D was a chip implementing an 8-channel amplifier and discriminator with fast response and good performance to match the strict requirements of the ALICE TOF MRPC. This is the NINO ASIC¹ chip [108]. Based on a $0.25 \mu\text{m}$ CMOS technology, it is able to handle differential input to profit from the differential signal from the MRPC, it provides fast signal amplification with less than 1 ns peaking time and it encodes the input charge into the width of the output signal by Time-Over-Threshold to allow for the computation of time-slewing correction. In addition, it has very low power consumption (40 mW per channel) with respect to similar devices.

Three NINO ASIC 8-channel chips are hosted on each FEA card, for a total of 24 channels per FEA. The 96 pads of each strip are read by a total of 4 FEAs and 12 NINO chips. Each FEA is mounted on the back of each module on the TOF module Interface Card PCB in thermal contact with serpentines cooled by a cold water circuit.

The signal amplified from the NINO chips are collected by the FEA cards and sent to dedicated Time to Digital Converters via low-noise Amphenol cables.

¹Application-specific integrated circuit

The Front End Analogue Control: FEAC

FEAs are powered and managed by the Front End Analogue Control (FEAC) card, also located in the front-end area. Up to six groups of two FEAs are connected in daisy-chain via flat cables to a single FEAC card. The FEAC card distributes the low voltage (2.5 V) to 12 FEAs and collects their trigger signals (OR signals). Depending on the amount of strips each module has either 5 or 7 FEACs.

The TDC Readout Module: TRM

The discriminated and amplified signals coming from the FEAs are collected by the TDC Readout Module (TRM) via Amphenol cables. The TRMs are placed in custom crates positioned at the ends of the SM (two crates per side, sharing the readout of full strips). The management and the configuration of the TRM boards is handled via a VME interface, implemented by a FPGA² which also acts as readout controller, event manager and online Data Processor.

Each TRM is equipped with a set of 30 HPTDC [109]: a high performance multi-event TDC capable of sampling signals with 25 ps bin size³. 8 channels are hosted by each HPTDC chip in the very high resolution mode. Every hit is recorded by the HPTDC in 32 bit words. In order to transfer the information on both edges (leading and trailing) of the signals coming from the FEAs, two separate words are used. For this reason the overall word size per hit is 64 bits. The multi-hit capability is granted by attaching a 256 words (128 hits) deep buffer to every pair of channels. Hits are propagated to a 256 words deep FIFO⁴ buffer shared between four channels. The 30 HPTDCs are arranged in three identical sub-cards with piggy-back connections, for a total of $30 \times 8 = 240$ TDC channels per TRM.

Time measurements are matched to a trigger time tag within a user programmable time window. In the current configuration, upon receiving a L1 trigger signal from the CTP, the HPTDC looks for hits in a time window of 600 ns shifted in the past of 8.850 μ s with respect to the arrival of the trigger signal. Both window duration and delay with respect to the L1 signals can be changed depending on the user needs. The hits are collected through the FIFO and stored in RAM event buffers. The L2 signal from CTP is used to decide whether to transmit the recorded data via the VME bus. After this decision RAM buffers are cleared

²The Altera APEX Field-Programmable Gate Array.

³Different running modes are available from the 40 MHz clock: low resolution mode with 800 ps LSB, medium resolution mode with 200 ps LSB, high resolution mode with 100 ps LSB, very high resolution mode with 25 ps LSB.

⁴A First In First Out method buffer.

trough the DRM. This strategy does not introduce any dead time in the data acquisition from HPTDCs.

Each TRM board can read 240 TDC channels, corresponding to 2.5 entire strips or 5 half-strips. All 91 strips of a SM are read by 38 TRMs. The channel of 36.2 TRMs would be enough to handle all 8736 readout channels of a SM. The additional two TRM boards, located in the left crate on each side of the SM, receive signals from a single half strip. The remaining readout channels in these TRMs are dedicated to receive signals from the four LTM cards.

The Data Readout Module: DRM

The interface between the TOF electronics and the central DAQ/CTP is handled by the Data Readout Module (DRM) board. One DRM is placed in each crate of the SM, its connection with the central DAQ is ensured trough optical links (DDL). The L1 and L2 signals are received from the CTP by the DRM and propagated to the TRMs to trigger the data transmission and the reset of the buffer registers. DRMs read data from TRMs in case of a positive answer from CTP, they also provide data encoding for the transmission to the central DAQ.

The Clock and Pulser Distribution Module: CPDM

The Clock and Pulser Distribution Module (CPDM) propagates the LHC clock to every board of the SM crates. One CPDM is enough to serve two neighbouring crates located on each side of the SM. Two CPDMs are needed per SM. The LHC High-Quality clock is received by the CPDM via optical fibers, it is then split into 24 LVDS clock signals that are delivered to the boards in the crates trough specific cables. The common clock source ensures the synchronization of all the TOF electronics. The CPDM is also designed to generate the pulse signals to test the MRPCs.

The Local Trigger Module: LTM

The trigger signals generated by the front-end FEAs and collected by the FEAC are sent to the Local Trigger Module (LTM). This constitutes the first layer of the TOF trigger system. Each LTM is connected to 8 FEAC cards and is designed to handle a total of 48 input signals with a dedicated FPGA. Each of the four VME crates in the SM hosts one LTM. The total trigger data for the whole TOF are processed by 72 LTMs.

Device	Relative Quantity
FEA	one per 8 PCB pickup pads
FEAC	one per 12 FEACs
TRM	one per 30 FEAs
VME crate	four per SM
DRM	one per VME crate
CPDM	one per VME crate pair
LTM	one per VME crate
CTTM	one for all 72 LTMs

Table 4.2 Total and relative amount of the different components of TOF detector.

The Auxiliary Control Module: ACM

Located further away from the detector area, outside the solenoid magnet and below the muon spectrometer, are installed the Auxiliary Control Module (ACM) boards. Each one of the five ACM cards handles BUSY and PULSE signals via 16 RJ45 connections. BUSY signals received from DRMs are elaborated to produce a global busy signal that is propagated to the CTP. PULSE signals are sent to DRMs to trigger the pulse generation in the CPDM.

The Cosmic and Topology Trigger Module: CTTM

The Cosmic and Topology Trigger Module (CTTM) [110] constitutes the second layer of the TOF trigger. The CTTM is a custom board designed to process all the data received from the 72 LTMs. The board is located in the same area of the ACM, below the muon spectrometer. The connection between the LTMs and the CTTM is ensured through purpose-designed 60 m long cables.

The CTTM implements the trigger logic based on hit multiplicity or hit topology. This feature allows for a cosmic muon trigger or a Ultra Peripheral Collision photon scattering trigger by requiring vertical back-to-back hits in coincidence. L0 and L1 decisions are generated in the CTTM and propagated to the central CTP using the LVDS standard. The TOF trigger information has been used since the start of Run 1 to collect cosmic events when no beam is circulating in the LHC and UPCs collisions when the LHC is injected with ions. While both cases are important per se for the physics information that can be extracted, cosmic events are necessary to assess the detector alignment for tracking.

Chapter 5

Performance of the ALICE Time-Of-Flight detector in Run 2 and preparation for Run 3

Particle identification with the TOF detector is performed by measuring the *time-of-flight* of the particle, defined as:

$$\text{time-of-flight} = t_{\text{TOF}} - t_{ev} \quad (5.1)$$

t_{TOF} is the time of arrival of particles to the TOF array. t_{TOF} is measured by the TOF detector and assigned to reconstructed tracks reaching TOF by dedicated algorithms. t_{ev} is the event time, that is, the time at which the collision occurred. The event time can be estimated with the T0 and TOF detectors.

The procedures for the event time estimation and for the time assignment to reconstructed tracks are described in this chapter. The calibration of the TOF detector is also illustrated. The validation of the calibration and of the track matching procedure was extensively studied during the work carried out for this thesis. This information is used to assess the performance of the ALICE TOF detector, in preparation for Run 3. The developments for the upgrade of the ALICE TOF detector are also part of this thesis.

5.1 Reconstruction and calibration

Tracks produced in the central barrel are reconstructed with the ITS and TPC detectors. The procedure for track reconstruction in ALICE is sketched in Fig. 5.1, as described in [11].

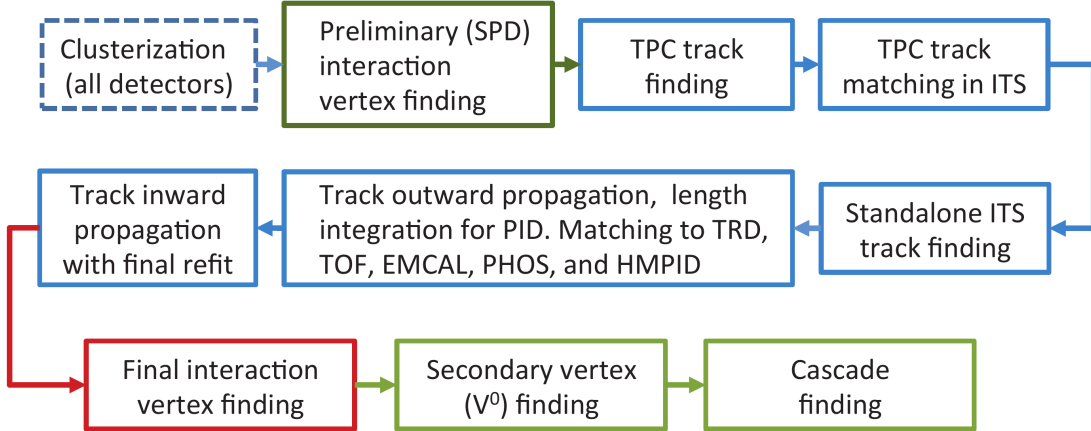


Fig. 5.1 Workflow of the reconstruction algorithm in the ALICE experiment [11].

Tracks that are propagated beyond the TPC can be matched to a hit in the TOF detector and assigned to a time measurement. The information on the track momentum is used for the TOF calibration and event time determination. The procedure to match reconstructed tracks to TOF hits, the TOF detector calibration and the event time determination are described in this section.

5.1.1 Track matching

The software dedicated to the simulation, data handling and reconstruction are based on modified versions of Root [111]: AliRoot [112] and AliDPG [113]. The reconstruction starts after all hits are clusterized by single-detector algorithms (the definition of cluster is specific to each detector). The preliminary position of the vertex is determined with good precision along the beam axis z by using the SPD [114]. At this point, track finding and fitting in TPC and ITS is performed in an inward-outward-inward scheme by using the Kalman filter algorithm [115]. Concurrently, the ITS stand-alone reconstruction described in Chapter 3 is carried out. Due to the large computational task, the ITS stand-alone reconstruction is performed by default in pp collisions and only if required in high occupancy environments such as Pb–Pb collisions. Reconstructed tracks are propagated outwards, matched to clusters in the outer central barrel detectors and fitted. The track length, as well as the *time-of-flight* computed for various particle species (e , μ , π , K , p , d et cetera), are integrated during each outward propagation step. Tracks reaching TOF are matched to TOF clusters with a dedicated procedure described below. The track length and *time-of-flight* step-by-step integration are stopped at this stage. The expected *time-of-flight* measurements t_{exp} for the particle species i are computed as:

$$t_{exp,i} = \sum_k^{Integration\ steps} \Delta t_{exp,i} = \sum_k^{Integration\ steps} \frac{\sqrt{p_k^2 + m_i^2}}{p_k} \Delta l_k \quad (5.2)$$

These quantities are used for PID purposes: the *time-of-flight* measured with the TOF detector can be compared with the expected one, computed for several mass hypotheses. This takes into account the slowdown of particles due to their energy loss in the material. The next step in the reconstruction refits all tracks towards the interaction vertex. The track quality can be assessed at this point by considering the value of the χ^2/NDF obtained in the fit. Tracks which are not able to fit the clusters of a particular detector are labeled accordingly, this information can be used when selecting tracks for analysis purposes. At this stage, the most precise position of the primary interaction vertex is determined by using the reconstructed tracks. Additional steps for the reconstruction of secondary vertices originating from photon conversions in the material and decays of strange hadrons (K_S^0 et cetera) are carried out.

The TOF track matching procedure, described in detail in [90, 7, 85, 86, 11], has the purpose to assign a TOF cluster to each track propagated outside the TPC. A research region is defined around the position in which the extrapolated track would impinge on the TOF active area. TOF hits in this “matching window” are selected as matchable candidates. During the Run 1 and Run 2 of LHC the matching window has been set to 10 cm in the reconstruction of low occupancy environments (such as pp, p–Pb and peripheral Pb–Pb collisions) and it is 3 cm for events with high multiplicity (i.e. AA collisions). The two behaviour are used to limit the effect of the combinatorial background. The geometrical distance between the position of the cluster and the extrapolated track hit is computed. This “residual distance” is computed in the xy (d_{xy}) plane and along z (d_z). The track is matched to the nearest available cluster. Once a cluster is matched, it is removed from the sample of matchable hits so as to avoid double assignments. This procedure is not immune to erroneous matching, in which case the track is connected to an uncorrelated time. This condition is known as “track mismatch” or simply “mismatch”. In order to reduce the mismatch probability, tracks with smaller curvature are matched first. The amount of mismatched tracks depends on the event multiplicity and on the size of the matching window. Further studies on the track mismatch are shown in Section 5.3.3.

The same tracking and matching procedures are used for both real data and Monte Carlo simulation. The TPC-TOF matching efficiency is reported as obtained in real data and Monte Carlo simulation as a function of p_T in Fig. 5.2. The good agreement of the two ensures that the real data is correctly described in the MC.

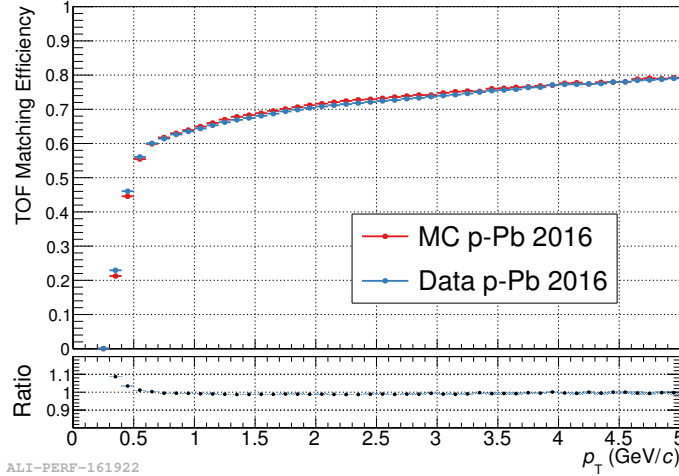


Fig. 5.2 TPC-TOF matching efficiency as a function of p_T , as measured in both recorded and simulated p–Pb collisions. The agreement of the two matching efficiencies is crucial to reproduce the detector response.

5.1.2 Time calibration procedure

The extraction of the TOF calibration calibration requires a full track reconstruction in the ALICE detector in order to make use of the track momentum information. As a consequence, the calibration constants are to some degree coupled to the calibration of the tracking detectors, in particular that of the TPC. The time calibration procedure is aimed at determining the three corrections [9]:

1. Global offset, common to all readout channels.
2. Single channel offset accounting for electronics/cable delays.
3. Single channel time-slewing correction.

The global offset takes into account the shift of the LHC clock due to variations in the local temperature that cause a change in the refractive index of the optical fiber. This affects the LHC clock distributed to the experiments in a time-dependent way. The global offset is computed every 10 minutes from a sample of tracks with momenta larger than $0.5 \text{ GeV}/c$ to ensure good tracking performance by dedicated online algorithms. The integrated times computed for the pion hypothesis ($t_{exp,\pi}$) during tracking are subtracted from the arrival time measured with the TOF detector. The resulting distribution is fitted with a Gaussian function whose mean corresponds to the global channel offset for the time interval under study. The global calibration offset computed during a fill of the LHC Run 1 is shown as a function of time in Fig. 5.3. The contribution of the global offset is non negligible as it is shown to double its value over a period of 10 hours of data taking.

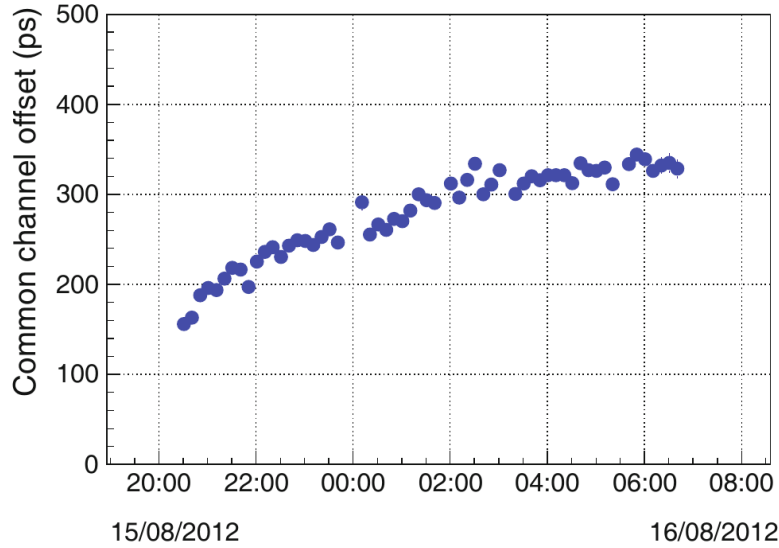


Fig. 5.3 Global calibration offset as measured as a function of time during one LHC fill of Run 1 [9].

The single-channel offset is used to account for delays in the measured times (t_{TOF}) due to different electronics and cable lengths. The procedure to extract this calibration constant is similar to the one used for the global offset with the difference that a single-channel granularity is used in this case. A Gaussian fit is performed to the single-channel $\text{tof} - t_{\text{exp},\pi}$ distributions. The mean of the fit is used as calibration offset. With respect to the extraction of the global calibration offset, a much larger track sample is needed to ensure a sufficient number of tracks per channel, thus a reliable fit. These offsets do not vary significantly with time [9] and can be obtained by using the data collected over several hours of data taking. Nonetheless, the single-channel calibration is repeated at regular time intervals to correctly take into account any possible variation in the TOF readout chain.

The last correction takes into account time-slewing effect, represented in Fig. 5.4. The two signals shown in the figure share the same origin but would be assigned to different times as they cross the fixed threshold in two successive instants. The time-slewing correction, evaluated channel-by-channel, takes into account this effect. This single-channel correction is obtained by fitting the correlation between the measured time and the signal width (Time-Over-Threshold, ToT) which are both given by the HPTDC. The ToT corresponds to the time interval during which the signals are above the threshold of the discriminator. The parameterizations extracted during calibration are used to correct the hit time measurement according to the signal ToT.

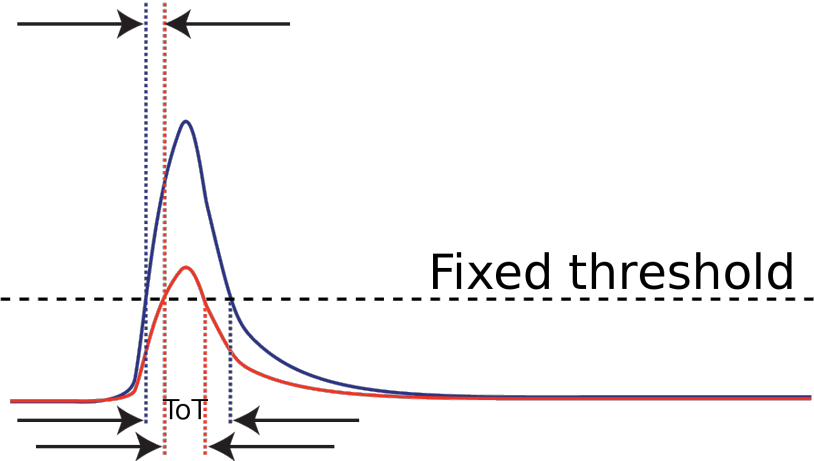


Fig. 5.4 Time slewing due to finite time rise of signals and fixed thresholds.

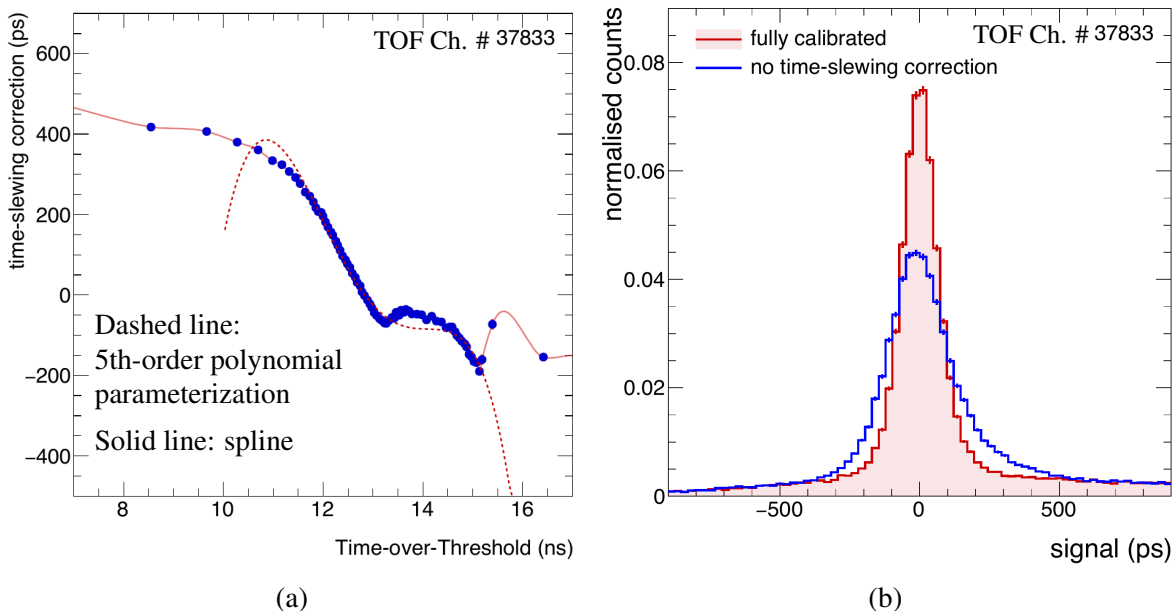


Fig. 5.5 (a) Correlation between the ToT and the measured time for the single TOF channel 37833. Two parameterizations of the behaviour are reported: the dashed line indicates a 5th-order polynomial (Run 1 situation), the solid line represents the point-by-point spline parameterization (Run 2 situation). (b) Distribution of the measured times before and after the time-slewing correction.

The time-slewing correction was parametrized during the LHC Run 1 with a 5th-order polynomial. During Run 2, the correction was significantly improved by using a point-by-point spline parameterization¹. The two different approaches are shown in Fig. 5.5a. The polynomial parameterization reproduces only partially the measured values, especially for small and large ToTs. With respect to the polynomial parameterization, the point-by-point splines allows to improve the time-slewing calibration. The effect of the calibration on the measured time distribution is shown in Fig. 5.5b.

Large statistics are necessary to measure these two dimensional calibration. For this purpose the calibration procedure uses the data collected during several weeks of data taking as no significant time dependence of the time-slewing effect is expected. Due to the available statistics, the calibration was performed during Run 1 with the granularity of eight channel groups (corresponding to a single FEA) whereas, during Run 2, a calibration at the single-channel level was made possible. This change also improves the overall detector response. The stability of the time-slewing calibration is shown in Fig. 5.6. During the 2017 data taking campaign the majority of channels did not exhibit any dependence of the calibration constants with time. This ensures that the time-slewing correction has a long lifetime and can be used, without any significant change, to correct data that were not used for calibration. The effects of the calibration on the detector performance and the comparison of the Run 1 and Run 2 performance are discussed in Section 5.2.1.

5.1.3 Event time determination

In order to perform PID with the TOF detector one needs the arrival time measured by the TOF but also the event time (t_{ev}) that is the time of the collision, common to all produced particles in the event. The t_{ev} varies with each collision and has to be measured directly [8]. The event time measurement can be obtained from the information of the bunch crossing time recorded by the LHC (t_{ev}^{Fill}). However in this case, there is a significant uncertainty in establishing the event time due to the finite size of the bunches. Depending on the accelerator configuration, the resolution on the event time obtained from the LHC varies between 80 and 200 ps. This resolution affects the overall precision of the *time-of-flight* measurement by significantly reducing its PID potential.

The ALICE T0 detector (described in Section 3.1.5) is dedicated to the measurement of the event time. The T0 array is divided into two subsystems (T0A and T0C located on each side of the interaction point). If both T0A (t_{ev}^{T0A}) and T0C (t_{ev}^{T0C}) measurements are available, the information of the two is combined to achieve the best resolution (t_{ev}^{T0AC}). However it

¹A spline is a function defined piece-wise by polynomials.

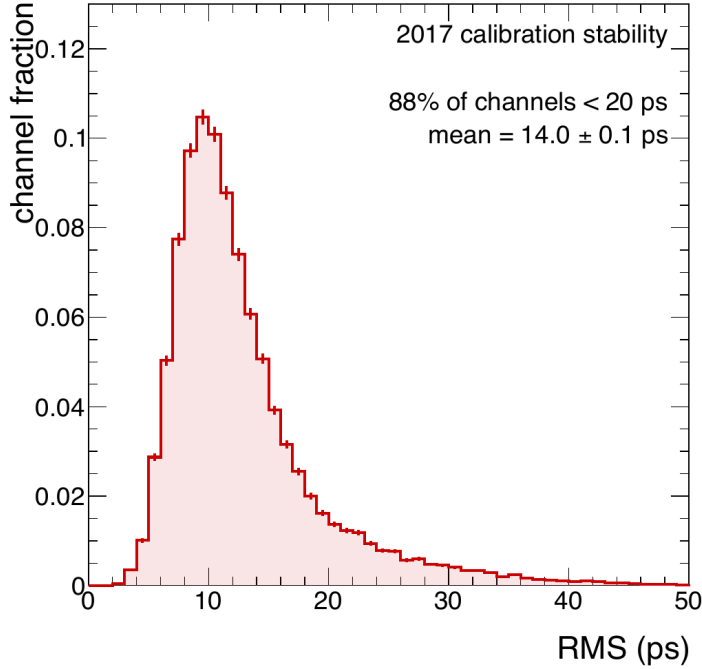


Fig. 5.6 Single-channel time slewing calibration stability, in terms of RMS of the calibration constants, during the 2017 data taking campaign.

may happen that, especially in low multiplicity environments such as pp collisions, no signal is observed in any of the T0 detectors. For these events no estimate of the event time is available from the T0 detector and one has to rely on the information from the LHC bunch crossing time. The average resolution on the event collision time t_{ev}^{T0AC} ($\sigma_{t_{ev}^{\text{T0AC}}}$) are about 25 and 50 ps for Pb–Pb and pp collisions, respectively. The difference in the resolution for the two collision systems is due to the different average multiplicity of the events, resulting in different signal amplitudes. The average resolution on the event collision time in Pb–Pb collisions is $\sigma_{t_{ev}^{\text{T0A}}} \sim 50$ ps for t_{ev}^{T0A} and $\sigma_{t_{ev}^{\text{T0C}}} \sim 30$ ps for t_{ev}^{T0C} . In pp collisions the resolution is ~ 100 ps for t_{ev}^{T0A} and ~ 60 ps for t_{ev}^{T0C} [8]. The difference in the $\sigma_{t_{ev}^{\text{T0A}}}$ and $\sigma_{t_{ev}^{\text{T0C}}}$ is due to the different distance of the two arrays from the interaction point.

The event time can be also obtained directly using the information of the TOF detector in events with at least three tracks matched to a TOF signal. In this case, the t_{ev} determination is performed via a dedicated combinatorial algorithm. Assuming a common event time t_{ev} , the algorithm compares the measured TOF times to the expected times (for the π , K or p mass hypotheses) obtained from the information on the track momentum and track length. The event time for the k track can be obtained from a weighted average over all tracks (except the k^{th} track) of the difference between the measured times t_{TOF} and the expected times t_{exp} :

$$t_{ev}^{\text{TOF}} = \frac{\sum_{j=1, j \neq k}^{n_{\text{tracks}}} w_j(i) (t_{\text{TOF},j} - t_{\text{exp},i,j})}{\sum_{j=1, j \neq k}^{n_{\text{tracks}}} w_j(i)} \quad (5.3)$$

The expected times depend on the particle mass hypothesis, hence the i index. The k^{th} track is not considered in the average to avoid the risk of auto-correlation biases, especially for low multiplicity events. The resolution on the event time can be obtained as:

$$\sigma_{t_{ev}^{\text{TOF}}} = \sqrt{\frac{1}{\sum_{j=1, j \neq k}^{n_{\text{tracks}}} w_j(i)}} \quad (5.4)$$

The weights $w_j(i)$ consider the uncertainties on the time measurement (σ_{TOF}) and on the expected time for the species i ($\sigma_{t_{\text{exp},i}}$):

$$w_j(i) = \frac{1}{\sigma_{\text{TOF},j}^2 + \sigma_{t_{\text{exp},i,j}}^2} \quad (5.5)$$

t_{ev}^{TOF} is then obtained via a χ^2 -minimization procedure. The χ^2 is defined as:

$$\chi^2 = \sum_{j=1, j \neq k}^{n_{\text{tracks}}} \frac{\left[(t_{\text{TOF},j} - t_{\text{exp},i,j}) - t_{ev}^{\text{TOF}} \right]^2}{\sigma_{\text{TOF},j}^2 + \sigma_{t_{\text{exp},i,j}}^2} \quad (5.6)$$

The χ^2 is evaluated for all possible mass hypotheses ($i = \pi, K, p$) and is minimized. For each track, the minimization procedure allows to obtain a particle mass hypothesis whose expected time is in agreement with the measured t_{TOF} .

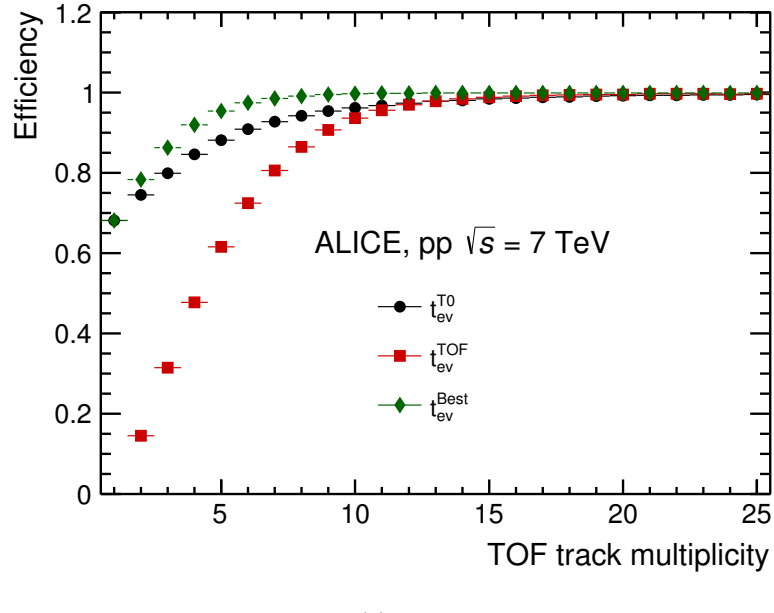
The procedure described so far evaluates the average t_{ev}^{TOF} and performs the χ^2 minimization for all measured tracks. This solution is rather impractical because of the large computational cost it implies². In the present implementation of the algorithm, the minimization is carried out only ten times instead of n_{tracks} times. This is achieved by classifying the tracks into ten 1 GeV/c wide sub-samples of increasing momenta. An event time is extracted for each sub-sample by using all the tracks that are not part of it. The χ^2 value is checked for each track used in the sum to verify that the measured time is compatible with at least one particle mass hypothesis and is not completely uncorrelated (i.e. originating from mismatched tracks). At the end of t_{ev}^{TOF} evaluation, the value of the minimized χ^2 is verified to eventually mark the minimization procedure as unsuccessful. In this case the t_{ev} estimation relies on the measurement of the T0 detector (t_{ev}^{T0}) or the LHC bunch crossing time (t_{ev}^{Fill}). The procedures to determine the event time with the T0 and TOF detectors are independent.

²especially in Pb–Pb collisions where more than 2000 particles can be produced per unit of pseudorapidity [31].

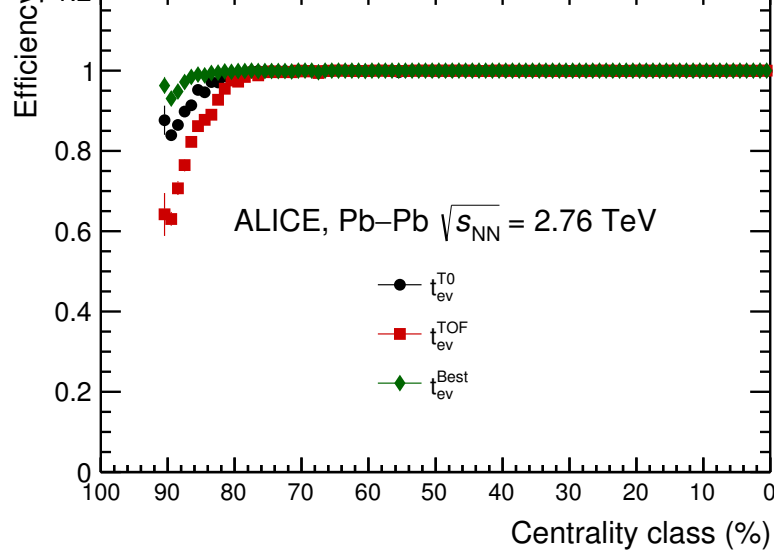
The t_{ev}^{T0} and t_{ev}^{TOF} values can be combined to obtain the more precise estimate of the event time (t_{ev}^{Best}). The t_{ev}^{Best} is available if the event time is measured with either T0 or TOF.

The efficiency of the event time evaluation procedure depends on the number of tracks available, the success rate is higher for events with larger charged particle multiplicity. The efficiency of the t_{ev}^{T0} , t_{ev}^{TOF} and t_{ev}^{Best} is shown as a function of the track multiplicity, measured in both pp and Pb–Pb collisions in Fig. 5.7. The t_{ev}^{Best} efficiency saturates already for events having six charged tracks matched to TOF (see Fig. 5.7a), while the t_{ev}^{TOF} becomes fully efficient for events with more than ~ 15 tracks. In Pb–Pb collisions the larger charged particle densities ensures high efficiencies for most of the events³.

³In pp collisions at $\sqrt{s} = 7$ TeV the $\left\langle \frac{dN_{\text{ch}}}{d\eta} \right\rangle \sim 4.6$ [116], significantly lower than the one reached in Pb–Pb collisions.



(a)



(b)

Fig. 5.7 Efficiencies of the different event time evaluation methods t_{ev}^{T0} (circles), t_{ev}^{TOF} (squares) and t_{ev}^{Best} (diamond) [8]. (a) As a function of the charged particle multiplicity reaching TOF, measured in pp collisions at $\sqrt{s} = 7$ TeV. (b) As a function of the Centrality class for Pb–Pb collisions $\sqrt{s_{NN}} = 2.76$ TeV.

5.2 PID performance of the TOF detector

The results on the performance of the ALICE TOF detector are presented in this section, a recent review can be found in [117, 118].

The particle *time-of-flight*, defined as:

$$\text{time-of-flight} \equiv \text{tof} = t_{\text{TOF}} - t_{ev} \quad (5.7)$$

Is used to perform PID with the TOF detector. The largest separation power is achieved with the best timing resolution on t_{TOF} and t_{ev} . The resolution on t_{TOF} (the time measured with the TOF detector) has several independent contributions.

$$\sigma_{t_{\text{TOF}}}^2 = \sigma_{\text{MRPC}}^2 + \sigma_{\text{TDC}}^2 + \sigma_{\text{FEE}}^2 + \sigma_{\text{Calibration}}^2 \quad (5.8)$$

These are the intrinsic MRPC resolution σ_{MRPC} , the TDC and Front End Electronics resolutions σ_{TDC} , σ_{FEE} and the contribution associated to the calibration $\sigma_{\text{Calibration}}$. The measured tof is compared with the expected time t_{exp} for a given particle species to construct the discriminating quantity (t_{PID}) for the PID:

$$t_{\text{PID}} = \text{tof} - t_{exp} = t_{\text{TOF}} - t_{ev} - t_{exp} \quad (5.9)$$

The resolution (σ_{PID}) on the discriminating quantity t_{PID} includes the contribution of tracking σ_{tracking} from in the expected time t_{exp} .

$$\sigma_{\text{PID}}^2 = \sigma_{t_{\text{TOF}}}^2 + \sigma_{\text{tracking}}^2 + \sigma_{t_{ev}}^2 \quad (5.10)$$

In case the event time is obtained with the TOF detector, the resolution on the t_{ev} can be derived from Eq. 5.4 as:

$$\sigma_{t_{ev}} \sim \frac{\sigma_{t_{\text{TOF}}}}{\sqrt{n_{\text{tracks}}}} \quad (5.11)$$

As a consequence, the signal resolution depends on the multiplicity of charged tracks matched to a TOF hit.

The TOF resolution can be evaluated for tracks with high momentum ($p > 1 \text{ GeV}/c$) so that a good tracking resolution is achieved. The best option is to rely on the signal of pions that are more abundant than heavier species and reach relativistic velocities at lower momenta with respect to heavier particles. The TOF signal resolution is shown in Fig. 5.8 as a function of the multiplicity of charged tracks matched to a TOF hit, as obtained in p–Pb collisions at $\sqrt{s_{\text{NN}}} = 5.02 \text{ TeV}$. The Gaussian fit to the signal shape used to extract the

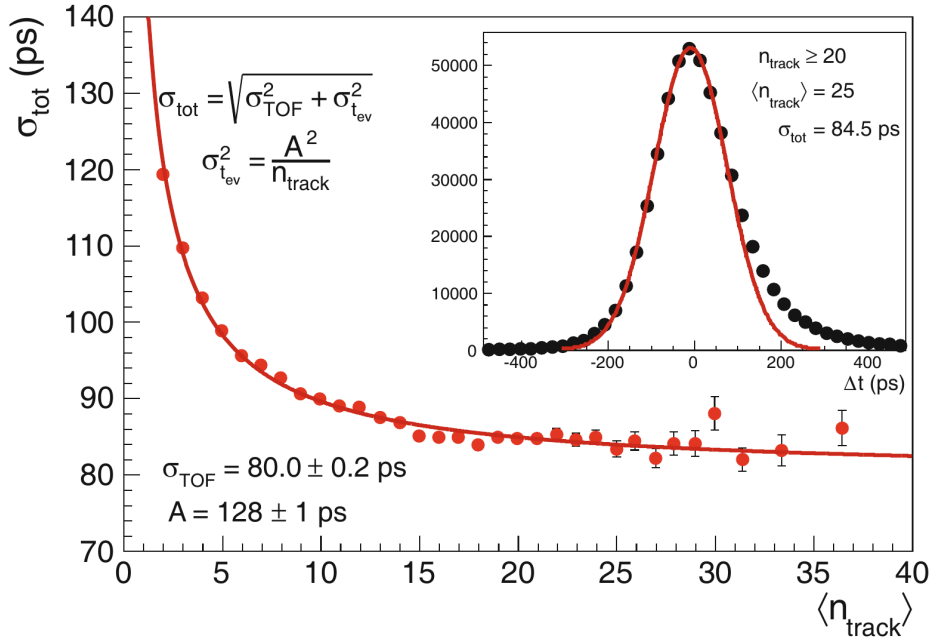


Fig. 5.8 TOF signal resolution for pion tracks with $0.95 < p < 1.05 \text{ GeV}/c$ as a function of the multiplicity of charged tracks matched as obtained from Run 1 p–Pb collisions during Run 1 [9]. The inset shows the TOF signal distribution for events with track multiplicity reaching TOF greater than 20.

resolution values is shown in the inset. The best *tof* resolution achieved during Run 1 is $\sim 80 \text{ ps}$.

5.2.1 TOF detector calibration in Run 2

During Run 2 the more precise channel-by-channel calibration described in Section 5.1.2 was made available. The resolution on t_{PID} , obtained in Pb–Pb collisions at $\sqrt{s_{\text{NN}}} = 5.02 \text{ TeV}$ for events with resolution on the event time $\sigma_{t_{\text{ev}}} \sim 5 \text{ ps}$ is reported in Fig. 5.9. Two results obtained by using different calibrations are shown: in red the 5th-order polynomial calibration used during Run 1 (standard) and in blue the channel-by-channel one (improved). With the channel-by-channel calibration the resolution is improved by about 20 ps with respect to the resolution achieved in Run 1.

Thanks to the improvements in σ_{TOF} , a better precision on the event time was also achieved. The resolution on $t_{\text{ev}}^{\text{TOF}}$ is shown as a function of the number of charged tracks matched to TOF, as measured in Pb–Pb collisions at $\sqrt{s_{\text{NN}}} = 5.02 \text{ TeV}$. With the new calibration the $t_{\text{ev}}^{\text{TOF}}$ can be estimated with an uncertainty lower than 5 ps starting from events with ~ 600 tracks. The resolution on the $t_{\text{ev}}^{\text{TOF}}$ with improved calibration is shown as a function of the charged particle multiplicity reaching TOF in Fig. 5.10 and compared to the

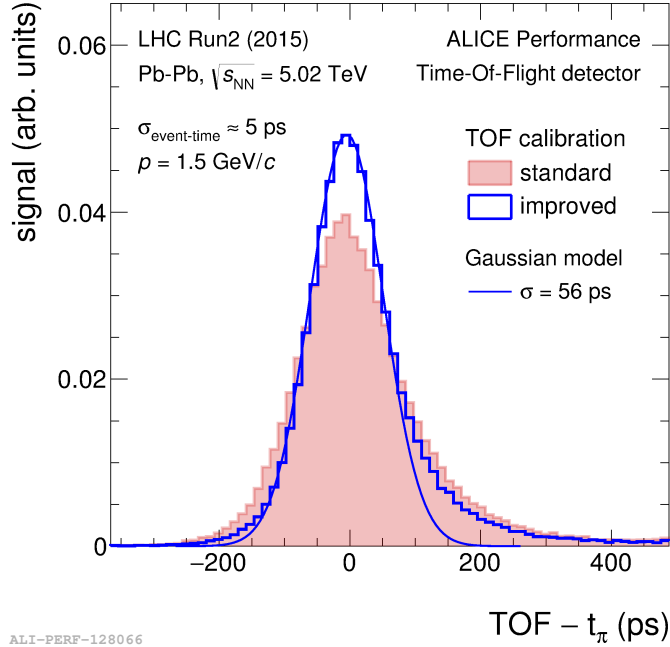


Fig. 5.9 Resolution on t_{PID} for the pion hypothesis as obtained with standard (Run 1) and improved (Run 2) calibrations [119].

resolution achieved in Run 1 in Fig. 5.11. The resolution on t_{ev}^{TOF} depends only on the track multiplicity and not directly on the collision system, as defined in Eq. 5.11. The improvement in the detector calibration is reflected in the precision achieved during Run 2.

The information on the detector resolution is of primary importance to understand the limits of applicability of the TOF PID. The separation power, measured in terms of $n\sigma$, can be used to assess the range of applicability of the PID technique. With t_{PID} as the discriminating quantity, the separation power can be defined as:

$$n\sigma = \frac{t_{\text{PID}}}{\sigma_{\text{PID}}} \quad (5.12)$$

The separation power achieved with the TOF detector is reported in Fig. 5.12. Two scenarios are shown, one with $\sigma_{\text{PID}} = 80$ ps representing the situation during Run 1 and the other with $\sigma_{\text{PID}} = 60$ ps for Run 2. With respect to the Run 1 calibration, the improved channel-by-channel one extends the 3σ level of the π/K and K/p separations of about ~ 500 MeV/ c . This considerably extends the PID capabilities of the TOF detector.

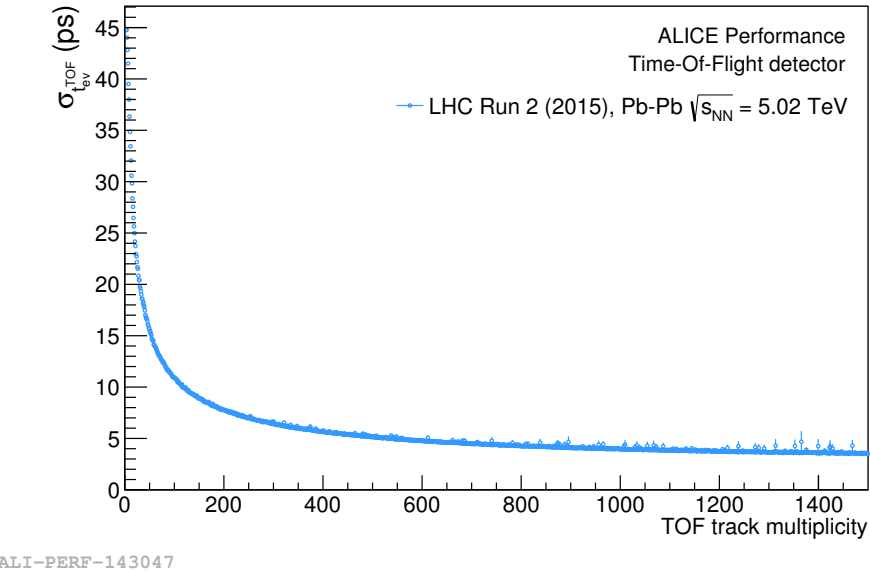


Fig. 5.10 Event time resolution during Run 2 with the improved TOF time-slewing calibration.

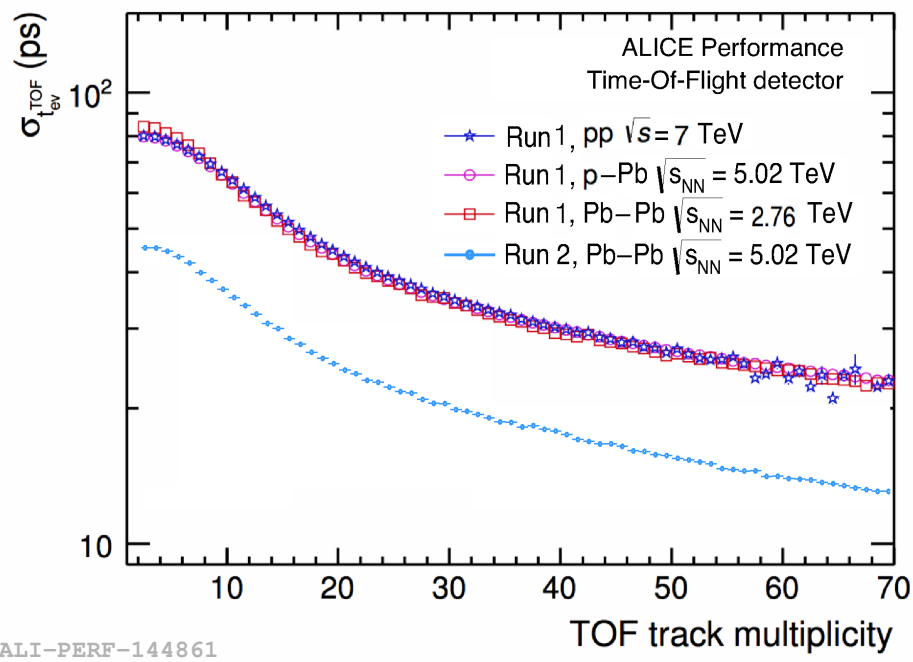


Fig. 5.11 Comparison between the $\sigma_{t_{ev}}^{\text{TOF}}$ in Run 1 and Run 2 for different collision systems.

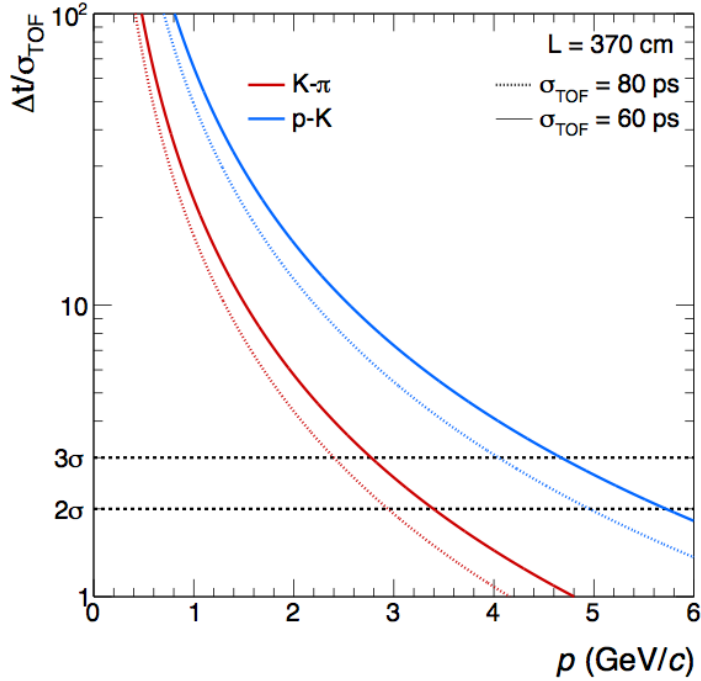


Fig. 5.12 The impact of the improved resolution on the PID is depicted together with lines at 2 and 3 σ .

5.2.2 Signal shape of the TOF detector

The signal distribution shown in Fig. 5.9 shows a typical shape of the TOF signal. A non-Gaussian tail is visible on the right side of the peak. This tail was not observed during the test beams [9] and was discovered after the first data with collisions were recorded. The origin of the non-Gaussian tail was extensively discussed and several explanations were proposed:

- Residual miscalibrations could induce a tail in the signal as, so far, no time walk effects related to the position of the track inside of the readout pad have been considered.
- The tail could be due to delayed signals originating from weak decays, forming a background correlated with the signal.

Nonetheless, the TOF signal can be described by a modified Gaussian. The detector signal response is obtained by convoluting a Gaussian (with parameters μ and σ) with an exponential function, with parameter τ . The parameterization includes three parameters μ , σ , τ :

$$f(t) = \begin{cases} \frac{1}{\sigma\sqrt{2\pi}}e^{-\frac{1}{2}\left(\frac{t-\mu}{\sigma}\right)^2} & \text{if } t \leq \mu + \tau \\ \frac{1}{\sigma\sqrt{2\pi}}e^{-\frac{1}{2}\left(\frac{\mu+\tau-\mu}{\sigma}\right)^2 - \tau \cdot \frac{x-\mu-\tau}{\sigma^2}} & \text{if } t > \mu + \tau \end{cases} \quad (5.13)$$

The parametrized TOF signal shape ensures continuity and differentiability.

5.2.3 PID separation power

The particle separation can be seen in the β distribution measured as a function of momentum in Pb–Pb collisions at $\sqrt{s_{\text{NN}}} = 5.02$ TeV (Fig. 3.9c), pp collisions at $\sqrt{s} = 5.02$ TeV (Fig. 5.13a) and Xe–Xe collisions at $\sqrt{s_{\text{NN}}} = 5.44$ TeV (Fig. 5.13b). The data with Xe–Xe collisions were collected with a low magnetic field configuration in the solenoid, $B = 0.2$ T instead of the nominal $B = 0.5$ T. As a consequence of this particular setup, the probability for low momentum tracks to reach the TOF array is higher. This is particularly visible in Fig. 5.13b, where the bands of protons and muons extend to lower momenta with respect to the $B = 0.5$ T setup (Fig. 5.13a).

The β distribution can be sliced in momentum bins to better appreciate the separation between signals. These distributions are shown for several momentum bins in Fig. 5.14. Starting at 400 MeV/ c the signals of pions, electrons and muons are clearly visible. The peak associated to deuteron is shown in Fig. 5.14c at momenta of 3 GeV/ c . Protons are well separated from kaons at $p = 5$ GeV/ c (Fig. 5.14d).

5.2.4 Standards for the Quality Assurance of data

The performance of the TOF detector are monitored by online and offline algorithms to assess the quality of the recorded data and spot possible issues in the data taking conditions of the detector or in the reconstruction and calibration. The TOF offline Quality Assurance (QA) monitors the parameters of the reconstructed tracks to verify the stability of the detector response. The QA algorithms validate the recorded data by checking the information on PID, track matching, calibration end event time determination for all reconstructed runs. The tools developed for the analysis of the TOF Quality Assurance can be found in [120].

As an example of the checks for the TOF QA, the residual difference between the position of the matched tracks and the TOF cluster along the z direction is shown for every MRPC strip as measured in pp and Pb–Pb collisions in Fig. 5.15. The strip index identifies the position in the TOF array along z (or η): the strip indices 0 and 90 correspond to $|\eta| = 0.9$, while $\eta \sim 0$ corresponds to strip ~ 45 . As one would expect from the matching procedure described in Section 5.1.1, the residuals for the strips are distributed around zero and show no asymmetry in the two sides of the TOF detector. The different width of the matching windows used for Pb–Pb (high multiplicity) and pp (low multiplicity) are visible. In low multiplicity events the maximum distance used to search for track matching candidates is set to 10 cm. In high multiplicity environments, such as Pb–Pb collisions, the region is limited

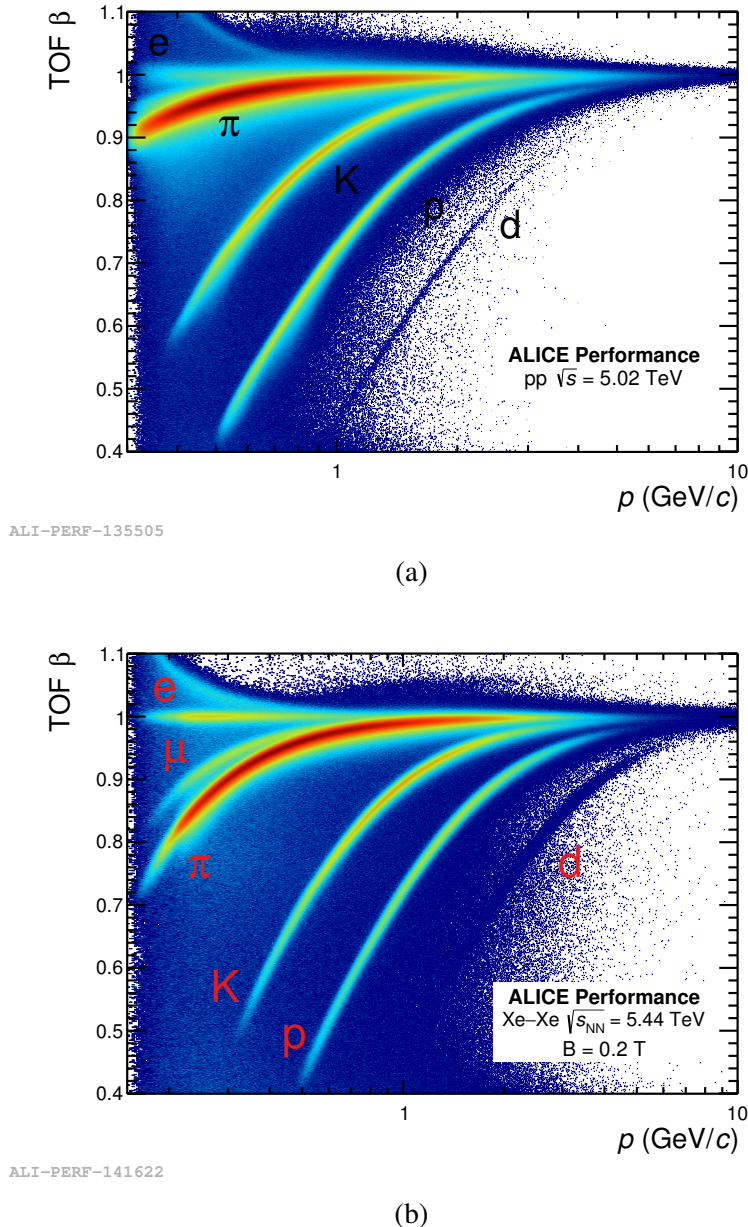


Fig. 5.13 Distribution of the particle velocity β measured with the TOF detector as a function of the track momentum p in Xe–Xe collisions with $B = 0.2$ T (b) and pp collisions (a) $B = 0.5$ T. The visible bands are from e , μ , π , K , p and d . The contribution from wrongly associated tracks (track mismatch) can be seen outside the bands.

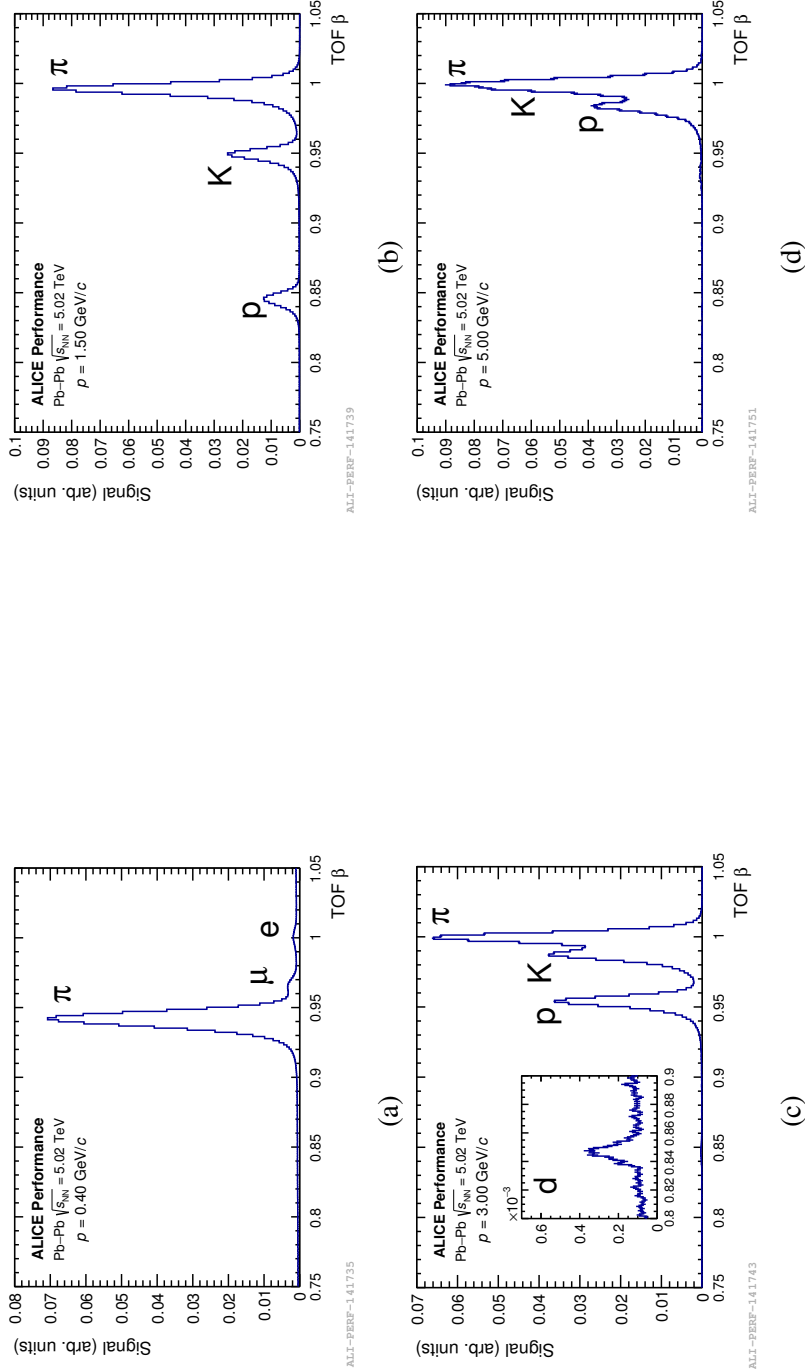


Fig. 5.14 Distribution of the particle velocity (β) as measured with the TOF detector in different momentum intervals as shown as a function of momentum in Fig. 3.9c. The signals from each particle species are clearly visible up to high momenta.

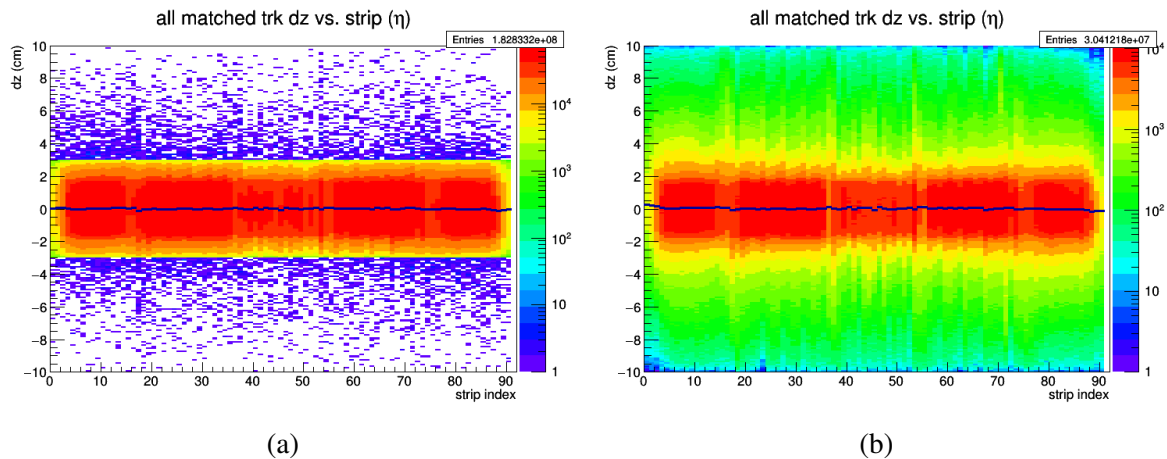


Fig. 5.15 Example of residual difference between the position of the extrapolated track and the position of the matched TOF cluster along the z direction as measured in 2015 in Pb–Pb collisions at $\sqrt{s_{\text{NN}}} = 5.02$ TeV (a) and pp collisions at $\sqrt{s} = 5.02$ TeV (b).

to 3 cm to reduce the contribution of combinatorial background (track mismatch). The points located at $dz > 3$ cm in Pb–Pb collisions are given by hits from very low multiplicity events specifically triggered for Ultra Peripheral Collisions (UPC). In these cases the 10 cm window is used also for heavy-ion collisions to increase the TPC-TOF matching probability. Deviations from zero could hint at the presence of a problem in tracking (e.g. imprecise calibration of the TPC).

The timing resolution is checked for all runs so as to check the stability of the detector response. The mean resolution is shown in Fig. 5.16 as a function of the data taking interval index. The resolution is expected to be stable in time.

The PID capabilities are checked by computing the $n\sigma$ distributions of pions, kaons and protons. These distributions are shown in Fig. 5.17 as a function of the track momentum. A fit with a Gaussian and a Gaussian with exponential tail (Eq. 5.13) is used to compute the mean and the width of the distribution. As one would expect the mean value of the distribution is aligned to 0 and the σ to 1, as long as the signals of different particle species are well separated. This is true as long as the particle momenta are sufficiently high so that a good tracking resolution is achieved ($p > 1 \text{ GeV}/c$).

This is the case for Fig. 5.17a while in Fig. 5.17b the situation is rather not ideal for PID. The abnormal behaviour of the second case is due to a problem of the solenoid magnet that caused a modification of magnetic field in the central barrel region. In this case, the expected times do not reproduce correctly the data.

More details on the TOF QA can be found in Appendix D.

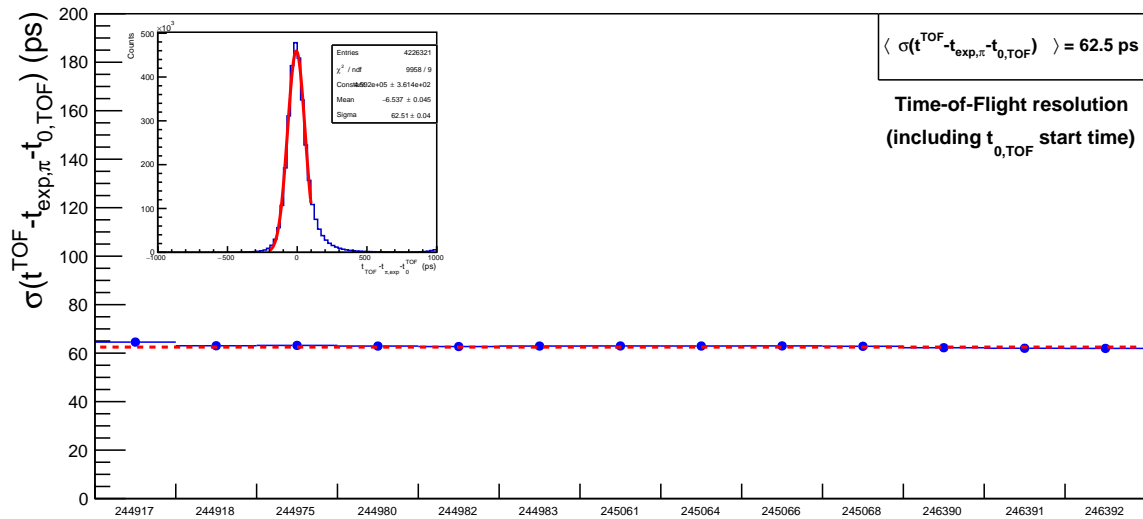


Fig. 5.16 Mean time resolution (including the contribution on the t_{ev}^{TOF}) as a function of the data taking interval index (time), measured in Pb–Pb collisions at $\sqrt{s_{\text{NN}}} = 5.02$ TeV. The pion signal at 1 GeV/ c is reported in the inset together with the Gaussian fit used to extract the time resolution.

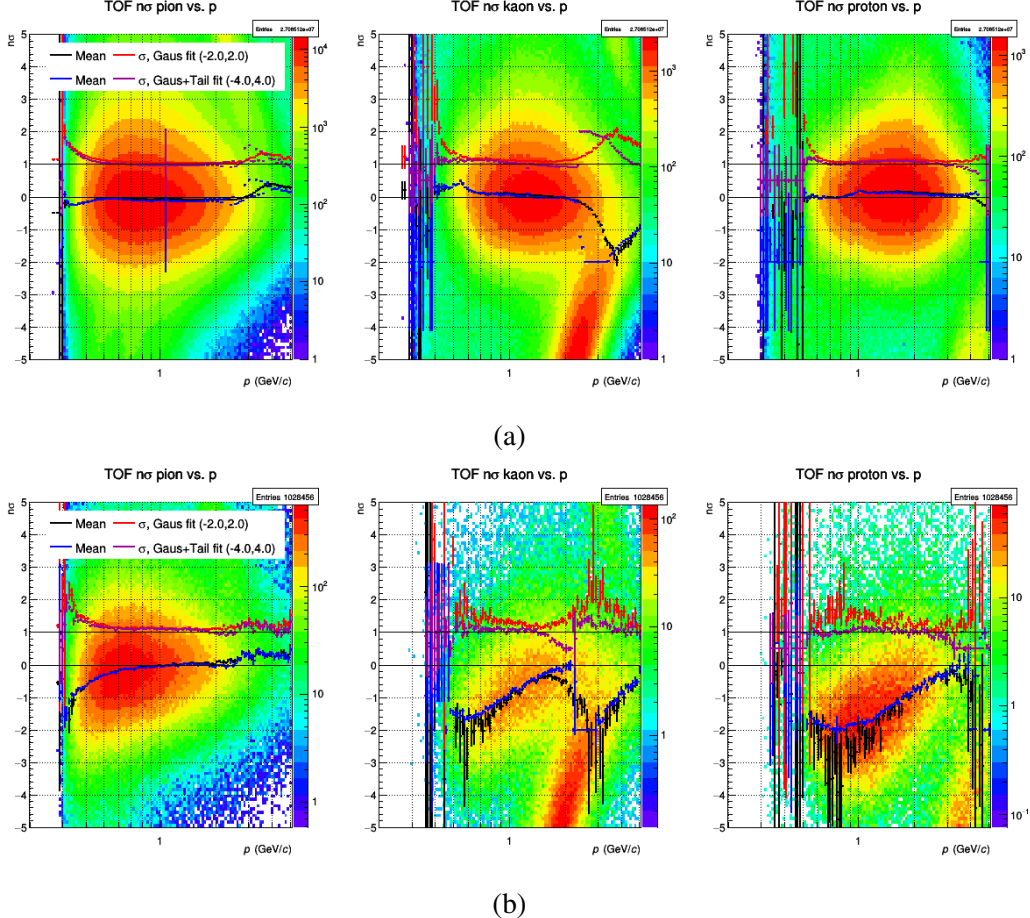


Fig. 5.17 Example of the typical QA distributions used to verify the performance of the TOF PID. The mean and width parameters of the Gaussian (Gaussian with exponential tail) fitting function, are reported in red and black (blue and magenta) respectively. (a) TOF $n\sigma$ for pions (left), kaons (middle) and protons (right) as measured in Pb–Pb collisions at $\sqrt{s_{NN}} = 5.02$ TeV showing the correct, expected behaviour. (b) The same distributions are shown as measured in a second case. In this case abnormal trends with mean deviating from zero are observed due to the expected times not reproducing correctly the data as a consequence of a sudden modification of magnetic field during data taking.

5.3 Developments for Run 3

Starting from the end of 2018 the LHC will enter the second Long Shutdown phase, the LS 2. During this period of two years the accelerator and the experiment detectors will undergo a series of upgrades to improve their performance. The data taking campaign is expected to resume in 2021 with the start of Run 3.

The ALICE experiment will upgrade its ITS [121], TPC [122] and forward detectors during the LS 2. Before the start of LS 2, ALICE will record Pb–Pb collisions up to an interaction rate of 8 kHz. The maximum readout rate of the present ALICE detector is limited to 500 Hz for Pb–Pb collisions. Exceeding this limitation is crucial for the development of the physics program of ALICE in the research of rare probes in heavy-ion collisions. During Run 3 the LHC will be delivering collisions of Pb–Pb at $\sqrt{s_{\text{NN}}} = 5.5$ TeV with rates up to 50 kHz. The detector readout will change dramatically to cope with the higher interaction rates. The ALICE sub-systems will implement a continuous readout process to deal with event pile-up and avoid trigger-generated dead time [123]. The resulting data throughput from the detector for Pb–Pb collisions has been estimated to be greater than 1 TB/s: two orders of magnitude more than during Run 1. In order to handle the expected data rates in the most efficient way, the ALICE computing model beyond Run 2 is designed to achieve a maximal reduction of the data volume as early as possible during the data-flow. The data compression is to be achieved by reconstructing the data synchronously with the data taking. This will allow to merge the online and offline components of the data taking and processing into one single project, called O² [124].

During Run 3 the hardware of the TOF detector will remain mostly unchanged, for this reason it is important that the detector performance is confirmed to be stable, without any sign of aging. An upgrade of the TOF readout electronics will be needed to meet the requirements of the O². The new DRM2 board, shown in Fig. 5.18, has been developed for the continuous readout configuration [10] and will be replacing the present DRM cards. The DRM will be the only element to be substituted in the TOF readout electronics during LS 2. The new board was developed to cope with faster triggers and equipped with improved data bandwidth to transfer higher data payload to the DAQ. The update in the DRM will also come with a modification of the readout logic for the buffers of the TRM HPTDCs. An improved version of the low voltage power supply modules used to power the crate boards and the FEE will also be installed at the beginning of LS 2. This upgraded modules will have better resistance to ionizing particles, a key aspect for the data taking of Run 3.



Fig. 5.18 New DRM2 board designed to replace the DRM in Run 3 [10].

5.3.1 Detector stability during Run 1 and Run 2

Several tests and analyses were performed during Run 1 and Run 2 with the scope to validate the stability of the TOF detector response over time. Stability in the detector response is a sign that no aging is occurring in the detector electronics and the MRPCs.

In order to assess the stability of the TOF trigger chain, the average rate of cosmic events triggered over a period of more than three years was analyzed. The TOF trigger rate of cosmic events, reported a function of the time in Fig. 5.19, is found to be stable. This indicates that the detector behaviour is stable and not showing any sign of degradation over several years.

The tests include the monitoring of the detector working conditions when subjected to a high charged particle flux. During Run 3 the highest particle load is expected to be reached in high interaction rate (50 kHz) Pb–Pb collisions at $\sqrt{s_{\text{NN}}} = 5.5$ TeV. This situation can be reproduced, by increasing the collision rate of pp collisions delivered by the LHC. Several high interaction rate tests were performed during Run 2 (2015–2018) to verify the stability of the detectors that will be used during Run 3, including the TOF detector. The increased particle load produces more charge in the active volume of the MRPC strips and causes an increase in the total current between the cathodes and anodes in the MRPCs. The current can be measured by monitoring the supply line powering the strips. The total current measured by the TOF detector is shown in Fig. 5.20 as a function of the instantaneous luminosity in pp collision at $\sqrt{s} = 13$ TeV and the equivalent ones in p–Pb collisions at $\sqrt{s_{\text{NN}}} = 5.02$ TeV and Pb–Pb collisions at $\sqrt{s_{\text{NN}}} = 5.5$ TeV (planned for Run 3). The total current flowing in the MRPCs is rather small ($\sim 10 \mu\text{A}$ in normal conditions, $\sim 1 \text{ mA}$ at the 50 kHz Pb–Pb collisions at $\sqrt{s_{\text{NN}}} = 5.5$ TeV equivalent). In addition, the detector response is found to be linear as a function of the charged particle flux, meaning that this observable can be used

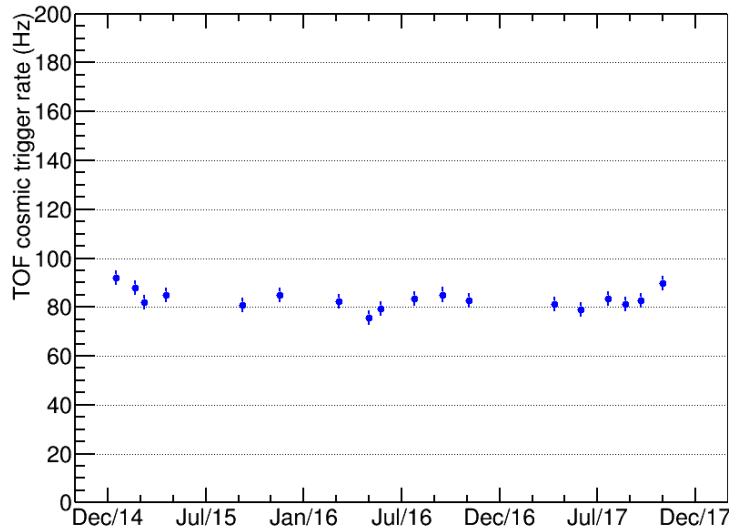


Fig. 5.19 TOF trigger rate of cosmic events.

experimentally to determine the luminosity via linear regression. So far, the findings suggest that the MRPCs show no sign of aging, nor saturation in the current as a function of the charged particle flux.

In order to verify that the MRPCs do not lose detection efficiency as a consequence of aging, the TPC-TOF matching efficiency was analyzed with Run 2 data and compared to the one obtained in Run 1. The two efficiencies are reported together as a function of p_T in Fig. 5.21. The results of the comparison are the following:

- At high momenta ($p_T > 5 \text{ GeV}/c$) the efficiencies are compatible, this indicates that the intrinsic MRPC efficiency is the same for the two samples.
- At low momenta ($p_T < 3 \text{ GeV}$) the discrepancy between the two cases is expected. In Run 1 not all TRD modules were installed (10/18 modules) [125], resulting in less material for particles to cross before reaching the TOF array.
- In addition, the comparison of the matching efficiency measured in Run 2 with the simulation (Fig. 5.2) shows that the effect is completely reproduced.

Further investigations were carried out during Run 2 to check the electronics and readout chain. A test performed during September 2017 with pp collisions at $\sqrt{s} = 13 \text{ TeV}$ verified the capability of the TOF system to record the full amount of particles produced in Pb–Pb collisions Run 3. For this purpose, the usual instantaneous luminosity of $\sim 2 \text{ Hz}/\mu\text{b}$ used in

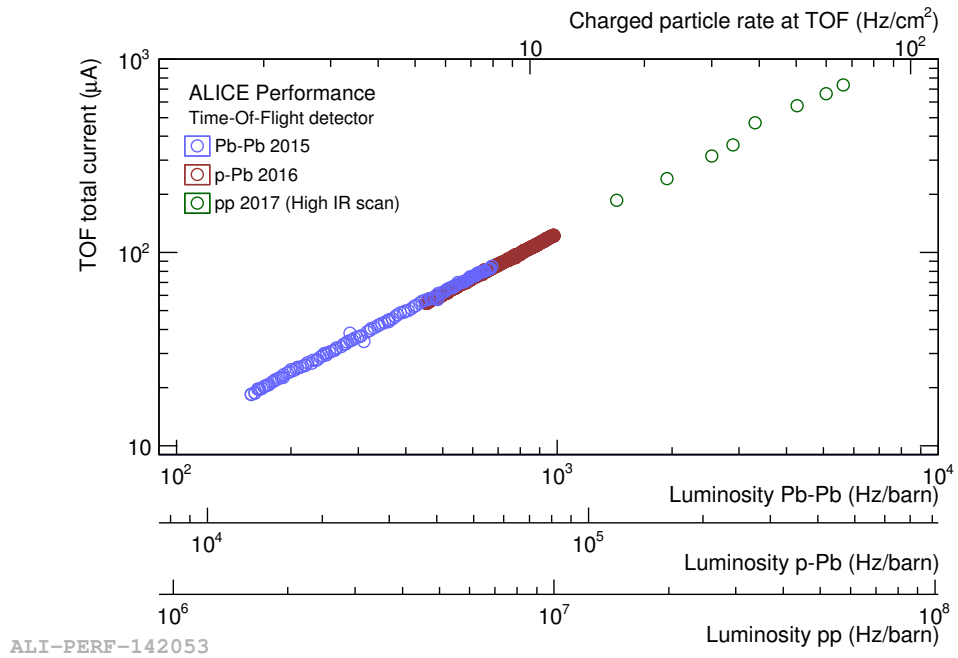


Fig. 5.20 Total MRPC current measured by the TOF detector as a function of the charged particle load and luminosity in pp, p–Pb ad Pb–Pb collisions.

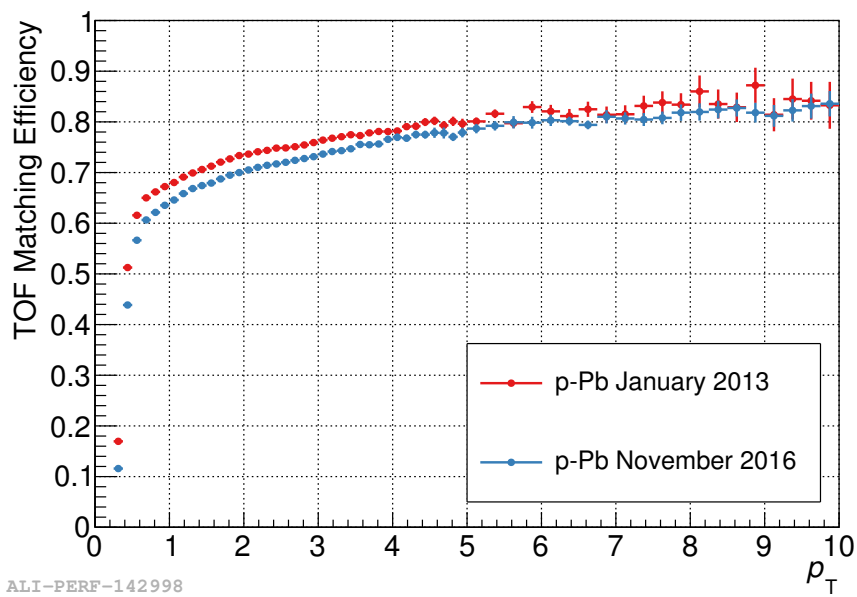


Fig. 5.21 TPC-TOF matching efficiency as a function of p_T , as measured in p–Pb collisions during Run 1 and Run 2. The agreement of the two matching efficiencies is crucial to reproduce the detector response.

pp collisions was scaled up to ~ 25 times. During this test, in order to mimic the continuous readout configuration of Run 3, the readout time window of the HPTDC was extended from $2 \mu\text{s}$ to $\sim 30 \mu\text{s}$ with a time delay of $31 \mu\text{s}$ with respect to the L1 trigger signal received from the CTP. The expected total number of words per crate at the highest charged particle flux of Run 3 was computed by analyzing the raw data recorded detector and counting the mean number of hits per crate in a single event. Every hit is considered including the leading and trailing words. The analysis outcome is reported in Fig. 5.22. The Interaction Rate (IR) in pp collisions can be computed from the instantaneous luminosity \mathcal{L}_{pp} and the interaction cross section $\sigma_{\text{pp}} \sqrt{s}=13 \text{ TeV} \sim 73 \text{ mb}$:

$$\text{IR}_{\text{pp}} = \mathcal{L}_{\text{pp}} \times \sigma_{\text{pp}} \quad (5.14)$$

The charged particle flux is obtained by scaling the IR by the mean number of charged particles per unit of rapidity ($\left\langle \frac{dN_{\text{ch}}}{d\eta} \right\rangle_{\text{pp}}$) produced in a single collisions:

$$\Phi_{\text{pp}} = \text{IR}_{\text{pp}} \times \left\langle \frac{dN_{\text{ch}}}{d\eta} \right\rangle_{\text{pp}} \quad (5.15)$$

The IR needed to have the same charged particle flux in Pb–Pb collisions can be obtained as:

$$\text{IR}_{\text{Pb–Pb}} = \text{IR}_{\text{pp}} \times \left\langle \frac{dN_{\text{ch}}}{d\eta} \right\rangle_{\text{pp}} / \left\langle \frac{dN_{\text{ch}}}{d\eta} \right\rangle_{\text{Pb–Pb}} \quad (5.16)$$

By replacing in Eq. 5.16 the values of the measured charged particle multiplicity in pp collisions at $\sqrt{s} = 13 \text{ TeV}$ and Pb–Pb collisions at $\sqrt{s_{\text{NN}}} = 5.5 \text{ TeV}$ one obtains:

$$\text{IR}_{\text{Pb–Pb} \sqrt{s_{\text{NN}}}=5.5 \text{ TeV}} = \text{IR}_{\text{pp} \sqrt{s}=13 \text{ TeV}} \times 5.31/492.5 \quad (5.17)$$

The mean number of words per crate, extrapolated with a linear fit at the equivalent rate of 50 kHz in Pb–Pb collisions at $\sqrt{s_{\text{NN}}} = 5.5 \text{ TeV}$, is about 160. Considering that each TOF Super Module is read by 38 TRM read, placed in four crates, the mean number of words per TRM is therefore ~ 16 . This value is well within the limits imposed by the buffer size of one TRM. The TRM boards are not planned to be substituted during the LS 2.

5.3.2 Effects of the TPC calibration on the TOF performance

The calibration of the TOF detector is performed after the main reconstruction with the inner detectors (ITS, TPC), as described in Section 5.1. For this reason there is a non trivial correlation between the TOF calibration and that of the tracking detectors. It is important to test the influence of the configuration of tracking detectors such as the TPC on the TOF

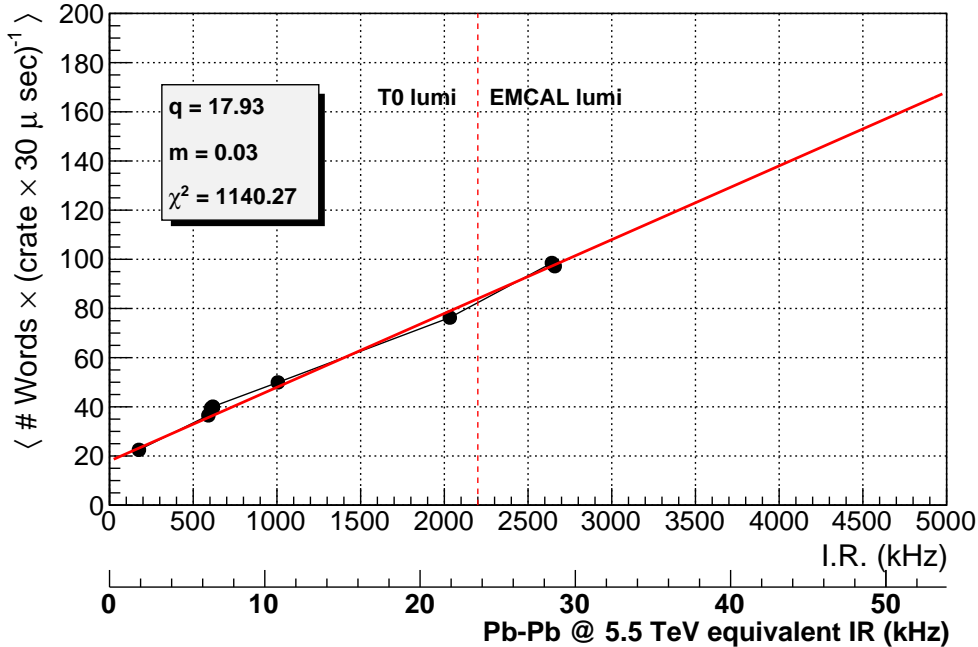


Fig. 5.22 Words per crate as a function of the interaction rate (IR) in pp collisions at $\sqrt{s} = 13$ TeV and compared to the equivalent IR in Pb–Pb collisions at $\sqrt{s_{\text{NN}}} = 5.5$ TeV.

performance to prepare for the trigger-less readout scenario foreseen for Run 3. For this purpose, the TOF performance was studied by means of a Monte Carlo simulation with modified TPC calibration of the drift velocity (v_{drift}) of charges in the gas [126]. The drift velocity was varied by $\pm 10\%$ with respect to the value determined during the TPC online calibration. The simulation was performed in the AliDPG framework. 200 pions per event were injected in the mid-rapidity region ($|\eta| < 1$), with momenta distributed from 0 to 20 GeV/c with uniform probability. Pions were propagated through a detailed description of the full ALICE detector geometry in Run 2 with the GEANT3 transport code. The generated events were reconstructed with the standard procedure. The effect of the TPC calibration are sizable when considering the TPC-TOF matching algorithm. In particular, the TOF matching residuals in the simulation with modified and standard TPC calibration are shown in Fig. 5.23. The strip index corresponds to the pseudorapidity of the track (indices 0 and 90 correspond to $|\eta| \sim 0.9$, index 45 corresponds to $\eta \sim 0$). Tracks matched to the strip located at mid-rapidity are shorter, but at the same time, the charge generated by ionization in the TPC covers a longer distance before reaching the readout pads located at the end caps of the TPC. These tracks are mostly affected by any inaccuracy in the v_{drift} , thus explaining the

behaviour observed in Fig. 5.23 where central strips exhibit larger offsets with respect to zero.

Variations of the v_{drift} in the TPC calibration affect significantly the matching of tracks but not their timing quality. As shown in Fig. 5.24 the mean and the resolution of the TOF signals, obtained considering t_{ev}^{Fill} , are rather constant as a function of the strip index. The mean values do not change significantly in the three cases. This suggests that the present timing response of the TOF calibration is not much affected by the value of the TPC drift velocity used in reconstruction.

5.3.3 The new TOF geometry in the O²

The transition from AliRoot, the current software of the ALICE experiment, to the new ALICE O² framework, is an important component of the ALICE upgrade for Run 3. In parallel to the studies on the TOF performance, the work carried out for this thesis includes the development of the new TOF software in the O² project.

The O² software is based on general libraries and tools such as Root, but also on two dedicated frameworks called ALFA and FairRoot [124]. The ALFA framework is the result of the joined effort between ALICE and FAIR (Facility for Antiproton and Ion Research [127]) experiments to provide the underlying common parts for a multi-process system. The Root software tailored to the requirements of the ALICE and FAIR experiments is developed in FairRoot. The fundamental classes needed to implement in the ALICE O² the detector geometry, the data simulation and reconstruction are inherited from FairRoot. In 2017 the description and parameterization of the TOF geometry was implemented according to the new coding standards of the O². This ingredient is essential to perform simulations to study the detector performance and develop new detector algorithms.

As outcome of the implementation, the geometry can be visualized in the O² framework. For instance, in Fig. 5.25 two Super Modules are shown . The single MRPC strips are visible in the fiberglass case, together with the aluminum honeycomb. The FEE is represented in the figure. The two Super Modules differ in the central module, which is installed only in 15/18 sectors. All 91 strips are oriented so as to face perpendicularly the particles coming from the interaction point. The different materials used for the construction of the TOF detector are implemented in the description so as to compute the total material budget. The geometrical parameterization is used in the propagation of tracks in the Monte Carlo simulations with transport codes such as GEANT3 or GEANT4 [128].

The readout electronics of the whole TOF array is shown in Fig. 5.26. In the figure, the SM external case and the crates located at the edges of each SM are rendered as semitransparent to allow the visualization of the FEAs, while MRPCs are not shown.

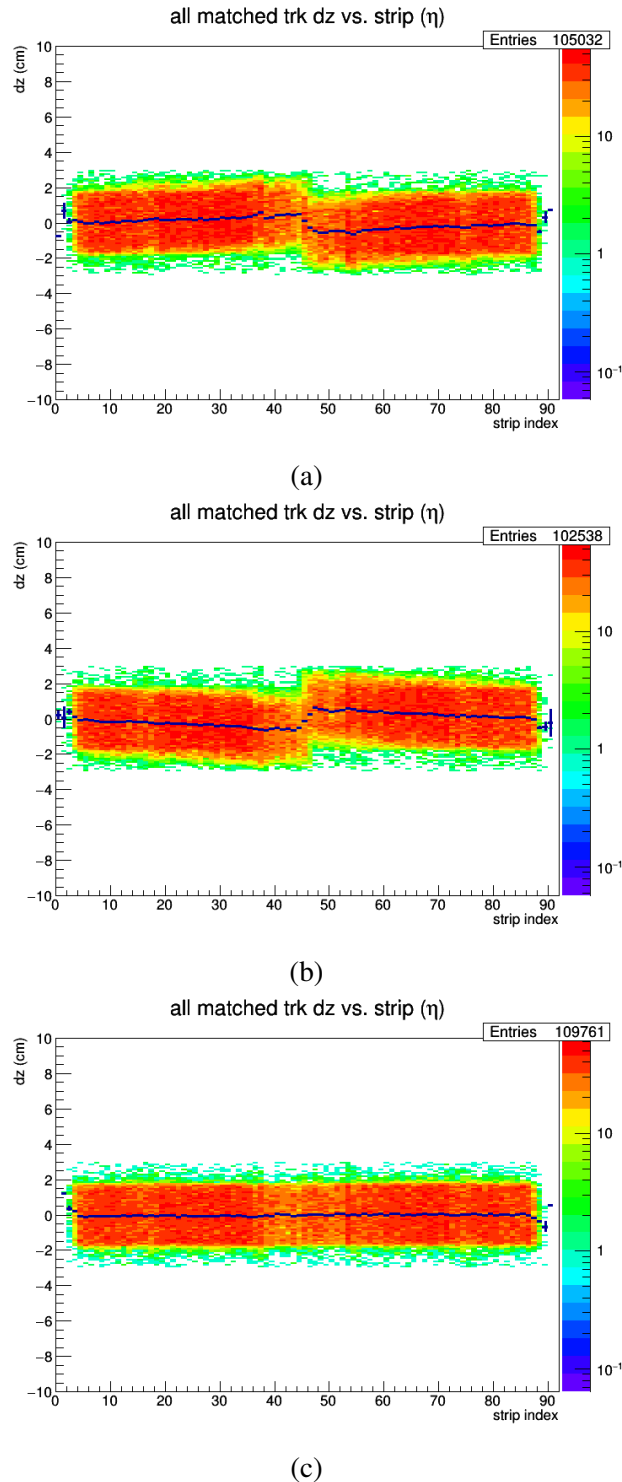


Fig. 5.23 Matching residuals between the TOF matched cluster and the position of the track in the z direction as a function of the strip index for (a) simulation in which the TPC v_{drift} is increased by 10%, (b) simulation in which the TPC v_{drift} is decreased by 10% and (c) TPC v_{drift} determined by the online calibration.

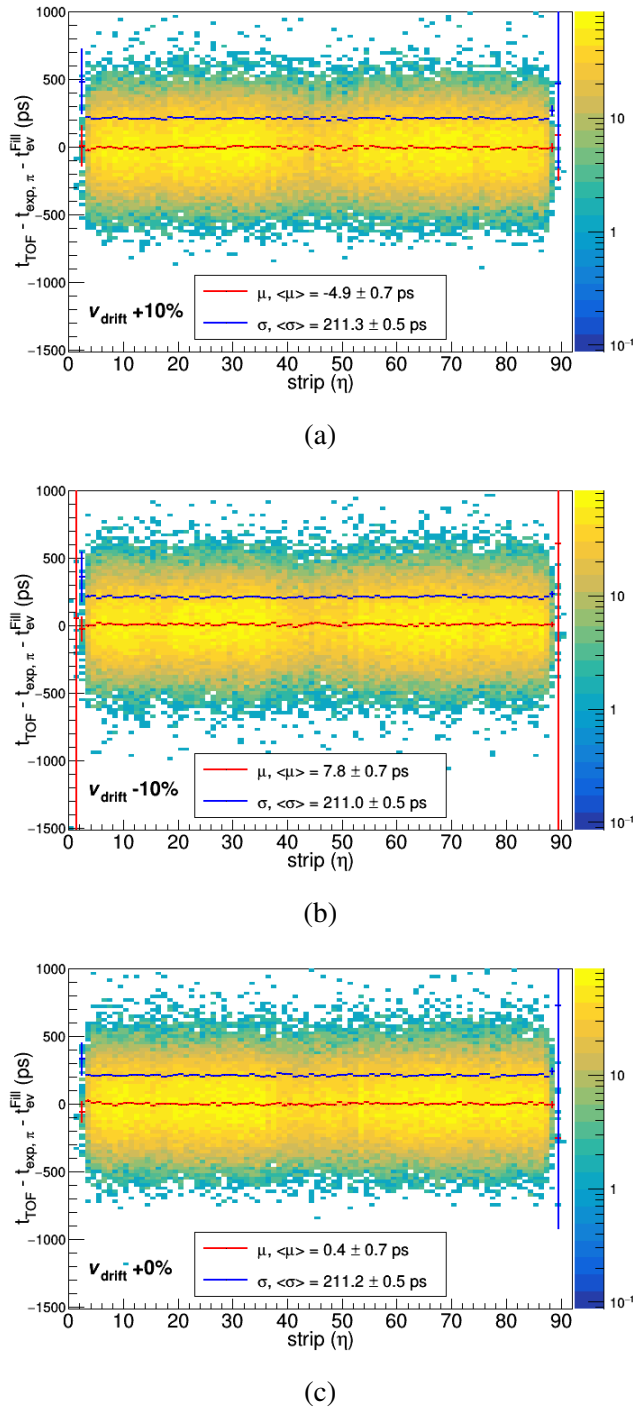


Fig. 5.24 Distribution of the *time-of-flight* measured with $t_{\text{ev}}^{\text{Fill}}$ (event time given by the bunch crossing time) as a function of the strip index for (a) +10% TPC v_{drift} , (b) -10% TPC v_{drift} and (c) TPC v_{drift} determined by the online calibration.

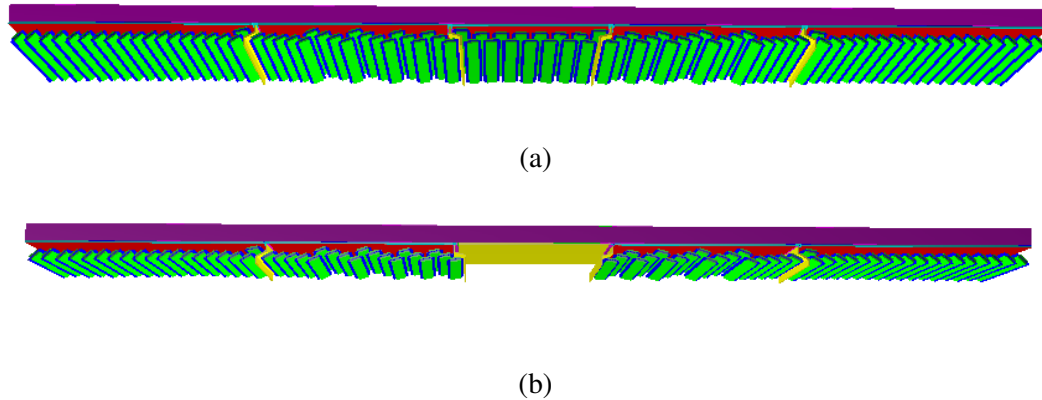


Fig. 5.25 Full SM (a) and SM without the central module (b) of the TOF detector modelization implemented in the new O² framework.

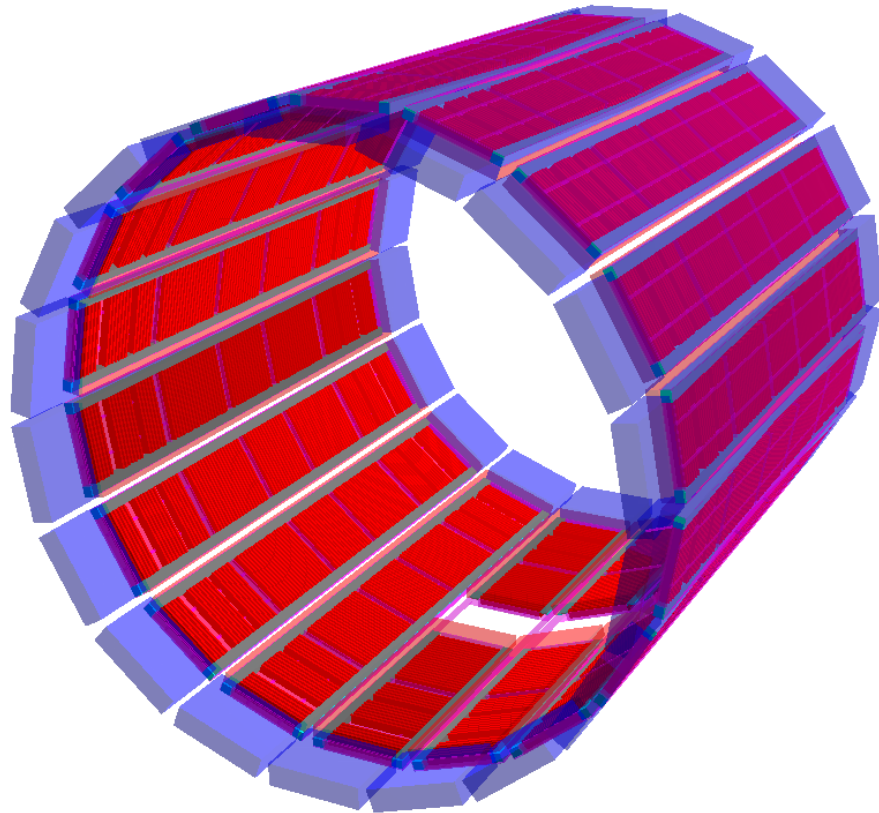


Fig. 5.26 Full representation of the TOF detector in the O² framework. In blue are represented the crates located at both ends of each SM.

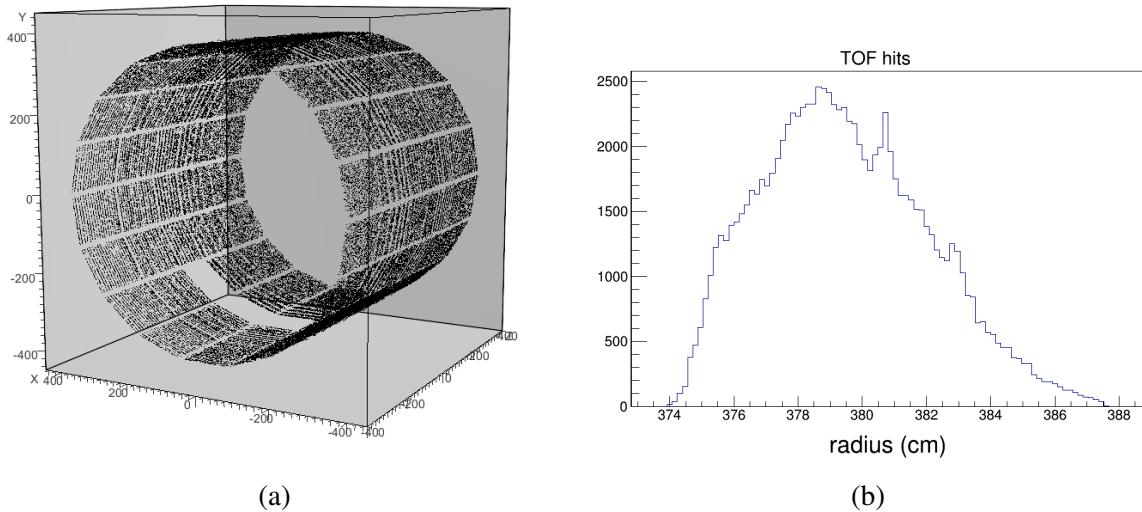


Fig. 5.27 Spatial distribution of the particle hits in a MC simulation using the new TOF geometry in the ALICE O² framework. Three dimensional representation (a) and radial distribution (b).

The new detector geometry was derived from the one currently implemented in AliRoot and allowed to perform a first simulation of the particle hits in the detector active area. An example of the hit distribution in the TOF array of particles generated in the ALICE O² framework is shown in Fig. 5.27. The hits are correctly located on the sensitive surface of the detector, demonstrating that the detector geometry has been implemented correctly. The distribution of the time of arrival at the TOF array is reported in Fig. 5.28.

Analyzing the TOF mismatch with machine learning A preliminary study involving neural networks was carried out for the development of a new track matching algorithm for in the O² project [129]. The study was performed on simulated Pb–Pb collisions at $\sqrt{s_{\text{NN}}} = 5.02$ TeV. The correct or incorrect track matching to a TOF cluster can be verified in the simulation. This information is used to train a deep neural networks implemented with the TMuLayPerceptron (TMLP) [130, 131] C++ library of Root. A representation of the neural network is used for this analysis is given in Fig. 5.29. The variables used to train the neural network include information on tracking such as p_T , η , φ et cetera. In addition, the timing information from all the TOF clusters, the expected times and the residuals are used. To perform the categorization and response of the last neuron is considered. This value is computed from in the network using as input only variables that are available in data.

For this analysis the activation function of the neurons is of the Sigmoid type. For the training procedure an equal amount of correctly matched and mismatched tracks was used.

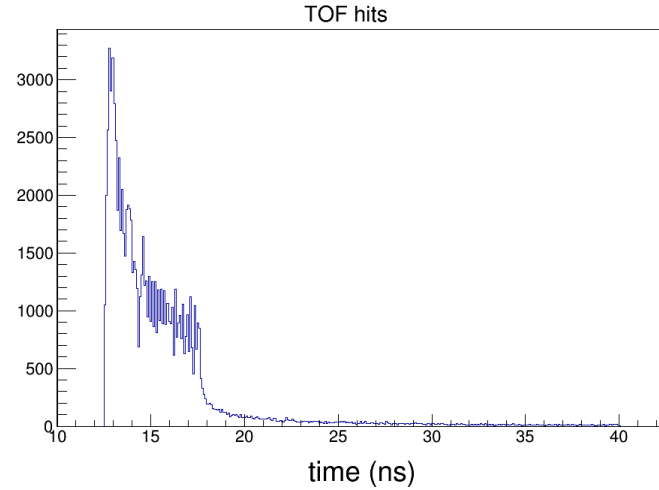


Fig. 5.28 Spatial distribution of the particle hits in a MC simulation using the new TOF geometry in the ALICE O² framework.

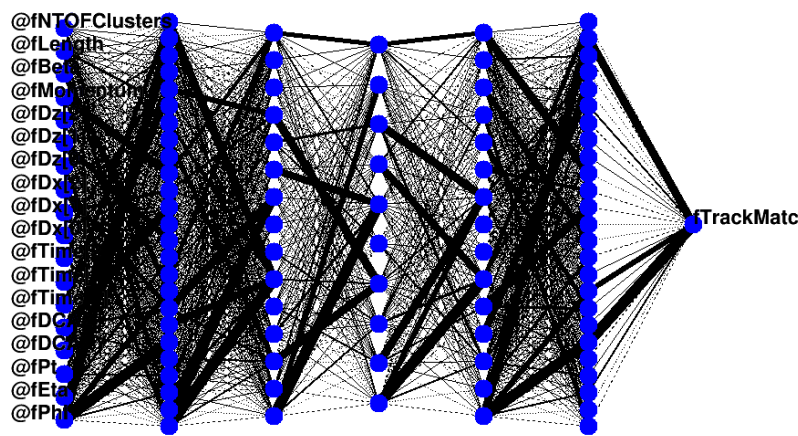


Fig. 5.29 Representation of the neural network used for the analysis of mismatched tracks. On the left side are located the input neurons, on the left side there is the response neuron used for the classification.

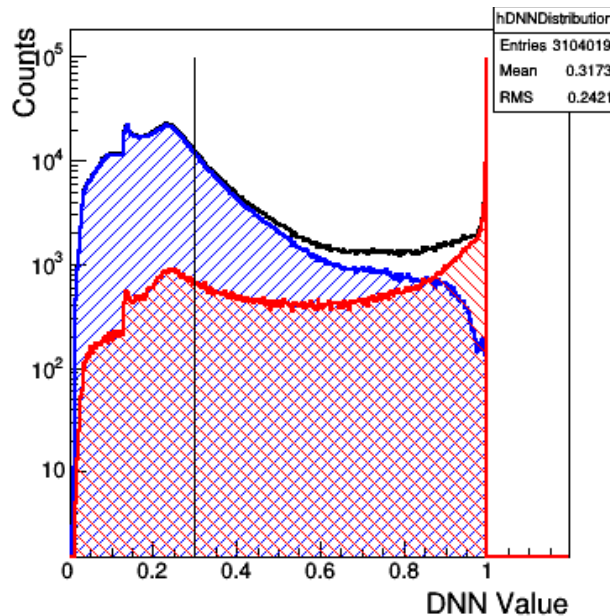


Fig. 5.30 Value of the network response for correctly matched tracks (in blue) and mismatched tracks (in red).

The network response is given by the value of the last neuron, which is between 0 and 1. The response is reported in Fig. 5.30 for correctly matched tracks (in blue) and mismatched ones (in red). The value of the network, evaluated for each track, can be used to differentiate between correctly matched tracks and the mismatched ones based on the input. For the results reported in this section, the cut used to tag tracks as correct match or mismatch is set to 0.3.

The efficiency⁴ and the residual contamination from mismatched tracks are reported for different limits of the network response value in Fig. 5.31. The contamination and efficiency with no selection applied on the neural network response are also shown in the figure. In this case the fraction of mismatched tracks in the sample represents the normal conditions obtained in simulated Minimum Bias Pb–Pb collisions, indicating that at 1 GeV/*c*, mismatched tracks are ∼ 4 % of the reconstructed ones.

An example of the results that can be obtained by applying the selection based on the neural network is given in Fig. 5.32. The figures show the β distributions measured with the TOF detector as a function of the track momentum. The distributions of several track samples are shown:

- Unselected sample of tracks:

⁴In this case, the efficiency is computed as the ratio between the number of tracks tagged as correct matched and the number of reconstructed tracks

distribution computed without any selection on the neural network, nor on the Monte Carlo information.

- Mismatched:

distribution computed with tracks that are wrongly matched to a TOF hit, thus yielding a *time-of-flight* uncorrelated with the particle species.

- Tagged mismatched:

distribution computed with tracks that are tagged as wrongly matched by the neural network.

- Matched:

distribution computed with tracks that are correctly matched to a TOF hit.

- Tagged matched:

distribution computed with tracks that are tagged as correctly matched by the neural network.

The band that extends at $\beta > 1$ is due to mismatched tracks. It is possible to see that in case the selection based on the network response is applied to reject wrongly matched tracks, the bands corresponding to the particle species are enhanced, while tracks with $\beta > 1$ are discarded.

In parallel to the usage of the neural network with the TMLP library, the same study was repeated with the Keras library [132] with TensorFlow [133] package. Similar results are obtained with this approach.

The results obtained from these preliminary studies indicate that the TPC-TOF mismatch can be tagged with the use of machine learning techniques. These studies will continue for the preparation of Run 3 to possibly implement a complete TPC-TOF matching algorithm that could be used in the tracking.

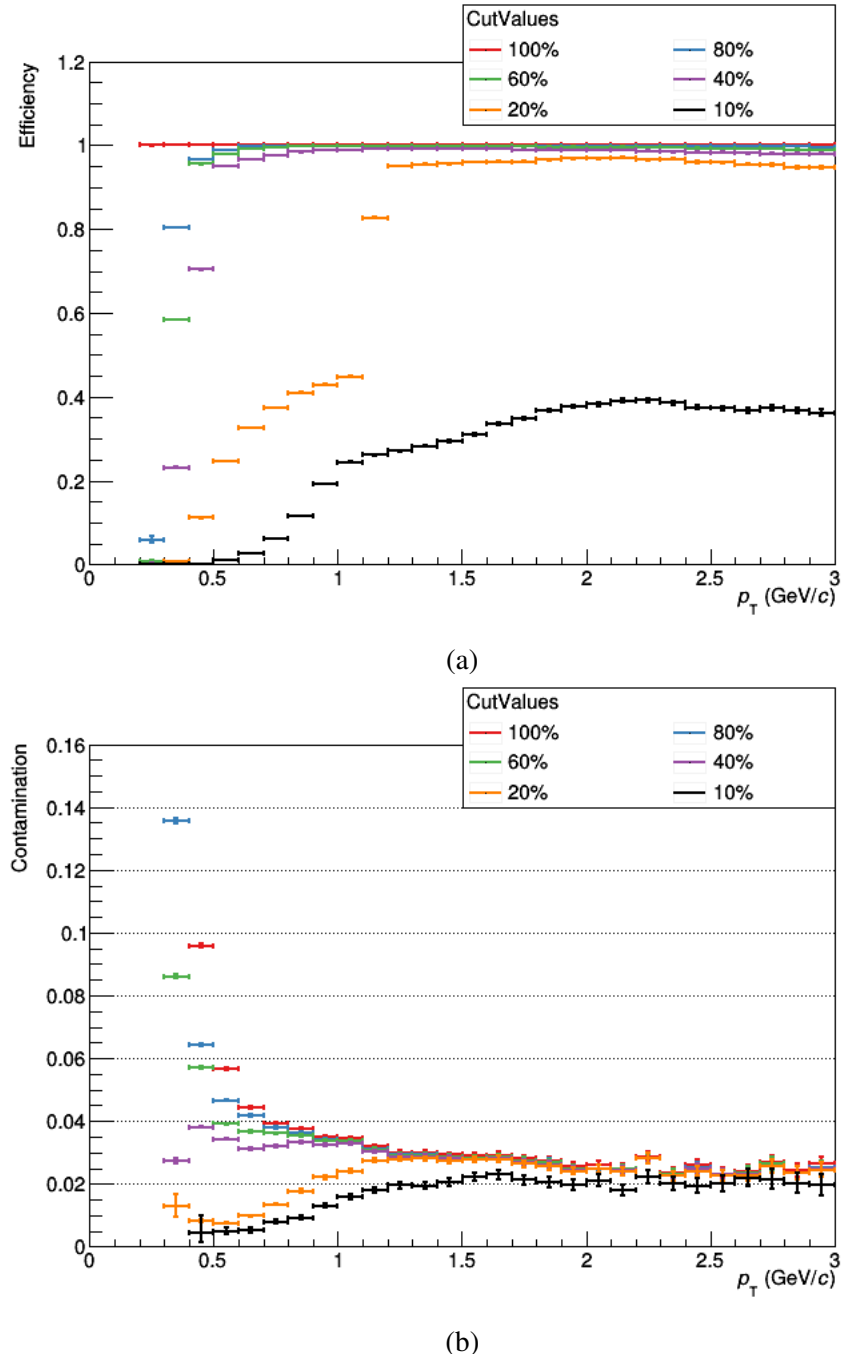


Fig. 5.31 (a) Efficiency and (b) residual contamination in the track sample tagged as correct match with different cuts on the value of the network response.

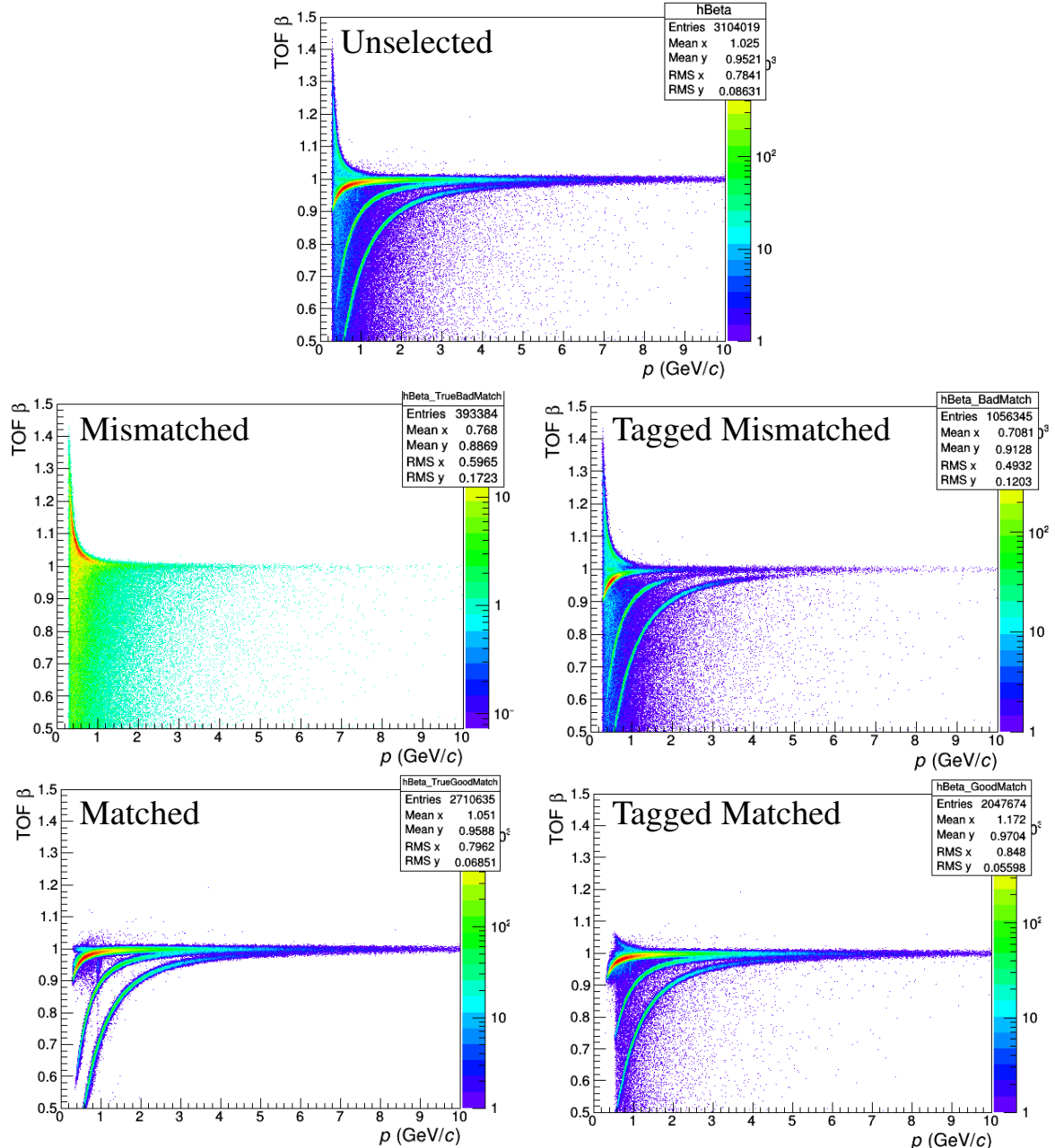


Fig. 5.32 β distribution measured with the TOF detector as a function of the track momentum for unselected, correctly matched and mismatched tracks and for the tracks tagged as correct match and mismatch with the neural network, see text for details.

Chapter 6

π^\pm, K^\pm, p and \bar{p} production in Pb–Pb and pp collisions

The details of the measurement of the π^\pm, K^\pm, p and \bar{p} production using the ALICE TOF detector are described in this chapter. The results of the analysis are shown and discussed in relation to models and measurement at lower energies and different collision systems in Chapter 7.

The measurement of the identified particle production is fundamental for the characterization of the QGP. These data provide strong constrains to theoretical models. In addition, the measurement of light flavor hadrons such as π, K, p are used as a reference for the production of light nuclei, hyper-nuclei and to evaluate the strangeness enhancement.

Since Run 1 the ALICE Collaboration has been measuring the production of several light flavor particle species, including π^\pm, K^\pm, p and \bar{p} in all the collision systems provided by the LHC (pp, p–Pb, Xe–Xe and Pb–Pb). The identified particle production proved to be a strong tool to constrain theoretical models. In addition, several measurements use the light flavor particles as a reference to quantify relative enhancement or suppression of the observables.

In 2015, Pb–Pb collisions at the highest energy ever achieved in laboratory ($\sqrt{s_{\text{NN}}} = 5.02 \text{ TeV}$) were recorded. For the first time, the quantitative comparison of particle production in Pb–Pb collisions at different energies at the LHC was made possible. The ALICE experiment, thanks to its excellent tracking performance coupled with extensive Particle IDentification (PID) capabilities, is particularly well suited for the study of identified hadron production over a wide range of transverse momenta. This is achieved by combining multiple PID techniques that allow, at mid-rapidity, to perform hadron identification starting from $100 \text{ MeV}/c$, up to $\sim 20 \text{ GeV}/c$. The measurement of the π, K, p production is split into several sub-analyses, each one optimized for a particular momentum range. The final result is obtained by combining the result of every sub-analysis. The measurement at

$\sqrt{s_{\text{NN}}} = 5.02$ TeV is performed by combining the analyses carried out with the ITS, TPC, TOF and HMPID detectors. These analyses use a single detector to build the discriminating quantity to perform the PID. In addition for the first time in Pb–Pb collisions, kaons are identified by their weak decay topology (“Kinks” analysis). The analysis using the ITS information profits from the dedicated reconstruction described in Section 3.1.1 to maximize the particle detection efficiency at low momentum. All remaining analyses use global tracks, reconstructed with both TPC and ITS. The TPC analysis is divided into two parts: the one at low momentum, where identification is possible because particle are far from the minimum ionizing particle regime, and the one at high momentum, taking advantage of the relativistic rise of the dE/dx in the TPC gas.

In this chapter, the measurement of pions, kaons and protons at intermediate momenta (from ~ 600 MeV/c to ~ 5 GeV/c) is presented. The extraction of the total particle yield is achieved by performing PID exclusively with the TOF detector. The parameterizations of the TOF signal and background are described in Section 6.2.1.

The PID technique used in this analysis is based on previous works [40, 134] for both pp and Pb–Pb collision systems. The analysis strategy, as it will be explained in Section 6.2.3, is based on the statistical deconvolution of the distributions obtained by comparing the measured *time-of-flight* to the expected time obtained from the reconstructed track length, computed for each mass hypothesis.

The recorded events are stored in the ALICE data catalogue in Root files. The first data processing is performed in parallel with a custom C++ analysis task¹, taking advantage of the capabilities of the ALICE Grid [103]. The output of the Grid analysis is merged and processed locally by a multi-core machine. This post processing part is handled by a custom TSelector, tailored for the purpose of the analysis. This technique allows to split the whole task into several sub-jobs (one per physical core), using the Proof utility of Root [136]. Further data processing is achieved with custom C++ or Python functions. All the utilities developed for the analysis have been made publicly available to the ALICE Collaboration as integral part of the analysis software libraries [135, 112].

6.1 Data sample

The data sample analyzed, the trigger selection, the event quality cuts and the centrality evaluation are described in this section.

¹PWGLF/SPECTRA/PiKaPr/TOF/PbPb502/task/AliAnalysisTaskTOFSpectra.h in AliPhysics [135].

6.1.1 Pb–Pb and pp data samples

The data used for this analysis was recorded in 2015 at $\sqrt{s_{\text{NN}}} = 5.02$ TeV. The Pb–Pb sample, was recorded with a low interaction rate so as to limit event pile-up and the degradation of the quality of reconstructed tracks due to effect of charge distortions in the TPC gas. The large charged particle fluxes experienced at higher interaction rates cause a charge buildup in the detector that induces local changes in the configuration of electric field. This effect results in a change in the drift velocities that needs to be corrected offline. During this particular phase the collision rate varied from ~ 25 Hz up to ~ 500 Hz. Only a limited amount of data were recorded with the low IR configuration, the rest of the statistics was collected at higher rates, reaching up to ~ 8 kHz. The reference sample of pp collisions was taken at the same energy per nucleon pair of the Pb–Pb sample. Both pp and Pb–Pb samples were recorded with a B-field of 0.5 T inside the solenoid magnet.

6.1.2 Monte Carlo samples

A set of Monte Carlo simulations are used to study the detector inefficiencies and estimate corrections for the measured spectra. Depending on the collision system, these simulations use different event generators. The simulation of Pb–Pb collisions is carried out with the HIJING event generator [137]. For the pp analysis, the events are generated with the Pythia8 event generator with the Monash 2013 tune [73]. In both cases, the particles produced by the generator are transported through a detailed description of the ALICE detector with the GEANT3 transport code [128]. The detector configuration during data taking (magnetic field, number of active channels, detector calibration et cetera) is considered in the simulation in order to reproduce the detector response.

6.1.3 Event selections

The recorded events used for the analysis are selected based on specific requirements to ensure a uniform acceptance for tracks and a precise determination of the primary vertex. Collisions originating from background events (e.g. beam-gas events) are discarded by using the information of the detectors located at forward rapidity.

Trigger and background rejection

Both pp and Pb–Pb analyses are based on data recorded with a Minimum Bias trigger, requiring a trigger signal in both V0A and V0C arrays. The selection is refined during the offline data analysis and background events are rejected. A selection based on V0 timing

information, shown in Fig. 6.1a, is applied. In the figure, background events from Beam 1 and background events from Beam 2 are located at (-14.3 ns, -8.3 ns) and (14.3 ns, 8.3 ns) respectively. Spurious events originating from beam-gas events are also rejected by correlating the number of hits and tracklets² in the SPD, as shown in Fig. 6.1b. Events of interest should have a good correlation between the number of hits and the number of reconstructed tracklets.

The selection of Pb–Pb collision candidates can also profit from the signals in the two ZDC arrays to suppress the background. In Fig. 6.2 the timing information of the ZNA and ZNC is shown as measured in Pb–Pb collisions at $\sqrt{s_{\text{NN}}} = 2.76$ TeV [11]. Equal delays are expected in the two ZDCs for genuine collisions.

The pile-up rejection is implemented by discarding events with multiple vertices reconstructed using the SPD. Events with secondary vertices, reconstructed inside the collision diamond³, that are sufficiently distant from the primary vertex (by default 8 mm) and are pointed to by enough tracklets (by default at least three contributors) are tagged as pile-up and discarded. In the filling scheme of the LHC, particle bunches are separated by 25 ns.

In addition, the Past Future Protection (PFP) [138] is used to discard the out-of-bunch beam-beam pile-up and the out-of-bunch beam-gas pile-up⁴. The PFP allows to veto the trigger if another collision happens in a given time window before and/or after the trigger.

Vertex selection

The “primary” vertex of the collision is reconstructed by using independently the information provided by ITS and TPC. By default the position of the primary vertex is obtained from the reconstructed tracks (V_{Trk}). If not available, the position of the vertex can be estimated by using the tracklets reconstructed by the SPD (V_{SPD}). Events whose vertex is reconstructed outside a ± 10 cm range along the z axis from the Interaction Point (IP) are discarded, to guarantee a uniform acceptance for the reconstructed tracks.

The vertex has to be reconstructed with a sufficient number of contributing tracks (or tracklets) to achieve a good precision on its determination. Events whose vertex is determined with an insufficient number of tracks (tracklets) are discarded. The resolution of the vertex determined with the SPD along the z axis is required to be better than 0.25 cm. If both V_{Trk} and V_{SPD} are available, events are selected for which their distance along z satisfies the condition: $|Z_{V_{\text{Trk}}} - Z_{V_{\text{SPD}}}| < 0.5$ cm.

²Track segments obtained by connecting two clusters in the two layers of the SPD.

³The region of the bunch crossing.

⁴ Out-of-bunch or other bunch pile-up is defined as pile-up occurring from real collisions or beam gas events in bunches different from the one which triggered the acquisition.

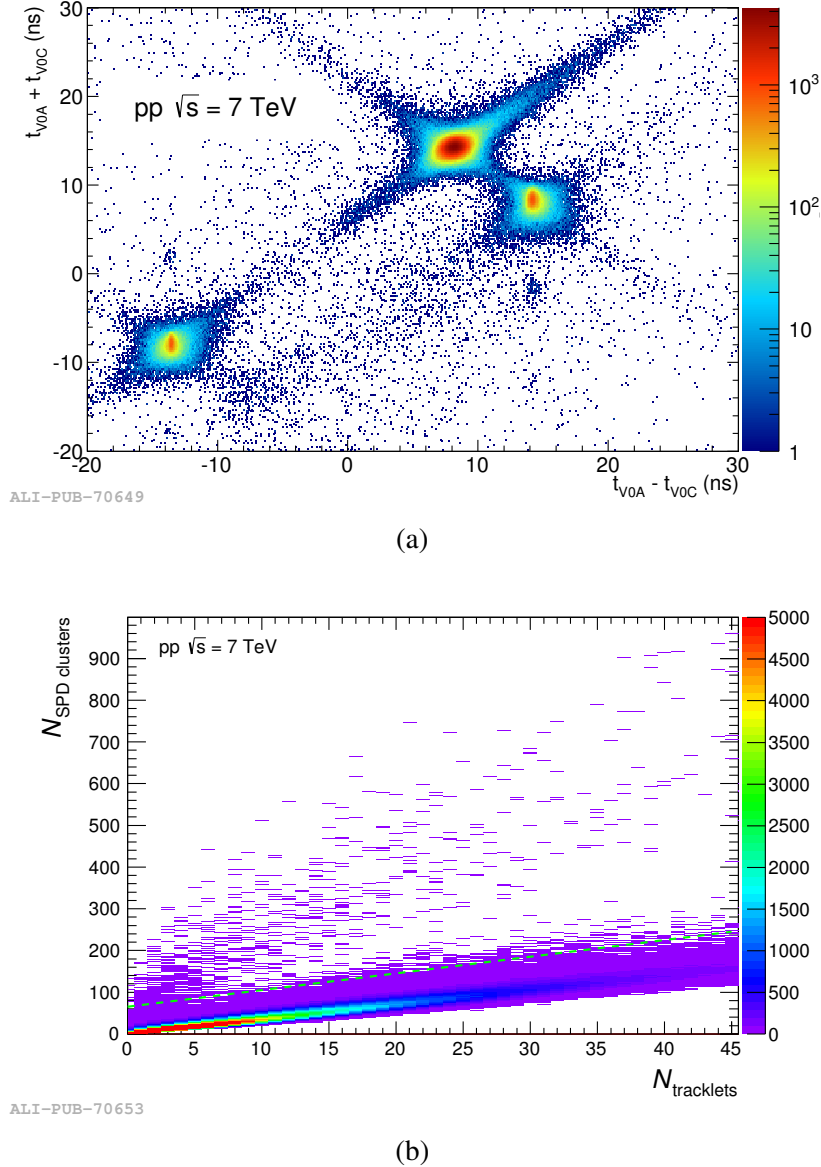


Fig. 6.1 (a) Correlation between the sum and difference of signal times in V0A and V0C as measured in pp collisions at $\sqrt{s} = 7$ TeV [11]. Background events from Beam 1 and background events from Beam 2 can be seen at (-14.3 ns, -8.3 ns) and (14.3 ns, 8.3 ns) respectively. (b) Correlation between SPD clusters and reconstructed SPD tracklets [11]. Two bands are visible, they correspond to the genuine collisions and machine induced background. The dashed line represents the cut used in the offline selection: events lying in the region above the line are tagged as background and rejected.

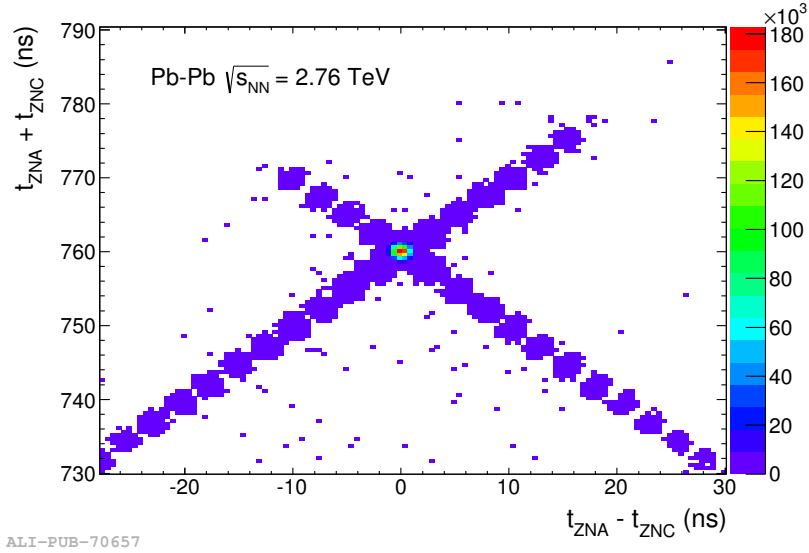


Fig. 6.2 Correlation between the sum and the difference of times recorded by the neutron ZDCs on either side (ZNA and ZNC) in Pb–Pb collisions at $\sqrt{s_{NN}} = 2.76$ TeV [11]. Genuine collisions between ions in the nominal bunch of both beams correspond to the the large cluster centered at (0 ns, 760 ns). The small clusters distributed along the diagonals correspond to collisions in which one of the ions is displaced by one or more bunches.

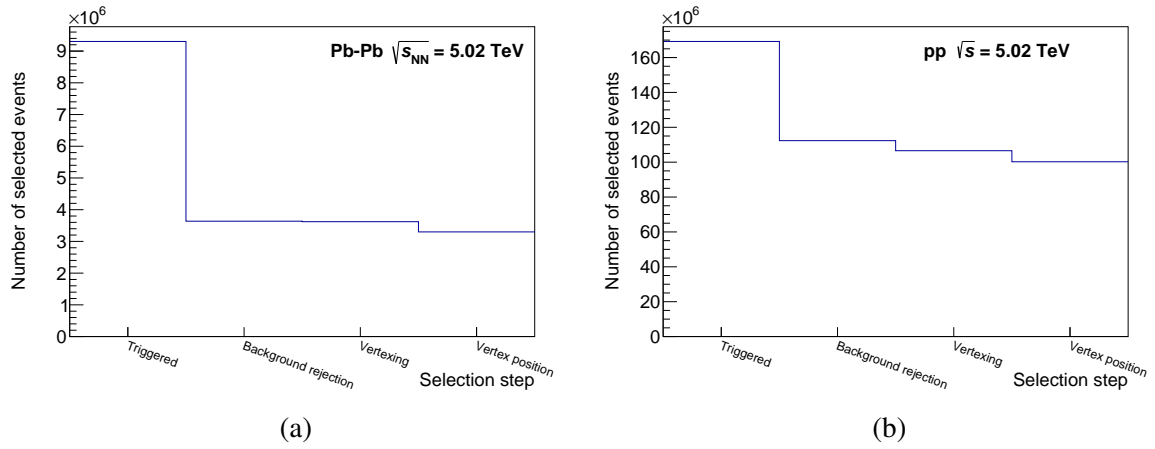


Fig. 6.3 Number of events analyzed in (a) Pb–Pb and (b) pp collisions. The number of events surviving each selection criteria is shown.

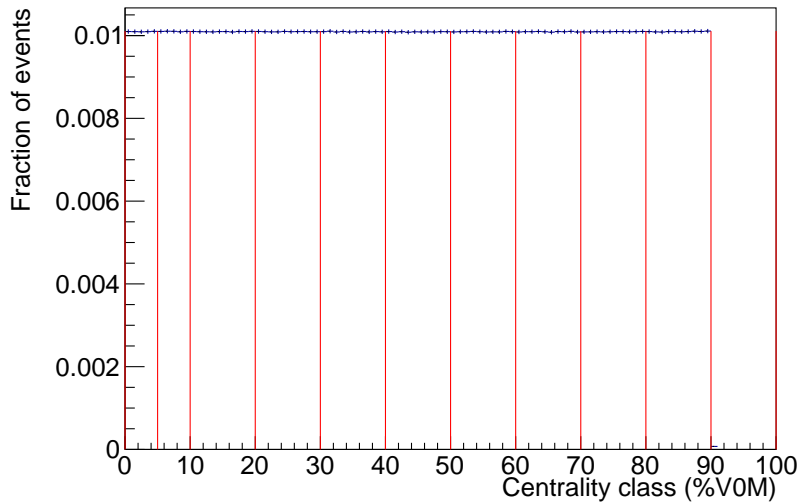


Fig. 6.4 Fraction of events per centrality classes as measured in Pb–Pb collisions at $\sqrt{s_{\text{NN}}} = 5.02$ TeV. The red lines indicate each centrality class.

Centrality selection

Pb–Pb events are sampled into classes based on centrality, quantified in fractions of the total Pb–Pb cross section (~ 7.7 b). The average signal of the two V0 counters (V0M) is used to define the event centrality. The centrality is calibrated on the data selected with the criteria described above so that events are uniformly distributed in each centrality class. The V0M amplitude is shown in Fig. 3.17 as measured in Pb–Pb collisions at $\sqrt{s_{\text{NN}}} = 5.02$ TeV. Based on this distribution, the geometrical properties of the collision are obtained, as described in Section 3.3.2.

The analysis of Pb–Pb events is divided into eleven centrality classes:

0-5%, 5-10%, 10-20%, 20-30%, 30-40%, 40-50%, 50-60%, 60-70%, 70-80%, 80-90%

The centrality-integrated sample (0-90%) is referred to as “MB”.

The fraction of events per centrality class is shown in Fig. 6.4. As expected, events are uniformly distributed across centrality.

6.1.4 Track selection

The tracks used for the analysis are chosen based on criteria optimized for the selection of tracks with high quality reconstruction and coming from the primary vertex of the collision (“primary tracks”), as summarized in Table 6.1.

Track selection	Value
Minimum TPC Crossed Rows	70
Minimum TPC clusters	$80\% \times \text{TPC crossed rows}$
Maximum track Global χ^2 per NDF	4
Maximum Global χ^2 per NDF for tracks constrained to the primary vertex	36
Maximum track DCA_z	2 cm
Maximum track DCA_{xy}	7σ , see Eq. 6.2
Minimum track length	350 cm
Pseudorapidity	$ \eta < 0.8$
Rapidity	$ y < 0.5$
Track is refitted in TPC	yes
Track is refitted in ITS	yes
Minimum number of clusters in SPD	1
Track matched to TOF	yes
Minimum track p_T	50 MeV/ c
Geometrical cut	yes

Table 6.1 Summary of the cuts used to select the track sample. These include selection on the reconstruction quality, acceptance and TPC-TOF matching. See text for details.

Selected tracks are required to have crossed at least 70 out of 159 readout rows in the TPC chamber depicted in Fig. 6.5. Tracks with less TPC clusters than 80% of the crossed rows are rejected. Each track is required to successfully fit the detector hits in both ITS and TPC. All tracks are required to have a SPD cluster associated. Tracks with χ^2/NDF larger than 4 are discarded⁵. Tracks are also discarded based on reconstructed geometrical length calculated in the TPC readout plane [5]. This is carried out by excluding the information from pads located at the sector boundaries (~ 3 cm from the sector edges). The track length in the TPC is required to be larger than:

$$l_{\text{Cut}} = \alpha - \beta p_T^{-\gamma} \quad (6.1)$$

A selection on l_{Cut} (“geometrical cut”) is implemented with $\alpha = 130$ cm, $\beta = 2.0$ cm · c / GeV, $\gamma = 1.5$ and p_T in units of GeV/ c is used to remove tracks that cross inefficient regions of the TPC, thus granting better agreement of the simulated response with the one in data.

⁵ In this case NDF is considered to be the number of clusters available for the reconstruction. Since clusters can be identified by two coordinates the actual number of degrees of freedom (NDF*) correspond to twice the number of clusters associated to a track. With this alternative notation the quality cut corresponds to requiring χ^2/NDF^* larger than 2.

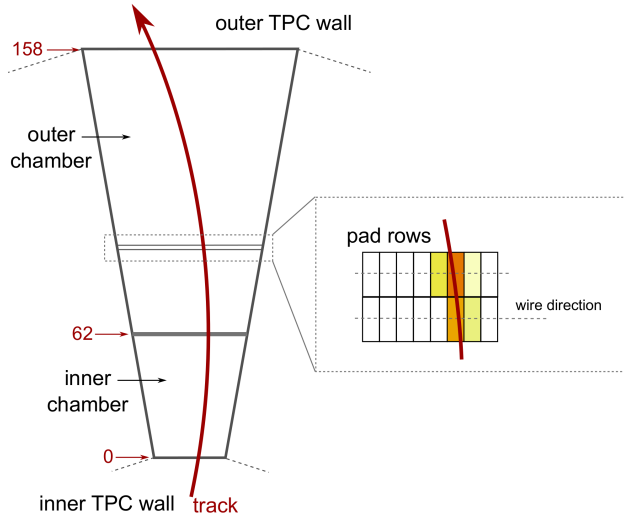


Fig. 6.5 TPC readout segmentation into sectors and pad rows [140].

Tracks are required to be inside the detector acceptance ($|\eta| < 0.8$). In addition, for the purpose of this analysis, analyzed tracks are selected within the rapidity interval $|y| < 0.5$ depending on the particle mass hypothesis.

The purpose of the analysis is to measure primary particles and not the ones originating from particle weak decays or from particle knockout in the detector material. A contamination from secondary particles would constitute a bias to the information on the particle production that can be extracted from the measurement of primary particles. Primary particles [139] are generated directly in the primary collisions or in strong decays of heavy particles (hadronic resonances, heavy-flavor mesons et cetera) that occur within few μm from the primary vertex.

Primary particle tracks are selected based on the Distance of Closest Approach (DCA) to the primary vertex. A representation of the track DCA is given in Fig. 3.13. The DCA along the z direction in the xy plane, are considered. As reported in Table 6.1, a 2 cm limit is used to select primary particles along the z axis. The DCA_{xy} selection is parametrized as a function of p_T as the best precision is achieved in the xy plane. The p_T dependence of the $\text{DCA}_{xy \ max}$ is parametrized to represent a $7\ \sigma$ equivalent selection:

$$\text{DCA}_{xy \ max} = 0.0105 + 0.0350/p_T^{1.1} \quad (6.2)$$

In addition to quality requirements, tracks are required to be matched to a TOF cluster to perform PID.

These track selections are varied in order to estimate the effect of a given criterion on the analysis result and evaluate the systematic uncertainties. This will be described in Section 6.4.

6.2 Particle identification with TOF

The analysis strategy relies on tracks reconstructed in the TPC which are extrapolated to the TOF surface and matched to a hit in the TOF active area. The assignment of a TOF cluster to the propagated track allows for the precise measurement of the particle arrival time t_{TOF} . This information, together with the measurement of the event time t_{ev} , is used to provide PID in the intermediate transverse momentum region, as extensively discussed in Section 5.2. The particle velocity can be measured from the *time-of-flight* and the track length information given by the TPC, as in Eq. 4.2. The measured particle velocity is reported as a function of the track momentum measured in the tracking system in Fig. 5.13a for pp collisions and in Fig. 3.9c for Pb–Pb collisions at $\sqrt{s_{\text{NN}}} = 5.02$ TeV.

For the analysis reported in this work, the identification of different particle species is performed with a statistical approach from the *time-of-flight* distributions. The *time-of-flight* is defined as the difference between the time measured by the TOF detector t_{TOF} and the event time t_{ev} :

$$tof = t_{\text{TOF}} - t_{ev} \quad (6.3)$$

For a given track, the expected *time-of-flight* (t_{exp}) is computed for every particle species by taking into account the track length and the energy loss in the material, as reported in Eq. 5.2. The resolution on the *time-of-flight* can be obtained from Eq. 6.3 as:

$$\sigma_{tof}^2 = \sigma_{\text{TOF}}^2 + \sigma_{t_{ev}}^2 \quad (6.4)$$

Particle identification thus takes advantage of the separation power between different particle species defined as:

$$n\sigma_i = \frac{tof - t_{exp,i}}{\sigma_i} \quad (6.5)$$

In Eq. 6.5, the difference between the expected time for the species i ($t_{exp,i}$) and the measured *time-of-flight* is divided by the expected resolution, σ_i , parametrized as a function of the track momentum for different particle species. $n\sigma_i$ indicates the distance expressed in terms of number of sigmas of the measured value from the expectation under a specific mass hypothesis.

$$\sigma_i^2 = \sigma_{\text{TOF}}^2 + \sigma_{t_{ev}}^2 + \sigma_{t_{exp,i}}^2 \quad (6.6)$$

The t_{ev} can be determined with different methods, each one having different resolutions (see Section 5.1.3). The measurement of the t_{ev} with the TOF is fully efficient in Pb–Pb

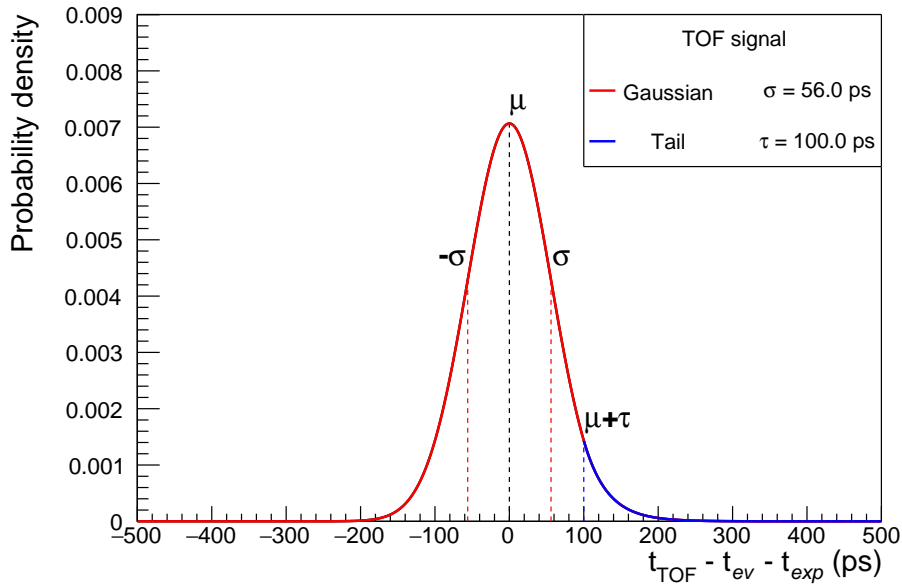


Fig. 6.6 Representation of the TOF signal parameterization as reported in Eq. 5.13. Vertical bands corresponding to value of $\pm\sigma$, μ and $\mu + \tau$ are shown.

collisions. Only in peripheral collisions (80-90%) the multiplicity of tracks reaching TOF is not sufficiently large to ensure the determination of the event time for every event. This is also the case in pp collisions, where the measurement of the start time relies mostly on the T0 detector or, in case this is not available, on the bunch crossing time ($t_{\text{ev}}^{\text{Fill}}$) which has a coarse resolution.

6.2.1 TOF signal description

In order to perform particle identification with the TOF detector one needs to parametrize the detector response. The TOF signal is described by the composite function reported in Eq. 5.13, namely by a Gaussian distribution (with mean μ and width σ) convoluted with an exponential tail (with parameter τ) on the right side of the peak. The convolution is performed so as to ensure continuity and differentiability of the signal. The TOF signal, is depicted in Fig. 6.6 with its two components.

The effect of the parameter variation of the TOF signal is shown in Fig. 6.7. While increasing the σ parameter widens the signal distribution, lowering the τ parameter extends the distribution tail to larger times.

This parameterization of the TOF signal with parameters μ , σ and τ is used to build the templates needed for the statistical deconvolution of the detector response. To this end, the

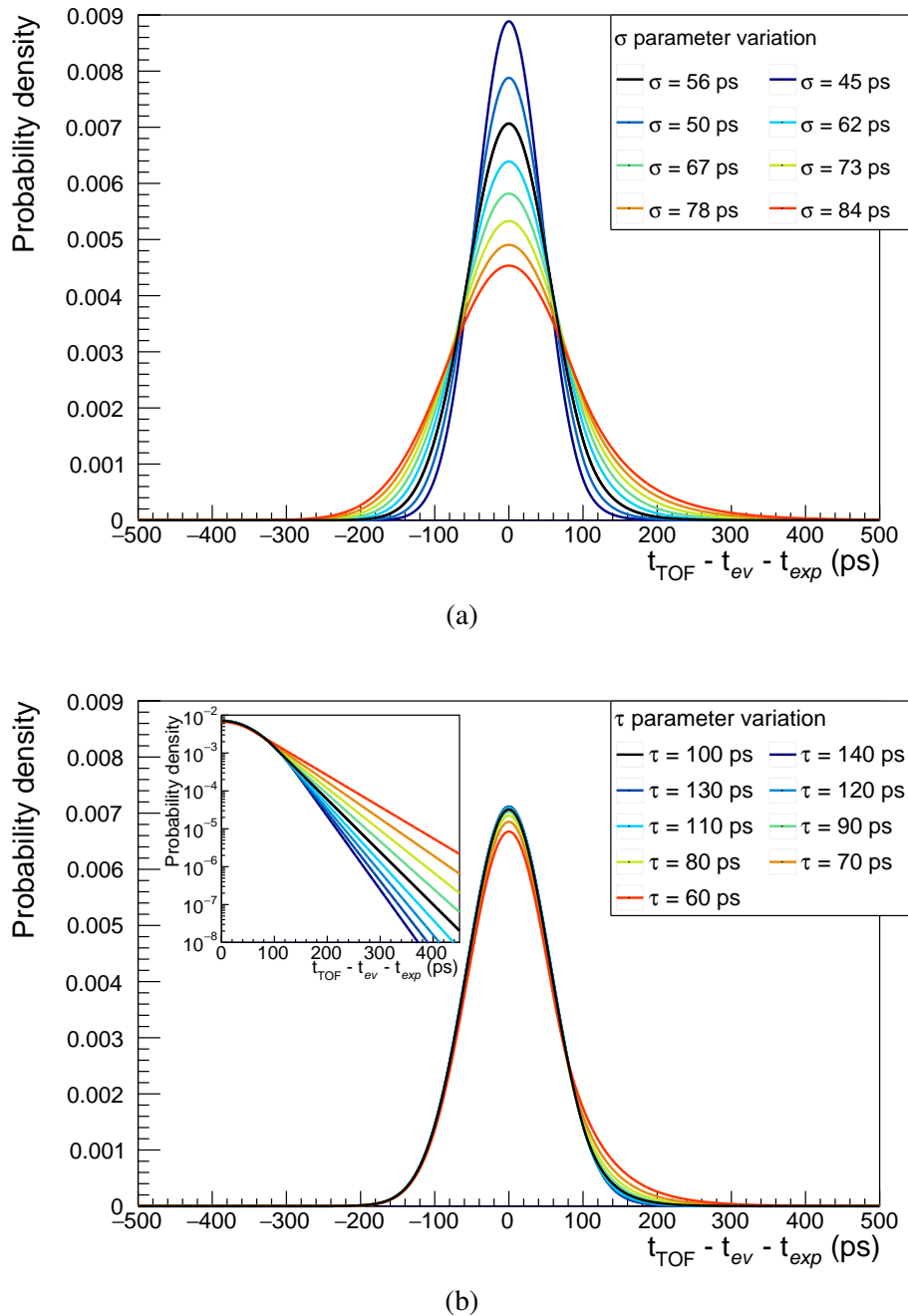
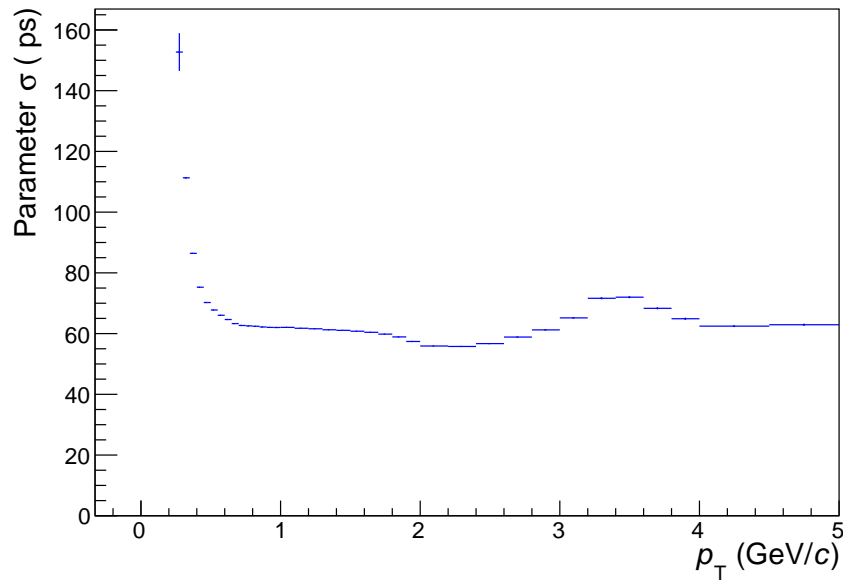
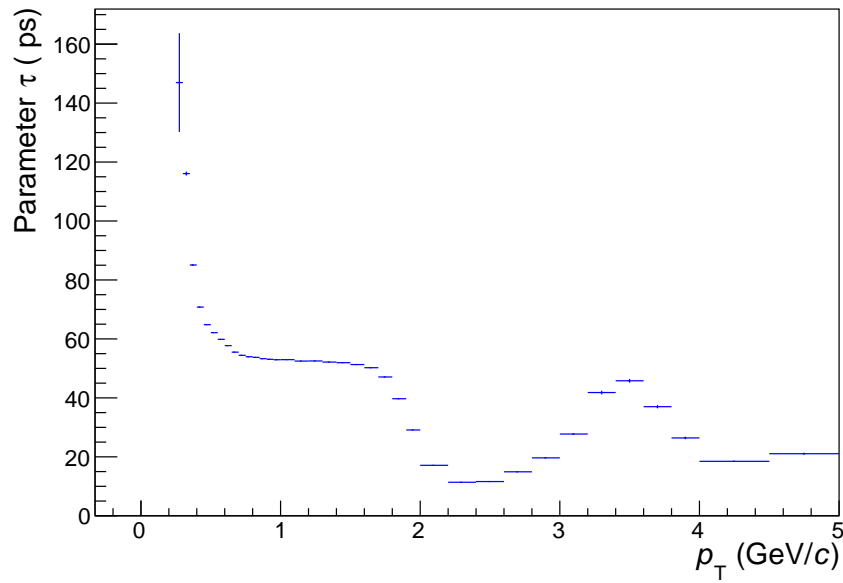


Fig. 6.7 (a) Effect of the variation of the resolution parameter σ on the TOF signal parameterization. (b) Effect of the variation of the tail parameter τ on the TOF signal parameterization. The logarithmic scale is used in the subfigure to enhance the visibility of the effect.

determination of the parameters of the TOF signal are extracted from a fit to the distributions of $t_{\text{PID}}(\pi) = t_{\text{TOF}} - t_{\text{exp},\pi} - t_{\text{ev}}$ obtained from data. The results of such fit are shown as a function of p_T in Fig. 6.8 for the σ and τ parameters. The TOF signal parameterization is fixed with the parameters obtained at 1 GeV/c, where the signal for π is clearly separated from other particle species. At lower momenta the results of the fit are affected by the poor resolution on the parameters of the extrapolated track ($t_{\text{exp},\pi}$), thus the increase in the σ and τ parameters. At higher p_T the fit result is affected by the contamination from kaons and protons, these modify the signal shape in the range of the fit. Examples of such fit are shown for different p_T intervals in Fig. 6.9.



(a)



(b)

Fig. 6.8 (a) σ and (b) τ parameters as a function of p_T . The parameters are obtained by fitting the $t_{\text{TOF}} - t_{\text{exp},\pi} - t_{\text{ev}}$ distributions in every p_T interval with the TOF signal function described in Eq. 5.13.

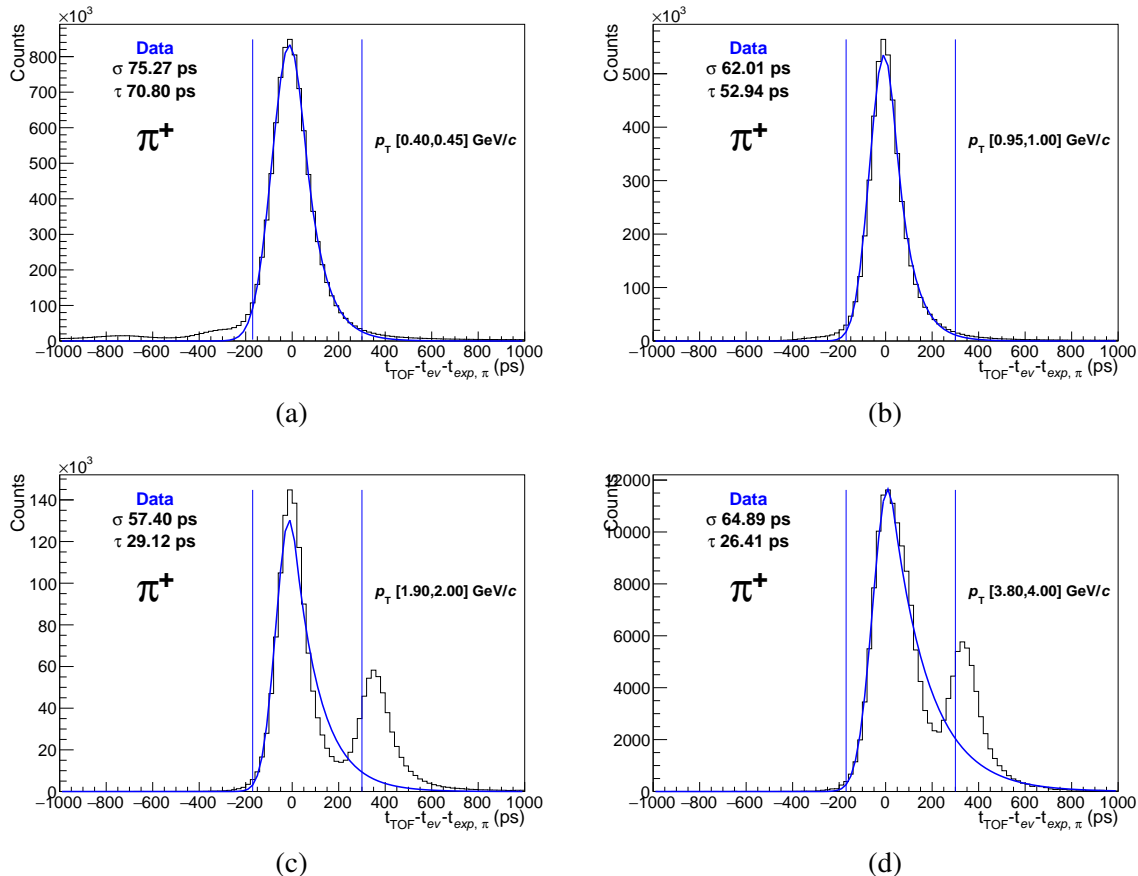


Fig. 6.9 Distribution of TOF signal under the pion mass hypothesis for different p_T intervals fitted with the Gaussian with exponential tail function described in Eq. 5.13. The parameters of the fit are reported for each transverse momentum interval in each figure. The limits of the fitting range are shown with blue lines. In figure (c) and (d) the peaks of kaons and protons are visible.

6.2.2 Mismatch parameterization

In high-occupancy environments such as Pb–Pb collisions, due to combinatorial background, there is a finite probability that a track which is correctly reconstructed in TPC is wrongly matched to a time signal that is generated by a different particle. This uncorrelated background is known as “mismatch” and has to be taken into account in yield extraction and efficiency corrections. Mismatch is also present in pp collisions but the magnitude of the effect is smaller.

A data driven approach is chosen to parametrize the TOF mismatch for the analysis presented in this work. The mismatch distributions are computed for each particle hypothesis i , the procedure is as follows. The distributions of the single-channel TOF time (t_{TOF}) are obtained from data, as reported in Fig. 6.10. The periodic distribution shown in the figure is related to the scheme used for ordering channels, in this representation the channels of j -th TOF Super Module are within the range⁶ $[8736 \times j, 8736 \times (j+1)]$. The minimum t_{TOF} is measured where tracks are shorter i.e. at mid-rapidity or at the center of every Super Module (corresponding to channel $4368 + 8736 \times j$). Tracks located at large rapidity experience a larger *time-of-flight*. The 18 sectors can be identified by counting the number of minima in the distribution. The uncorrelated background is obtained by sampling the distribution of TOF times t_{TOF} shown in Fig. 6.10:

$$\text{tof}_{\text{mismatch}} = t_{\text{sample}} - t_{\text{exp},i} \quad (6.7)$$

The $\text{tof}_{\text{mismatch}}$ is generated for each track, by using the channel number associated to the matched cluster. t_{sample} indicates the time obtained from the sampling procedure, it is randomly extracted from the distribution of t_{TOF} measured by the channel corresponding to the matched cluster. The t_{TOF} distribution shown in Fig. 6.10 is obtained from the same track sample used for the analysis. There is a non negligible probability that the t_{sample} extracted from the sampling corresponds to the t_{TOF} associated to the track. To avoid this possibility, channels are grouped into MRPC strips halves (48 channels for each half) and the t_{sample} is obtained for each track by sampling the neighbouring half. This solution is acceptable for the purpose of the analysis as the strip halves are located at the same rapidity.

6.2.3 Yield extraction

For both pp and Pb–Pb analyses, the uncorrected yields for species i are extracted with a template fit to the $(\text{tof} - t_{\text{exp},i}) / \sigma_i$ distributions whose components have been described

⁶The total amount of channels per Super Module is 8736 and the index of the Super Module goes from 0 to 17.

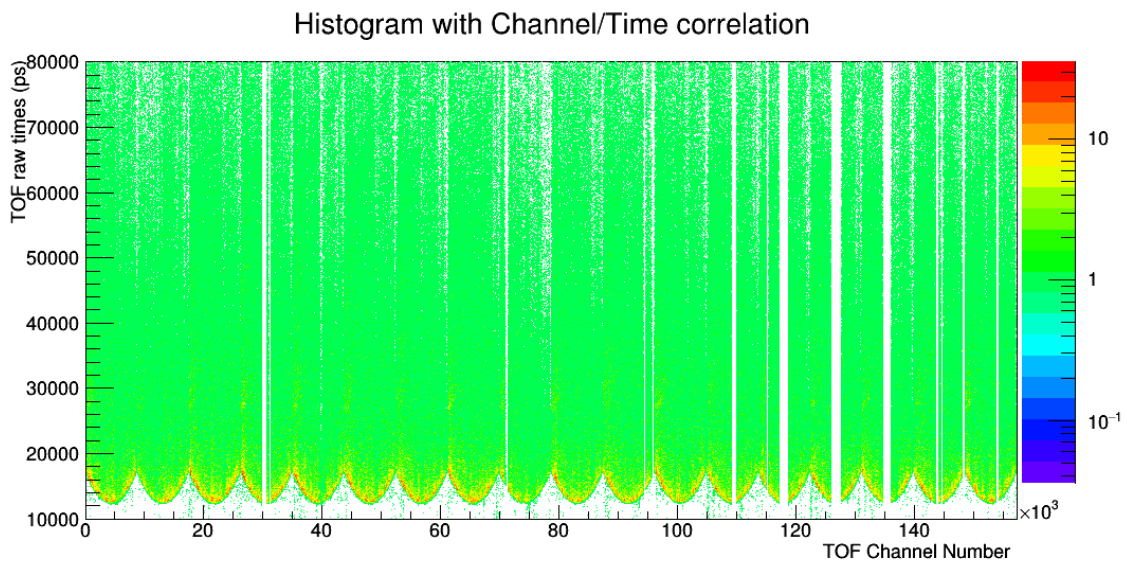


Fig. 6.10 TOF raw time - TOF channel number correlation extracted from data. The periodic structure is due to the location along the z -axis of the different channels. 18 main structures are visible, they correspond to the 18 sectors of the TOF detector. The empty vertical bands represent channels which were not read during data taking (inactive, inefficient or problematic channels). The missing channels that constitute 3 vertical bands approximately in the range between 115000 and 140000 are due to the missing modules in front of the PHOS detector as described in Section 4.3.

in Section 6.2.1 and Section 6.2.2. The template fits are performed by maximizing the likelihood via the *RooFit* package [141] of Root. The only free parameters used in the fit are the normalizations of the template shapes, corresponding to the yield of the particle under study.

The essential difference between the analysis of the pp and Pb–Pb samples consists in the separate treatment of events where the t_{ev} cannot be evaluated with the TOF or T0 detectors. The yield extraction procedure is performed separately for events with a precise t_{ev} evaluation and the ones relying on the bunch crossing time. These two separate approaches are necessary due to the dependence of the t_{ev} resolution on the method used for its determination. In Pb–Pb collisions, thanks to the high number of particles produced, the TOF detector is fully efficient in the determination of the t_{ev} , ensuring good and uniform resolution across all events. Due to the lower multiplicity reached in pp collisions, the determination of the t_{ev} is subject to higher uncertainty in a non-negligible fraction of events. In order to cope with this, the track sample for pp collisions is split into two sub-samples based on the t_{ev} resolution. The first sample has at least one among t_{ev}^{TOF} and t_{ev}^{T0} , while the other sample has only t_{ev}^{Fill} . Each one is fitted separately. The total raw yields are computed by summing the yields in the two samples. This procedure is used to avoid bi-modal $n\sigma$ distributions for background particles due to the sudden change in t_{ev} resolution. The separation in the two sub-samples could be in principle avoided thanks to the template fit procedure but it was decided to keep it to have better control on the “*secondary tails*”, a feature of the signal that will be described later.

Template generation

The procedure for the yield extraction requires the templates ($\text{Template}_{i,j}$) of both signal and background particles. Signal templates have $i = j$, while background templates have $i \neq j$. The template generation procedure is repeated for each particle species $i = \pi, K, p$ (the signals of interest) and $j = e, \mu, \pi, K, p, d$. The indices correspond to the different particle species.

The template for particle species j which is used for the extraction of the yield of the particle species i (signal), is generated from the expected arrival times $t_{exp,i}$ and $t_{exp,j}$:

$$t_{\text{template},i,j} = t_{exp,i} - t_{exp,j} + \Delta_j \quad (6.8)$$

In order to take into account the shape of the TOF signal for each species j , the $t_{\text{template},i,j}$ value is shifted by Δ_j , defined as:

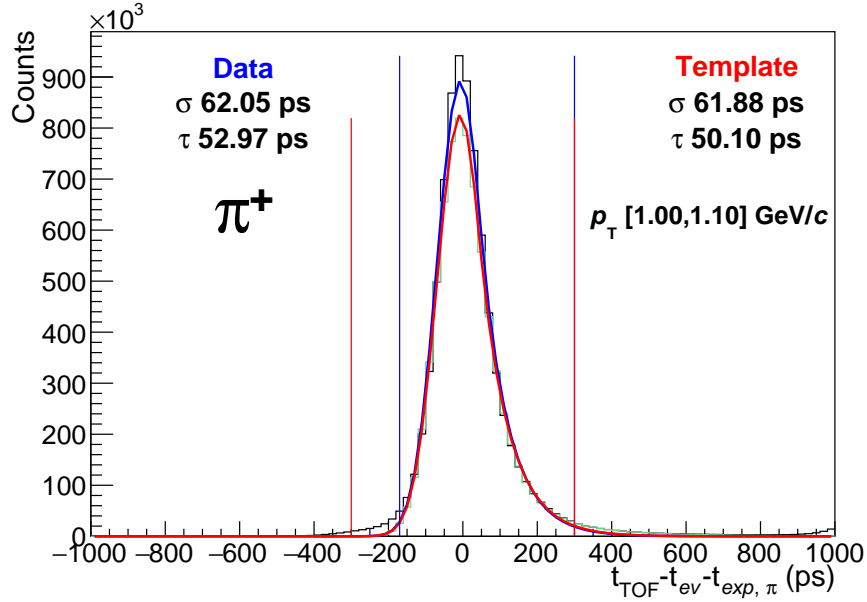


Fig. 6.11 The $t_{\text{TOF}} - t_{\text{exp},\pi} - t_{\text{ev}}$ distribution for pions (black histogram) is fitted with the TOF signal parameterization. The template for pions, extracted with the measured parameters, is shown in green. The latter is fitted with the signal parameterization to verify the consistency of the template generation procedure.

$$\Delta_j = \Delta_{\text{TOF signal}} + \Delta_{\text{Smearing},j} \quad (6.9)$$

The $\Delta_{\text{TOF signal}}$ is obtained by sampling the TOF signal distribution (Eq. 5.13) with parameters fixed from data as described in Section 6.2.1 and shown in Fig. 6.11. The $\Delta_{\text{Smearing},j}$ term is obtained for each template by sampling a Gaussian distribution and accounts for the uncertainty on tracking (p_T dependent) and t_{ev} determination (event dependent):

$$\Delta_{\text{Smearing},j} = \text{Gaus}(0, \sigma_j) \quad (6.10)$$

The σ_j parameter of the Gaussian distribution is obtained for each track from the resolution on the expected time $t_{\text{exp},j}$, according to:

$$\sigma_j = \sqrt{\sigma_{t_{\text{exp},j}}^2 - \sigma_{\text{Data}}^2} \quad (6.11)$$

Being σ_{Data}^2 the width of the Gaussian extracted from the fit in Fig. 6.8a. The measured $t_{\text{TOF}} - t_{\text{exp},\pi} - t_{\text{ev}}$ is shown together with the template obtained for the pion mass hypothesis in Fig. 6.11. The distributions are fitted with a TOF signal parameterization to verify the agreement between the two signal shapes.

Due to the rapidity selection in the interval $|y| < 0.5$, the distributions obtained for the three particle mass hypotheses of interest do not use the same track sample for the yield extraction. The rapidity of each track is evaluated under the mass hypothesis corresponding to species i . This step makes it impossible to extract the yield for all particle species in one iteration. Three separate fits under different mass hypotheses are required for the extraction of the π , K and p yields.

As a consequence, the template generation procedure is quite expensive from the computational point of view as it involves the generation of two random numbers per track, per species i , per species j . This results in a total of $2 \times 3 \times 6 = 36$ samplings. In order to reduce the processing time, a parallel approach is implemented in a TSelector by using the Proof package of Root. With this approach, events are processed in parallel by several jobs, corresponding to the number of available cores in the machine used for analysis.

Secondary tails The TOF signal shape is found not to be completely described by the parameterization of Eq. 5.13. This feature, more evident for low momentum tracks, manifests as a non-Gaussian tail that extends up to large times. These tails are distinct features with respect to the exponential tail described in Eq. 5.13 as they have a different origin. While being particularly visible for pions, the effect is also present for other particle species and has to be included in the template generation procedure in order to describe correctly the signal shape.

A detailed study is performed to quantify this effect by using a Monte Carlo simulation. These tails are found to be due to a *correlated mismatch* originating from particles decaying right before reaching the TOF surface. This type of mismatch differs from the uncorrelated one as it results in a delayed arrival times of the secondary particle with respect to the mother particle, thus contributing mostly to the right side of the TOF signal peak. In summary, the term *secondary tails* is used in this work to refer to the contribution from correlated mismatch to the TOF signal.

The parameterization of the secondary tails is carried out by using the information present in the Monte Carlo simulation about the particles and their decay products. The simulated time of arrival t_{MC} is used for this purpose. In Fig. 6.12 the three contributions to the $t_{\text{MC}} - t_{\text{ev}} - t_{\exp,i}$ distributions extracted from the simulation for the pion, kaon and proton mass hypotheses are shown:

1. Signal formed by genuine primary tracks which did not undergo any decay and were correctly matched to a TOF cluster (the red distribution).
2. Correlated mismatch due to tracks having the same identity of the hypothesis but originating from a weak decay (the blue distribution).

3. Uncorrelated mismatch, given by primary tracks wrongly associated to a TOF cluster, resulting in a *time-of-flight* measurement uncorrelated to the particle hypothesis (the green distribution).

The secondary tails can be added to the template generation algorithm by sampling the distributions obtained from the simulation for each track. In the template generation procedure the distribution of correctly matched tracks was constrained at zero, so as to avoid an ulterior smearing of the TOF signal shape. The templates obtained with this procedure are shown to reproduce satisfactorily the correlated mismatch in the data. In Fig. 6.13 the $(t_{\text{TOF}} - t_{ev} - t_{exp})/\sigma$ distribution is reported with and without secondary tails, under the hypothesis of the pion mass for p_T [0.70, 0.75] GeV/c as measured in Minimum Bias pp collisions. The templates of pions, kaons and mismatch are shown. If no secondary tails are used on the right side of the pion peak a clear deficit of the template is visible when confronting with the data distribution. This lack of a (long-range) secondary tail in the template shape is a second order correction for the pure yield extraction but is important for the sake of the fit quality. The deficit of the template is cured by including in the template generation algorithm the contribution from secondary tails.

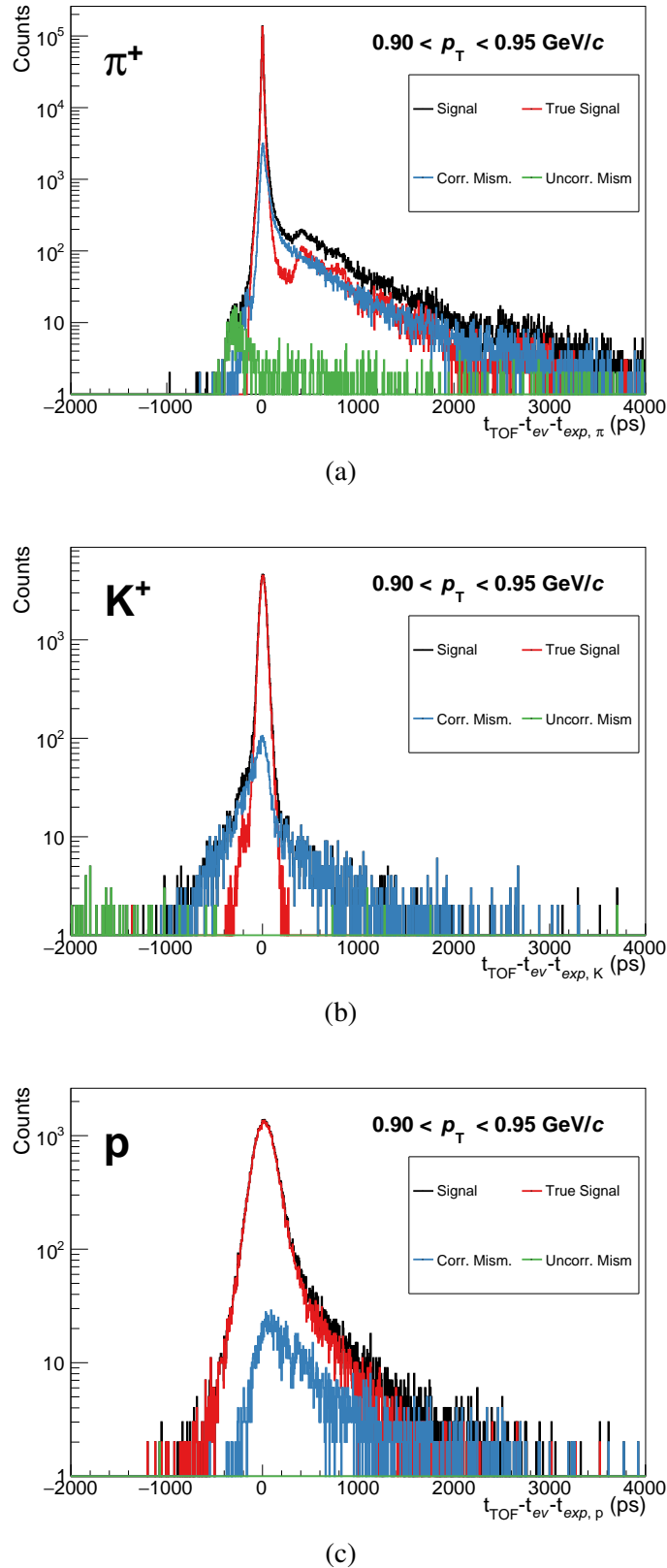


Fig. 6.12 Distribution of $t_{MC} - t_{ev} - t_{exp,i}$ obtained in the simulation under the hypothesis of pion (a), kaon (b) and proton (c). The identity of the particles is required to coincide with each hypothesis. Three source of signals are considered: 1) genuine signal (in red) 2) correlated mismatch (in light blue) 3) uncorrelated mismatch (in green).

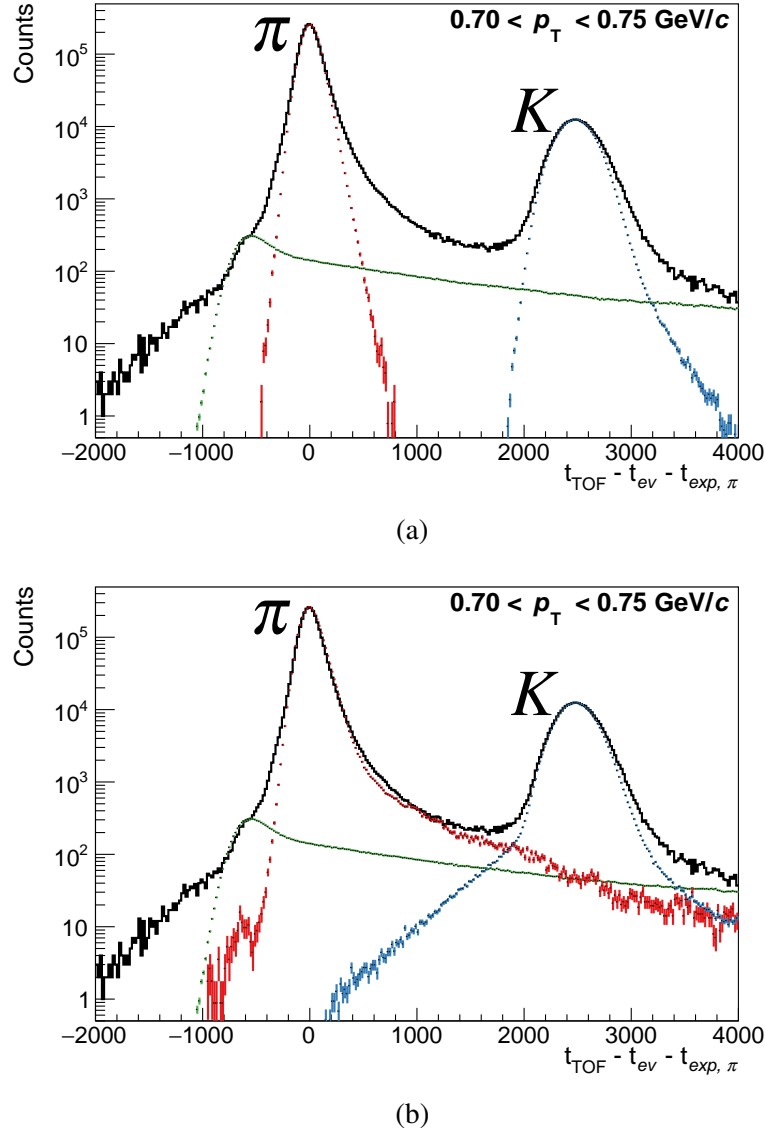


Fig. 6.13 $(t_{\text{TOF}} - t_{\text{ev}} - t_{\text{exp}})/\sigma$ distribution in TOF, under the pion hypothesis, with templates for pions, kaons and mismatch for $0.70 < p_T < 0.75 \text{ GeV}/c$ as measured in Minimum Bias pp collisions. (a) templates without secondary tails. (b) templates with secondary tails.

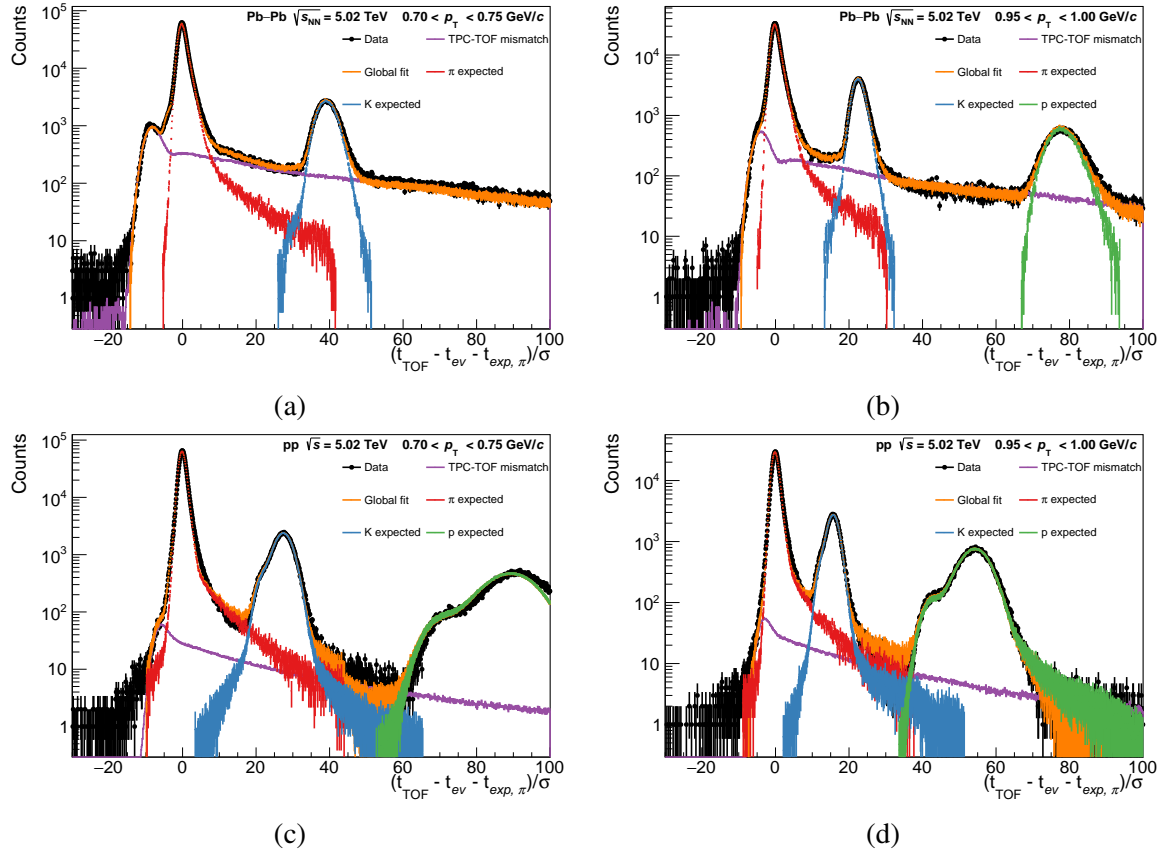


Fig. 6.14 Example of yield extraction fit (a), (b) in central Pb–Pb collisions (0–5%) and (c), (b) in MB pp collisions for the π hypothesis.

Examples of the template fit used to extract the particle yields in pp and Pb–Pb collisions are shown in Fig. 6.14. The difference in the overall TOF resolution between the pp and Pb–Pb samples is the cause of the different separation power observed in Fig. 6.14a and Fig. 6.14c. In Minimum Bias pp collisions the resolution is worse than in the Pb–Pb case due to the lower number of charged particles produced. This affects the resolution on the event time measurement ($\sigma_{t_{ev}}$). In addition, the large event-by-event variations in the event time resolution for pp collisions cause the distortions visible in the distribution of Fig. 6.14c and Fig. 6.14d for particle species that constitute the background (in this case kaons and protons). This effect is due to the propagation of $\sigma_{t_{ev}}$ in the expected resolution used at the denominator to compute the separation power. The templates used for the fit take into account any variation in $\sigma_{t_{ev}}$ and they are able to reproduce well the measured data.

6.2.4 Contamination from feed-down

In order to measure the spectra of primary particles, tracks are selected based on the distance of closest approach to the primary vertex in the xy -plane (DCA_{xy}), as a function of the p_T , as described in Section 6.1.4. This removes most of the secondary tracks but alone it is not sufficient for the purpose of the analysis. The residual contamination from secondary particles produced in weak decays and knock out in material is estimated with a data driven approach. As a first step, the DCA_{xy} distribution is determined in p_T intervals for each particle species in both data and simulation. In the latter case, the particle identity is known (“MC truth”) together with the mechanism of production (primary particle, secondary from strange hadron decay or from material). This information is used to estimate the DCA_{xy} distributions for primary particles and the ones originating in secondary interactions. In data the selection of a pure sample of each particle species is performed by combining the signal in TPC and TOF, as:

$$\sigma_{\text{TPC-TOF},i} = \sqrt{\sigma_{\text{TPC},i}^2 + \sigma_{\text{TOF},i}^2} \quad (6.12)$$

The sample is identified with a 2σ selection on the TPC-TOF signal. An example of the combined TPC and TOF PID discriminator is shown in Fig. 6.15 for pions and for protons. This PID technique allows to obtain a pure sample for each particle species up to momenta where the primary fraction becomes preponderant ($p_T > 2 \text{ GeV}/c$).

The fractions of each component within the DCA_{xy} selection are obtained by performing a template fit to the data. The fit is performed using the `TFractionFitter` class of Root so as to unfold the various components of the distributions. This approach implements a likelihood fit using Poisson statistics to take into account the limited statistics of the simulation. As a consequence, the templates are varied leading to additional contributions to the overall likelihood [142]. The overall likelihood term is formed by parameters accounting for the normalization of template templates. In addition, the likelihood includes one parameter per bin per template to take into account the Poisson statistics. The conditions of applicability of the fit procedure are verified for every iteration [143]. For this reason, the fits are limited to the low momentum range ($p_T < 2.5 \text{ GeV}/c$) and are extrapolated by using an ad-hoc function. The DCA_{xy} distributions obtained in the simulation are adjusted to reproduce the ones obtained in data by performing an extended likelihood fit. An example of the fit is shown for π^+ and p in Fig. 6.16. A non-negligible contribution from secondary particles does not get rejected by applying the selection on the DCA_{xy} as in Eq. 6.2. The template fit allows to correctly take into account these residual contributions.

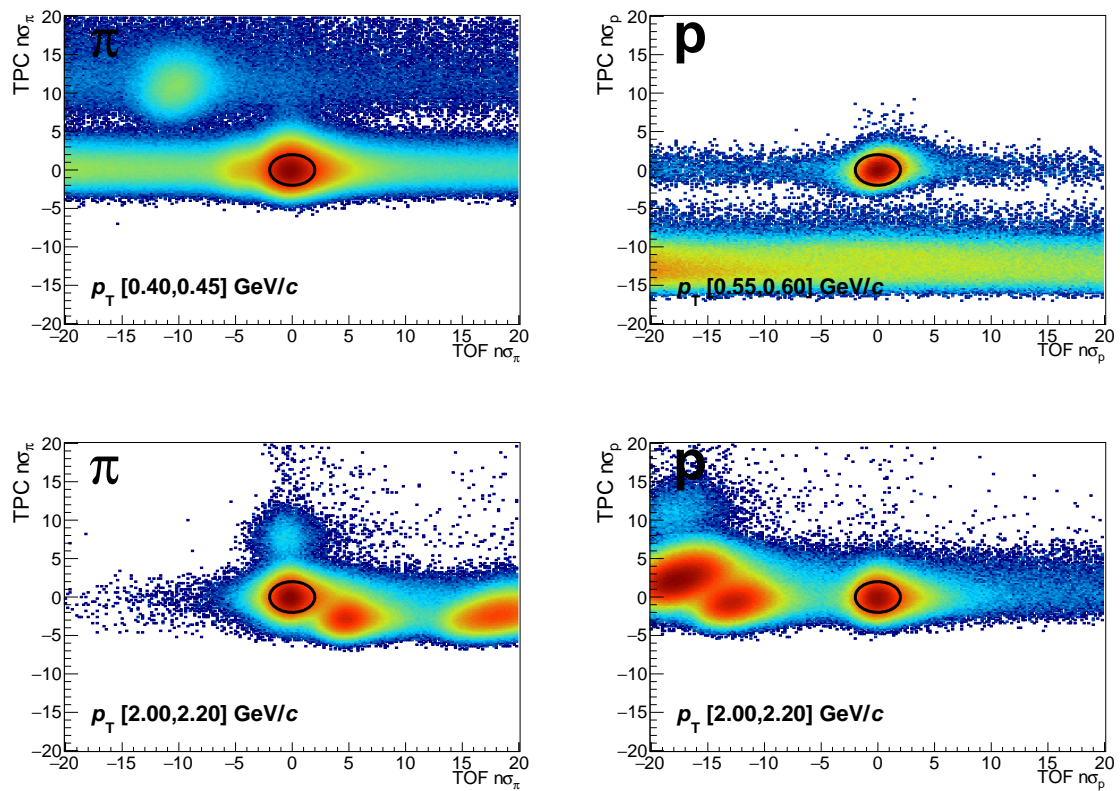
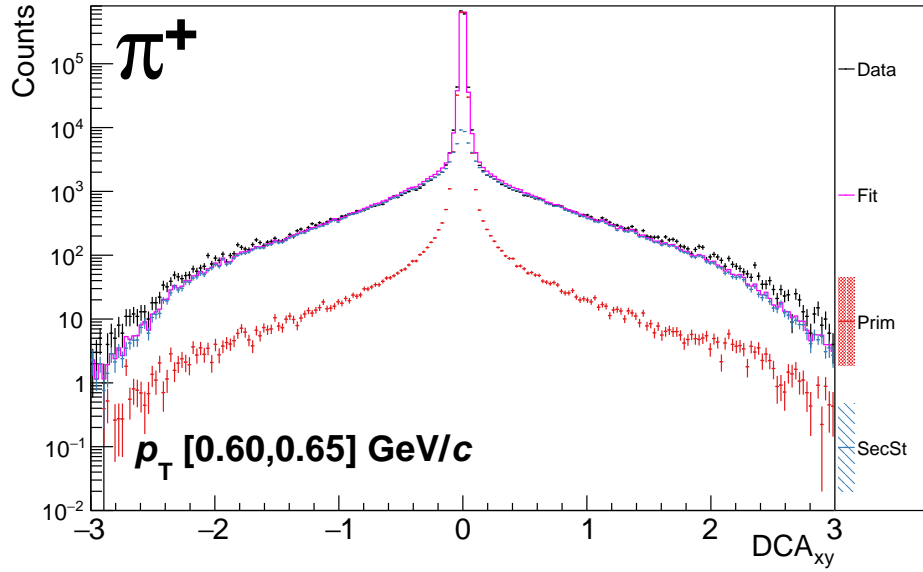
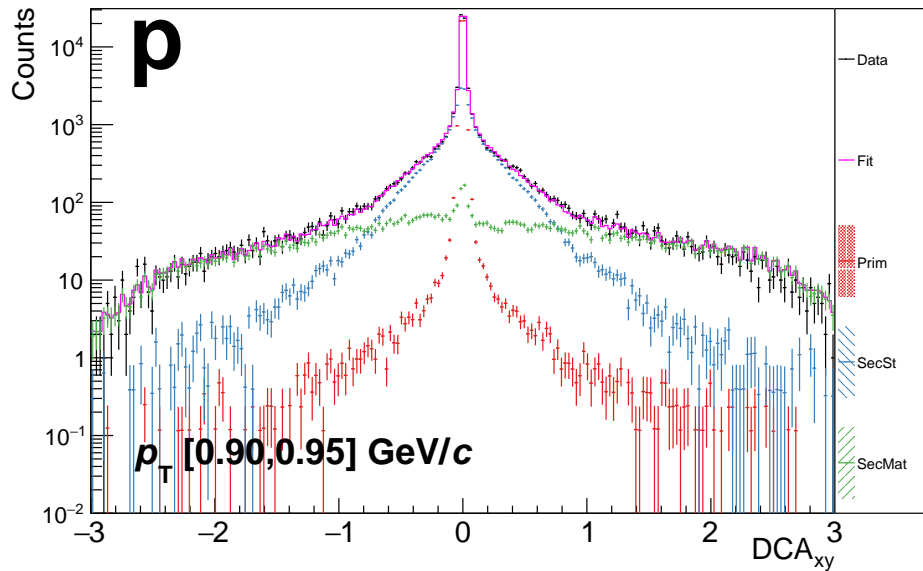


Fig. 6.15 PID separation power for the pion and proton hypotheses performed with TOF (x-axis) and TPC (y-axis) for two different p_T bins. The black circle represents a 2σ selection on the combined signal as reported in Eq. 6.12. The continuous bands which are evenly distributed over a large range in TOF $n\sigma_\pi$ ($n\sigma_p$) are due to tracks wrongly matched between TPC and TOF.



(a)



(b)

Fig. 6.16 In black, DCA_{xy} distribution measured in data for π^+ (a) and p (b) in two momentum intervals. The fitted templates for primary particles (in red), the one from weak decays (in blue) and the one from particle knockout in material (in green, only for protons) are shown. The yield of primary particles is obtained by integrating the red template within the range defined by the DCA_{xy} selection defined in Eq. 6.2.

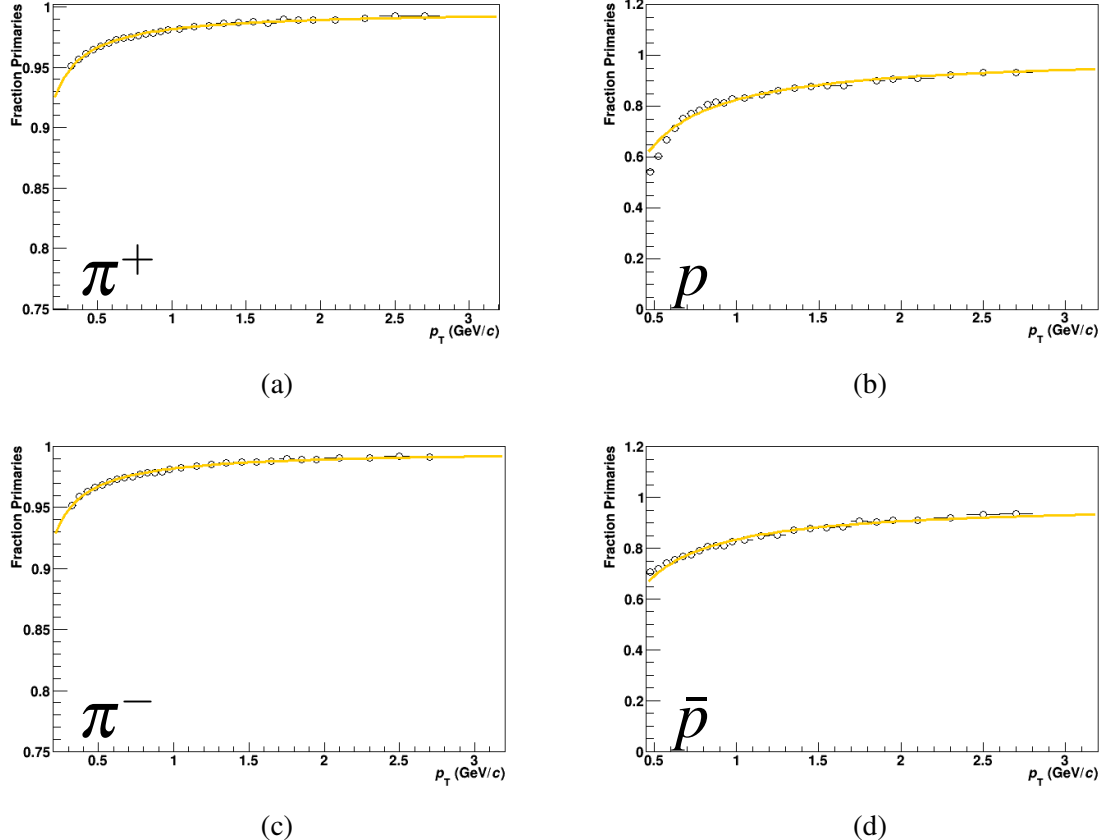


Fig. 6.17 Primary fraction for π^+ (a), p (b), π^- (c) and \bar{p} (d) as a function of p_T with fit function Eq. 6.13.

The fraction of each component is obtained by integrating the fitted distributions in simulation in the range defined by the DCA_{xy} selection. The feed-down correction is necessary only for π^\pm , p and \bar{p} as it is negligible for kaons. The contribution from particle knockout in the material is considered only for protons as it is negligible for the other particles species.

The template fits are performed in the p_T interval where a high purity is guaranteed with the TPC-TOF PID (up to ~ 2.5 GeV/ c). In order to extend the measurement of the primary fraction to higher p_T the values are fitted with the ad-hoc function:

$$f_{\text{Primaries}}(p_T) = \alpha + \beta \cdot e^{\gamma \cdot p_T} \quad (6.13)$$

Then extrapolated up to the saturation region. The feed-down correction is parametrized with the three parameters α , β and γ . The overall correction is obtained by using the measured values at low p_T and the extrapolated ones at higher momenta, as reported in Fig. 6.17.

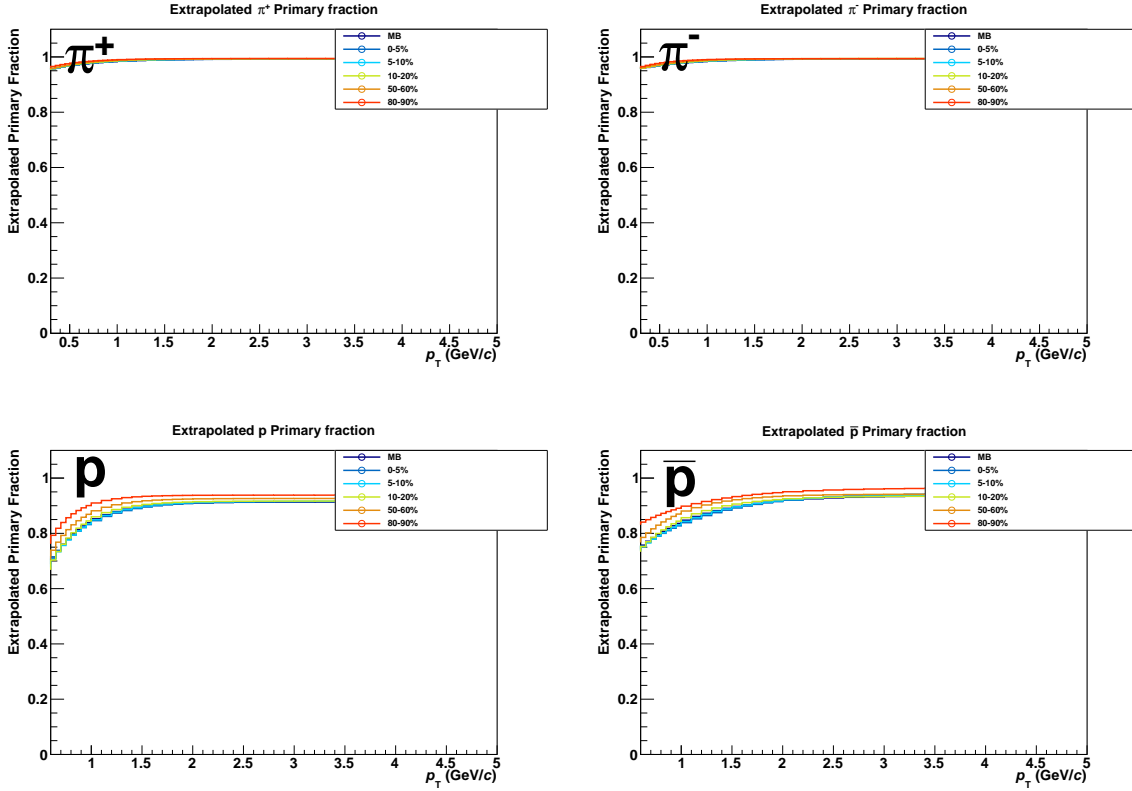


Fig. 6.18 Primary fraction of π^\pm , p and \bar{p} as measured in different centrality classes of Pb–Pb collisions at $\sqrt{s_{\text{NN}}} = 5.02$ TeV.

Centrality dependence of the feed-down correction Particle composition depends on the centrality of the event in Pb–Pb collisions. Therefore, the feed-down correction needs to be estimated for different centrality classes. The relative particle abundance, shown in Fig. 6.18, is extracted with centrality-integrated (MB) templates from simulations so as to avoid fluctuations due to the limited statistics. The ratio of the feed-down correction computed in each centrality class relative to the MB one is shown in Fig. 6.19. In the figures, it is shown that the fraction of primary fraction is lower in central collisions, with respect to peripheral ones. This is understood as an effect of the different particle production mechanisms at play in central collision (e.g. stronger strangeness enhancement).

6.3 Acceptance and efficiency corrections

Due to the track requirements listed in the previous sections, the efficiency correction can be computed by considering the tracking efficiency and the matching efficiency of

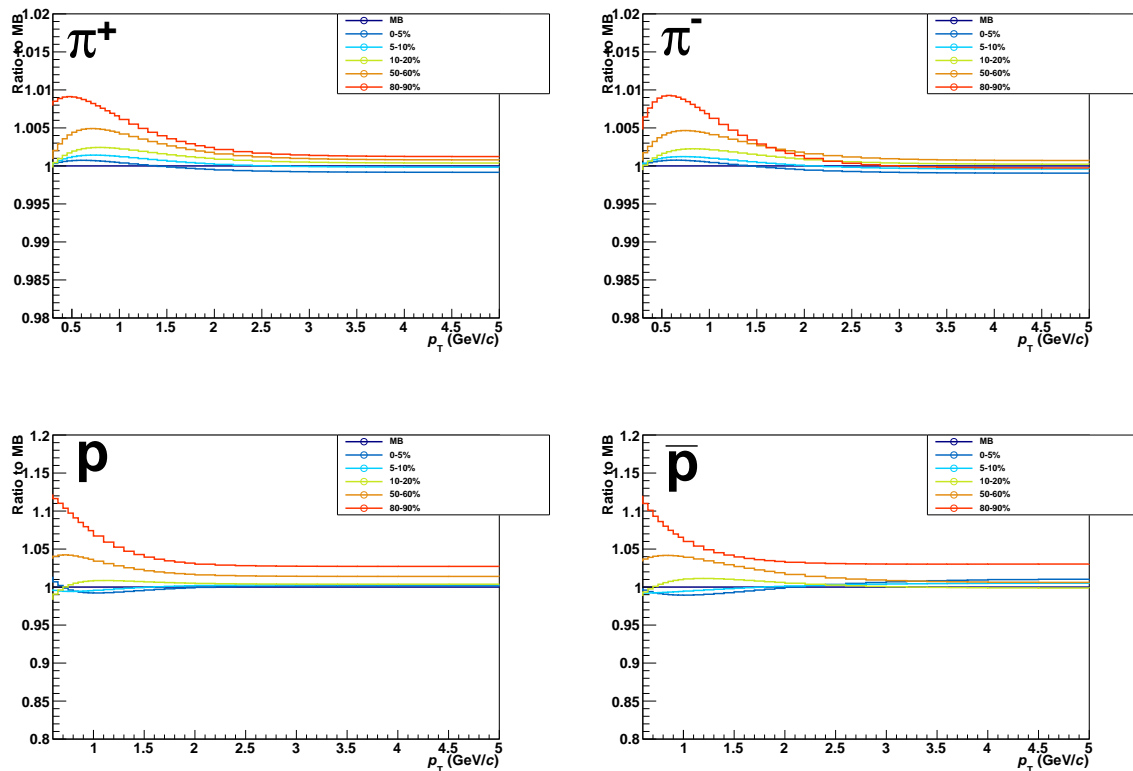


Fig. 6.19 Ratio to the MB of the primary fraction of π^\pm , p and \bar{p} as measured in different centrality classes of Pb–Pb collisions at $\sqrt{s_{\text{NN}}} = 5.02$ TeV.

tracks from TPC to TOF. The overall efficiency correction is the convolution of the two contributions:

$$\epsilon_{\text{Tot}} = \epsilon_{\text{Tracking}} \times \epsilon_{\text{Matching}} \quad (6.14)$$

The determination of these corrections is based on the information available in the simulation. The efficiency corrections include also the detector acceptance. The definitions of the tracking and matching efficiencies are given below.

6.3.1 Tracking efficiency

The tracking efficiency is defined as the ratio between the number of tracks that are reconstructed and selected according to a given set of criteria, and the number of those that are generated in the detector acceptance,

$$\epsilon_{\text{Tracking}} = \frac{\text{Reconstructed tracks (MC PID, primaries, } |y| < 0.5, |\eta| < 0.8)}{\text{Generated particles (MC PID, primaries, } |y| < 0.5)} \quad (6.15)$$

Only primary particles identified via their true identity in the simulation are considered at both numerator and denominator because raw spectra are already corrected for feed-down contamination with the data-driven approach described in Section 6.2.4. The MC truth on the particle identity is required. The same track selection criteria are applied to reconstructed tracks as used for data. The tracking efficiency in Pb–Pb collisions at $\sqrt{s_{\text{NN}}} = 5.02$ TeV is shown for all particle species in Fig. 6.20. The same is reported for pp collisions at $\sqrt{s} = 5.02$ TeV in Fig. 6.21. No significant difference is observed between the efficiency for positive and negative pions or kaons. The tracking efficiency for p and \bar{p} is significantly different at low momentum ($p_T < 2$ GeV/ c) due to the \bar{p} absorption in the material. The shape of the tracking efficiency correction strongly depends on the cuts used for track selection. In this case, the non-monotonic behavior of the tracking efficiency is due to the cut on the track length in TPC.

Efficiencies for all species saturate at a common value at large momenta ($p_T > 4\text{-}5$ GeV/ c), where interactions in the material (e.g. hadronic processes or absorption) are negligible.

The tracking efficiency is shown for different centrality classes in Fig. 6.22 for pions, Fig. 6.23 for kaons and Fig. 6.24 for protons. The dependence of the tracking efficiency on the event centrality is only limited to the very low momentum region not relevant for

this analysis, indicating the stability of the tracking detectors in the Pb–Pb collisions. The efficiency estimated for MB pp collisions at $\sqrt{s} = 5.02$ TeV is shown in Appendix E.

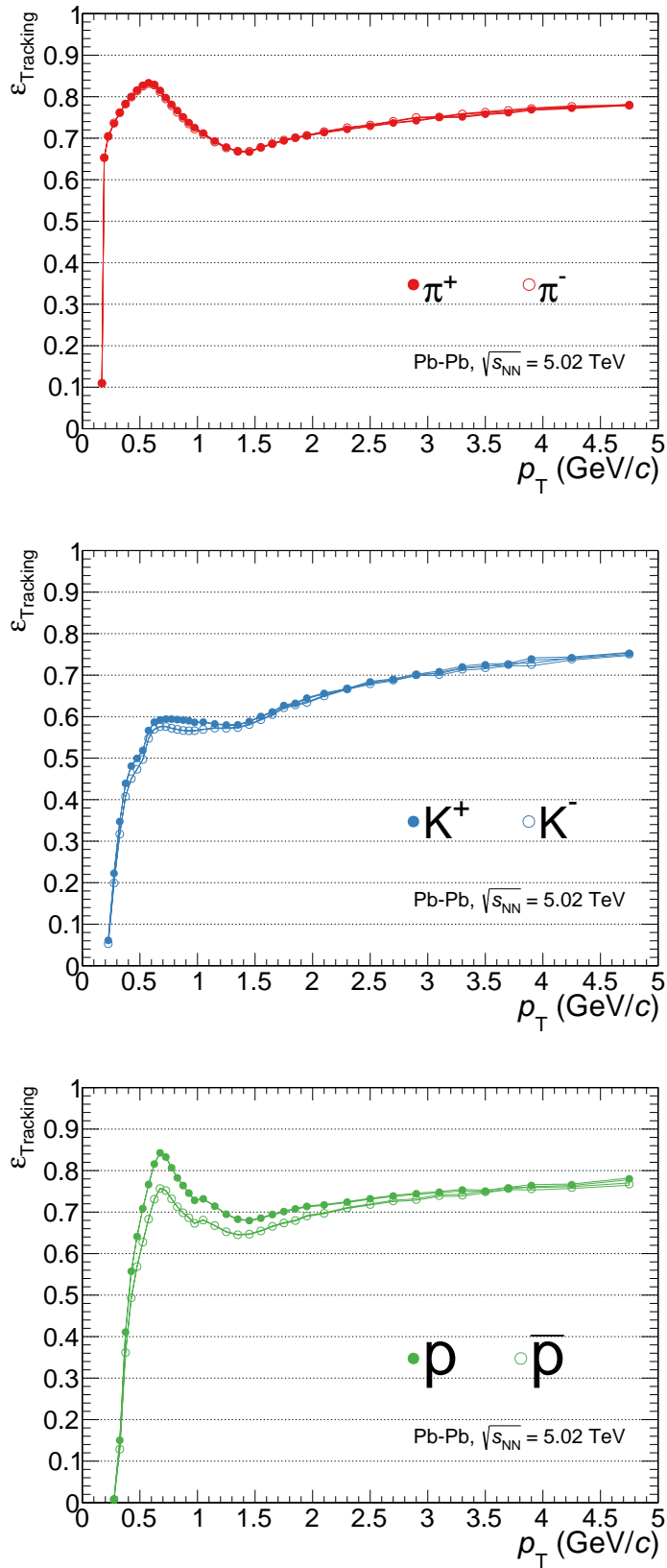


Fig. 6.20 Tracking efficiency for both positive and negative π , K and p as measured in Minimum Bias Pb–Pb collisions at $\sqrt{s_{\text{NN}}} = 5.02 \text{ TeV}$.

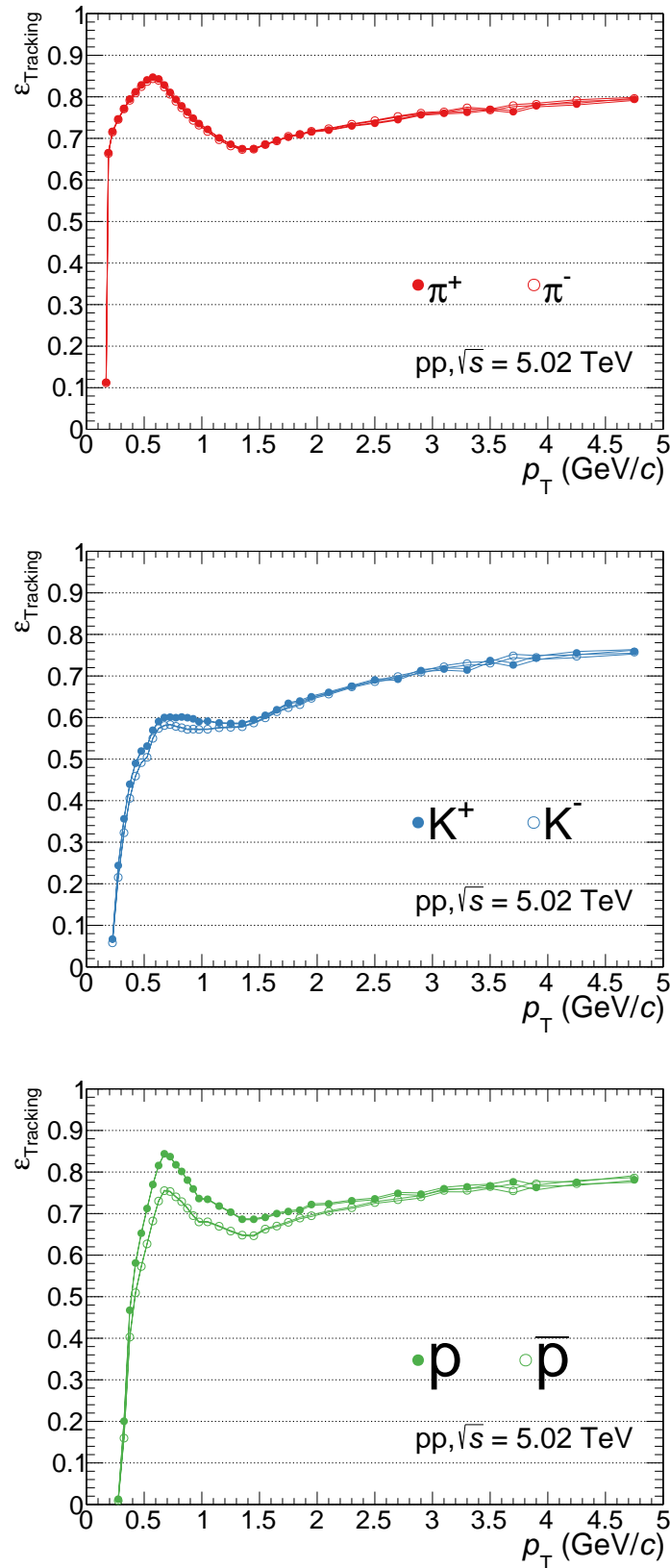


Fig. 6.21 Tracking efficiency for both positive and negative π , K and p as measured in Minimum Bias pp collisions at $\sqrt{s} = 5.02 \text{ TeV}$.

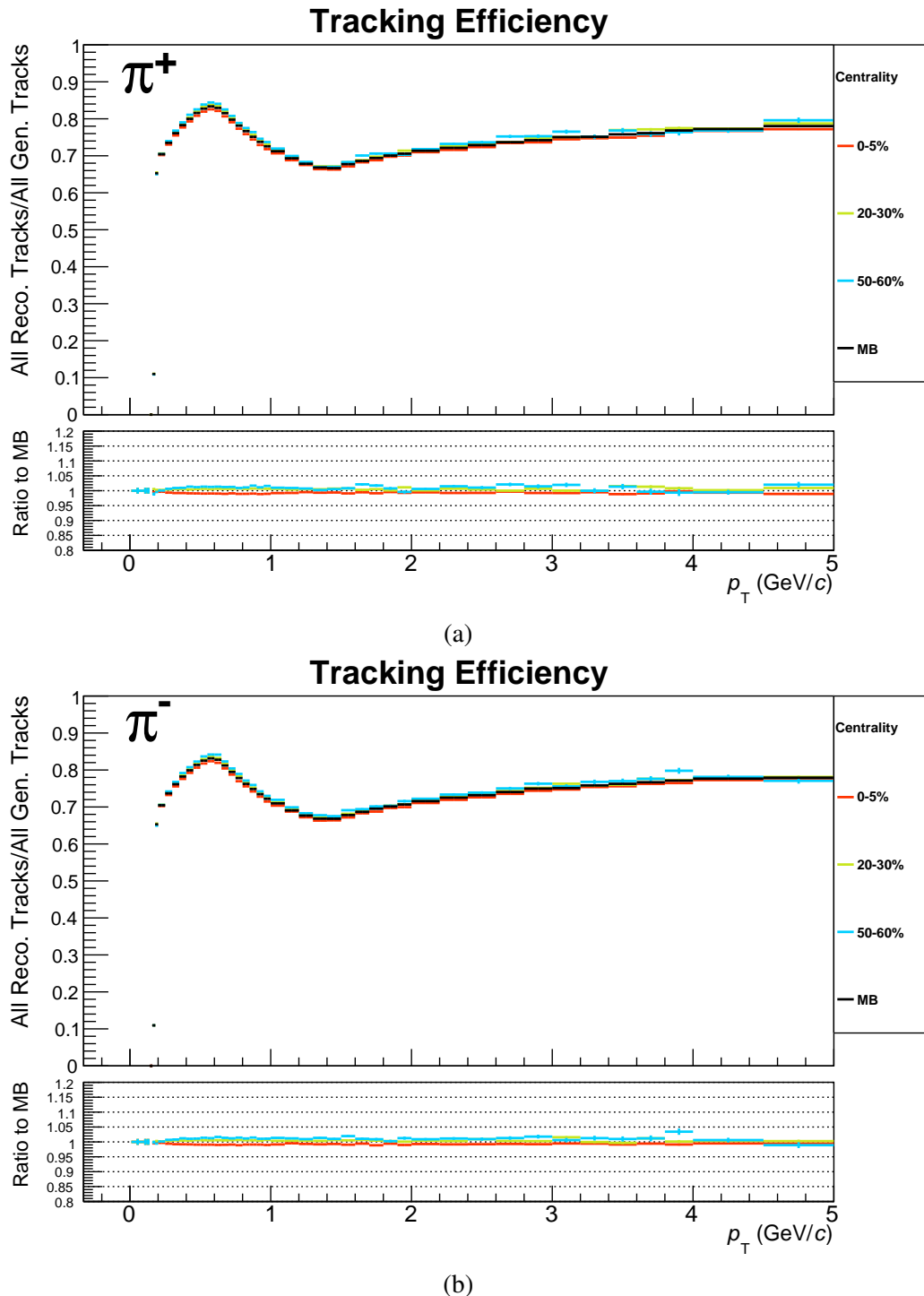


Fig. 6.22 Tracking efficiency for both positive and negative π as measured in Pb–Pb collisions, in different centrality classes.

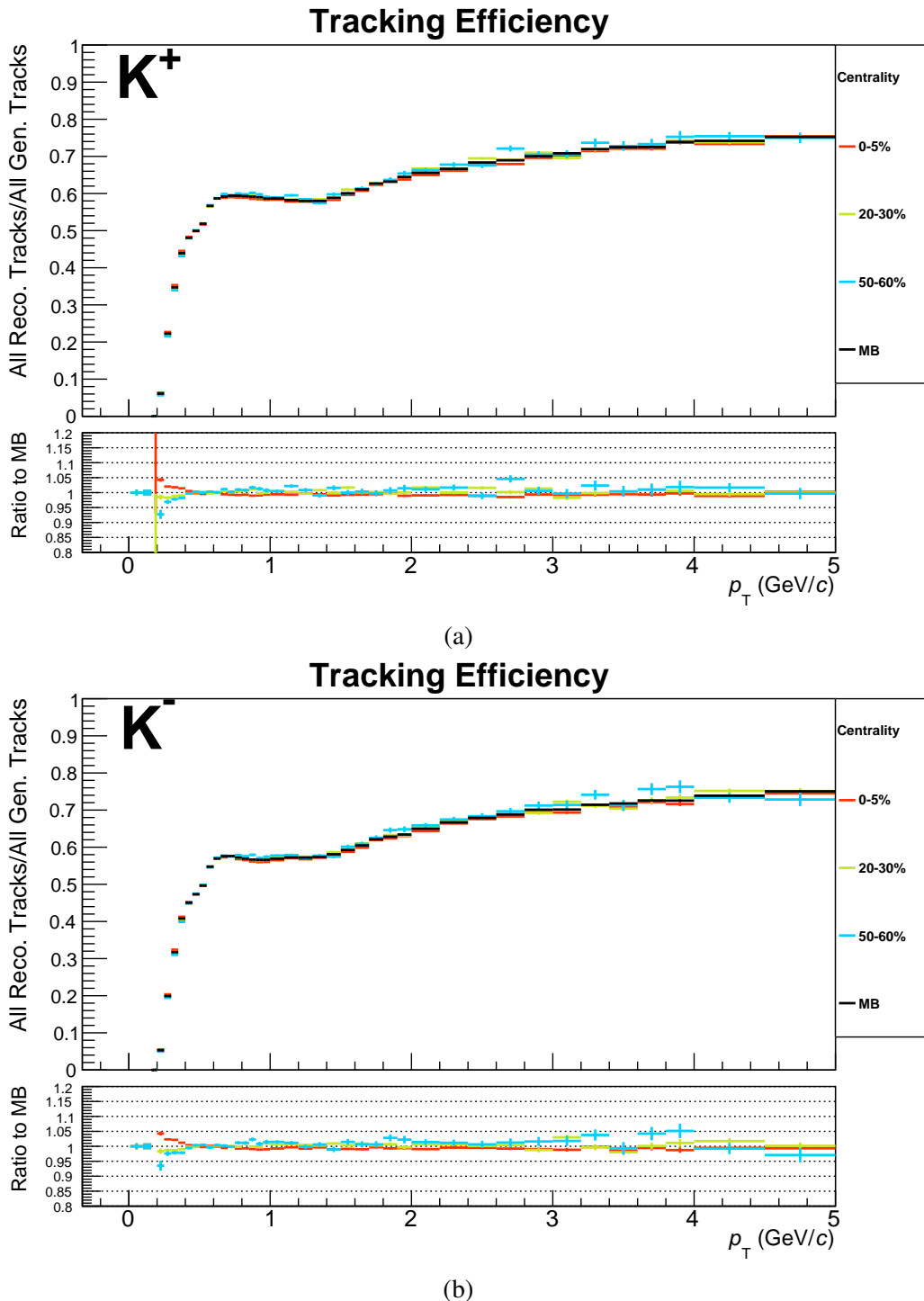


Fig. 6.23 Tracking efficiency for both positive and negative K as measured in Pb–Pb collisions, in different centrality classes.

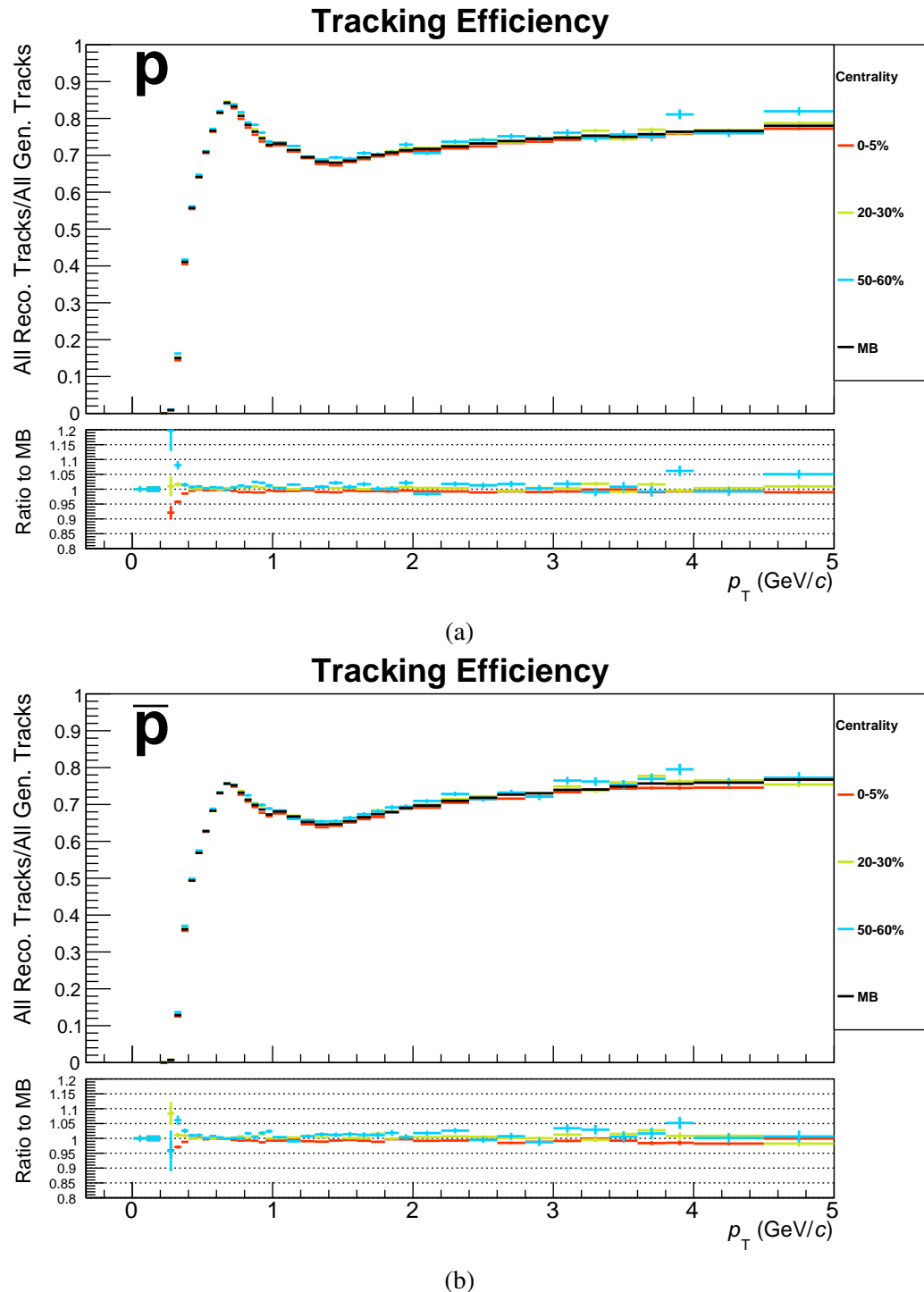


Fig. 6.24 Tracking efficiency for both positive and negative p as measured in Pb–Pb collisions, in different centrality classes.

6.3.2 Matching efficiency

The matching efficiency is obtained from the Monte Carlo simulation by computing the ratio between the number of tracks that are matched to the TOF and the number of tracks reconstructed in TPC. By definition, the denominator of the matching efficiency is equal to the numerator of the tracking efficiency.

$$\epsilon_{\text{Matching}} = \frac{\text{Tracks matched to TOF}(\text{MC PID, primaries}, |y| < 0.5, |\eta| < 0.8)}{\text{Reconstructed tracks}(\text{MC PID, primaries}, |y| < 0.5, |\eta| < 0.8)} \quad (6.16)$$

The matching of the track to the correct TOF cluster can be verified in the simulation. The matching efficiency obtained by imposing this condition at the numerator defines the $\epsilon_{\text{Matching, MC truth}}$. This efficiency is lower than the $\epsilon_{\text{Matching}}$, obtained without the strict requirement of a “true” match.

In this work, mismatched tracks are considered as a background for the signal and cannot be identified. This track loss has to be included in the correction, which is computed by requiring either the true match⁷ or a TOF signal compatible with the particle hypothesis under study. This technique allows one to correctly take into account the correlated mismatch, which is track mismatch *de facto*.

The TPC-TOF matching efficiency in Pb–Pb collisions at $\sqrt{s_{\text{NN}}} = 5.02$ TeV is reported for all particle species in Fig. 6.25. The same is reported for pp collisions at $\sqrt{s} = 5.02$ TeV in Fig. 6.26. The matching efficiency saturates for all particles species at p_{T} larger than 4 GeV/*c*. Particle absorption in the material between TPC and TOF causes a non negligible decreases of the efficiency for anti-protons. It is worth to note that the different matching efficiencies observed in pp and Pb–Pb collisions is due to the different matching window used during tracking (see Section 5.1.1).

The matching efficiency is shown for different centrality classes in Fig. 6.27 for pions, Fig. 6.28 for kaons and Fig. 6.29 for protons. Contrary to the case of the tracking efficiency, the dependence of the matching efficiency on the event centrality extends up to the p_{T} region subject of this analysis. This effect originates from the combinatorial background which increases the track mismatch probability and is correlated with the event multiplicity.

The TPC-TOF matching efficiency estimated for MB pp collisions at $\sqrt{s} = 5.02$ TeV is shown in Appendix E.

⁷The MC truth is asked for the TPC-TOF match either for the particle under study or the particle it originated from, in case of a weak decay.

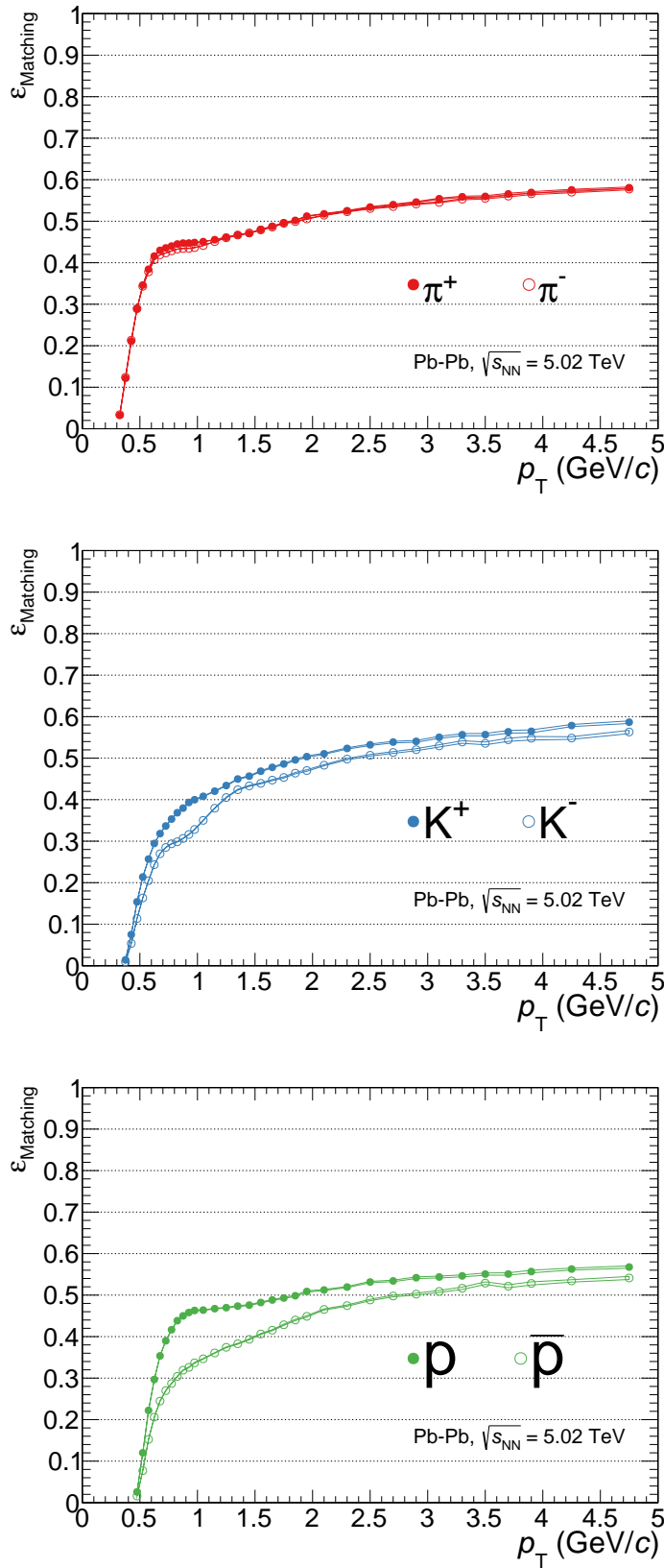


Fig. 6.25 Matching efficiency for both positive and negative π , K and p as measured in Minimum Bias Pb–Pb collisions at $\sqrt{s_{\text{NN}}} = 5.02 \text{ TeV}$.

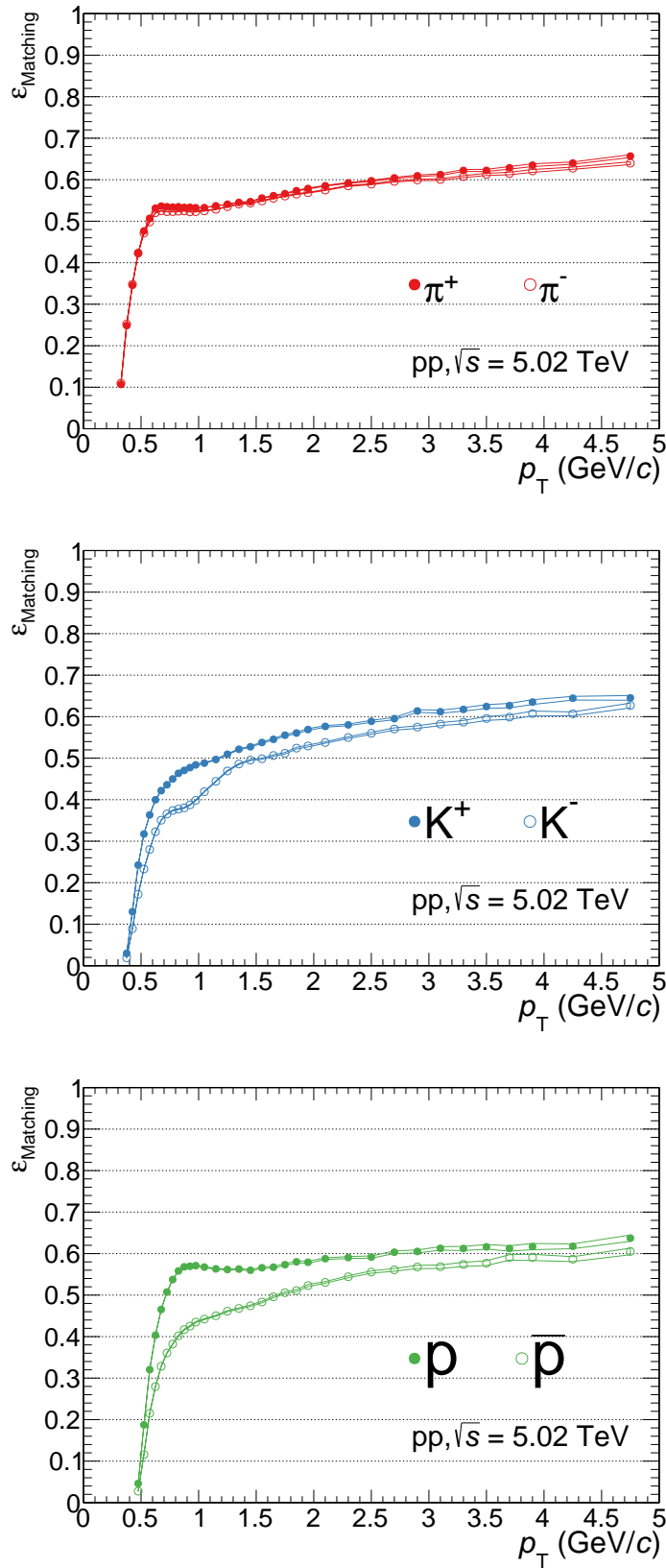


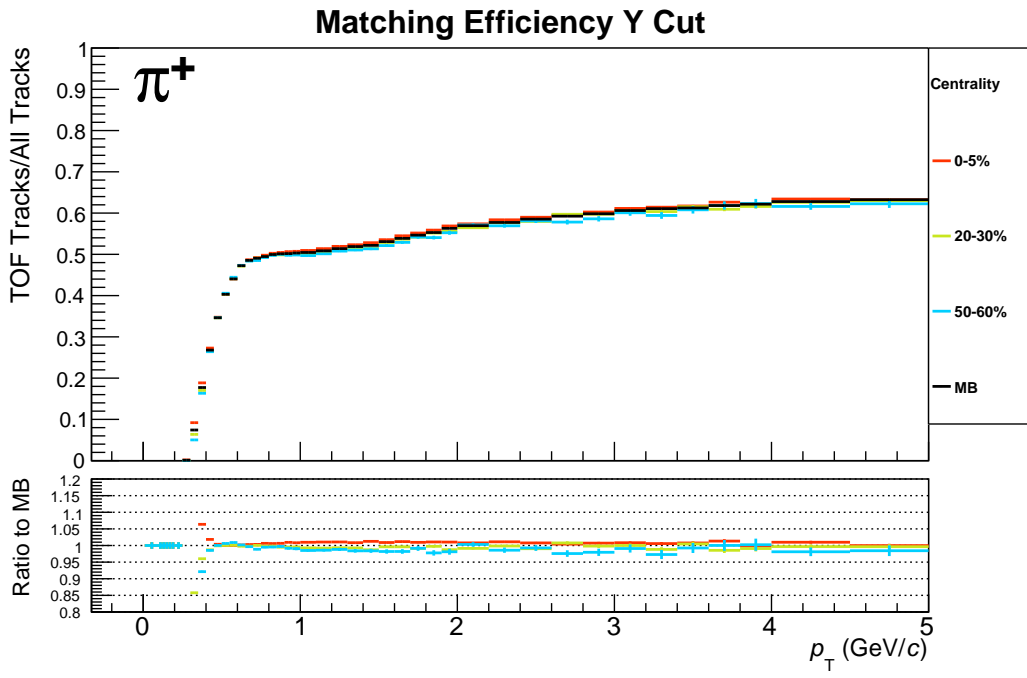
Fig. 6.26 Matching efficiency for both positive and negative π , K and p as measured in Minimum Bias pp collisions at $\sqrt{s} = 5.02 \text{ TeV}$.

The matching efficiency for unidentified charged particles can be determined also in data. This is used to verify the consistency between $\varepsilon_{\text{Matching}}$ in data and simulation and to validate the corrections applied to particle yields to obtain the results.

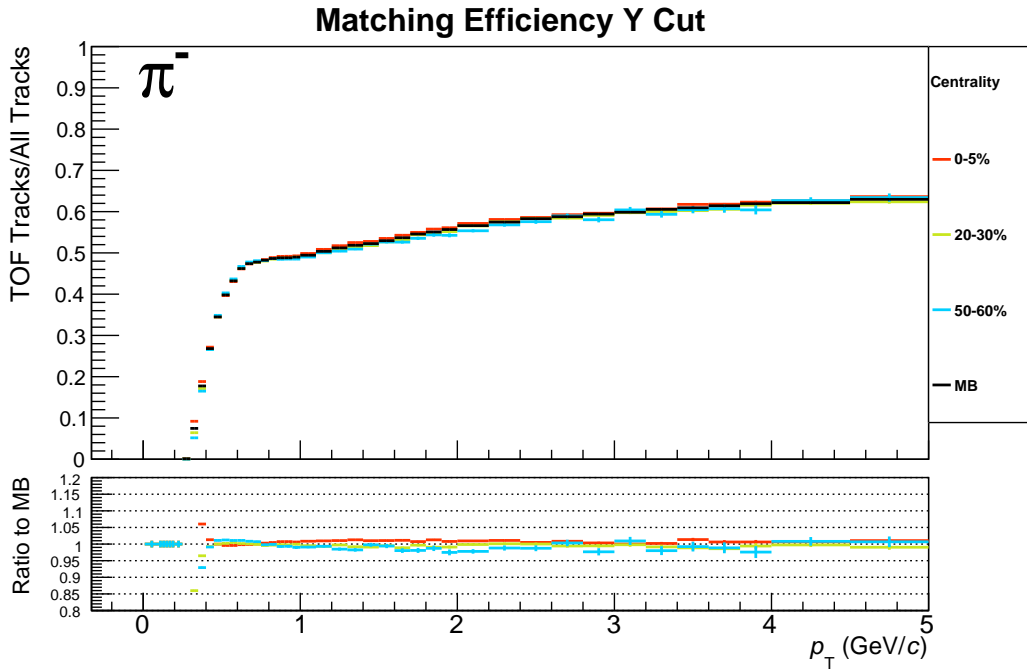
The same track selection as the one applied for the yield extraction (except for the rapidity cut) is required. The matching efficiency is computed as in Eq. 6.17 and is shown for MB Pb–Pb collisions as a function of p_{T} , η and the azimuthal angle φ in Fig. 6.30 for positive and negative particles. In order to avoid the effects of multiple scattering and particle absorption in the material that is preponderant at low p_{T} and may not be described in the simulation, tracks with p_{T} lower than 500 MeV/c are discarded before computing the efficiency as a function of η and φ .

$$\varepsilon_{\text{Matching}}^{ch} = \frac{\text{Tracks matched to TOF}(|\eta| < 0.8)}{\text{Reconstructed tracks}(|\eta| < 0.8)} \quad (6.17)$$

The efficiency reported as a function of p_{T} reach saturation for $p_{\text{T}} > 4$ GeV/c. The modulation that is present as a function of η and φ is due to the detector configuration (active readout channels) and to the absence of three modules in the position corresponding to the PHOS detector ($\varphi \sim 270^\circ$). The comparison of the data and the simulation shows a constant downward shift of $\sim 5\%$ for the $\varepsilon_{\text{Matching}}^{ch}$ computed in the Monte Carlo simulation. The same comparison is show for pp collisions as a function of p_{T} , η and φ in Fig. 6.31. Tracks with $p_{\text{T}} < 0.5$ GeV/c are not considered for the efficiency as a function of η and φ , so as to reach the saturation region of the $\varepsilon_{\text{Matching}}^{ch}$. The comparison between data and Monte Carlo for this case shows some improvement in the absolute value of the matching efficiency ratio with respect to the one obtained in Pb–Pb collisions. Interestingly, the overall trends are mostly unmodified.

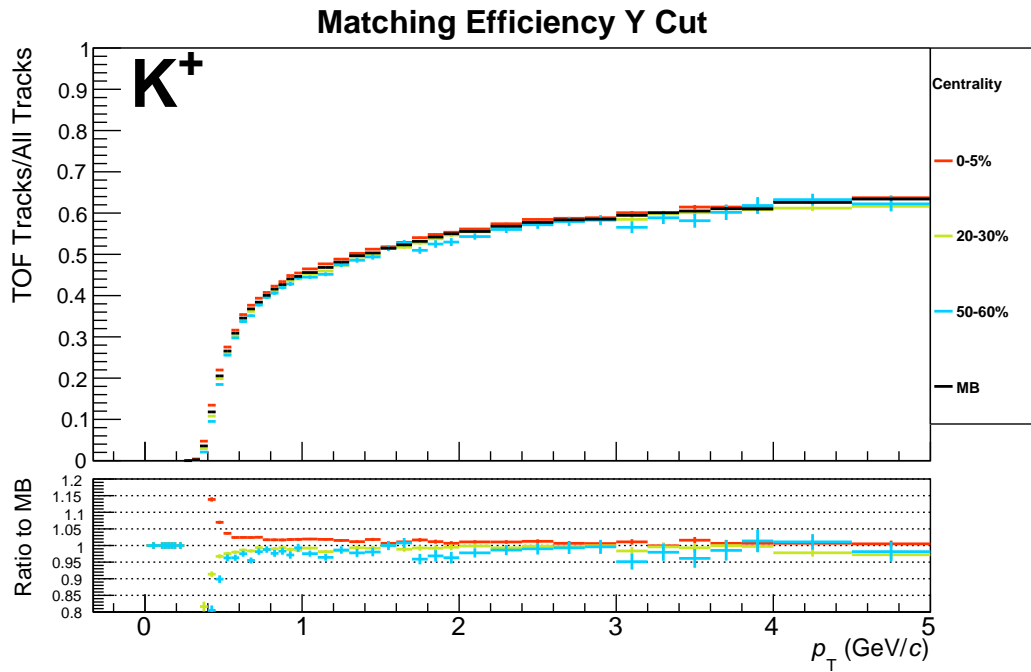


(a)

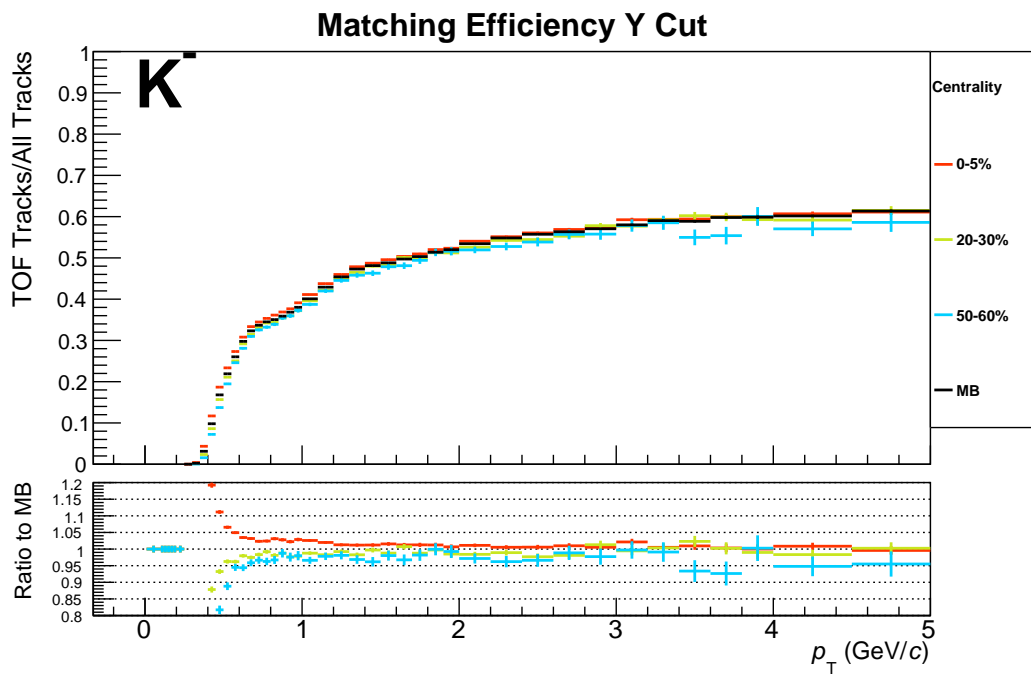


(b)

Fig. 6.27 Matching efficiency for both positive and negative π as measured in Pb–Pb collisions, in different centrality classes.

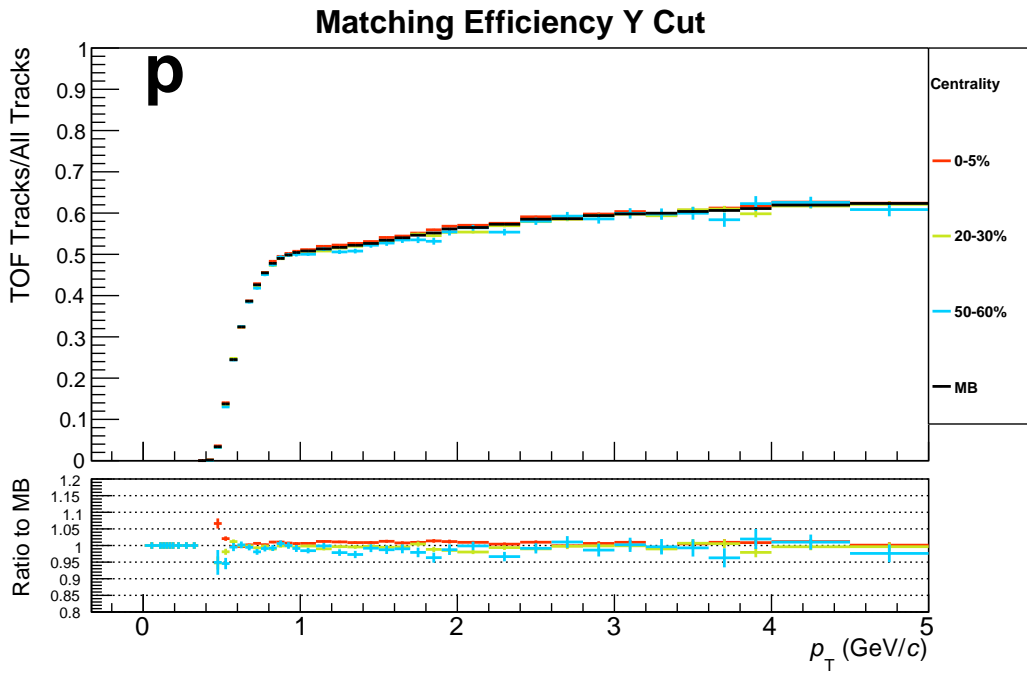


(a)

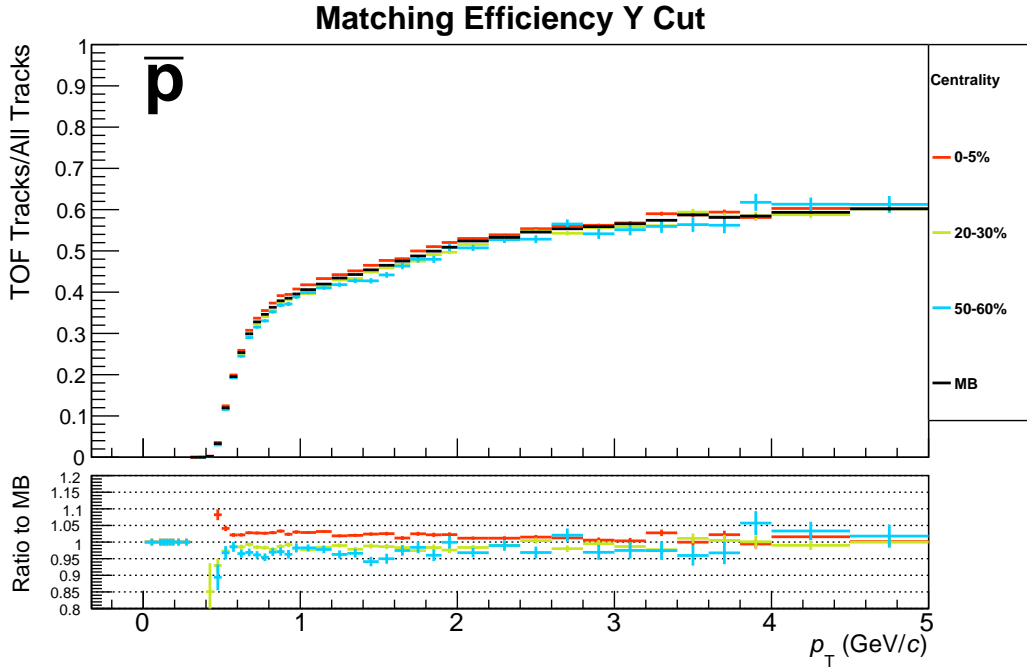


(b)

Fig. 6.28 Matching efficiency for both positive and negative K as measured in Pb–Pb collisions, in different centrality classes.



(a)



(b)

Fig. 6.29 Matching efficiency for both positive and negative p as measured in Pb–Pb collisions, in different centrality classes.

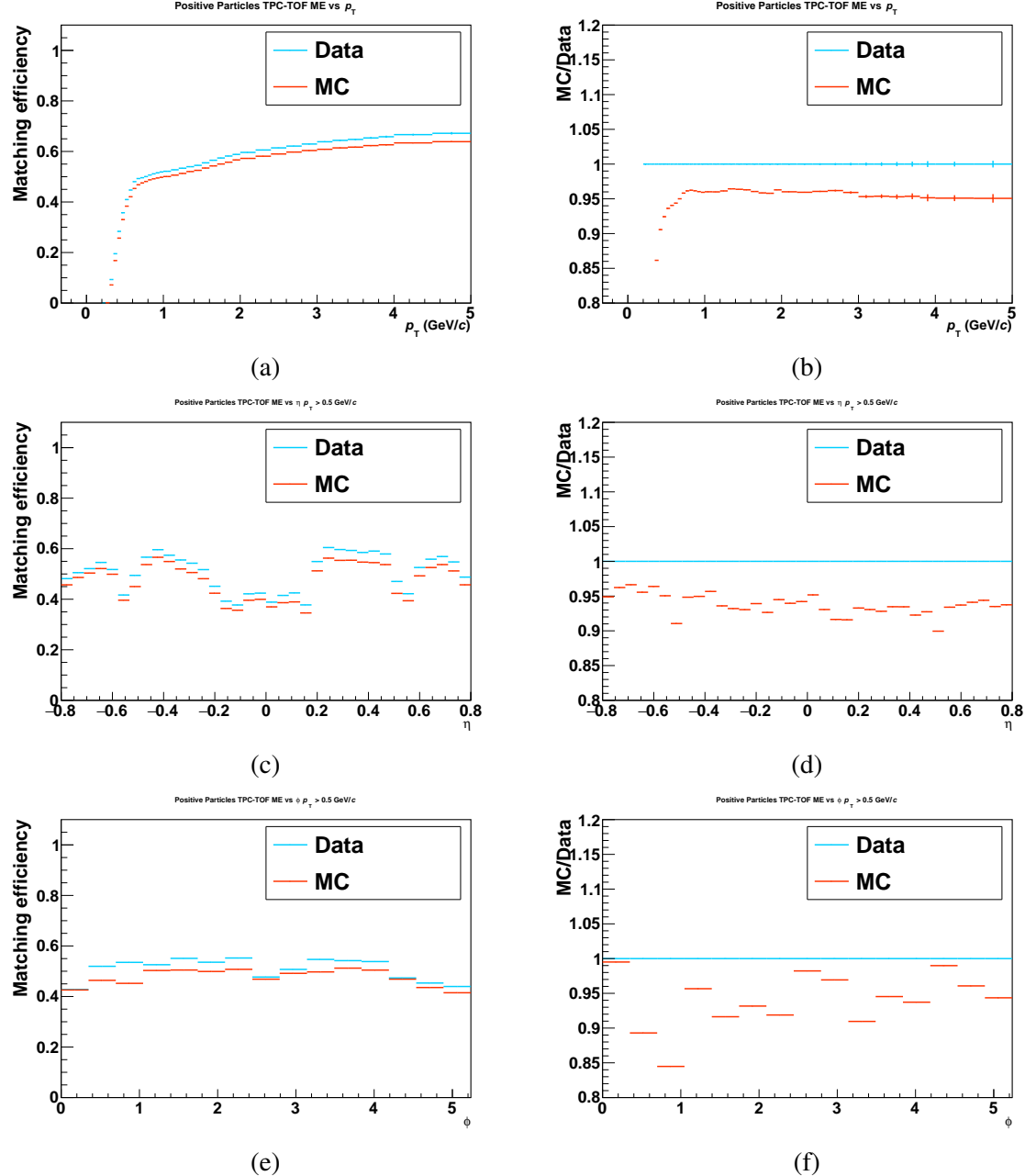


Fig. 6.30 Matching efficiency for unidentified positive and negative particles for data and Monte Carlo MB Pb-Pb collisions as a function of p_T , η and ϕ . The efficiency as a function of η and ϕ are computed without tracks with p_T lower than 0.5 GeV/c. Tracks used for the computation of the efficiency are selected and processed in the same way for real data and Monte Carlo. Track cuts used for selection are the same as for the ones used for the yield extraction.

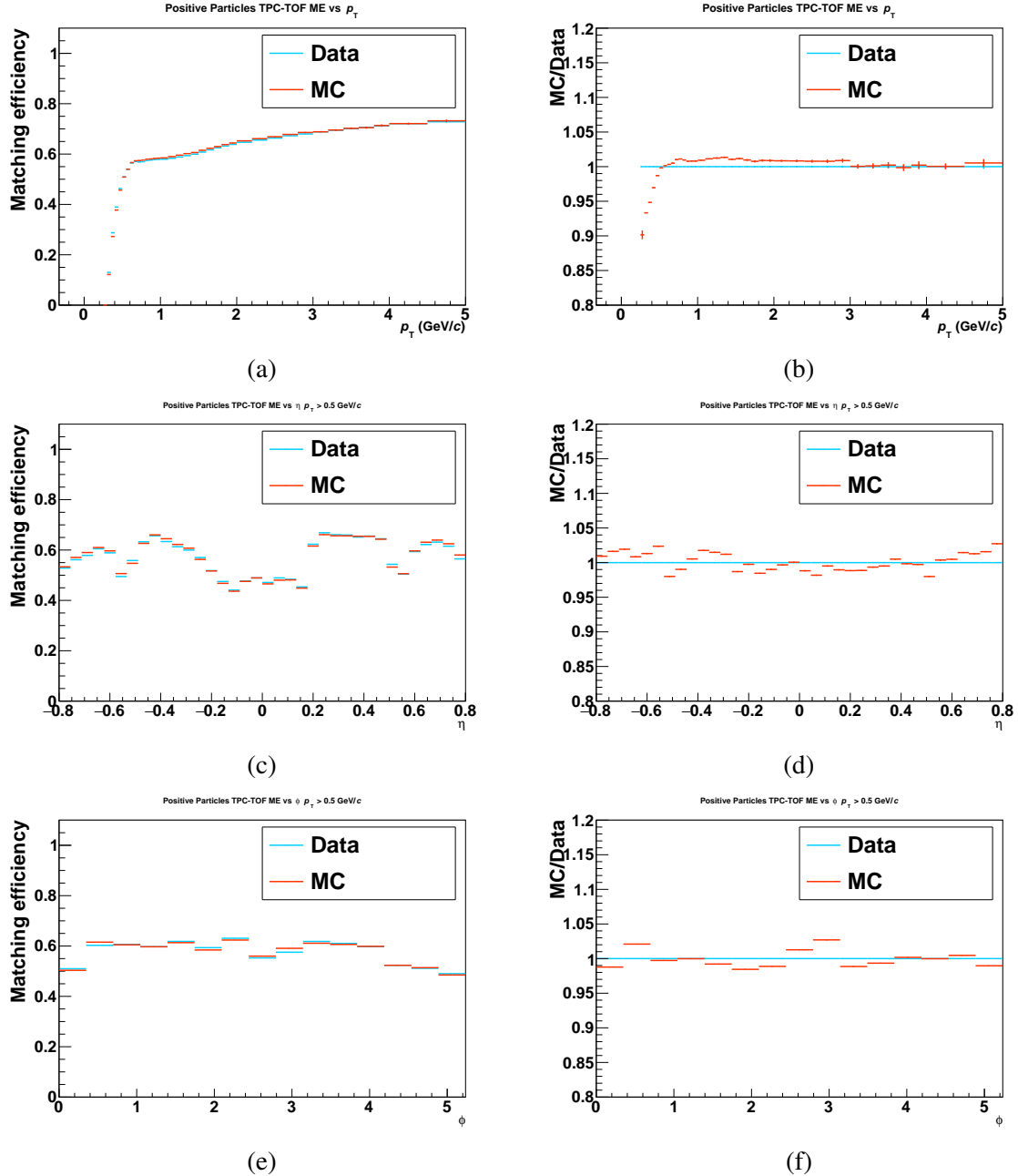


Fig. 6.31 Matching efficiency for unidentified positive and negative particles for data and Monte Carlo MB pp collisions as a function of p_T , η and ϕ . The efficiency as a function of η and ϕ are computed without tracks with p_T lower than 0.5 GeV/c. Tracks used for the computation of the efficiency are selected and processed in the same way for real data and Monte Carlo. Track cuts used for selection are the same as for the ones used for the yield extraction.

Matching efficiency for identified π , K and p

To further check the simulation and data agreement, the TPC-TOF matching efficiency for particles identified with the same procedure in both samples is compared. This efficiency is not used to correct the particle yields. A pure sample of pions, kaons and protons can be identified by reconstructing secondary vertices where they are produced. The matching efficiency is computed by identifying:

1. π^\pm , identified from K_S^0 decays
2. K^\pm , identified from ϕ decays
3. p and \bar{p} , identified from Λ and $\bar{\Lambda}$ decays

The resulting data-driven matching efficiency is defined as:

$$\epsilon_{\text{Matching}}^{ID} = \frac{\text{Tracks matched to TOF (PID from decay, } |y| < 0.5, |\eta| < 0.8\text{)}}{\text{Reconstructed tracks (PID from decay, } |y| < 0.5, |\eta| < 0.8\text{)}} \quad (6.18)$$

The $\epsilon_{\text{Matching}}^{ID}$ is defined by computing the particle yields with both samples of TPC tracks and TPC +TOF tracks. After repeating the procedure for each p_T bin, the spectra with the TOF requirement are divided by the ones obtained with global tracks.

The TPC-TOF matching efficiency computed in this way for both data and Monte Carlo is shown in Fig. 6.32 for Pb–Pb collisions and in Fig. 6.33 for pp collisions. The trends qualitatively reproduce the ones obtained for unidentified particles. The largest discrepancy is observed in the p_T intervals which are not used for the purpose of this analysis. The data/simulation values between 1 and 2 GeV/ c are used to extract the mean value of the ratio by performing a fit with a 0th-order polynomial function.

- For the Pb–Pb case, the ratio between the Monte Carlo and data strengthens the observation already reported as a function of φ , η and p_T for unidentified particles in Fig. 6.30: the discrepancy between data and the Monte Carlo ($\sim 5\%$) is confirmed to be independent on the particle species. The $\sim 5\%$ effect is due to a specific tune of the Monte Carlo simulation that corrects the TOF matching efficiency by this constant factor to take into account the track mismatch probability in Pb–Pb collisions. This value is shown to be excessive for the purpose of this analysis. For this reason, the corrected particle spectra will be scaled by the 5% factor and half of it will be accounted in the systematic uncertainty.

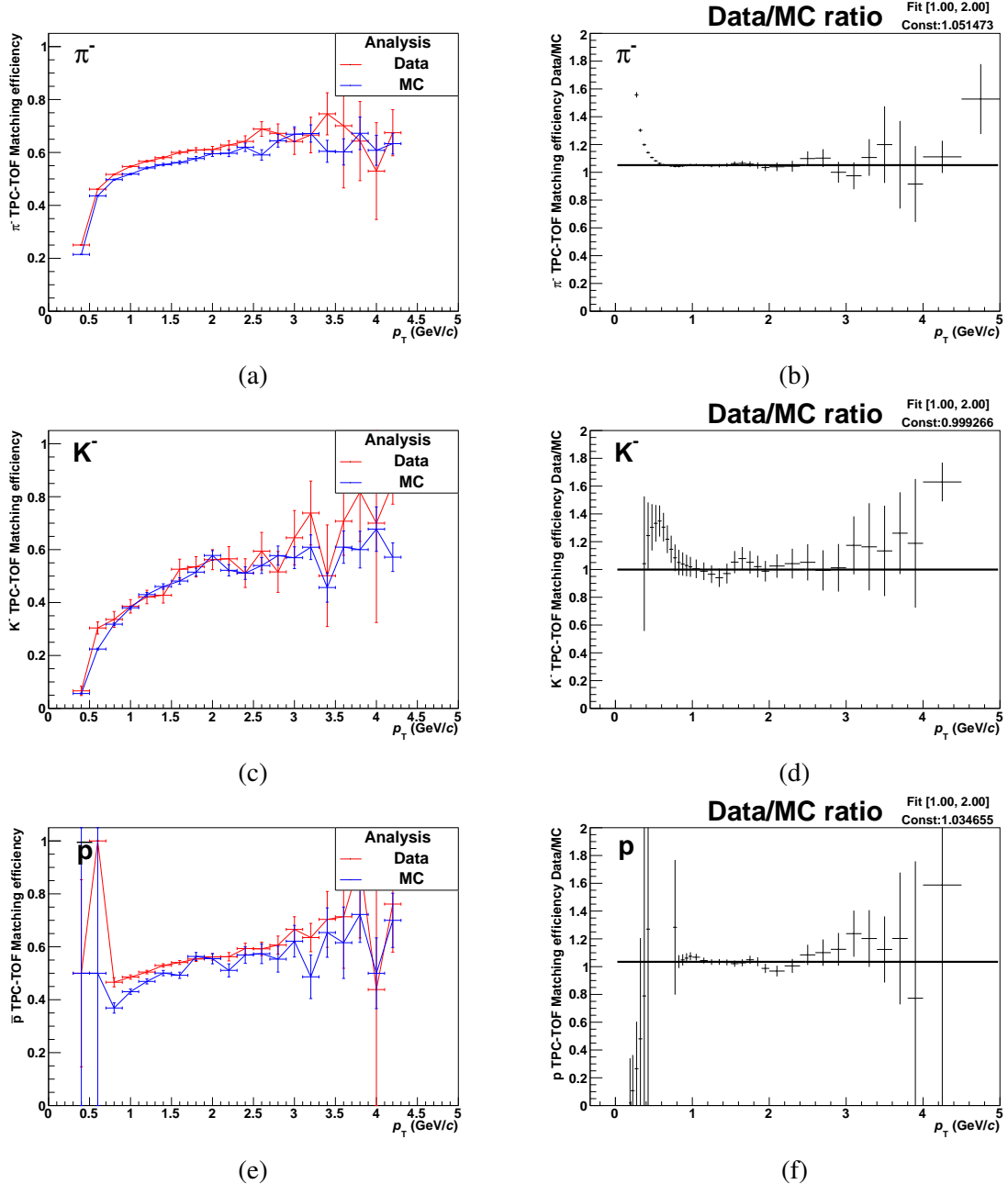


Fig. 6.32 Matching efficiency in Pb–Pb collisions at $\sqrt{s_{NN}} = 5.02$ TeV for identified π^\pm , K^\pm , p and \bar{p} in Monte Carlo and real Data as a function of p_T . Ratio between the matching efficiency computed in real Data and Monte Carlo in Pb–Pb collisions at $\sqrt{s_{NN}} = 5.02$ TeV for identified π^\pm , K^\pm , p and \bar{p} as a function of p_T . The values between 1 and 2 GeV/ c are used to extract the mean value of the ratio by performing a fit with a 0th-order polynomial function.

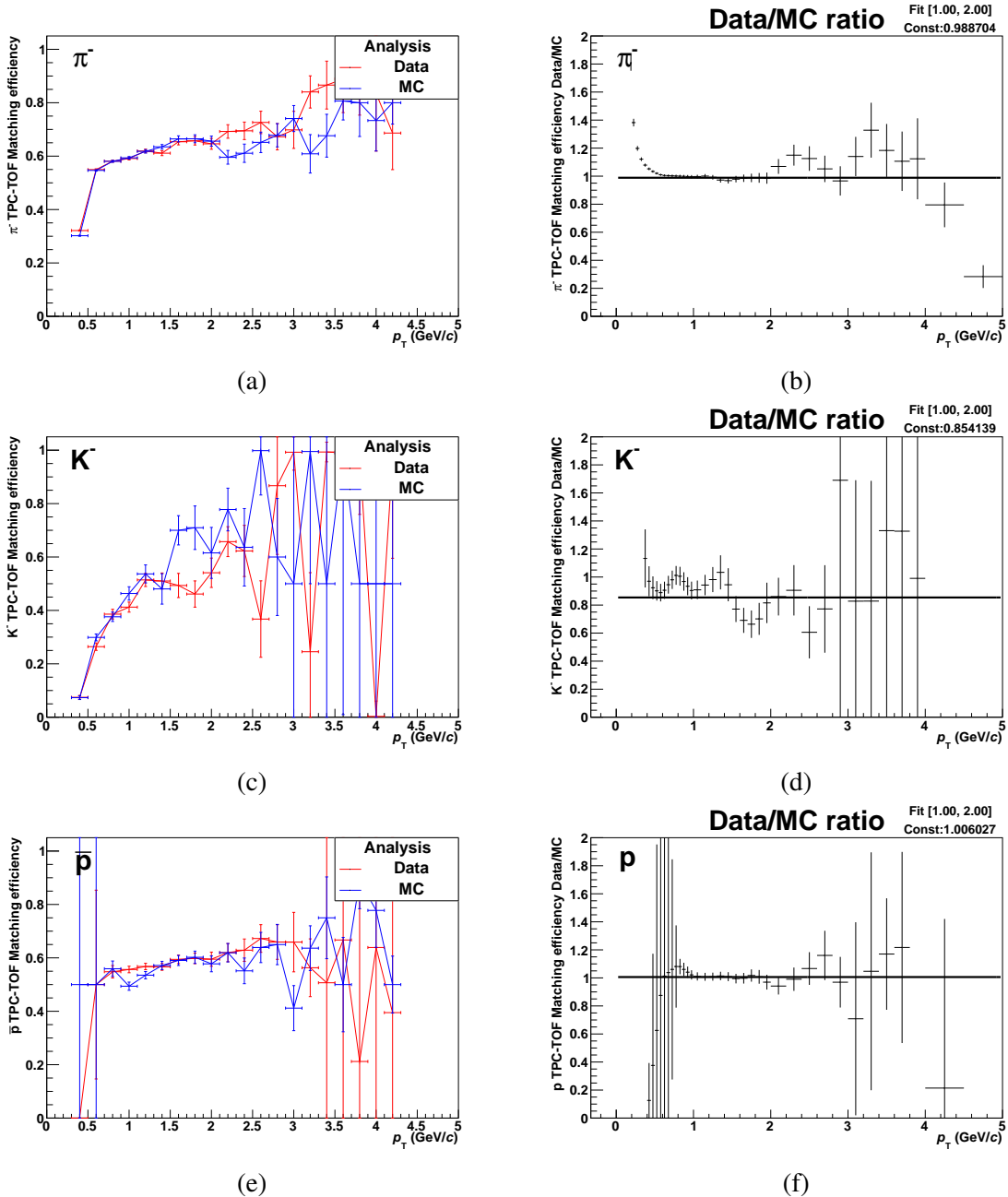


Fig. 6.33 Matching efficiency in pp collisions at $\sqrt{s} = 5.02$ TeV for identified π^\pm , K^\pm , p and \bar{p} in Monte Carlo and real Data as a function of p_T .

- In pp collisions, the agreement between the Monte Carlo and data is satisfactory. The comparison is considerably improved with respect to the Pb–Pb case.

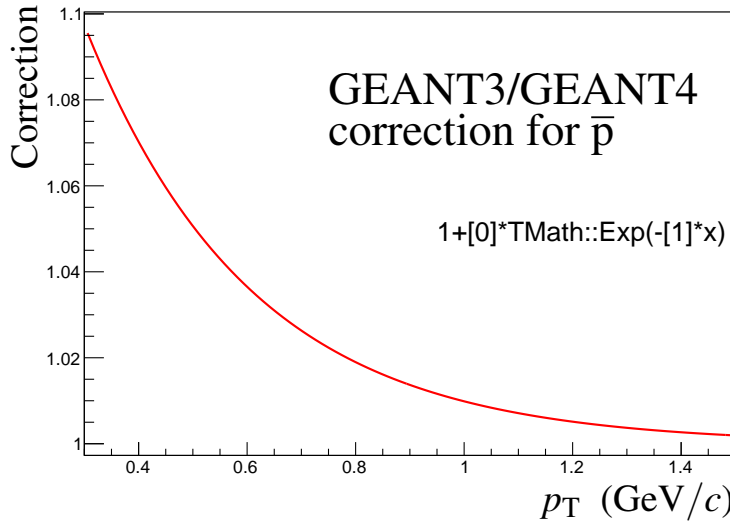


Fig. 6.34 Parameterization of the GEANT3/GEANT4 correction for \bar{p} as a function of p_T .

Transport code

The GEANT3 transport code, the default transport code used in this work, is known not to reproduce the cross sections relevant for the interactions of \bar{p} and K^- at low p_T with the material [144] thus leading to an inaccurate parameterization of the energy loss in material for these particles. To correct for this effect, the tracking efficiency obtained using the GEANT3 and GEANT4 transport codes are compared. The parametrized GEANT3/GEANT4 correction for \bar{p} is shown as a function of p_T in Fig. 6.34. The contribution of the GEANT3/GEANT4 correction is found to be non negligible for p_T lower than 1 GeV/ c .

The K^- instead, are corrected by using a dedicated simulation with the FLUKA [145] transport code, as in [40]. This evolution of this correction with p_T was expressed with the parameterization $0.97 + 0.011 \times p_T$.

Signal losses due to trigger selection

While the particle spectra in Pb–Pb collisions are normalized to the number of events accepted applying the criteria described in Section 6.1.3 for the analysis, the pp spectra are normalized to the number of inelastic events (INEL). This normalization requires an additional correction to take into account the losses of the signals due to the event selection. The correction is determined in the simulation as the ratio between the number of primary particles generated in INEL events and the number of particles selected by the event and trigger selections used for the analysis. The correction is determined for each particle species and reported in Fig. 6.35 as a function of p_T . The largest effect is observed at low p_T . The simulation used

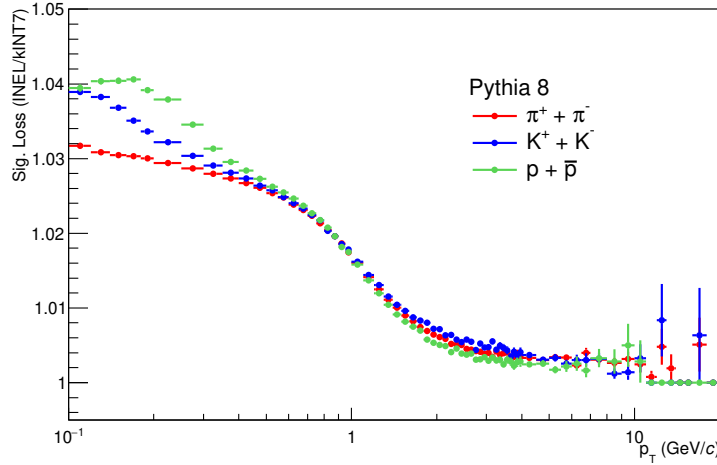


Fig. 6.35 Signal loss for π , K and p as computed from the MC simulation performed with the Pythia8 event generator.

to compute the correction was carried out with the Pythia8 event generator. The computed correction is applied to the combined spectra in the pp analysis to correctly take into account the signal loss due to event selection.

6.4 Systematic uncertainties

The analysis of identified particle spectra is affected by systematic uncertainties associated with five sources:

1. Event and track selection: effect of the selection criteria for tracks and events.
2. Particle identification: related to the yield extraction and parameterization of the TOF signal.
3. Feed-down evaluation: due to the procedure for the feed-down estimation.
4. TPC-TOF matching efficiency: accounting for the different matching efficiency in data and simulation.
5. Material budget: considering the uncertainty on the knowledge of the material budget of the detector

Details on each source as well as the procedure to estimate each contribution to the total uncertainty are given in this section.

6.4.1 Data sample and track selection

In order to evaluate the systematic uncertainties related to track selection the whole analysis chain starting from the extraction of uncorrected yields up to the final corrected spectra was repeated with different track samples. The track selection criteria described in Section 6.1.4 were varied as reported in Table 6.2.

The corrected spectra are obtained with the modified cuts and compared to the default case. This procedure requires the determination of both raw yields and corrections in each variation. The comparison of the corrected spectra obtained with the modified selection criteria is reported in Fig. 6.36 as evaluated in MB Pb–Pb collisions. The effect of the cut variation on the pp data is reported in Appendix F. The relative systematic uncertainty is evaluated in each p_T interval by taking the maximum deviation from unity. This uncertainty is assumed independent on the momentum.

Selection criteria	Modified values	Default value
TPC crossed rows	60; 80	70
Track Global χ^2 per NDF	5; 3	4
Track DCA _z	3 cm; 1 cm	2 cm
Geometrical Cut	No Geometrical cut; $\alpha = 130 \text{ cm}$, $\beta = 3.0 \text{ cm} \cdot c/\text{GeV}$, $\gamma = 1.5$ in Eq. 6.1 and $I_{\text{TPC}} \times 85\% > \text{TPC crossed rows}$ and $I_{\text{TPC}} \times 70\% > \text{TPC clusters}$	$\alpha = 130 \text{ cm}$, $\beta = 2.0 \text{ cm} \cdot c/\text{GeV}$, $\gamma = 1.5$ in Eq. 6.1

Table 6.2 Summary of the cut variation used to select the track sample.

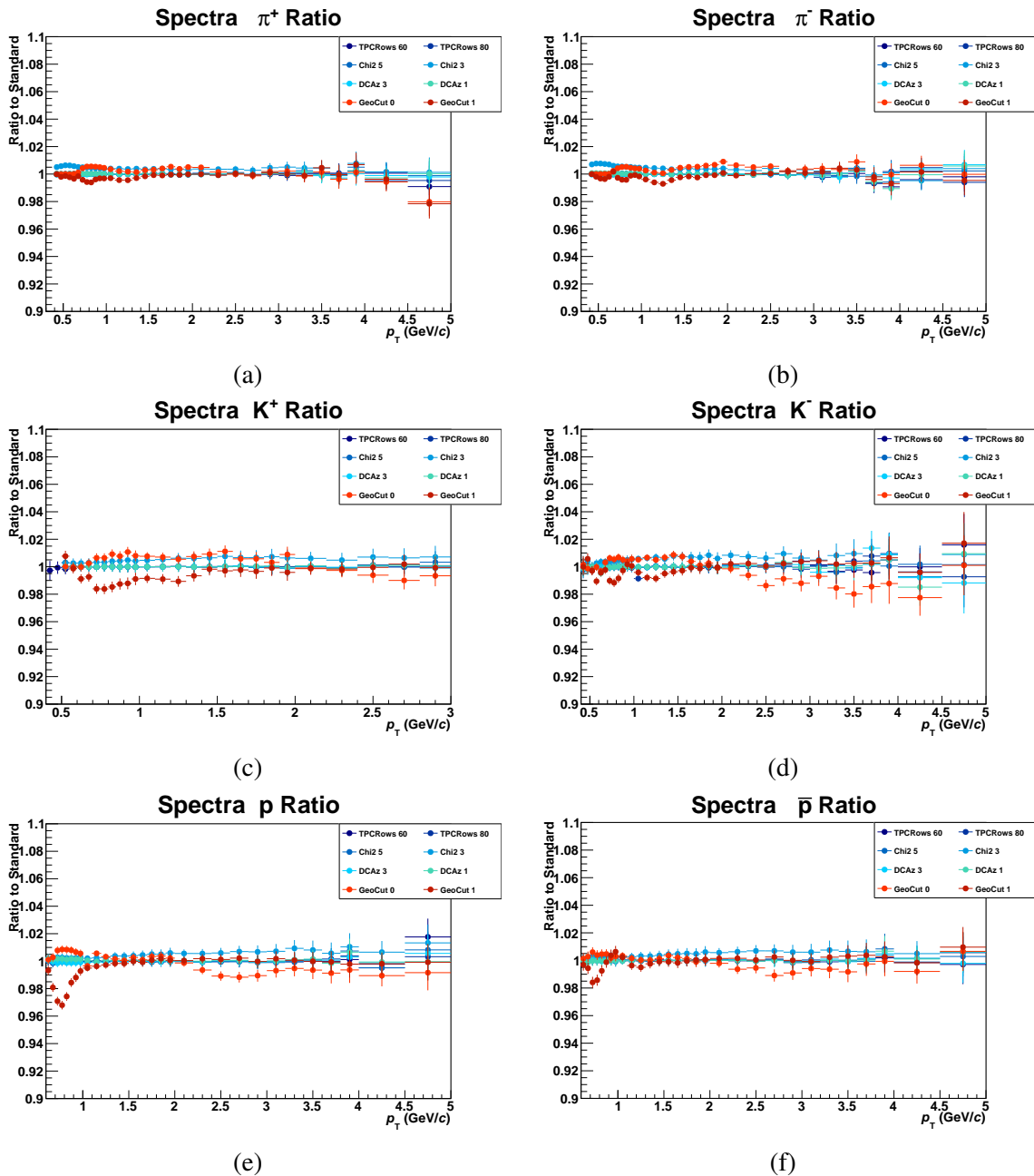


Fig. 6.36 Ratio between the spectra obtained with modified track selection criteria (as in Table 6.2) relative to the default analysis for MB Pb–Pb collisions.

6.4.2 Particle identification

The systematic uncertainty related to the PID were estimated by using different assumptions for the generation of the signal templates, i.e. by varying the TOF response parameterization with respect to the default case described in Section 6.2. The σ and τ parameters are varied by $\pm 10\%$ to cover all possible cases and study the effect on the measured yield.

The raw spectra are obtained with the modified signal templates and compared to the default case, as reported in Fig. 6.37 for MB Pb–Pb collisions and in Appendix G for pp collisions. Also in this case, the relative systematic uncertainty is determined in each p_T interval by taking the maximum deviation from unity. The deviations at low momenta (up to 2 GeV/ c) are averaged to obtain the uncertainty.

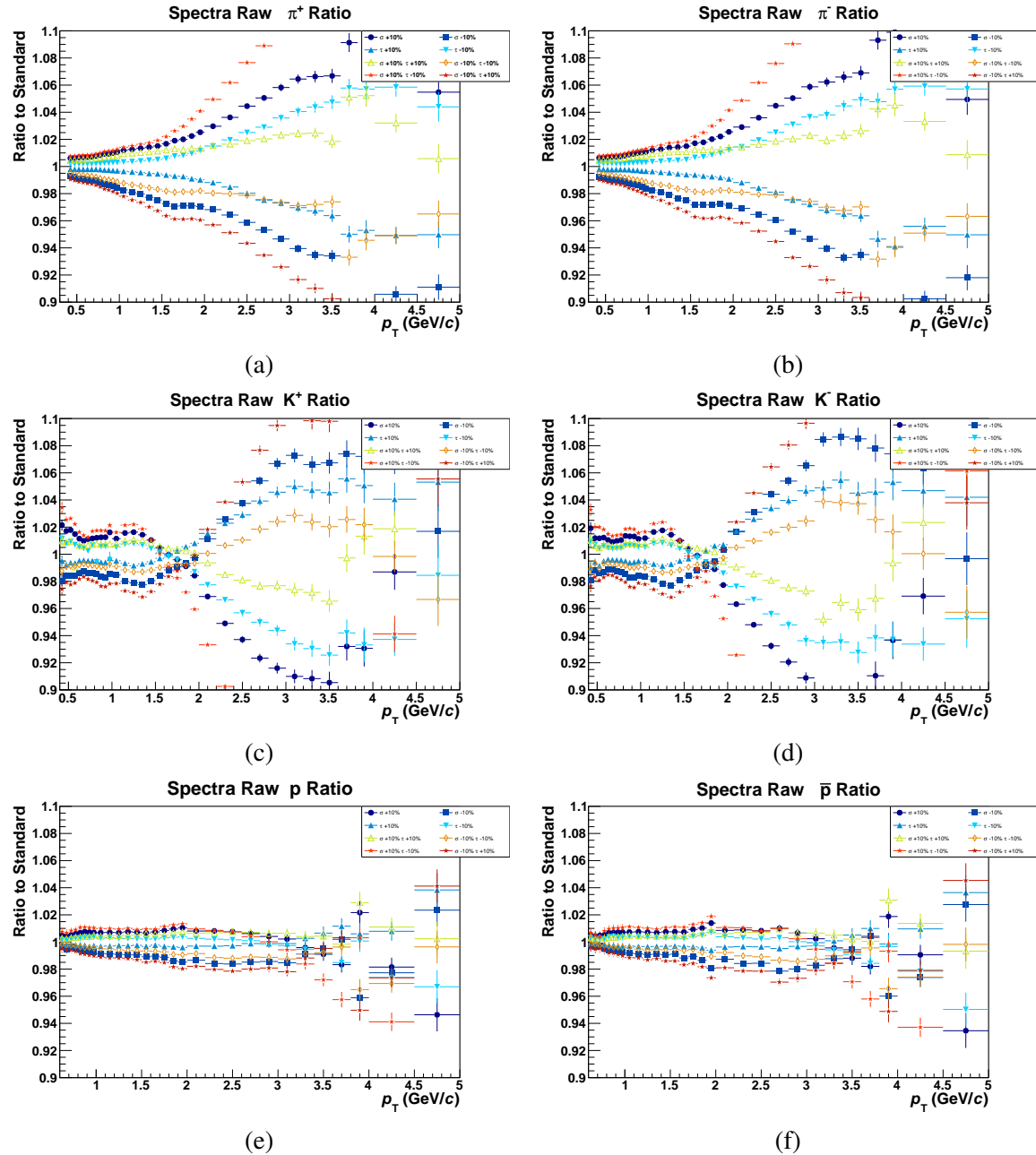


Fig. 6.37 Ratio between the spectra obtained with modified TOF response parameters and the default one for MB Pb–Pb collisions.

6.4.3 Feed-down and fraction of primary particles

The systematic uncertainty associated with the feed-down correction was estimated by changing the technique used for the extraction of the feed-down correction. It was discussed that the DCA_{xy} is the variable used to apply selection for primary particles. On top of this, the amount of feed-down we correct for is independent on the relative particle composition. The uncertainty on the feed-down was considered separately with respect to the variation of the track cuts used for the selection of primary particles. This choice is justified by the fact that this source of systematic uncertainty is intrinsic in the spectra measurement procedure, independently on the cuts used to select tracks. For the evaluation of the uncertainty the primary fraction obtained with the *TFractionFitter* and the one obtained with *RooFit* utilities were compared as it is shown in Fig. 6.38 for Pb–Pb and in Fig. 6.39 for pp. The difference between the two methods is taken as the systematic uncertainty associated to the feed-down corrections. Interestingly, the systematic uncertainty observed in pp collisions is smaller than the one in Pb–Pb. This is related to the magnitude of the overall correction obtained for the two systems, which is affected by the different mechanisms of particle production.

6.4.4 TPC-TOF matching

The requirement of a match between the track and a TOF cluster imposes to consider an additional source of systematic uncertainty i.e. the one related to the TPC-TOF matching efficiency and how this is well reproduced in the simulation used to extract efficiency corrections. The comparison of Monte Carlo simulation and data, is extensively described in Section 6.3.2 for unidentified particles and identified π , K and p . The ratio between simulation and data shown in Fig. 6.32 and in Fig. 6.33 is taken as the systematic uncertainty related to the TPC-TOF matching efficiency. The assigned systematic uncertainty is obtained by averaging the deviation from unity in the 1-2 GeV/ c interval.

6.4.5 Material budget

The uncertainty on the amount of material implemented in the description of the geometry of the ALICE detector implemented in the Monte Carlo simulation and considered by the transport code affects the identified particle measurement due to absorption, hadronic interactions and energy loss. This contribution is evaluated by computing the efficiency corrections (both tracking and TPC-TOF matching) in dedicated MC simulations. That use an increased or decreased material budget ($\pm 10\%$). In Fig. 6.40 and Fig. 6.41 the corrections obtained with the modified material budget are compared to the one extracted with the

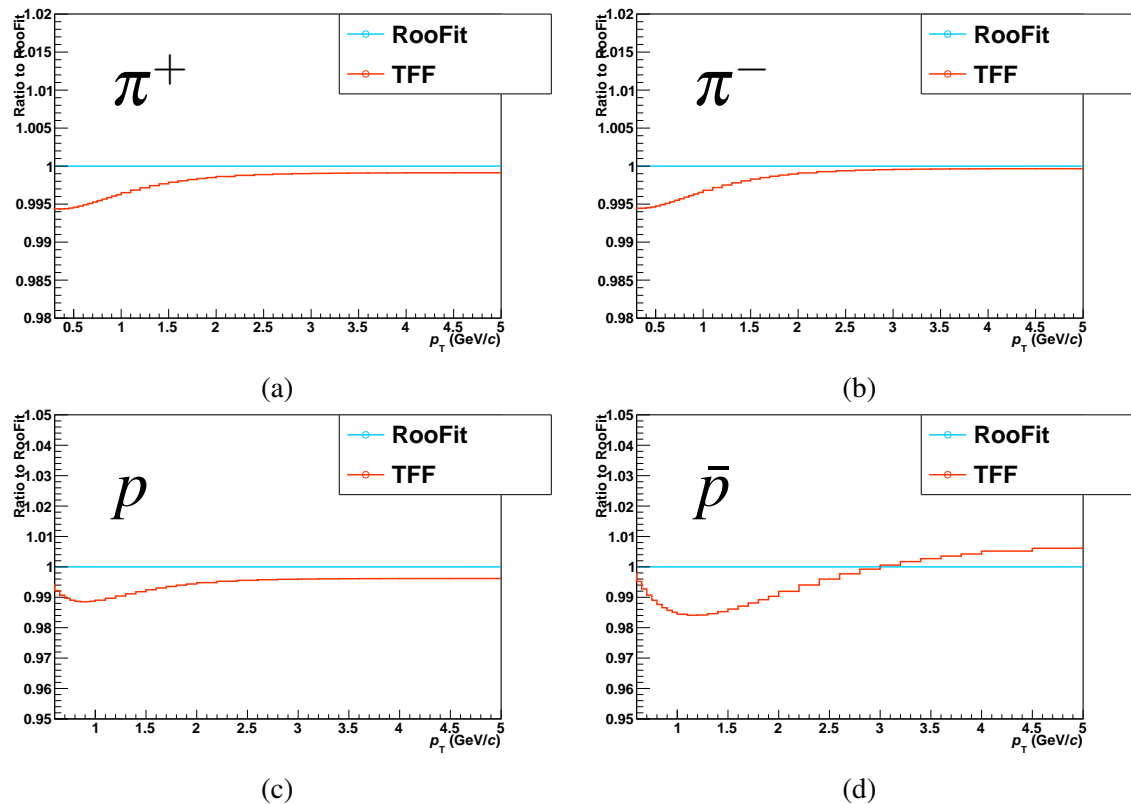


Fig. 6.38 Ratio between the primary particle fraction obtained with the *TFractionFitter* (TFF) utility of Root [111] and the one obtained with *RooFit* [141] in MB Pb–Pb collisions for (a) π^+ , (b) π^- , (c) p and (d) \bar{p} .

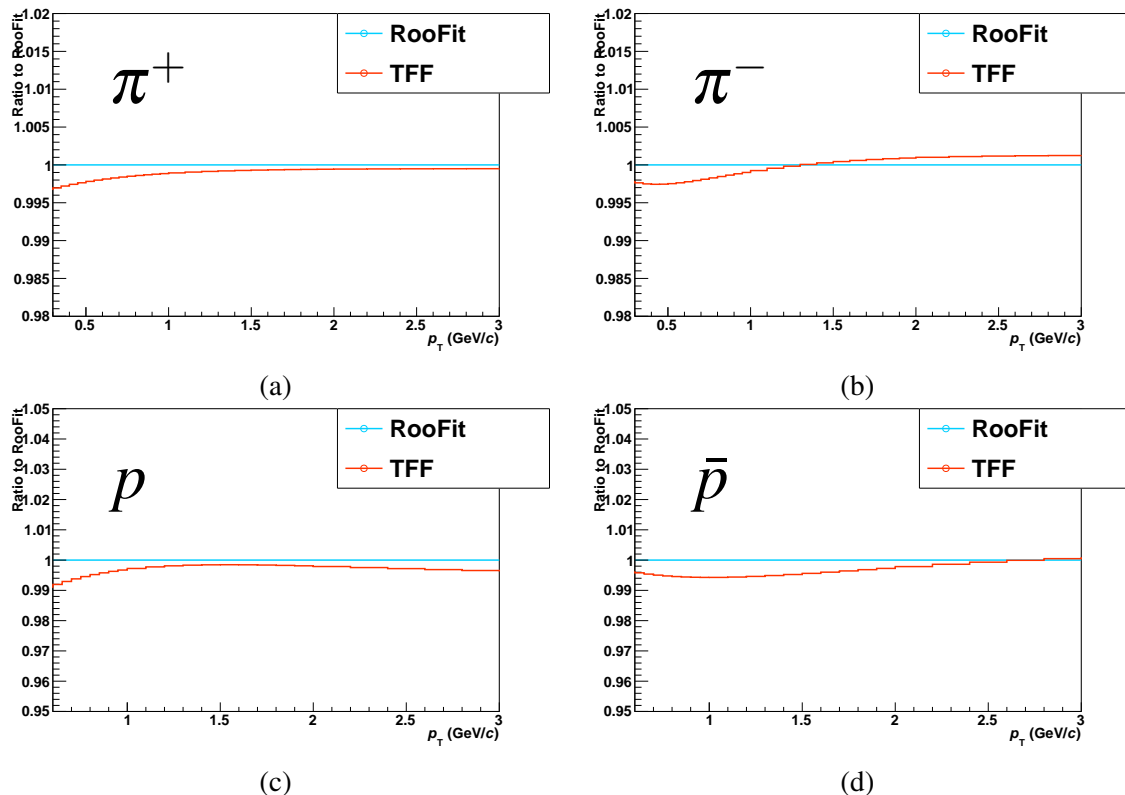


Fig. 6.39 Ratio between the primary particle fraction obtained with the *TFractionFitter* (TFF) utility of Root [111] and the one obtained with *RooFit* [141] in MB pp collisions for (a) π^+ , (b) π^- , (c) p and (d) \bar{p} .

standard parameterization and the maximum deviation from unity is assigned as a systematic uncertainty. The maximum variation for the tracking and matching efficiency is shown as a function of p_T in Fig. 6.42.

This uncertainty is the same for the pp and Pb–Pb samples and it is independent on the event multiplicity.

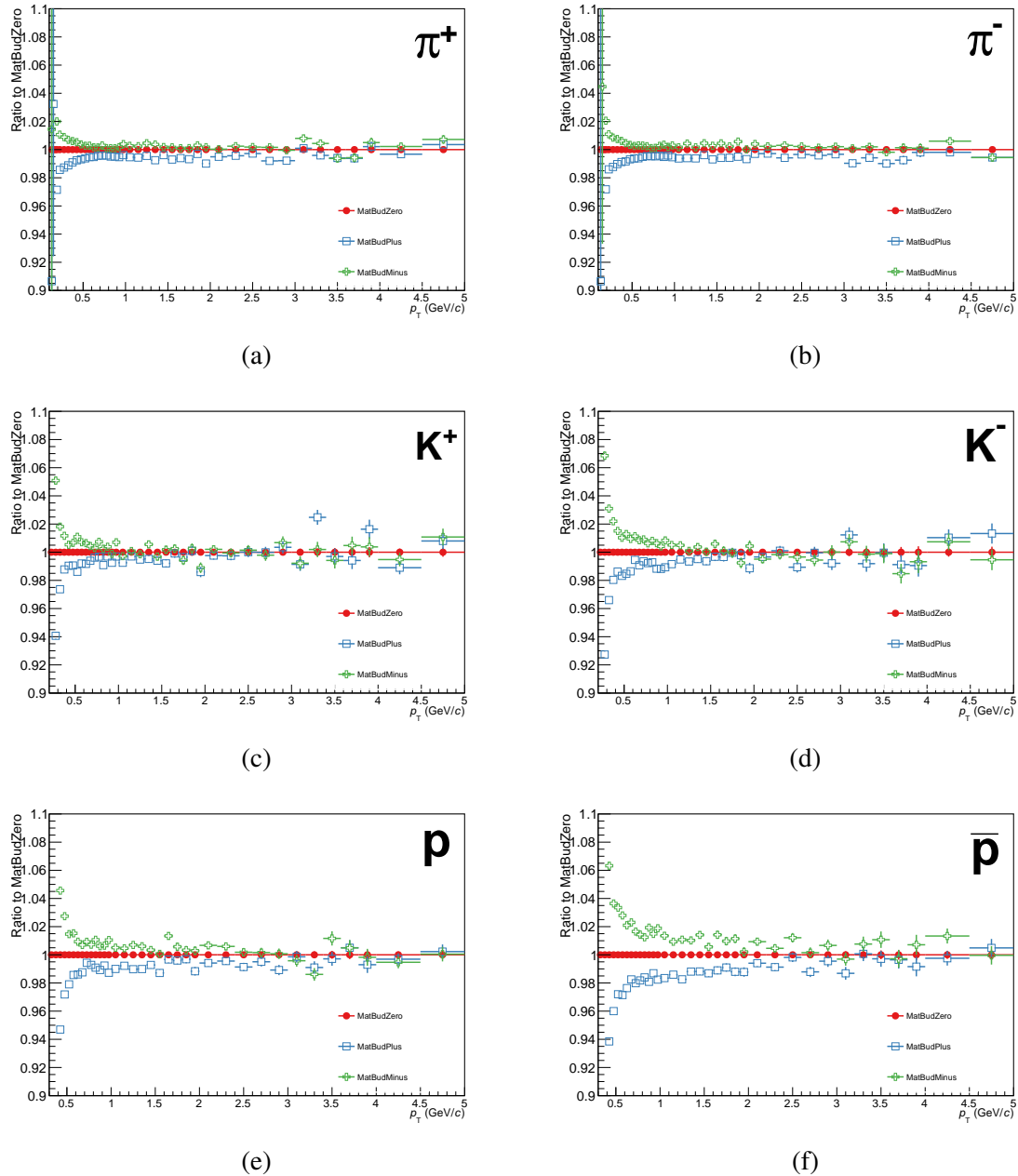


Fig. 6.40 Ratio to the default case of the tracking efficiency as obtained in simulations with modified material budget.

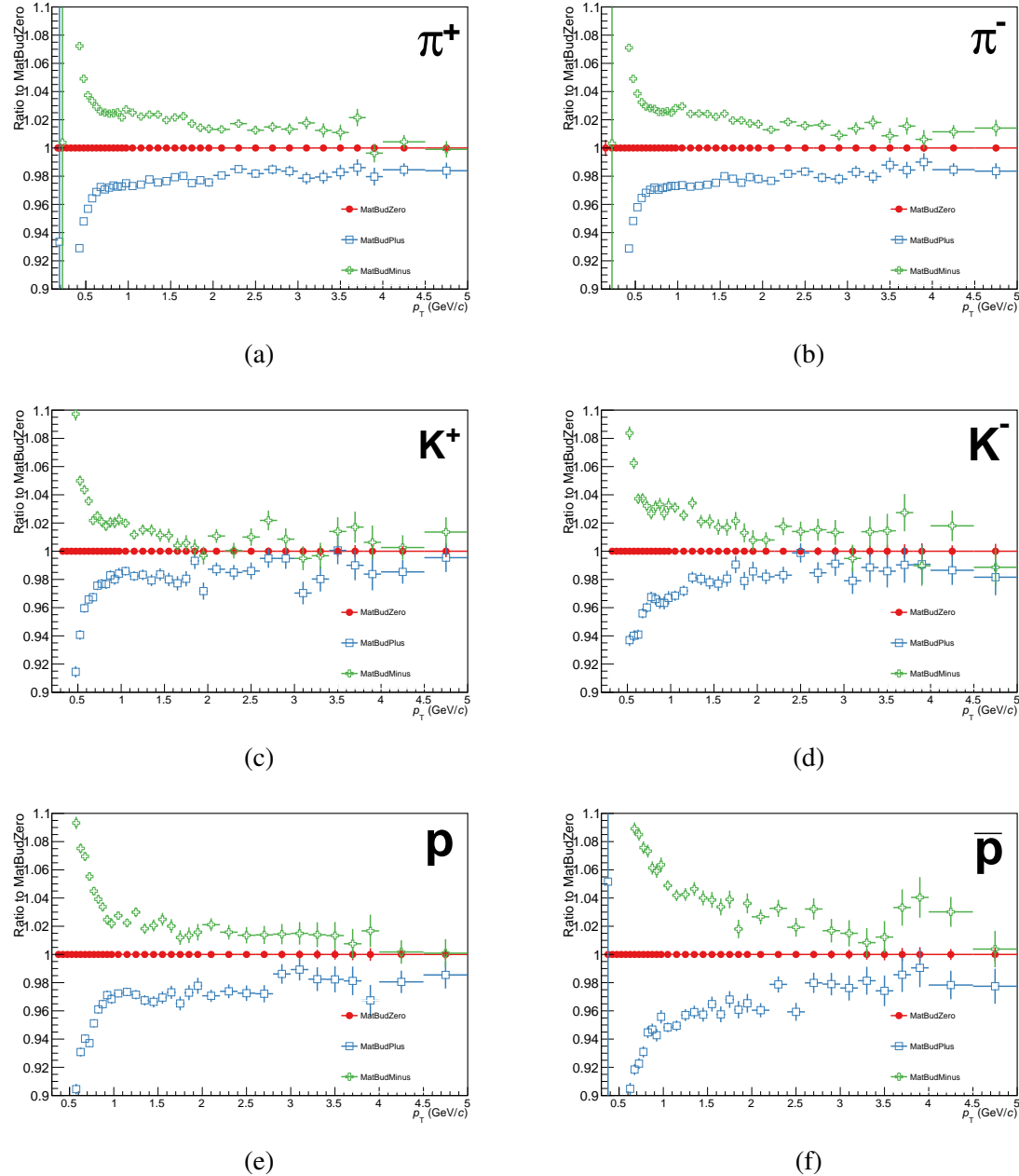


Fig. 6.41 Ratio to the default case of the TPC-TOF matching efficiency as obtained in three simulations with modified material budget.

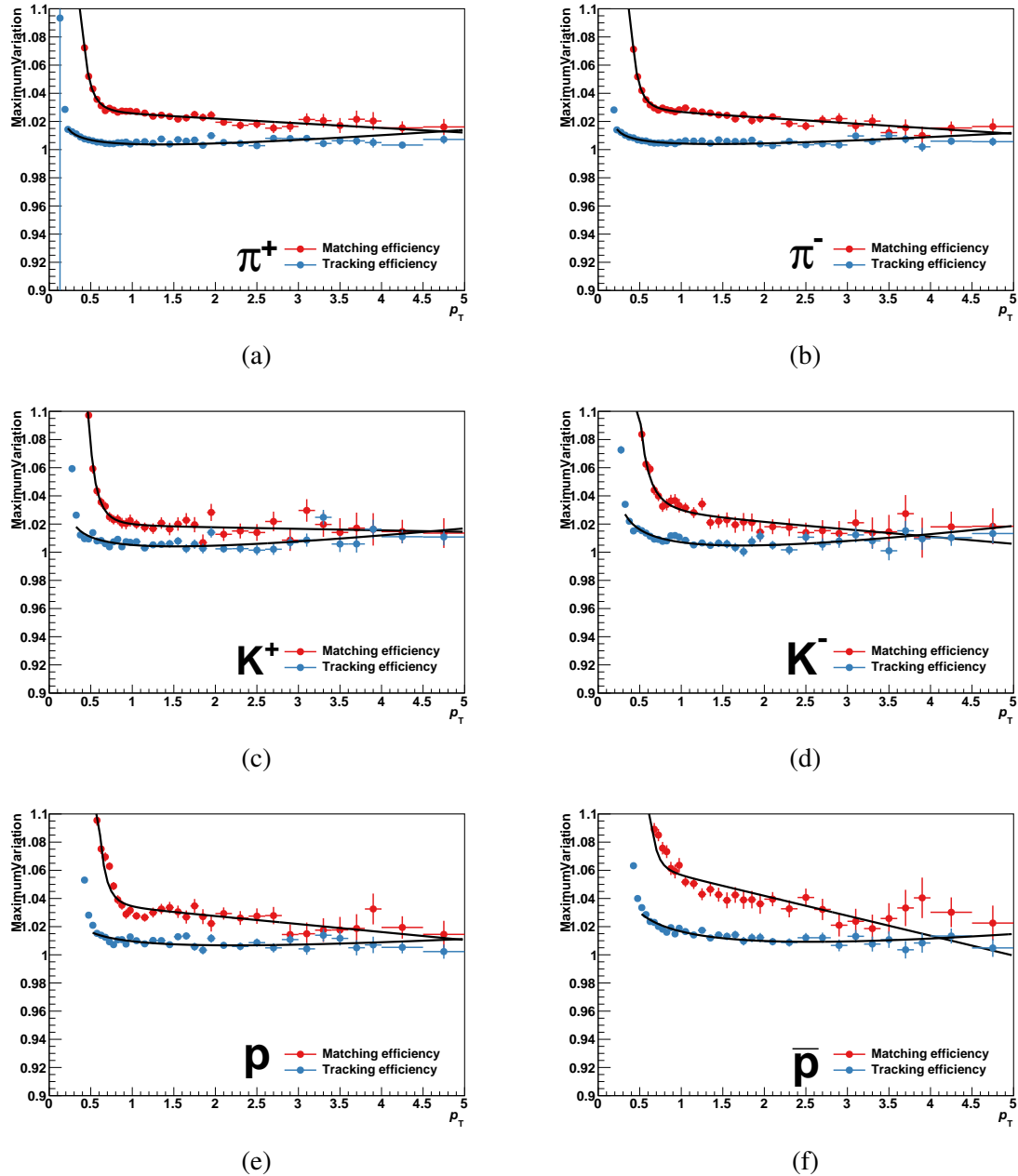


Fig. 6.42 Maximum deviation from unity, obtained from the comparison of the tracking and matching efficiencies, evaluated in simulations with modified material budget.

6.4.6 Total systematic uncertainty

The total systematic uncertainty is evaluated by summing all discussed contributions in quadrature. The systematic uncertainties for the π , K and p spectra are reported in Fig. 6.43 as computed in MB Pb–Pb collisions. The systematic uncertainty evaluated in pp collisions is reported in Appendix H.

The same analysis technique is used for the evaluation of the systematic uncertainty in the particle ratios. In this case, to take into account the possible cancellation of correlated effects, the estimation of the systematic uncertainty is carried out on the ratios.

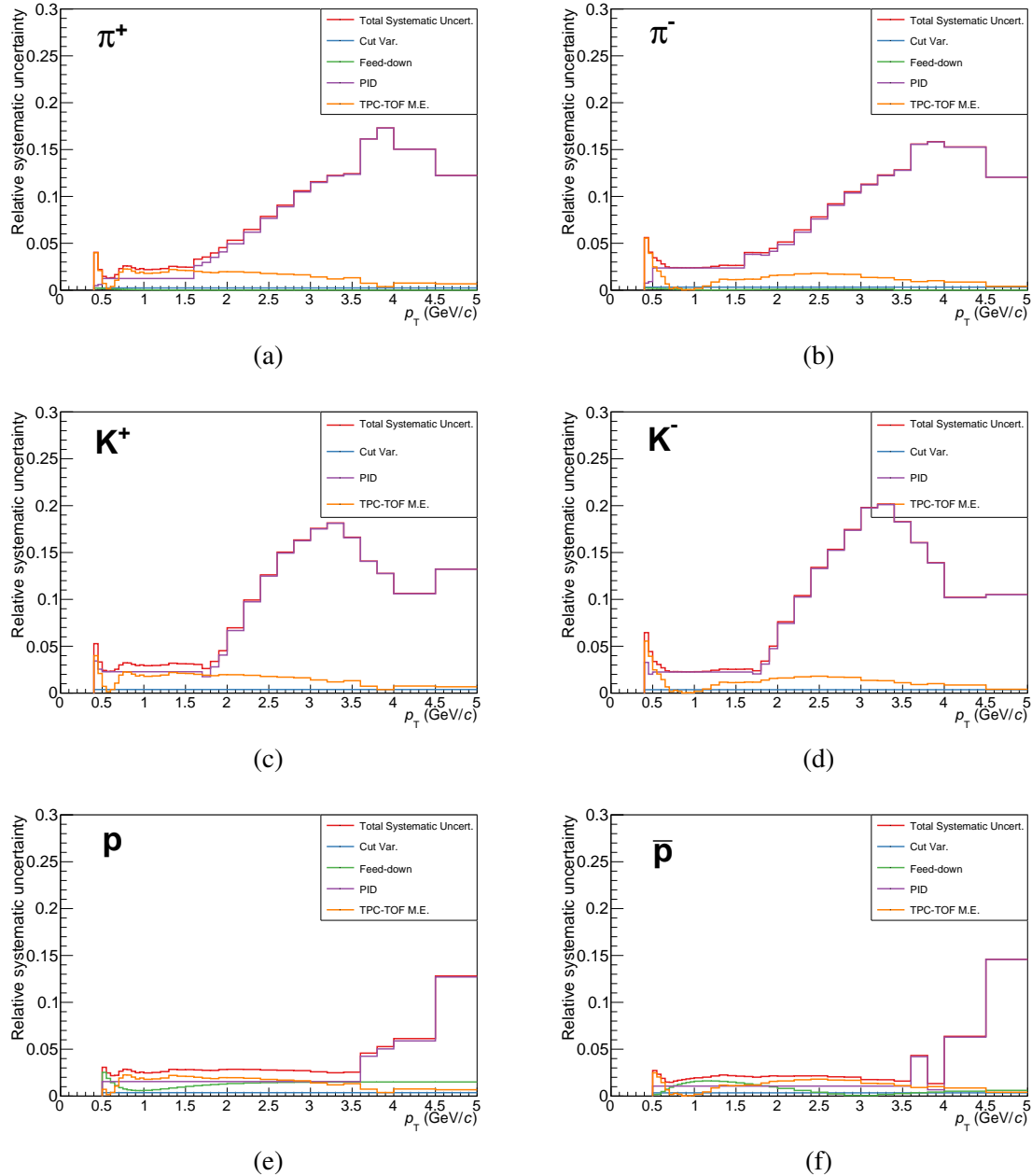


Fig. 6.43 Systematic uncertainty on the particle spectra as measured in Pb–Pb collisions at $\sqrt{s_{NN}} = 5.02$ TeV.

Chapter 7

Results and discussion

In this chapter, the results on π , K and p production in pp and Pb–Pb collisions at $\sqrt{s_{\text{NN}}} = 5.02$ TeV are presented. The results of the analysis based on TOF PID, described in Chapter 6, are combined with the analyses performed using identification with ITS, TPC, HMPID and Kinks analyses to extend the p_{T} reach of the measured spectra. Theoretical models are compared to data to gain insights into the particle production mechanism and to determine the microscopic properties of the medium created in the collisions. Results are discussed as a function of the centrality of the collision in Pb–Pb and compared to measurements at lower collision energy.

7.1 Transverse momentum distributions of π , K and p measured with the TOF detector

The raw yields of each particle species are normalized to the number of analyzed events and corrected for efficiencies and feed-down contamination, as discussed in Section 6.2 in order to obtain the particle p_{T} spectra. The corrected spectra can be expressed as:

$$\frac{d^2N}{dp_{\text{T}}dy} = \frac{1}{N_{Ev}} \cdot \frac{d^2N}{dp_{\text{T}}dy} \Big|_{Raw} \times \varepsilon_{\text{Tracking}} \times \varepsilon_{\text{Matching}} \times f_{\text{Primaries}} \times \varepsilon_{\text{Extra}} \quad (7.1)$$

The term $\varepsilon_{\text{Extra}}$ is used to take into account the signal loss due to the trigger selection in pp and is not needed in Pb–Pb collisions. Since tracking efficiencies do not depend on the centrality, these corrections are computed from events in the 0-90% class. This is not the case for the matching efficiency and feed-down correction which are computed and applied to the spectra for each centrality separately.

The results on π , K and p production obtained with the PID information from the TOF detector are reported as a function of p_T in Fig. 7.1 for Pb–Pb collisions at different centralities and Minimum Bias pp collisions. The comparison of the spectral shapes shows that in central collisions spectra are harder, this effect is more evident for heavier particles such as protons. The spectra measured in pp collisions exhibits a different spectral shape with respect to the Pb–Pb case.

The ratio between positive and negative particles is computed as a function of p_T . Within the systematic uncertainties, the ratios are in agreement with unity in the p_T range considered for the combination.

7.2 Combined π , K and p spectra

The results obtained with the TOF analysis are combined with the transverse momentum spectra of π , K and p measured with the ITS, TPC and HMPID detectors to extend the p_T range of the spectra. The results of the Kinks analysis are also used in the combination of the kaon spectra.

The combination of the particle spectra is performed by computing the weighted average of the data points for all the analyses in each the p_T interval:

$$\left. \frac{d^2N}{dp_T dy} \right|_{Combined} = \frac{\sum_{An} w_{An} \cdot \frac{d^2N}{dp_T dy}(An)}{\sum_{An} w_{An}} \quad (7.2)$$

The weight for the result of the single analysis, w_{An} , includes the contribution of the systematic and statistical uncertainty. The systematic and statistical uncertainties on the combined measurement are also obtained by averaging on the different analyses. The systematic uncertainties that are in common among several analyses are considered only once in the combination. This precaution allows for avoiding the double counting of uncertainties, such as the one related to the material budget, in the combined spectra.

The agreement of the different analyses is verified during the combination process. An example of such comparison is shown for central Pb–Pb collisions in Fig. 7.3. The figure shows the ratio of each spectra used for the combination, scaled by the combined spectra. Systematic and statistical uncertainties are reported. All analyses are in agreement with the combined result.

The results are obtained by combining the outcome from the single analyses in the p_T intervals reported in Table 7.1 for Pb–Pb collisions and in Table 7.2 for pp collisions.

The combined spectra, measured in Pb–Pb and pp collisions at $\sqrt{s_{NN}} = 5.02$ TeV are shown in Fig. 7.4 and Fig. 7.5 respectively.

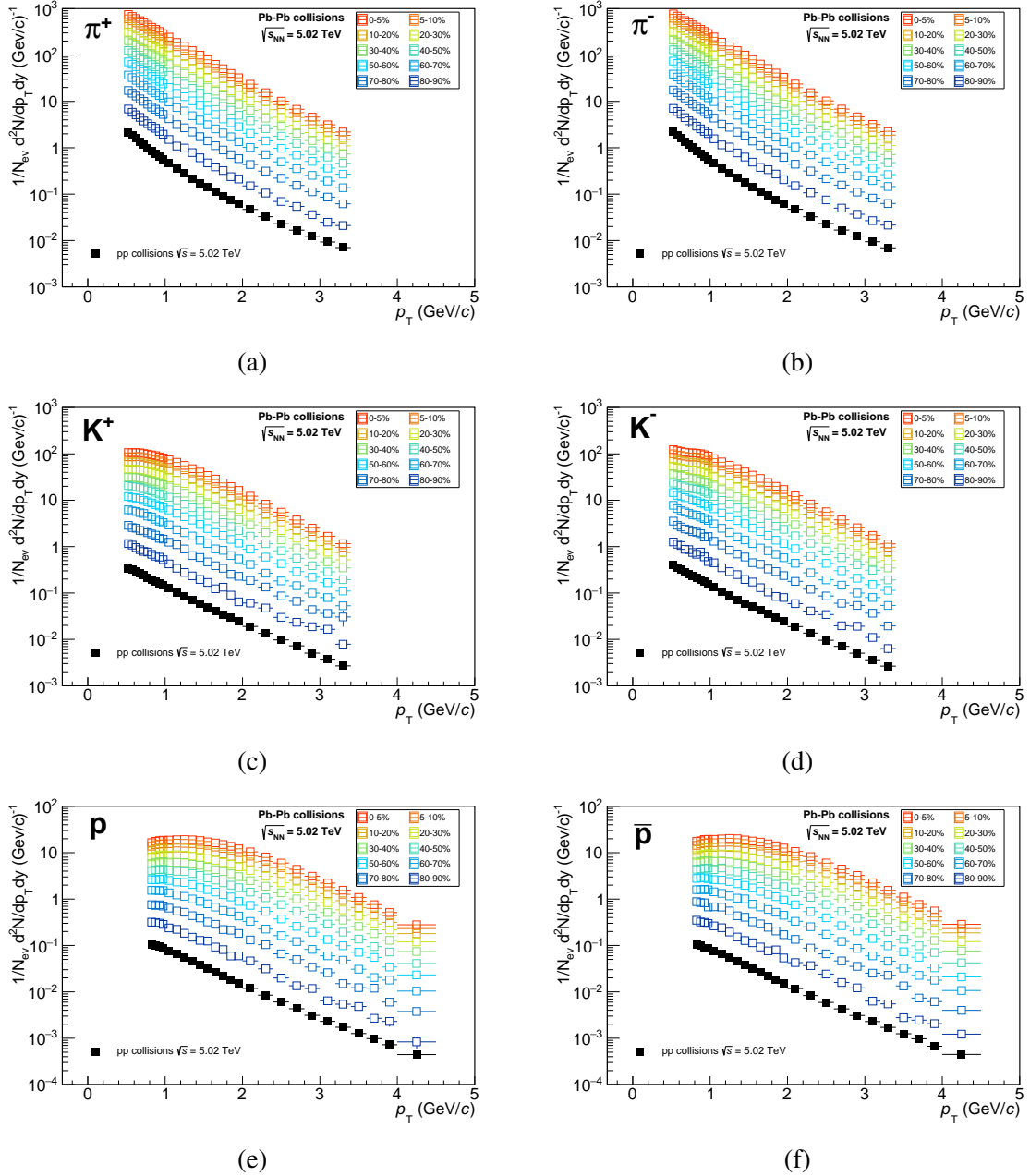


Fig. 7.1 Spectra for π^\pm , K^\pm , p and \bar{p} as obtained in Pb–Pb collisions at $\sqrt{s_{\text{NN}}} = 5.02 \text{ TeV}$ for the different centrality classes as reported in Section 6.1.3 and MB pp collisions.

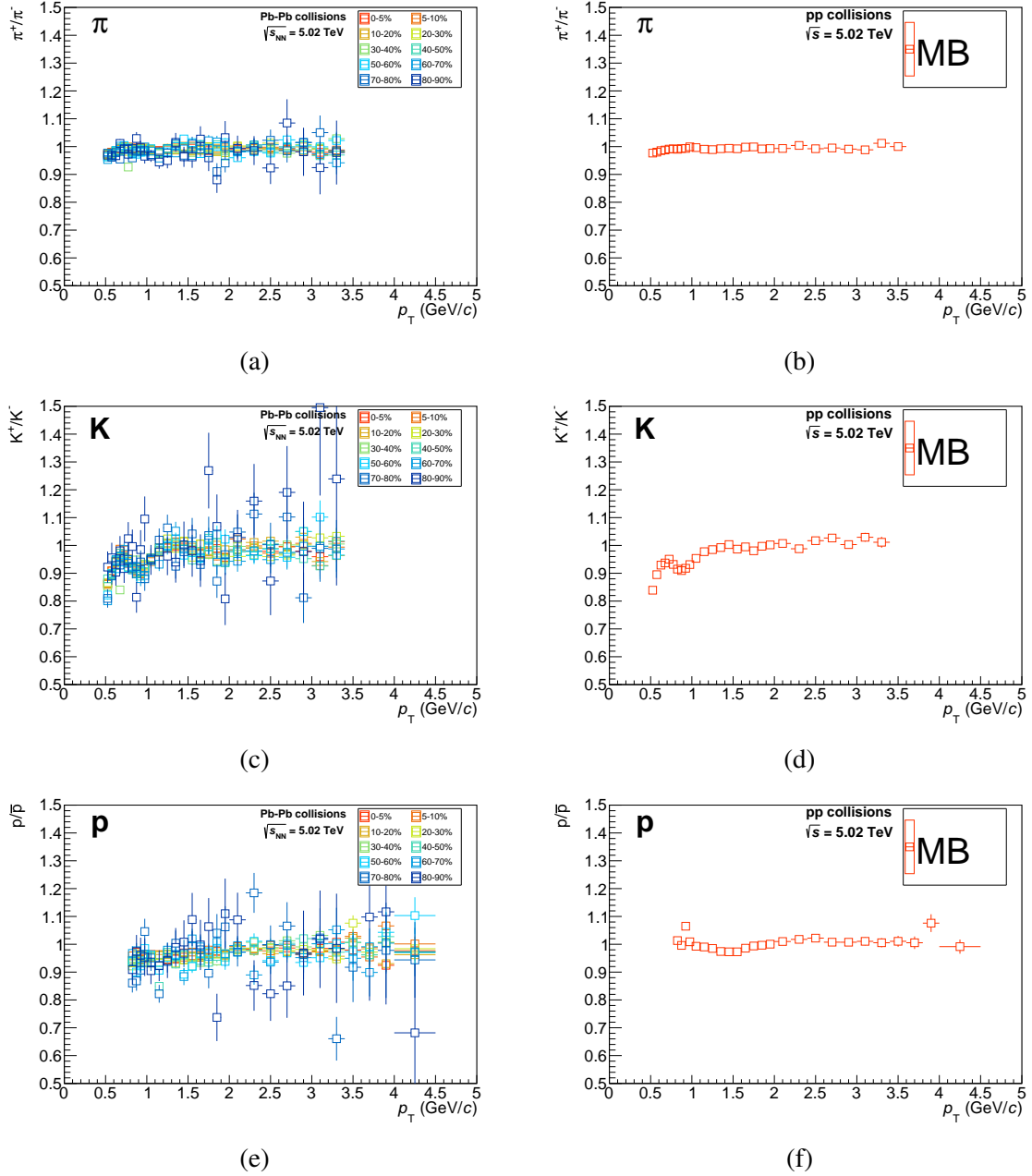


Fig. 7.2 p_T -differential π^+/π^- , K^+/\bar{K} and p/\bar{p} ratios for corrected spectra as obtained in Pb–Pb collisions for a selection of different centrality classes as reported in Section 6.1.3 (left) and in MB pp collisions (right). Only the statistical uncertainty are reported.

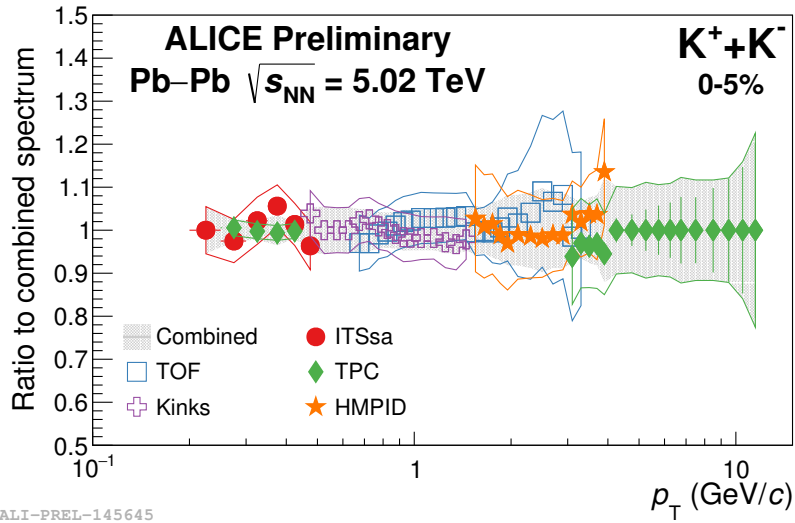


Fig. 7.3 Comparison between the combined spectra for charged kaons and the single analyses.

Analysis	π (GeV/c)	K (GeV/c)	p (GeV/c)
ITSSa	0.10 – 0.70	0.20 – 0.50	0.30 – 0.60
TPC	0.25 – 0.70	0.25 – 0.45	0.45 – 0.80
TOF	0.60 – 3.40	0.70 – 3.40	0.80 – 4.00
TPC rel. rise	2.00 – 20.00	3.00 – 20.00	3.00 – 20.00
Kinks	-	0.20 – 5.00	-
HMPID	1.50 – 4.00	1.50 – 4.00	1.50 – 6.00

Table 7.1 π , K and p p_T -ranges in GeV/c used by the different analyses in Pb–Pb analysis.

Analysis	π (GeV/c)	K (GeV/c)	p (GeV/c)
ITSSa	0.10 – 0.70	0.20 – 0.60	0.30 – 0.65
TPC	0.30 – 0.70	0.30 – 0.45	0.45 – 0.80
TOF	0.60 – 3.40	0.70 – 3.40	0.80 – 4.00
TPC rel. rise	2.00 – 20.0	3.00 – 20.00	3.00 – 20.00
Kinks	-	0.45 – 4.00	-
HMPID	1.50 – 4.00	1.50 – 4.00	1.50 – 6.00

Table 7.2 π , K and p p_T -ranges in GeV/c used by the different analyses in pp analysis.

In Pb–Pb collisions, the spectra become harder with increasing centrality. This hardening is found to be mass dependent as protons are more affected than pions, consistently with the presence of a radial flow. The common expansion velocity of the fireball manifests itself as a mass dependent blue-shift of the spectra. At high p_T ($p_T > 5 \text{ GeV}/c$) the slopes do not depend on the particle species as the production of hard partons is dominated by fragmentation processes.

The effect of radial flow can be better appreciated in Fig. 7.6, where the spectra of kaons and protons are divided by the ones of charged pions for each centrality class. The K/π distribution shows a rapid saturation for momenta of about $2 \text{ GeV}/c$. The p/π exhibits a depletion in the proton production at low momentum below $2 \text{ GeV}/c$ and a peak in the region between 3 and $4 \text{ GeV}/c$. At high momenta ($p_T > 8 \text{ GeV}/c$), the ratios tend to zero. With respect to Pb–Pb collisions at $\sqrt{s_{\text{NN}}} = 2.76 \text{ TeV}$, at $\sqrt{s_{\text{NN}}} = 5.02 \text{ TeV}$ the maximum of the peak is shifted towards higher p_T consistently for all centralities. This is understood as due to the fact that the effect of the radial flow is larger at higher energies. In pp collisions (see in Fig. 7.7), K/π and p/π ratios measured at $\sqrt{s} = 5.02 \text{ TeV}$ are in agreement with the ones measured at the other energies. The lack of a significant contribution from radial flow in pp collisions is visible in the p/π ratio as the maximum value of the distribution is significantly lower (about one third) than the one reached in central Pb–Pb collisions at the same energy.

The spectral shapes of π , K and p are studied in the framework the Boltzmann-Gibbs Blast-Wave model [56] describe in Section 2.2.1. For each centrality class, the spectra of the three species are simultaneously fitted with the model parameterization reported in Eq. 2.15. The agreement of the fitted distribution to the measured spectra is shown in Fig. 7.8. It is important to note that the parameters (β_T , T_{Kin} , n) extracted with this procedure strongly depend on the fitting range used [40]. The compatibility with results extracted at lower energies is ensured by using the same fitting range: pions are fitted in the interval $[0.5, 1] \text{ GeV}/c$, kaons in $[0.2, 1.5] \text{ GeV}/c$ and protons in $[0.3, 3] \text{ GeV}/c$. Low-momentum pions ($p_T < 0.5 \text{ GeV}/c$) are not included in the fit procedure as their distribution is affected by resonance decays that are not included in the BGBW model. The model is able to correctly describe the data within the fitting range.

The β_T , T_{Kin} , n parameters obtained with the simultaneous fit procedure are reported in Fig. 7.9 for several collision systems [40, 147, 72], as a function of the charged particle density $\langle dN_{\text{ch}}/d\eta \rangle$. Within the uncertainties, the T_{Kin} parameter evolves continuously from small to large collision systems. The n and $\langle \beta_T \rangle$ parameters in Pb–Pb collisions do not follow the same trend of small systems. This effect is also visible in Fig. 7.10, where in the correlation between the T_{Kin} and $\langle \beta_T \rangle$ parameters is shown. The color scale allows for the

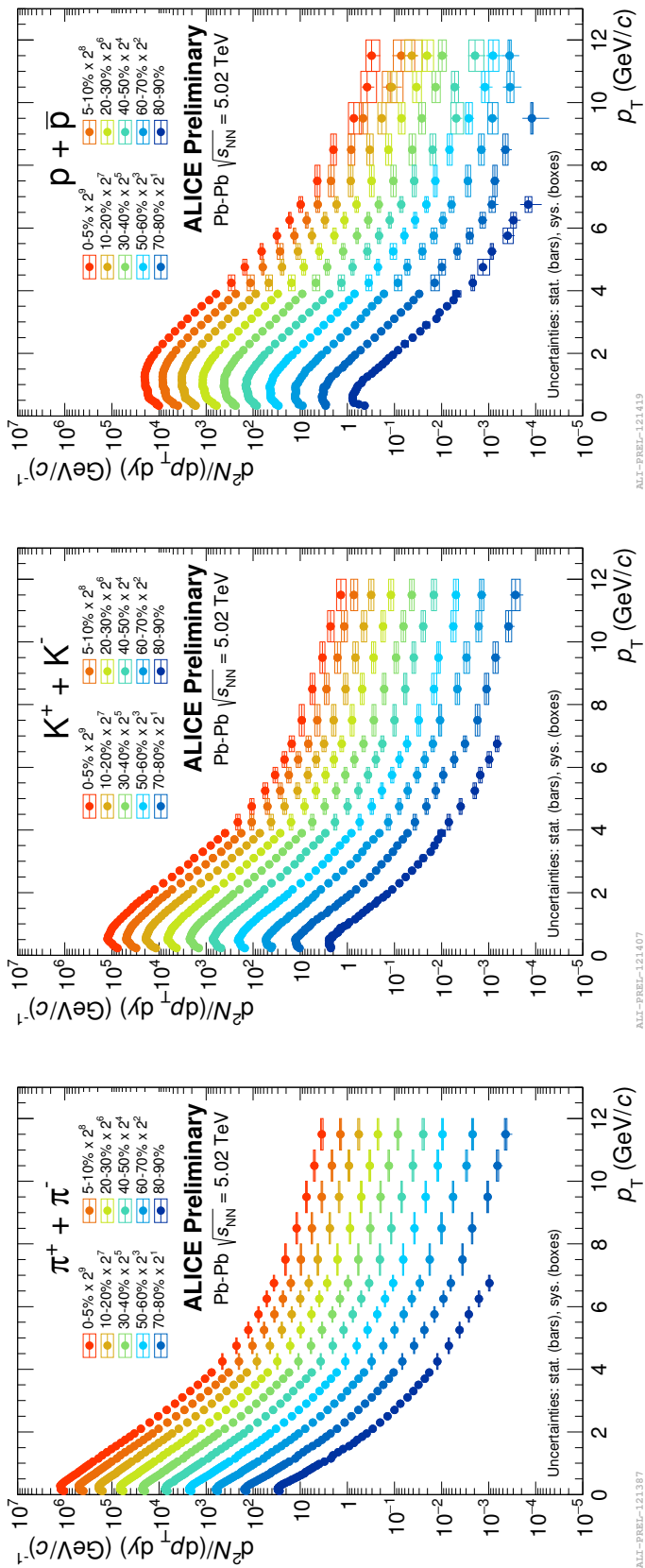


Fig. 7.4 Spectra of $\pi^+ + \pi^-$, $K^+ + K^-$ and $p + \bar{p}$ as obtained in Pb-Pb collisions at $\sqrt{s_{\text{NN}}} = 5.02 \text{ TeV}$ for several centrality classes [146] scaled by factors for better visibility.

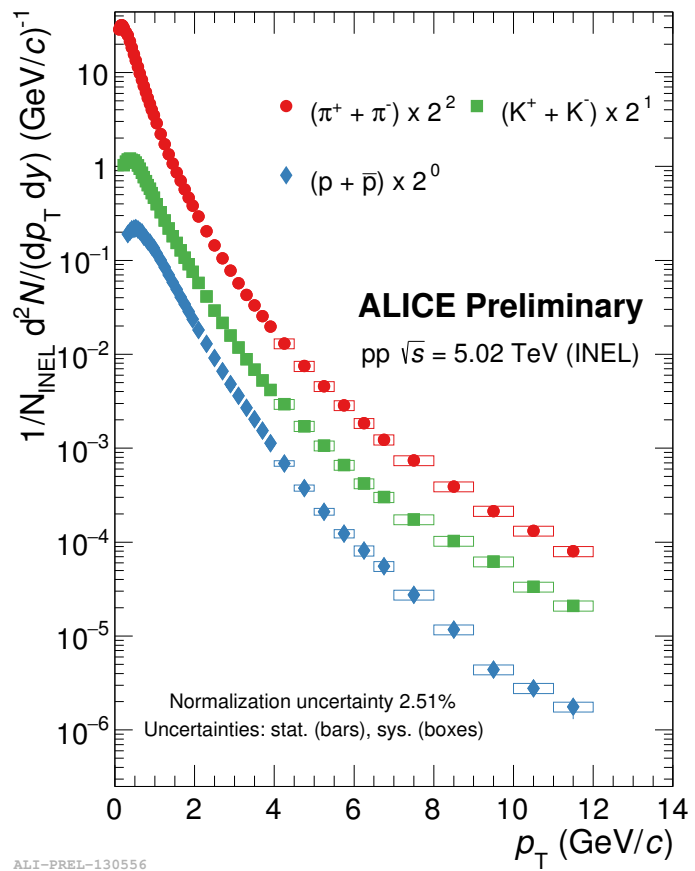


Fig. 7.5 Spectra of $\pi^+ + \pi^-$, $K^+ + K^-$ and $p + \bar{p}$ as obtained in Minimum Bias pp collisions at $\sqrt{s} = 5.02$ TeV. Normalization uncertainty due to the normalization to inelastic collisions.

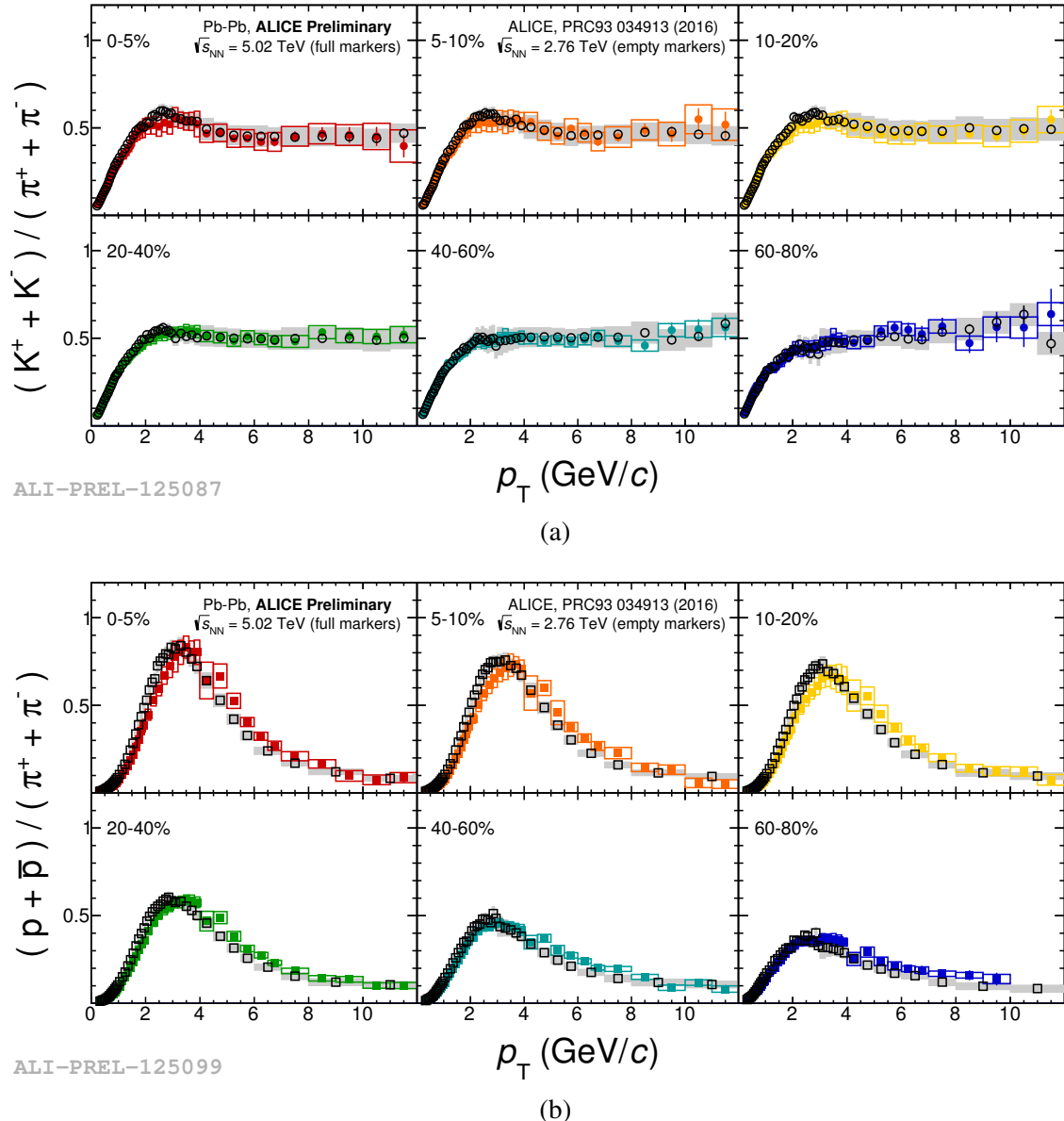


Fig. 7.6 Ratio of the spectra of kaons and protons to the ones of pions as a function of p_T as measured in Pb–Pb collisions at $\sqrt{s_{NN}} = 5.02$ TeV (this work) and at $\sqrt{s_{NN}} = 2.76$ TeV for several centrality classes.

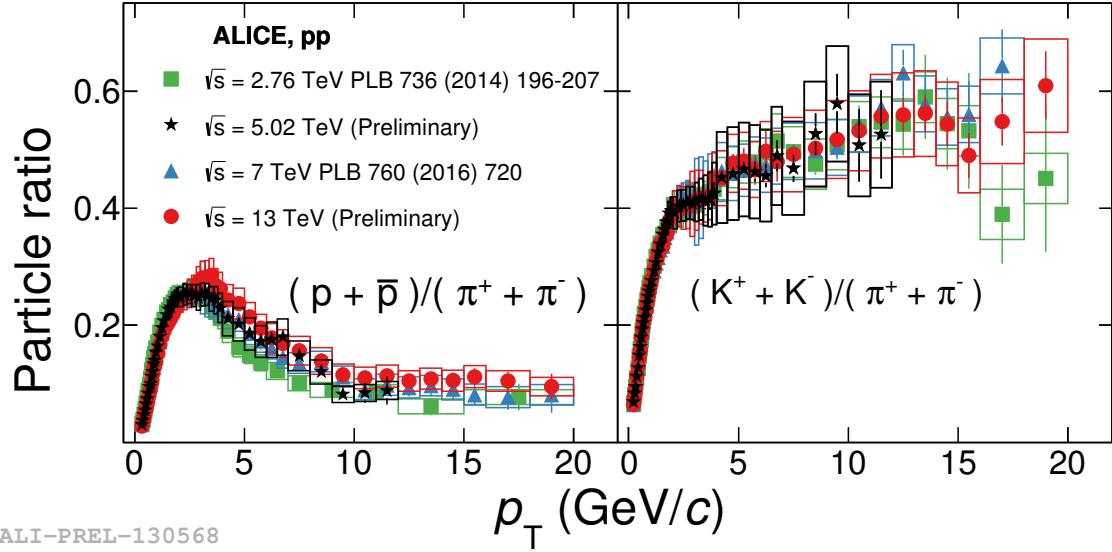


Fig. 7.7 Ratio of the spectra of kaons and protons to the ones of pions as a function of p_T as measured in pp collisions at $\sqrt{s} = 5.02 \text{ TeV}$ (this work), $\sqrt{s} = 2.76 \text{ TeV}$ [12], $\sqrt{s} = 7 \text{ TeV}$ [13] and $\sqrt{s} = 13 \text{ TeV}$.

identification of events with equal charged particle multiplicity. It is found that small systems have larger β_T with respect to extended systems with the same multiplicity.

It is worth noting that the largest expansion velocity $\langle \beta_T \rangle$ is reached at the highest collision energy, the maximum β_T value is $\approx 2\%$ larger than the one measured at $\sqrt{s_{NN}} = 2.76 \text{ TeV}$. This confirms the observation of stronger radial flow at $\sqrt{s_{NN}} = 5.02 \text{ TeV}$ with respect to $\sqrt{s_{NN}} = 2.76 \text{ TeV}$. The trends observed at $\sqrt{s_{NN}} = 2.76 \text{ TeV}$ are however confirmed and so is the different behavior between small and large systems.

7.2.1 Model comparison of the spectra

The spectral shapes are compared in Fig. 7.11 to the predictions from different hydrodynamic models such as iEBE-VISHNU with TRENTo and AMPT initial conditions [148, 149], IP-Glasma + MUSIC + UrQMD (referred to as ‘‘McGill’’ in this work) [150] and EPOS LHC [151]. The iEBE-VISHNU model implements viscous hydrodynamics (QGP expansion) coupled to a hadron cascade model (UrQMD) to simulate the evolution of the hadron resonance gas. The initial conditions are based on the TRENTo model which distributes the entropy proportional to the generalized mean of nuclear overlap density and on AMPT, in which the initial state includes fluctuations at the nucleonic and sub-nucleonic levels and considers pre-equilibrium dynamics of partonic matter. The EPOS LHC model implements a non uniform fireball divided in the core (high density) and corona (lower density).

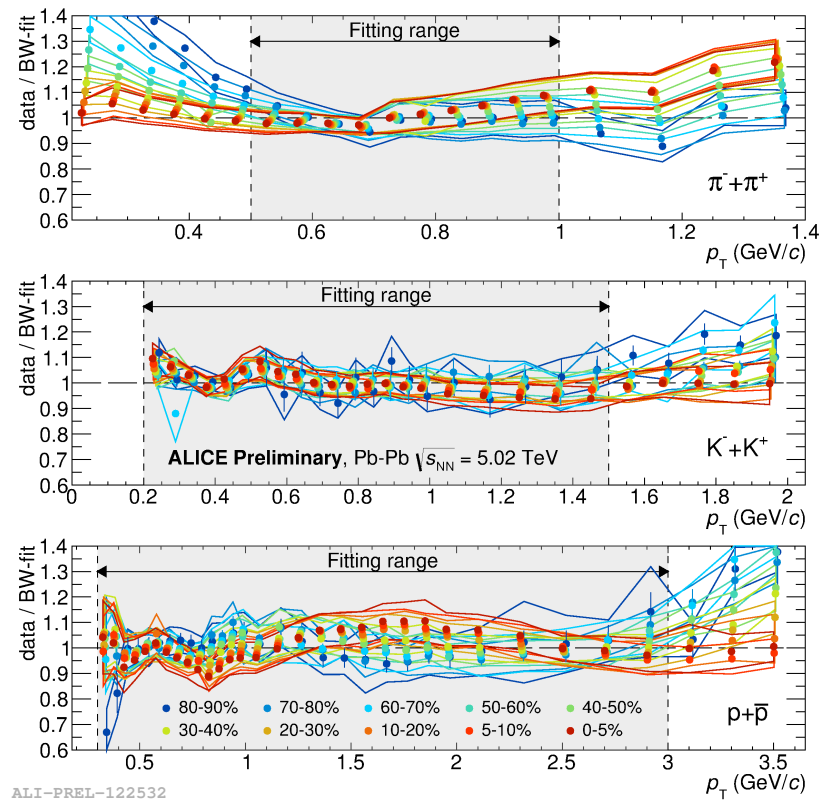


Fig. 7.8 Ratio between the measured particle spectra and the result of the simultaneous BGBW fit to π , K and p as obtained in Pb–Pb collisions at $\sqrt{s_{NN}} = 5.02$ TeV for several centrality classes.

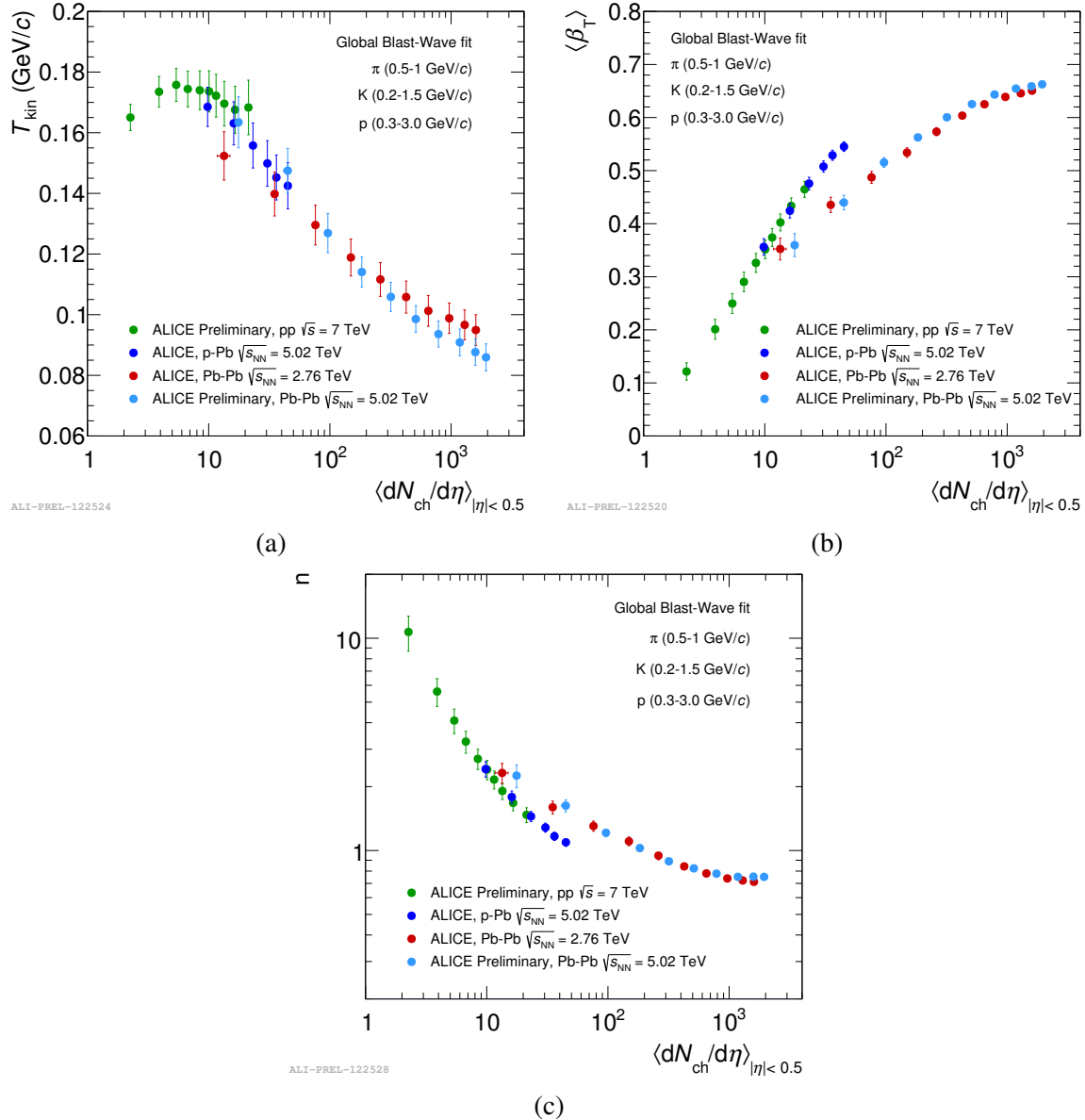


Fig. 7.9 (a) Kinetic freeze-out temperature T_{kin} , (b) expansion velocity $\langle \beta_T \rangle$ and (c) expansion velocity profile n parameters obtained from the simultaneous fit to the π , K and p spectra in several collision systems as a function of the pseudorapidity density of charged particles $\langle dN_{ch}/d\eta \rangle_{|\eta|<0.5}$.

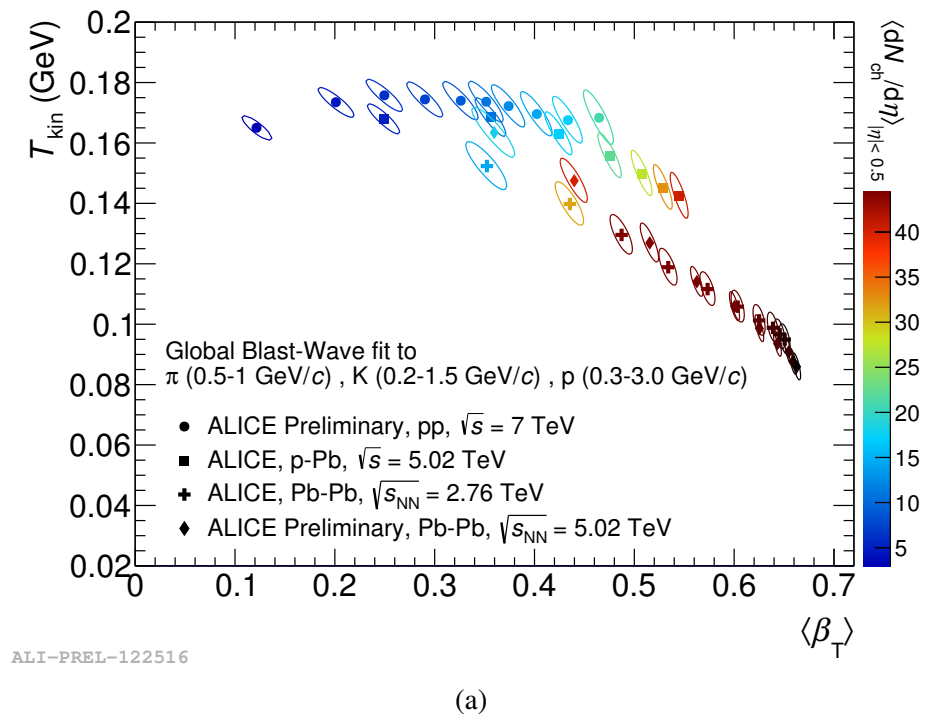


Fig. 7.10 Correlation between the T_{Kin} and $\langle \beta_T \rangle$ parameters for different collision systems and different charged particle density. The color scale corresponds to the pseudorapidity density of charged particles $\langle dN_{\text{ch}}/d\eta \rangle$. The contour represents the 1σ interval defined by the fit procedure.

This model does not simulate full microscopic processes, instead a parameterization is used to reproduce the LHC data. The McGill model uses IP-Glasma initial conditions matched to hydrodynamic variables and evolved using viscous hydrodynamic model (MUSIC). This model includes the modelization of the hadronic phase with the UrQMD description.

At low p_T , where hydrodynamics is expected to correctly describe the evolution of the fireball, the data are qualitatively reproduced by all models except for the EPOS LHC model. A better agreement between the model and data is observed in central collision with respect to peripheral ones. This is not the case for the EPOS LHC model, which is found to better describe peripheral collisions.

In Fig. 7.12 the p/π and K/π particle ratios are reported as a function of p_T and compared to the predictions of the hydrodynamic models. As for the particle spectra, in central collisions the best agreement is observed at low p_T (below 2 GeV/c) for the K/π ratio (meson/meson). The EPOS LHC model is able to reproduce the measured ratios up to high p_T , while the description of the spectral shape is only approximate. In peripheral collisions, only EPOS LHC is able to reproduce the data. This might be due to the separation, in the description of the fireball evolution, of the core and corona. The p/π ratio (baryon/meson) is well described at low p_T by the iEBE-VISHNU model, while McGill shows increasing discrepancies for large momenta (~ 4 GeV/c) and EPOS LHC agreement is limited to the data above 2 GeV/c. In peripheral collisions, the iEBE-VISHNU model describes the data below 1 GeV/c and EPOS LHC overestimates the value of the p/π ratio in the p_T range between 2 and 8 GeV/c. Predictions from the McGill model were not available for this centrality class. The two implementation of the iEBE-VISHNU model do not exhibit significant difference in the intermediate p_T range (up to $p_T \sim 1.5$ GeV). Initial conditions mostly affect the correlation in particle production e.g. anisotropic flow coefficients.

7.3 Nuclear modification factor

In order to evaluate the effect of the presence of the deconfined phase in heavy-ion collisions, the Nuclear Modification Factor (R_{AA}) of the identified particles are computed. The definition of R_{AA} , discussed in detail in Section 2.3.1, is given by Eq. 2.17:

$$R_{AA}(p_T) = \frac{1}{\langle N_{Coll} \rangle} \cdot \frac{d^2N_{AA}/dydp_T}{d^2N_{pp}/dydp_T} \quad (7.3)$$

The mean values of N_{Coll} are determined with a Glauber model analysis [152].

The R_{AA} are shown for pions, kaons and protons as a function of p_T for different centrality classes in Fig. 7.13. At large p_T ($p_T > 8$ GeV/c), a suppression with respect to

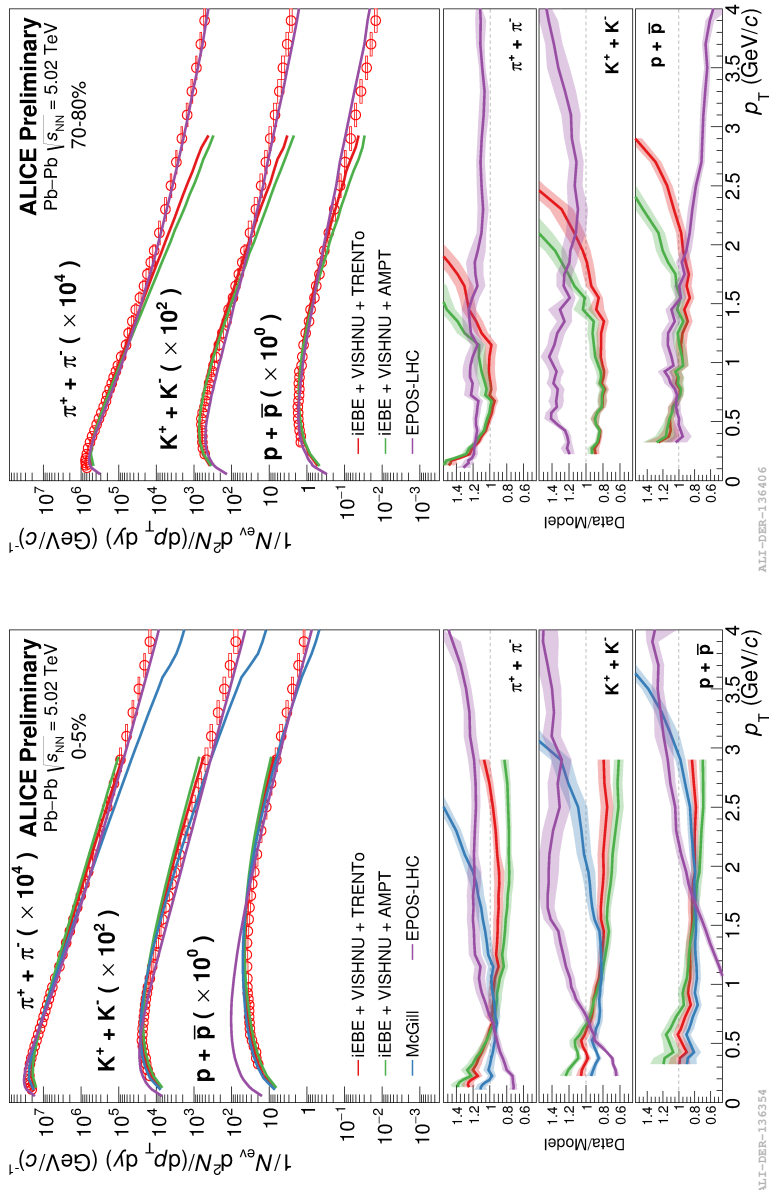
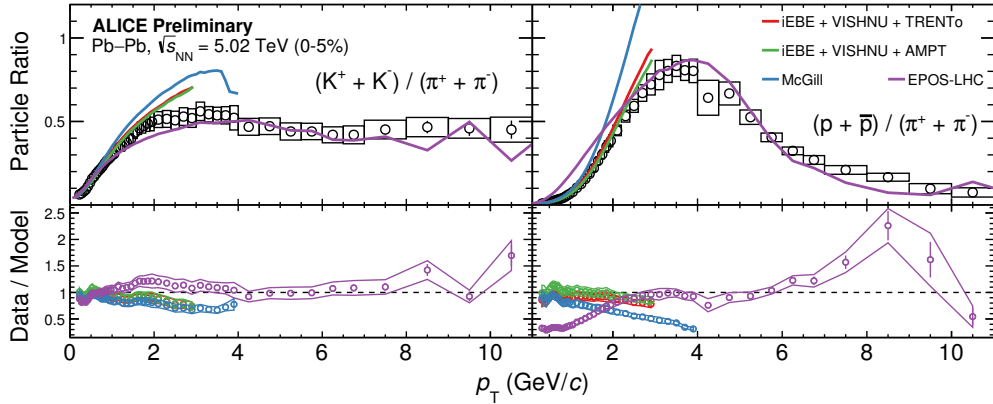
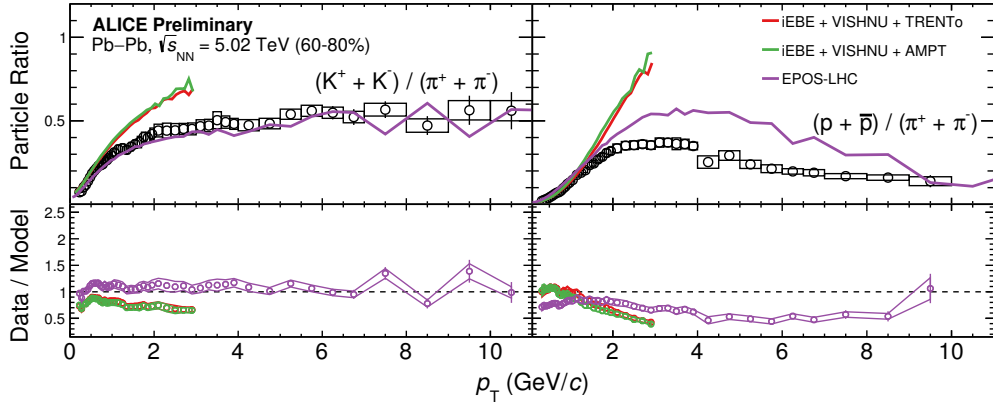


Fig. 7.11 Identified particle spectra as a function of p_T as measured in three different centrality classes and compare to the prediction of theoretical models.



ALI-DER-136346



ALI-DER-136350

Fig. 7.12 Particle spectra of kaons and protons scaled to the one of pions as a function of p_T as measured in three different centrality classes and compare to the prediction of theoretical models.

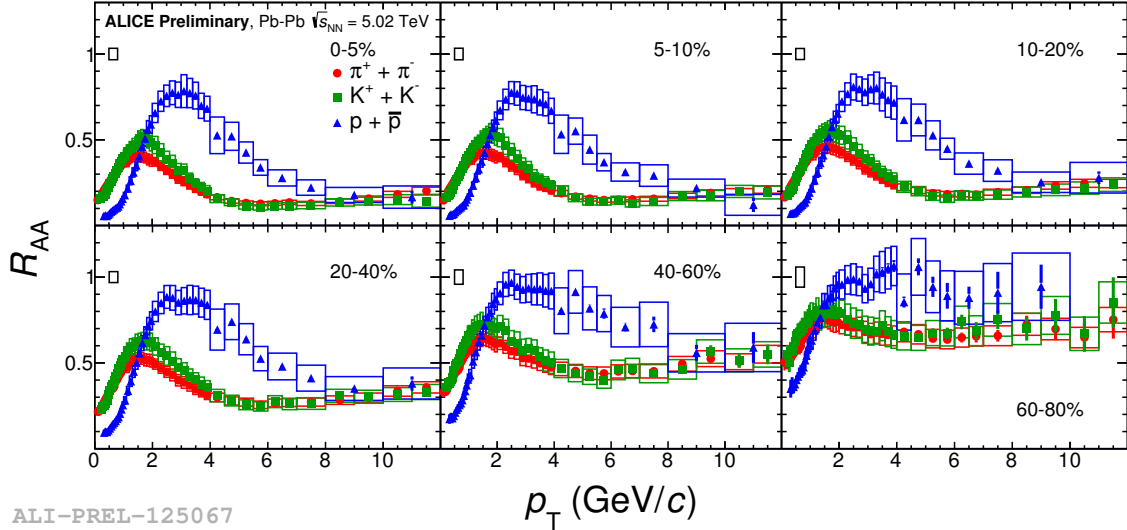


Fig. 7.13 Nuclear Modification Factor of π , K and p measured as a function of p_T in several centrality intervals of Pb–Pb collisions at $\sqrt{s_{NN}} = 5.02$ TeV.

the production in pp is observed, that is the same for all particle species under study. This result indicates that the energy loss of light quarks in the QGP medium does not depend on the flavour (u , d or s).

The evolution with centrality of the R_{AA} shows at large momenta ($p_T > 8$ GeV/ c) a large suppression in central collision, where a dense medium is expected to be created. In peripheral collisions the suppression is reduced, in agreement with the interpretation of the creation of a less dense system.

The R_{AA} measured at $\sqrt{s_{NN}} = 5.02$ TeV is compared to the one at $\sqrt{s_{NN}} = 2.76$ TeV [153] in Fig. 7.14, showing no significant dependence on the collision energy. At the same time, harder p_T spectra are measured at the top energy. These features are confirmed by the measurement of the R_{AA} of unidentified charged particles at $\sqrt{s_{NN}} = 5.02$ TeV [5]. Based on these considerations, the observation that R_{AA} suppression is similar at the two energies has been suggested as due to a stronger parton energy loss and a larger energy density of the medium at the higher energy.

7.4 p_T -integrated yields, ratios and average p_T

The p_T -integrated production yields of pions, kaons and protons have been extracted from the measured spectra. The yields, $\langle dN/dy \rangle$, and mean transverse momentum, $\langle p_T \rangle$, are computed by extrapolating the spectra down to $p_T = 0$ GeV/ c . The extrapolation is performed by fitting the single spectra using a BGBW function [56] in Pb–Pb collisions

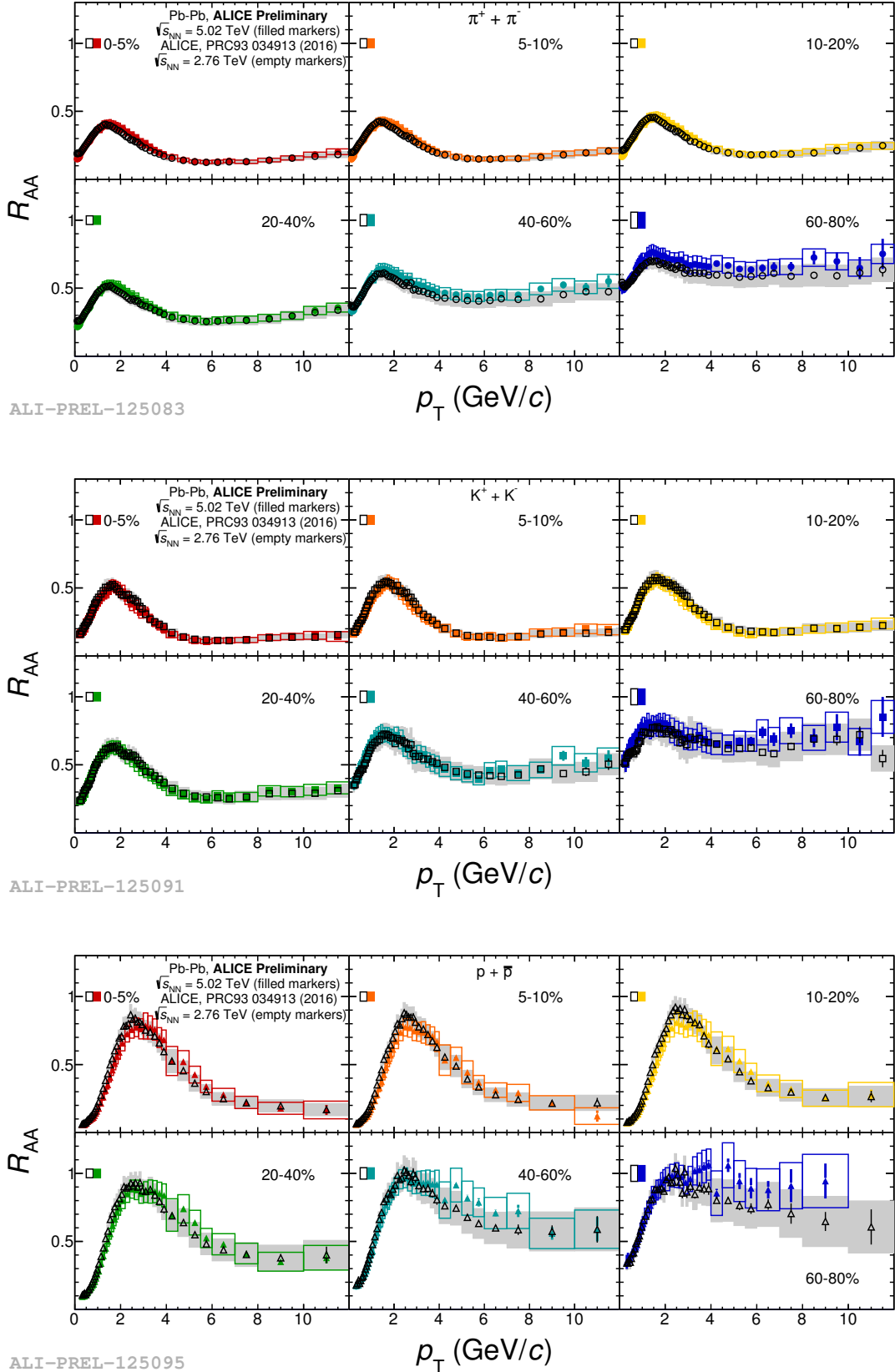


Fig. 7.14 Nuclear Modification Factor of π , K and p measured in Pb–Pb collisions at $\sqrt{s_{NN}} = 5.02$ TeV and $\sqrt{s_{NN}} = 2.76$ TeV for several centrality intervals.

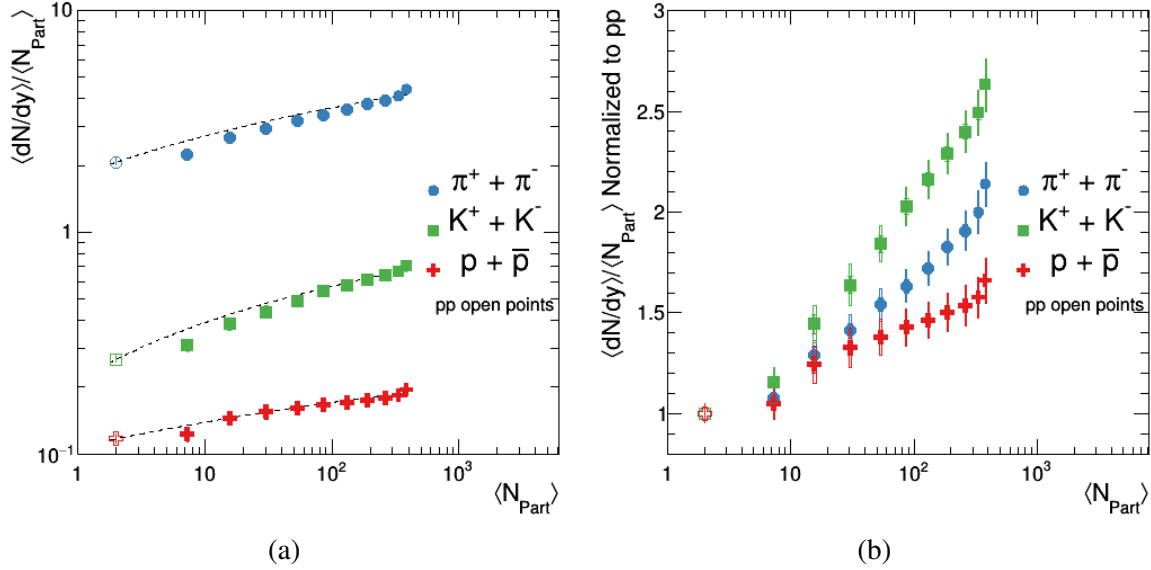


Fig. 7.15 (a) Integrated particle yields normalized to $\langle N_{\text{Part}} \rangle$ as a function of $\langle N_{\text{Part}} \rangle$ as measured in pp and Pb–Pb collisions at $\sqrt{s_{\text{NN}}} = 5.02$ TeV. A fit with a logarithm function is added to guide the eye. (b) Ratio of $\langle dN/dy \rangle / \langle N_{\text{Part}} \rangle$ to the value measured in pp collisions.

and a Lévy-Tsallis function [154, 155] in pp collisions. The estimation of the systematic uncertainty on the yields was carried out by fitting the highest and lowest spectra obtained by shifting all data points within their systematic uncertainty. In addition, the systematic uncertainty on the extrapolation was estimated by using a set of fit functions that differ in the functional slope at low p_T and by taking the maximum deviation from the BGBW or Lévy-Tsallis case for Pb–Pb and pp respectively.

The particle yields per unit of rapidity are reported normalized to the average number of participating nucleons, $\langle N_{\text{Part}} \rangle$, as a function of $\langle N_{\text{Part}} \rangle$ for both pp and Pb–Pb collisions at $\sqrt{s_{\text{NN}}} = 5.02$ TeV in Fig. 7.15a. In Fig. 7.15b, the values for each particle species are scaled to the ones measured in pp. The steep increase in the relative production of kaons is understood as the effect of strangeness enhancement [51].

The p_T -integrated yields of kaons and protons scaled to the ones of pions are reported as measured in Pb–Pb collisions at $\sqrt{s_{\text{NN}}} = 5.02$ TeV in Fig. 7.16 and in pp collisions at $\sqrt{s} = 5.02$ TeV in Fig. 7.17.

In Fig. 7.16, the results of the analysis presented in this work are reported as a function of the charged particle multiplicity density and compared with the ones measured across several collision systems: pp collisions at $\sqrt{s} = 7$ TeV [72], p–Pb collisions at $\sqrt{s_{\text{NN}}} = 5.02$ TeV [147] and Pb–Pb collisions at $\sqrt{s_{\text{NN}}} = 2.76$ TeV [40]. While the comparison of particle ratios measured in different systems highlights a continuous evolution as a function of the

particle multiplicity, the new data confirm the trends observed at lower energy in Pb–Pb collisions . The observation of similar trends at $\sqrt{s_{\text{NN}}} = 2.76$ TeV and $\sqrt{s_{\text{NN}}} = 5.02$ TeV is consistent with the expectations from the thermal-statistical model, which predicts no significant evolution between the two energies (see Section 7.4.1).

The K/π and p/π ratios, obtained in pp collisions at $\sqrt{s} = 5.02$ TeV, are reported in comparison to other collision energies in Fig. 7.17. The measurements at the LHC energies are in agreement within the present uncertainties. These results suggest the presence of a saturation in the proton production for energies above the TeV scale.

The $\langle p_T \rangle$ computed from the spectra of π , K and p measured in pp and Pb–Pb collisions is reported as a function of the charged particle multiplicity density in Fig. 7.18. With respect to the pp results, the increase in the average transverse momentum is larger for particles with heavier masses, as expected in the presence of radial flow. A stronger radial flow is observed for central collisions. The comparison with Pb–Pb collisions at $\sqrt{s_{\text{NN}}} = 2.76$ TeV shows that the effect of radial flow is larger at $\sqrt{s_{\text{NN}}} = 5.02$ TeV.

7.4.1 Interpretation of the results in the SHM

The production of light flavor particles measured in central Pb–Pb collisions can be used to extract the thermodynamic properties of the fireball by performing an analysis with the Statistical Hadronization Model (Fig. 2.2). The production of the majority of light-flavour hadrons and light nuclei in Pb–Pb collisions at $\sqrt{s_{\text{NN}}} = 2.76$ TeV, can be reasonably fitted by the Statistical Hadronization Model with a single chemical freeze-out temperature T_{Ch} of about 156 MeV [41]. The thermal model fits to the ALICE data for the yields of π , K , ϕ , p , Λ , Ξ , Ω , d , ${}^3\text{H}$, ${}^3\text{He}$ measured in central Pb–Pb collisions at $\sqrt{s_{\text{NN}}} = 5.02$ TeV are shown in Fig. 7.19. The results obtained with the analysis reported in this thesis are included in the fit. At $\sqrt{s_{\text{NN}}} = 5.02$ TeV, the χ^2 minimization procedure yields a value of T_{Ch} of about 153 ± 2 MeV and χ^2/NDF ranging from ~ 4 to ~ 6 , depending on the SHM implementation. The three different implementations of the thermal model that were considered provide fully consistent results. The values extracted from the fit are driven by the measured p/π ratio. The simultaneous description of the proton and pion yield is in tensions with the measured data ($\sim 2 \sigma$ for pions and $\sim 4 \sigma$ for protons). The differences between data and model values observed at $\sqrt{s_{\text{NN}}} = 2.76$ TeV are confirmed at the new energy.

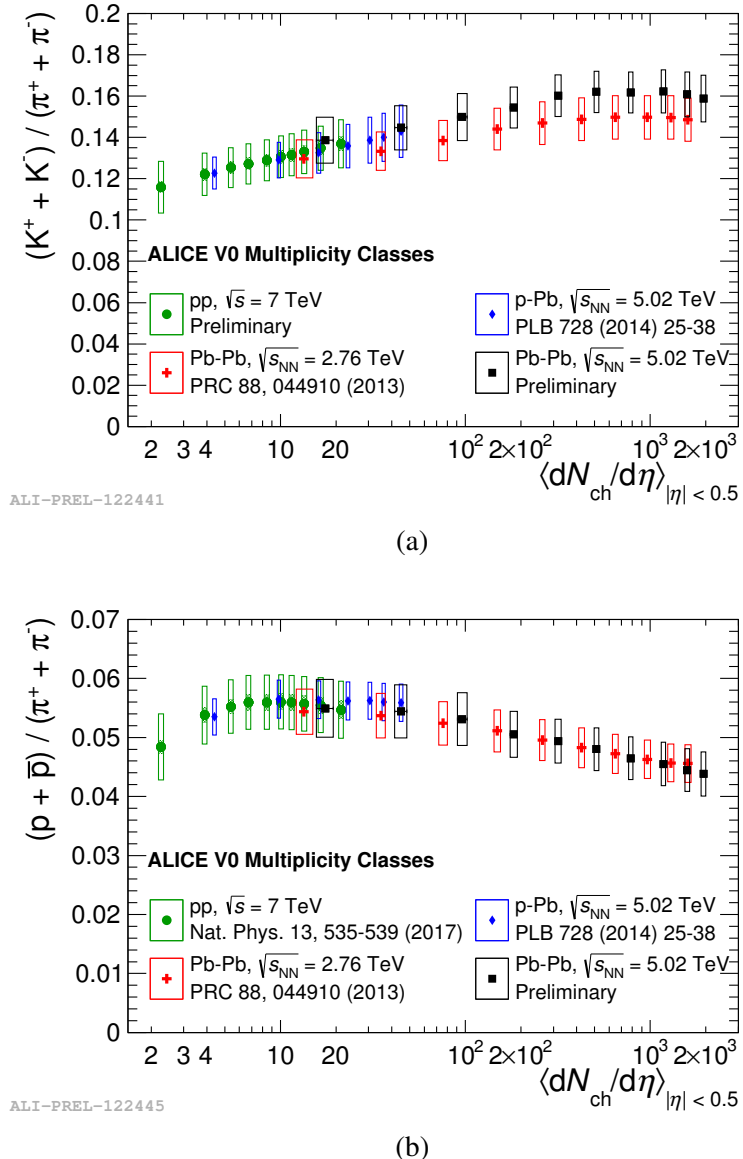


Fig. 7.16 $\langle dN/dy \rangle$ for kaons (a) and protons (b) relative to pion yields as a function of $\langle dN_{ch}/d\eta \rangle$ in Pb–Pb collisions at $\sqrt{s_{NN}} = 5.02$ TeV (this work) compared to several collision systems.

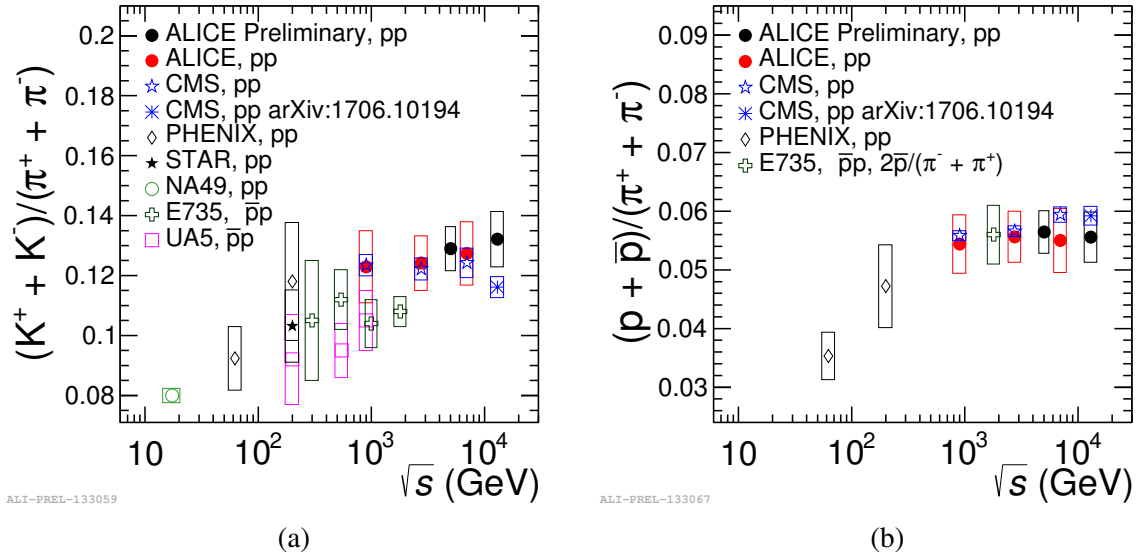


Fig. 7.17 $\langle dN/dy \rangle$ for kaons and protons relative to pion yields measured as a function of the collision energy in MB pp collisions.

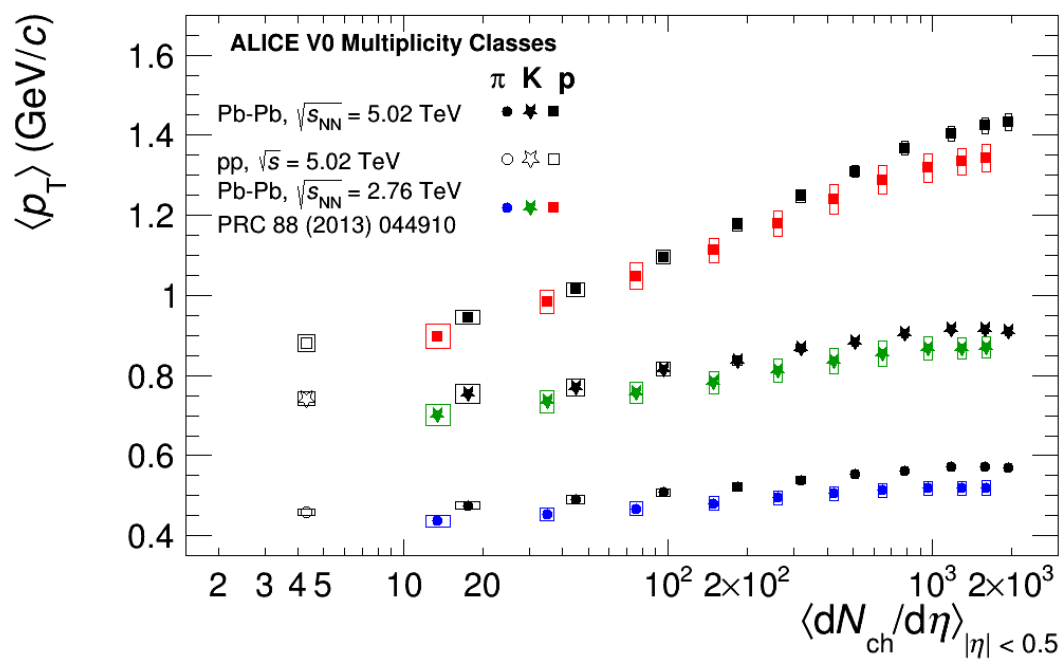


Fig. 7.18 $\langle p_T \rangle$ for π , K and p in pp collisions at $\sqrt{s} = 5.02$ TeV, Pb–Pb collisions at $\sqrt{s_{\text{NN}}} = 2.76$ TeV and $\sqrt{s_{\text{NN}}} = 5.02$ TeV.

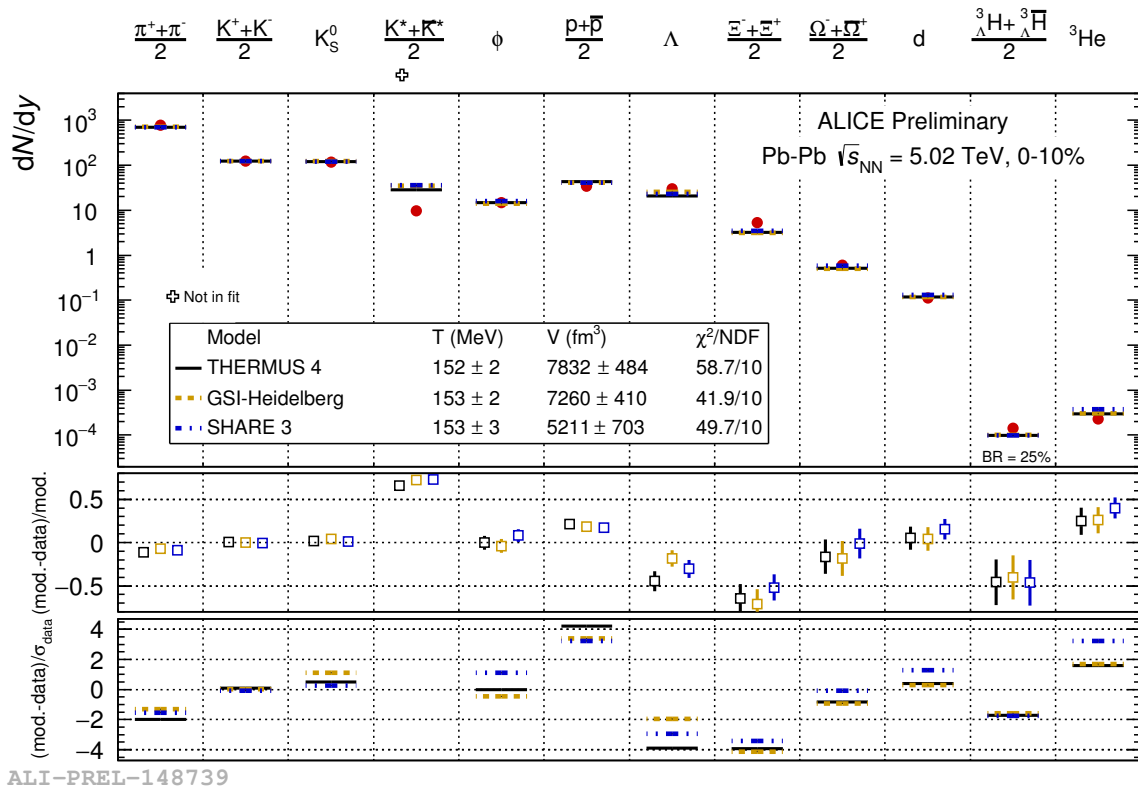


Fig. 7.19 Grand canonical (GC) equilibrium and non equilibrium thermal fit to identified light hadron and (hyper-)nuclei yields measured in 0-10% central Pb–Pb collisions at $\sqrt{s_{\text{NN}}} = 5.02$ TeV. Three different implementations of the SHM are used. The yield of K^* is not included in the fit.

Chapter 8

Conclusions

In this work the results on the production of identified pions, kaons and protons measured in Pb–Pb collisions and in inelastic pp collisions at $\sqrt{s_{\text{NN}}} = 5.02$ TeV are presented. The measurement is carried out using the ALICE TOF detector. This required an in-depth understanding of the detector response in order to achieve the best performance for PID. The knowledge acquired while performing activities of Quality Assurance, calibration and studies on the aging of the detector was beneficial to the optimization of the analysis strategy. The yields of π , K and p were obtained by performing a statistical deconvolution of the signal in the TOF detector using a template fit. A Monte Carlo simulation was used to compute the efficiency, acceptance and feed-down corrections. The production is measured as a function of centrality in the p_{T} range $0.5 – 3.4$ GeV/ c for pions and kaons, and in the p_{T} range $0.8 – 4.5$ GeV/ c for protons. The resulting yields are combined with the ones obtained with different PID techniques to extend the measurement at low and high momenta. The final spectra cover a range of $0.1 – 12$ GeV/ c for pions, $0.2 – 12$ GeV/ c for kaons, $0.3 – 12$ GeV/ c for protons. These results were approved as preliminary by the ALICE Collaboration in 2017 and presented by the candidate at the major conferences in the field during 2017 and 2018. A publication that discusses the measurements is in preparation.

The physics outcome and impact of these studies can be summarized as follows. A significant evolution of the spectral shapes is observed when going from peripheral to central Pb–Pb collisions, resulting in a blue-shift of the spectra. The hardening of the spectra is mass dependent, being more pronounced for heavier particles, as expected for a system where a strong radial flow is at play. The comparison with analogous measurements performed in Pb–Pb collisions at $\sqrt{s_{\text{NN}}} = 2.76$ TeV reveals a slightly larger ($\approx 2\%$) radial expansion velocity at $\sqrt{s_{\text{NN}}} = 5.02$ TeV. The results presented in this thesis consolidate the observations performed at lower energy. Hydrodynamic models describe to the 20-30 % level particle spectra at low transverse momentum, where radial flow drives particle production.

The ratios of p_T -integrated particle yields (K/π and p/π) measured as a function of the charged particle multiplicity density exhibit a continuous evolution across collision systems, which seems to depend only on the charged particle multiplicity, irrespective of the center-of-mass energy and the colliding system. The nuclear modification factors have been computed for pions, kaons and protons at $\sqrt{s_{NN}} = 5.02$ TeV, confirming that high- p_T ($p_T > 8 \text{ GeV}/c$) particle production is suppressed from peripheral to central Pb–Pb collisions due to energy loss in the QGP, as observed at $\sqrt{s_{NN}} = 2.76$ TeV. In addition, flavour-independence of the suppression is observed for light-flavour hadrons. Considerations on the chemical freeze-out temperature of the system can be drawn by performing an analysis within the framework of the Statistical Hadronization Model. The temperature obtained at $\sqrt{s_{NN}} = 5.02$ TeV using as input the measured light flavour hadron yields is about 3 MeV lower than the ~ 156 MeV, measured at $\sqrt{s_{NN}} = 2.76$ TeV, but in agreement within the uncertainties obtained from the SHM fit. Crucial to the interpretation of these results is the measurement of the p/π ratio in most central collisions that is one of the main results of this work.

References

- [1] Jaroslav Adam et al. Centrality dependence of the pseudorapidity density distribution for charged particles in Pb-Pb collisions at $\sqrt{s_{NN}} = 5.02$ TeV. *Phys. Lett.*, B772:567–577, arXiv, 1612.08966.
- [2] B. Abelev et al. $K^*(892)^0$ and $\phi(1020)$ production in Pb-Pb collisions at $\sqrt{s_{NN}} = 2.76$ TeV. *Phys. Rev. C*, 91:024609, Feb 2015.
- [3] [online] <https://www.quantumdiaries.org/wp-content/uploads/2011/02/FlowPr.jpg>.
- [4] S. Acharya et al. Anisotropic flow of identified particles in Pb-Pb collisions at $\sqrt{s_{NN}} = 5.02$ TeV. *JHEP*, 09:006, arXiv, 1805.04390.
- [5] Shreyasi Acharya et al. Transverse momentum spectra and nuclear modification factors of charged particles in pp, p-Pb and Pb-Pb collisions at the LHC. arXiv, 1802.09145.
- [6] Jaroslav Adam et al. Centrality dependence of particle production in p-Pb collisions at $\sqrt{s_{NN}} = 5.02$ TeV. *Phys. Rev.*, C91(6):064905, arXiv, 1412.6828.
- [7] P. Cortese et al. ALICE: Addendum to the technical design report of the time of flight system (TOF). 2002.
- [8] Jaroslav Adam et al. Determination of the event collision time with the ALICE detector at the LHC. *Eur. Phys. J. Plus*, 132(2):99, arXiv, 1610.03055.
- [9] A. Akindinov et al. Performance of the ALICE Time-Of-Flight detector at the LHC. *Eur. Phys. J. Plus*, 128:44, 2013.
- [10] Davide Falchieri. DRM2: the readout board for the ALICE TOF upgrade. *PoS*, TWEPP-17:081, 2018.
- [11] Betty Bezverkhny Abelev et al. Performance of the ALICE Experiment at the CERN LHC. *Int. J. Mod. Phys.*, A29:1430044, arXiv, 1402.4476.
- [12] Betty Bezverkhny Abelev et al. Production of charged pions, kaons and protons at large transverse momenta in pp and Pb-Pb collisions at $\sqrt{s_{NN}} = 2.76$ TeV. *Phys. Lett.*, B736:196–207, arXiv, 1401.1250.
- [13] Jaroslav Adam et al. Multiplicity dependence of charged pion, kaon, and (anti)proton production at large transverse momentum in p-Pb collisions at $\sqrt{s_{NN}} = 5.02$ TeV. *Phys. Lett.*, B760:720–735, arXiv, 1601.03658.

- [14] New State of Matter created at CERN. Un nouvel état de la matière. (PRESSCUT-2000-210. CERN-PR-2000-01-EN. CERN-PR-2000-01-FR):mult. p, 2000. Issued on 10 Feb 2000.
- [15] Lyndon Evans and Philip Bryant. LHC Machine. *JINST*, 3:S08001, 2008.
- [16] Guido Altarelli. The QCD Running Coupling and its Measurement. *PoS*, Corfu2012:002, arXiv, 1303.6065.
- [17] C. Patrignani et al. Review of Particle Physics. *Chin. Phys.*, C40(10):100001, 2016.
- [18] F. Karsch. Lattice results on QCD thermodynamics. *Nuclear Physics A*, 698(1):199 – 208, 2002. 15th Int. Conf. on Ultra-Relativistic Nucleus-Nucleus Collisions (Quark Matter 2001).
- [19] Alexei Bazavov. The QCD equation of state. *Nucl. Phys.*, A931:867–871, 2014.
- [20] U. Heinz. The Little Bang: searching for quark–gluon matter in relativistic heavy-ion collisions. *Nuclear Physics A*, 685(1):414 – 431, 2001. Nucleus-Nucleus Collisions 2000.
- [21] D. Blaschke and N. Chamel. Phases of dense matter in compact stars. arXiv, 1803.01836.
- [22] LHC collides ions at new record energy. Nov 2015.
- [23] Constantin Loizides et al. Improved monte carlo glauber predictions at present and future nuclear colliders. *Phys. Rev. C*, 97:054910, May 2018.
- [24] B. Abelev et al. Centrality determination of pb-pb collisions at $\sqrt{s_{NN}} = 2.76$ tev with alice. *Phys. Rev. C*, 88:044909, Oct 2013.
- [25] Michael L. Miller, Klaus Reygers, Stephen J. Sanders, and Peter Steinberg. Glauber modeling in high energy nuclear collisions. *Ann. Rev. Nucl. Part. Sci.*, 57:205–243, arXiv, nucl-ex/0701025.
- [26] J. D. Bjorken. Highly relativistic nucleus-nucleus collisions: The central rapidity region. *Phys. Rev. D*, 27:140–151, Jan 1983.
- [27] K. Alpgard et al. First Results on Complete Events from p anti-p Collisions at the Center-of-Mass Energy of 540-GeV. *Phys. Lett.*, 107B:310–314, 1981.
- [28] S. S. Adler et al. Systematic studies of the centrality and $s(\text{NN})^{**}(1/2)$ dependence of the $d E(T) / d \eta$ and $d (N(\text{ch})) / d \eta$ in heavy ion collisions at mid-rapidity. *Phys. Rev.*, C71:034908, arXiv, nucl-ex/0409015. [Erratum: *Phys. Rev.*C71,049901(2005)].
- [29] B. I. Abelev et al. Systematic Measurements of Identified Particle Spectra in $p\bar{p}$, d^+ Au and Au+Au Collisions from STAR. *Phys. Rev.*, C79:034909, arXiv, 0808.2041.
- [30] T. Alber et al. Transverse energy production in Pb-208 + Pb collisions at 158-GeV per nucleon. *Phys. Rev. Lett.*, 75:3814–3817, 1995.

- [31] Jaroslav Adam et al. Centrality dependence of the charged-particle multiplicity density at midrapidity in Pb-Pb collisions at $\sqrt{s_{NN}} = 5.02$ TeV. *Phys. Rev. Lett.*, 116(22):222302, arXiv, 1512.06104.
- [32] Kenneth Aamodt et al. Centrality dependence of the charged-particle multiplicity density at mid-rapidity in Pb-Pb collisions at $\sqrt{s_{NN}} = 2.76$ TeV. *Phys. Rev. Lett.*, 106:032301, arXiv, 1012.1657.
- [33] [online] <https://particlesandfriends.wordpress.com/2016/10/14/evolution-of-collisions-and-qgp/>.
- [34] Ulrich W. Heinz. Concepts of heavy ion physics. In *2002 European School of high-energy physics, Pylos, Greece, 25 Aug-7 Sep 2002: Proceedings*, pages 165–238, arXiv, hep-ph/0407360.
- [35] [online] <http://mathworld.wolfram.com/ModifiedBesselFunctionoftheSecondKind.html>.
- [36] S. Wheaton and J. Cleymans. THERMUS: A Thermal model package for ROOT. *Comput. Phys. Commun.*, 180:84–106, arXiv, hep-ph/0407174.
- [37] A. Andronic, P. Braun-Munzinger, and J. Stachel. Hadron production in central nucleus-nucleus collisions at chemical freeze-out. *Nucl. Phys.*, A772:167–199, arXiv, nucl-th/0511071.
- [38] F. Becattini, J. Manninen, and M. Gazdzicki. Energy and system size dependence of chemical freeze-out in relativistic nuclear collisions. *Phys. Rev.*, C73:044905, arXiv, hep-ph/0511092.
- [39] E. Abbas et al. Mid-rapidity anti-baryon to baryon ratios in pp collisions at $\sqrt{s} = 0.9$, 2.76 and 7 TeV measured by ALICE. *Eur. Phys. J.*, C73:2496, arXiv, 1305.1562.
- [40] Betty Abelev et al. Centrality dependence of π , K, p production in Pb-Pb collisions at $\sqrt{s_{NN}} = 2.76$ TeV. *Phys. Rev.*, C88:044910, arXiv, 1303.0737.
- [41] A. Andronic, P. Braun-Munzinger, K. Redlich, and J. Stachel. Hadron yields, the chemical freeze-out and the QCD phase diagram. *J. Phys. Conf. Ser.*, 779(1):012012, arXiv, 1611.01347.
- [42] Betty Abelev et al. Pion, Kaon, and Proton Production in Central Pb–Pb Collisions at $\sqrt{s_{NN}} = 2.76$ TeV. *Phys. Rev. Lett.*, 109:252301, arXiv, 1208.1974.
- [43] Betty Bezverkhny Abelev et al. K_S^0 and Λ production in Pb-Pb collisions at $\sqrt{s_{NN}} = 2.76$ TeV. *Phys. Rev. Lett.*, 111:222301, arXiv, 1307.5530.
- [44] Betty Bezverkhny Abelev et al. Multi-strange baryon production at mid-rapidity in Pb-Pb collisions at $\sqrt{s_{NN}} = 2.76$ TeV. *Phys. Lett.*, B728:216–227, arXiv, 1307.5543. [Erratum: *Phys. Lett.*B734,409(2014)].
- [45] Betty Bezverkhny Abelev et al. $K^*(892)^0$ and $\phi(1020)$ production in Pb-Pb collisions at $\sqrt{s_{NN}} = 2.76$ TeV. *Phys. Rev.*, C91:024609, arXiv, 1404.0495.

- [46] Jaroslav Adam et al. ${}^3_{\Lambda}\text{H}$ and ${}^3_{\Lambda}\overline{\text{H}}$ production in Pb-Pb collisions at $\sqrt{s_{\text{NN}}} = 2.76$ TeV. *Phys. Lett.*, B754:360–372, arXiv, 1506.08453.
- [47] Jaroslav Adam et al. Production of light nuclei and anti-nuclei in pp and Pb-Pb collisions at energies available at the CERN Large Hadron Collider. *Phys. Rev.*, C93(2):024917, arXiv, 1506.08951.
- [48] Anton Andronic, Peter Braun-Munzinger, Krzysztof Redlich, and Johanna Stachel. Decoding the phase structure of QCD via particle production at high energy. arXiv, 1710.09425.
- [49] F. Becattini and Ulrich W. Heinz. Thermal hadron production in p p and p anti-p collisions. *Z. Phys.*, C76:269–286, arXiv, hep-ph/9702274. [Erratum: Z. Phys.C76,578(1997)].
- [50] F. Becattini, M. Gazdzicki, and J. Sollfrank. On chemical equilibrium in nuclear collisions. *Eur. Phys. J.*, C5:143–153, arXiv, hep-ph/9710529.
- [51] Johann Rafelski and Berndt Muller. Strangeness Production in the Quark - Gluon Plasma. *Phys. Rev. Lett.*, 48:1066, 1982. [Erratum: Phys. Rev. Lett.56,2334(1986)].
- [52] H. Leutwyler. Mesons in terms of quarks on a null plane. *Nucl. Phys.*, B76:413–444, 1974.
- [53] E. Andersen et al. Enhancement of central Lambda, Xi and Omega yields in Pb-Pb collisions at 158 A-GeV/c. *Phys. Lett.*, B433:209–216, 1998.
- [54] Fred Cooper and Graham Frye. Single-particle distribution in the hydrodynamic and statistical thermodynamic models of multiparticle production. *Phys. Rev. D*, 10:186–189, Jul 1974.
- [55] P. V. Ruuskanen. Transverse Hydrodynamics With a First Order Phase Transition in Very High-energy Nuclear Collisions. *Acta Phys. Polon.*, B18:551, 1987.
- [56] Ekkard Schnedermann, Josef Sollfrank, and Ulrich Heinz. Thermal phenomenology of hadrons from 200A GeV S+S collisions. *Phys. Rev. C*, 48:2462–2475, Nov 1993.
- [57] Rüdiger Scheibl and Ulrich Heinz. Coalescence and flow in ultrarelativistic heavy ion collisions. *Phys. Rev. C*, 59:1585–1602, Mar 1999.
- [58] Olga Barannikova and Fuqiang Wang. Mid-rapidity π^\pm , K^- and \bar{p} spectra and particle ratios from STAR. *Nuclear Physics A*, 715:458c – 461c, 2003. Quark Matter 2002.
- [59] Sergei A. Voloshin, Arthur M. Poskanzer, and Raimond Snellings. Collective phenomena in non-central nuclear collisions. *Landolt-Bornstein*, 23:293–333, arXiv, 0809.2949.
- [60] Xin-Nian Wang. Systematic study of high p_T hadron spectra in pp, p A and A A collisions from SPS to RHIC energies. *Phys. Rev.*, C61:064910, arXiv, nucl-th/9812021.

- [61] T. Matsui and H. Satz. J/ψ Suppression by Quark-Gluon Plasma Formation. *Phys. Lett.*, B178:416–422, 1986.
- [62] Vardan Khachatryan et al. Observation of Long-Range Near-Side Angular Correlations in Proton-Proton Collisions at the LHC. *JHEP*, 09:091, arXiv, 1009.4122.
- [63] Betty Abelev et al. Long-range angular correlations on the near and away side in p -Pb collisions at $\sqrt{s_{NN}} = 5.02$ TeV. *Phys. Lett.*, B719:29–41, arXiv, 1212.2001.
- [64] Serguei Chatrchyan et al. Long-range and short-range dihadron angular correlations in central PbPb collisions at a nucleon-nucleon center of mass energy of 2.76 TeV. *JHEP*, 07:076, arXiv, 1105.2438.
- [65] Jesper R. Christiansen and Peter Z. Skands. String Formation Beyond Leading Colour. *JHEP*, 08:003, arXiv, 1505.01681.
- [66] [online] <http://home.thep.lu.se/Pythia/pythia82html/ColourReconnection.html>.
- [67] Cheuk-Yin Wong. Momentum Kick Model Description of the Ridge in (Delta-phi)-(Delta eta) Correlation in pp Collisions at 7 TeV. *Phys. Rev.*, C84:024901, arXiv, 1105.5871.
- [68] Mark Strikman. Transverse Nucleon Structure and Multiparton Interactions. *Acta Phys. Polon.*, B42:2607–2630, arXiv, 1112.3834.
- [69] Sara Alderweireldt and Pierre Van Mechelen. Obtaining the CMS Ridge effect with Multiparton Interactions. In *Proceedings, 3rd International Workshop on Multiple Partonic Interactions at the LHC (MPI@LHC 2011): Hamburg, Germany, 21-25 Nov 2011*, pages 33–40, arXiv, 1203.2048.
- [70] Piotr Bozek and Wojciech Broniowski. Correlations from hydrodynamic flow in p-Pb collisions. *Phys. Lett.*, B718:1557–1561, arXiv, 1211.0845.
- [71] K. Werner, Iu. Karpenko, and T. Pierog. The ‘Ridge’ in Proton-Proton Scattering at 7 TeV. *Phys. Rev. Lett.*, 106:122004, arXiv, 1011.0375.
- [72] Jaroslav Adam et al. Enhanced production of multi-strange hadrons in high-multiplicity proton-proton collisions. *Nature Phys.*, 13:535–539, arXiv, 1606.07424.
- [73] Torbjorn Sjostrand, Stephen Mrenna, and Peter Z. Skands. A Brief Introduction to PYTHIA 8.1. *Comput. Phys. Commun.*, 178:852–867, arXiv, 0710.3820.
- [74] Christoffer Flensburg. Heavy ion initial states from DIPSY. *Prog. Theor. Phys. Suppl.*, 193:172–175, 2012.
- [75] T. Pierog, Iu. Karpenko, J. M. Katzy, E. Yatsenko, and K. Werner. EPOS LHC: Test of collective hadronization with data measured at the CERN Large Hadron Collider. *Phys. Rev. C*, 92:034906, Sep 2015.
- [76] Christian Bierlich, Gösta Gustafson, Leif Lönnblad, and Andrey Tarasov. Effects of Overlapping Strings in pp Collisions. *JHEP*, 03:148, arXiv, 1412.6259.

- [77] Christian Bierlich, Gösta Gustafson, and Leif Lönnblad. A shoving model for collectivity in hadronic collisions. arXiv, 1612.05132.
- [78] Shreyasi Acharya et al. Multiplicity dependence of light-flavor hadron production in pp collisions at $\sqrt{s} = 7$ TeV. *Phys. Rev.*, C99(2):024906, arXiv, 1807.11321.
- [79] Nicolò Jacazio. Spettri in momento trasverso di π^\pm , K^\pm , p e \bar{p} in funzione della molteplicità di particelle cariche in collisioni p-p a $\sqrt{s} = 7$ TeV con l'esperimento ALICE, 2015.
- [80] Nicolò Jacazio. Light flavor hadron production as a function of the charged-particle multiplicity at the LHC. *Nuovo Cim.*, C40(1):7, 2017.
- [81] Nicolò Jacazio. Multiplicity dependence of light flavour hadrons in small systems with the ALICE experiment. *J. Phys. Conf. Ser.*, 832(1):012019, 2017.
- [82] S Baird. Accelerators for pedestrians; rev. version, Feb 2007.
- [83] [online] <https://home.cern/about/experiments>.
- [84] ALICE technical design report of the dimuon forward spectrometer. 1999.
- [85] P Cortese et al. ALICE: Physics performance report, volume I. *J. Phys.*, G30:1517–1763, 2004.
- [86] Christian Wolfgang Fabjan et al. ALICE: Physics performance report, volume II. *J. Phys.*, G32:1295–2040, 2006.
- [87] G. Dellacasa et al. ALICE technical design report of the inner tracking system (ITS). 1999.
- [88] G. Dellacasa et al. ALICE: Technical design report of the time projection chamber. 2000.
- [89] J. Alme et al. The ALICE TPC, a large 3-dimensional tracking device with fast readout for ultra-high multiplicity events. *Nucl. Instrum. Meth.*, A622:316–367, arXiv, 1001.1950.
- [90] G. Dellacasa et al. ALICE technical design report of the time-of-flight system (TOF). 2000.
- [91] S. Beole et al. ALICE technical design report: Detector for high momentum PID. 1998.
- [92] Levente Molnar. The ALICE HMPID detector ready for collisions at the LHC. *Nuclear Instruments and Methods in Physics Research Section A: Accelerators, Spectrometers, Detectors and Associated Equipment*, 595(1):27 – 30, 2008. RICH 2007.
- [93] Giacomo Volpe. Results from cosmics and first LHC beam with the ALICE HMPID detector. *Nucl. Phys.*, A830:539C–542C, arXiv, 0907.4579.
- [94] G. Dellacasa et al. ALICE technical design report of the zero degree calorimeter (ZDC). 1999.

- [95] ALICE Collaboration. The ALICE ZDC. [online] <http://alice.web.cern.ch/detectors/more-details-alice-zdc>.
- [96] P Cortese et al. ALICE technical design report on forward detectors: FMD, T0 and V0. 2004.
- [97] E. Abbas et al. Performance of the ALICE VZERO system. *JINST*, 8:P10016, arXiv, 1306.3130.
- [98] Jaroslav Adam et al. Particle identification in ALICE: a Bayesian approach. *Eur. Phys. J. Plus*, 131(5):168, arXiv, 1602.01392.
- [99] Francesco Noferini. The ALICE PID performance in Run 1 and perspectives in view of Run 2. In *Proceedings, 3rd Large Hadron Collider Physics Conference (LHCP 2015): St. Petersburg, Russia, August 31-September 5, 2015*, pages 523–528. Kurchatov Institute, Kurchatov Institute, 2016.
- [100] Christian Wolfgang Fabjan, L Jirdén, V Lindestruth, Lodovico Riccati, D Rorich, Pierre Van de Vyvre, O Villalobos Baillie, and Hans de Groot. *ALICE trigger data-acquisition high-level trigger and control system: Technical Design Report*. Technical Design Report ALICE. CERN, 2004.
- [101] CERN Collaboration. Accelerator Performance and Statistics. [online] <http://acc-stats.web.cern.ch/acc-stats>.
- [102] Jan Fiete Grosse-Oetringhaus, Chiara Zampolli, Alberto Colla, and Federico Carminati. The ALICE online-offline framework for the extraction of conditions data. *J. Phys. Conf. Ser.*, 219:022010, 2010.
- [103] P Cortese, Federico Carminati, Christian Wolfgang Fabjan, Lodovico Riccati, and Hans de Groot. *ALICE computing: Technical Design Report*. Technical Design Report ALICE. CERN, 2005. Submitted on 15 Jun 2005.
- [104] M. Yamaga et al. RPC systems for BELLE detector at KEKB. *Nucl. Instrum. Meth.*, A456:109–112, 2000.
- [105] R. Santonico and R. Cardarelli. Development of Resistive Plate Counters. *Nucl. Instrum. Meth.*, 187:377–380, 1981.
- [106] A. Alici, G. Cara Romeo, Jinsook Kim, D. Hatzifotiadou, Y. Sun, G. Valenti, M.C.S. Williams, D. Yakorev, and A. Zichichi. Aging and rate effects of the Multigap RPC studied at the Gamma Irradiation Facility at CERN. *Nuclear Instruments and Methods in Physics Research Section A: Accelerators, Spectrometers, Detectors and Associated Equipment*, 579(3):979 – 988, 2007.
- [107] G. Dellacasa et al. ALICE technical design report of the photon spectrometer (PHOS). 1999.
- [108] F. Anghinolfi, P. Jarron, A. N. Martemyanov, E. Usenko, H. Wenninger, M. C. S. Williams, and A. Zichichi. NINO: An ultra-fast and low-power front-end amplifier/discriminator ASIC designed for the multigap resistive plate chamber. *Nucl. Instrum. Meth.*, A533:183–187, 2004.

- [109] M. Mota and J. Christiansen. A high-resolution time interpolator based on a delay locked loop and an RC delay line. *IEEE Journal of Solid-State Circuits*, 34(10):1360–1366, Oct 1999.
- [110] A. Akindinov et al. A topological trigger based on the Time-of-Flight detector for the ALICE experiment. *Nucl. Instrum. Meth.*, A602:372–376, 2009.
- [111] R. Brun and F. Rademakers. ROOT: An object oriented data analysis framework. *Nucl. Instrum. Meth.*, A389:81–86, 1997. See also <http://root.cern.ch/>.
- [112] [online] <https://github.com/alisw/AliRoot>.
- [113] [online] <https://github.com/alisw/AliDPG>.
- [114] E Bruna, A Dainese, M Masera, and F Prino. Vertex reconstruction for proton-proton collisions in ALICE. Nov 2009.
- [115] R. Fruhwirth. Application of Kalman filtering to track and vertex fitting. *Nucl. Instrum. Meth.*, A262:444–450, 1987.
- [116] Jaroslav Adam et al. Charged-particle multiplicities in proton–proton collisions at $\sqrt{s} = 0.9$ to 8 TeV. *Eur. Phys. J.*, C77(1):33, arXiv, 1509.07541.
- [117] Francesca Carnesecchi. Performance of the ALICE Time-Of-Flight detector at the LHC. In *14th Workshop on Resistive Plate Chambers and Related Detectors (RCP2018) Puerto Vallarta, Jalisco State, Mexico, February 19-23, 2018*, arXiv, 1806.03825.
- [118] Nicolò Jacazio. PID performance of the ALICE-TOF detector in Run 2. In *6th Large Hadron Collider Physics Conference (LHCP 2018) Bologna, Italy, June 4-9, 2018*, arXiv, 1809.00574.
- [119] Preghenella Roberto. Un nuovo record per il Time of Flight di ALICE. [online] <https://www.primapagina.sif.it/article/602/un-nuovo-record-per-il-time-of-flight-di-alice>.
- [120] Nicolò Jacazio. [online] <https://gitlab.cern.ch/njacazio/TOFQA>.
- [121] B Abelev et al. Technical Design Report for the Upgrade of the ALICE Inner Tracking System, Nov 2013.
- [122] Upgrade of the ALICE Time Projection Chamber, Oct 2013.
- [123] P Antonioli, A Kluge, and W Riegler. Upgrade of the ALICE Readout and Trigger System, Sep 2013.
- [124] P Buncic, M Krzewicki, and P Vande Vyvre. Technical Design Report for the Upgrade of the Online-Offline Computing System, Apr 2015.
- [125] Shreyasi Acharya et al. The ALICE Transition Radiation Detector: construction, operation, and performance. *Nucl. Instrum. Meth.*, A881:88–127, arXiv, 1709.02743.
- [126] Nicolò Jacazio. [online] <https://gitlab.cern.ch/njacazio/TOFCalibration>.

- [127] H. H. Gutbrod, K. D. Gross, W. F. Henning, and V. Metag. An international accelerator facility for beams of ions and anti-protons. Conceptual design report. 2001.
- [128] René Brun, F. Bruyant, Federico Carminati, Simone Giani, M. Maire, A. McPherson, G. Patrick, and L. Urban. GEANT Detector Description and Simulation Tool. 1994.
- [129] Pierre-Alexandre Duverne. Using deep neural network to reduce mismatch in ALICE Time of Fligth. Sep 2018.
- [130] [online] <https://root.cern.ch/root/html516/TMultiLayerPerceptron.html>.
- [131] Carsten Peterson, Thorsteinn Rognvaldsson, and Leif Lonnblad. JETNET 3.0: A Versatile artificial neural network package. *Comput. Phys. Commun.*, 81:185–220, 1994.
- [132] François Chollet et al. Keras. <https://keras.io>, 2015.
- [133] Martín Abadi et al. TensorFlow: Large-scale machine learning on heterogeneous systems, 2015. Software available from tensorflow.org.
- [134] ALICE-ANA-2013-601. [online] <https://aliceinfo.cern.ch/Notes/node/124>.
- [135] [online] <https://github.com/alisw/AliPhysics>.
- [136] [online] <https://root.cern.ch/proof>.
- [137] Xin-Nian Wang and Miklos Gyulassy. HIJING: A Monte Carlo model for multiple jet production in p p, p A and A A collisions. *Phys. Rev.*, D44:3501–3516, 1991.
- [138] [online] <https://twiki.cern.ch/twiki/bin/viewauth/ALICE/AliceHMTFBeamBackground>.
- [139] The ALICE definition of primary particles. Jun 2017.
- [140] Antonin Maire. ALICE TPC sectors and pad rows. General Photo, Oct 2011.
- [141] Wouter Verkerke and David P. Kirkby. The RooFit toolkit for data modeling. *eConf*, C0303241:MOLT007, arXiv, physics/0306116. [,186(2003)].
- [142] Roger J. Barlow and Christine Beeston. Fitting using finite Monte Carlo samples. *Comput. Phys. Commun.*, 77:219–228, 1993.
- [143] A. Nappi. A Pitfall in the use of extended likelihood for fitting fractions of pure samples in mixed samples. *Comput. Phys. Commun.*, 180:269–275, arXiv, 0803.2711.
- [144] K. Aamodt et al. Midrapidity Antiproton-to-Proton Ratio in $p p$ Collisons at $\sqrt{s} = 0.9$ and 7 TeV Measured by the ALICE Experiment. *Phys. Rev. Lett.*, 105:072002, Aug 2010.
- [145] G. Battistoni, F. Cerutti, A. Fassò, A. Ferrari, S. Muraro, J. Ranft, S. Roesler, and P. R. Sala. The FLUKA code: description and benchmarking. *AIP Conference Proceedings*, 896(1):31–49, <https://aip.scitation.org/doi/pdf/10.1063/1.2720455>.

- [146] Nicolò Jacazio. Production of identified charged hadrons in Pb–Pb collisions at $\sqrt{s_{NN}} = 5.02$ TeV. *Nucl. Phys.*, A967:421–424, arXiv, 1704.06030.
- [147] Betty Bezverkhny Abelev et al. Multiplicity Dependence of Pion, Kaon, Proton and Lambda Production in p-Pb Collisions at $\sqrt{s_{NN}} = 5.02$ TeV. *Phys. Lett.*, B728:25–38, arXiv, 1307.6796.
- [148] Wenbin Zhao, Hao-jie Xu, and Huichao Song. *Eur. Phys. J. C*, 77:645, 2017.
- [149] Rajeev S. Bhalerao, Amaresh Jaiswal, and Subrata Pal. *Phys. Rev. C*, 92:014903, 2015.
- [150] S. McDonald et al. *Phys. Rev. C*, 95:064913, 2017.
- [151] T. Pierog et al. *Phys. Rev. C*, 92:034906, 2015.
- [152] Centrality dependence of the charged-particle multiplicity density at midrapidity in Pb-Pb collisions at $\sqrt{s_{NN}} = 5.02$ TeV. Dec 2015.
- [153] Jaroslav Adam et al. Centrality dependence of the nuclear modification factor of charged pions, kaons, and protons in Pb-Pb collisions at $\sqrt{s_{NN}} = 2.76$ TeV. *Phys. Rev.*, C93(3):034913, arXiv, 1506.07287.
- [154] Constantino Tsallis. Possible Generalization of Boltzmann-Gibbs Statistics. *J. Statist. Phys.*, 52:479–487, 1988.
- [155] B. I. Abelev et al. Strange particle production in p+p collisions at $s^{**}(1/2) = 200$ -GeV. *Phys. Rev.*, C75:064901, arXiv, nucl-ex/0607033.

Appendix A

Entropy, partition functions and global observables

In general indicating with k_B the Boltzmann constant, we can define the entropy \mathbb{S} for a system at equilibrium as:

$$\mathbb{S} = k_B \ln \Omega \quad (\text{A.1})$$

Where Ω is defined by the number of microstates that can be occupied by the system. Extending this definition to an ensemble of v copies of the system, the probability of finding the microstate i is $p_i = v_i/v$, where v_i is the number of times each microstate is observed (therefore $\sum_{\text{All } i} v_i \equiv v$). We define the number of microstates for that ensemble of v copies of the system as:

$$\Omega_v = \frac{v!}{\prod_{\text{All } i} v_i!} \quad (\text{A.2a})$$

$$\ln \Omega_v = v \ln v - v - \sum_{\text{All } i} (v_i \ln v_i - v_i) = \sum_{\text{All } i} v_i \cdot (\ln v - \ln v_i) \quad (\text{A.2b})$$

$$\ln \Omega_v = -v \sum_{\text{All } i} p_i \ln p_i \quad (\text{A.2c})$$

Therefore the entropy for the ensemble (Eq. A.3a) and the mean entropy (Eq. A.3b) are defined as:

$$S_v = k_B \ln \Omega_v = -v k_B \sum_{All\ i} p_i \ln p_i \quad (A.3a)$$

$$\langle S \rangle \equiv \frac{S_v}{v} = -k_B \sum_{All\ i} p_i \ln p_i \quad (A.3b)$$

This relation (Eq. A.3b) is valid independently on the type of chosen ensemble (micro-canonical, canonical, grand-canonical). For a grand-canonical ensemble the definition of p_i can be made by using the baryochemical potential μ_B introduced in Section 1.1.2 together with N_i i.e. the number of particles associated to it. In the grand-canonical ensemble charge conservation is only ensured on average as the system can exchange both particles and energy with its surroundings. The choice for this ensemble seems natural to treat particle production in heavy-ion collisions as the volume of the system created in a collision is considerably large with respect to the hadron dimensions.

$$p_i = \frac{e^{-\frac{(E_i - \mu_B N_i)}{k_B T}}}{Z} \quad (A.4)$$

At this point we can define the partition function Z :

$$Z \equiv \sum_{All\ i} p_i = \sum_{All\ i} e^{-\frac{(E_i - \mu_B N_i)}{k_B T}} \quad (A.5)$$

$$\beta \equiv \frac{1}{k_B T} \rightarrow Z = \sum_{All\ i} e^{-(E_i - \mu_B N_i) \cdot \beta} \quad (A.6)$$

The partition function Z carries important information on the system and it is the starting point for the derivation of the the mean energy $\langle E \rangle$ (Eq. A.7c):

$$-\frac{1}{Z} \frac{\partial Z}{\partial \beta} = \frac{\sum_{All\ i} (E_i - \mu_B N_i) e^{-(E_i - \mu_B N_i) \cdot \beta}}{Z} \quad (A.7a)$$

$$-\frac{1}{Z} \frac{\partial Z}{\partial \beta} = \frac{\sum_{All\ i} E_i e^{-(E_i - \mu_B N_i) \cdot \beta}}{Z} - \frac{\sum_{All\ i} \mu_B N_i e^{-(E_i - \mu_B N_i) \cdot \beta}}{Z} \quad (A.7b)$$

$$-\frac{1}{Z} \frac{\partial Z}{\partial \beta} = \langle E \rangle - \mu_B \langle N \rangle \rightarrow \langle E \rangle = -\left(\frac{\partial \ln Z}{\partial \beta}\right) + \mu_B \langle N \rangle \quad (A.7c)$$

From similar considerations one can obtain the mean number of particles $\langle N \rangle$:

$$\frac{1}{Z} \frac{\partial Z}{\partial \mu_B} = \frac{\sum_{All \ i} \beta \cdot N_i e^{-(E_i - \mu_B N_i) \cdot \beta}}{Z} \quad (A.8a)$$

$$\frac{1}{Z} \frac{\partial Z}{\partial \mu_B} = \beta \langle N \rangle \rightarrow \langle N \rangle = \frac{1}{\beta} \left(\frac{\partial \ln Z}{\partial \mu_B} \right) \quad (A.8b)$$

Finally from Eq. A.3b and using Eq. A.7c:

$$\langle S \rangle = -k_B \sum_{All \ i} p_i \ln \frac{e^{-(E_i - \mu_B N_i) \cdot \beta}}{Z} = -k_B \sum_{All \ i} p_i (-\beta \cdot (E_i - \mu_B N_i) - \ln Z) \quad (A.9a)$$

$$\langle S \rangle = \frac{1}{T} (\langle E \rangle - \mu_B \langle N \rangle) + k_B \ln Z \quad (A.9b)$$

$$\langle S \rangle = \frac{k_B T^2}{T} \frac{\partial \ln Z}{\partial T} + k_B \ln Z = k_B \frac{\partial (T \cdot \ln Z)}{\partial T} \quad (A.9c)$$

In order to extend these relations to describe the fireball one has to include the quantum mechanical behaviour of all type of particles (bosons and fermions). In addition, all particle species s that can potentially be created have to be considered for all the possible i states. This can be done by extending the partition function:

$$Z_s(T, V, \mu_s) = \sum_{All \ i} e^{-(E_i - \mu_s N_i) \cdot \beta} \quad (A.10)$$

N_i and E_i can be defined from the α eigenstates (with energy E_α), solution of the single particle Hamiltonian

$$N_i = \sum_{\alpha} n_{\alpha}^{(i)} \quad (A.11a)$$

$$E_i = \sum_{\alpha} n_{\alpha}^{(i)} \cdot E_{\alpha} \quad (A.11b)$$

By using Eq. A.11a and Eq. A.11b in Eq. A.10 with $\chi_{\alpha} = e^{-\beta \cdot (E_{\alpha} - \mu_s)}$ one obtains:

$$Z_s(T, V, \mu_s) = \sum_{All \ i} e^{-\beta \cdot \sum_{\alpha} (E_{\alpha} - \mu_s) \cdot n_{\alpha}^{(i)}} = \sum_{All \ i} \prod_{\alpha} e^{-\beta \cdot (E_{\alpha} - \mu_s) \cdot n_{\alpha}^{(i)}} \quad (A.12a)$$

$$Z_s(T, V, \mu_s) = \sum_{All \ i} \prod_{\alpha} \chi_{\alpha}^{n_{\alpha}^{(i)}} \equiv \prod_{\alpha} \sum_{All \ n_{\alpha}} \chi_{\alpha}^{n_{\alpha}} \quad (A.12b)$$

Now a differentiation is needed to take into account the Fermi-Dirac or Bose-Einstein statistics. For the first case the number available states per energy level E_α per is only 2 ($n_\alpha = 0, 1$):

$$Z_s(T, V, \mu_s) = \prod_{\alpha} \sum_{n_\alpha=0}^1 \chi_\alpha^{n_\alpha} = \prod_{\alpha} (\chi_\alpha^0 + \chi_\alpha^1) \equiv \prod_{\alpha} (1 + e^{-\beta \cdot (E_\alpha - \mu_s)}) \quad (\text{A.13})$$

For the Bose-Einstein statistics the number of states available for a single energy level is infinite:

$$Z_s(T, V, \mu_s) = \prod_{\alpha} \sum_{n_\alpha=0}^{\infty} \chi_\alpha^{n_\alpha} \equiv \prod_{\alpha} \frac{1}{1 - \chi_\alpha} = \prod_{\alpha} (1 - e^{-\beta \cdot (E_\alpha - \mu_s)})^{-1} \quad (\text{A.14})$$

With the condition for the convergence of the sum $\chi_\alpha < 1$ i.e. $E_\alpha - \mu_s > 0 \rightarrow E_\alpha > \mu_s, \forall \alpha \rightarrow E_0 > \mu_s$ (where E_0 is the least energetic state). The generic partition function for both fermions and bosons can be defined as:

$$Z_s(T, V, \mu_s) = \prod_{\alpha} (1 + \theta_s e^{-\beta \cdot (E_\alpha - \mu_s)})^{\theta_s} \quad (\text{A.15a})$$

$$\ln Z_s(T, V, \mu_s) = \sum_{\alpha} \theta_s \ln(1 + \theta_s e^{-\beta \cdot (E_\alpha - \mu_s)}) \quad (\text{A.15b})$$

With $\theta_s = 1$ for fermions and $\theta_s = -1$ for bosons. These considerations can easily be extended to the macroscopic case in a volume ΔV transforming the sum in Eq. A.15b in a integral over the particle momenta: $\sum_{\alpha} \rightarrow \frac{\Delta V}{s\pi^2\hbar^3} g_s \int p^2 dp$. Where g_i takes into account the spin degeneracy of the energetic level ($g_i = 2 \times \text{spin} + 1$) and $\lambda_s = e^{\beta\mu_s}$ is the “fugacity” term for the s species.

$$\begin{aligned} \ln Z_s(T, V, \mu_s) &= \frac{\Delta V g_s}{(2\pi\hbar)^3} \int d^3 p \theta_s \ln(1 + \theta_s e^{-\beta \cdot (E - \mu_s)}) \\ &\equiv \frac{\Delta V g_s}{2\pi^2\hbar^3} \int_0^\infty \theta_s p^2 dp \ln(1 + \theta_s \lambda_s e^{-\beta \cdot E}) \end{aligned} \quad (\text{A.16})$$

The particle multiplicity corresponding to each species s can now be determined from Eq. A.8b and Eq. A.16:

$$\begin{aligned} \langle N_s \rangle &\equiv \frac{1}{\beta} \left(\frac{\partial \ln Z}{\partial \mu_B} \right) = \frac{\Delta V g_s}{\beta 2\pi^2\hbar^3} \int_0^\infty p^2 dp \frac{\lambda_s \beta e^{-\beta \cdot E}}{(1 + \theta_s \lambda_s e^{-\beta \cdot E})} \\ &= \frac{\Delta V g_s}{2\pi^2\hbar^3} \int_0^\infty dp \frac{p^2}{e^{\beta \cdot E / \lambda_s} + \theta_s} \end{aligned} \quad (\text{A.17})$$

We can define the phase-space distribution of particles of type s in local thermal equilibrium as:

$$f_s = \frac{g_s}{e^{\beta \cdot E} / \lambda_s + \theta_s} \quad (\text{A.18})$$

This definition is valid in the rest frame (as for the local heat bath), we can generalize by using the 4-momenta and 4-velocity $E \rightarrow p \cdot u$ and obtaining the same result when $u^\mu = (1, 0, 0, 0)$ (in the rest frame).

$$f_s(x, p) = \frac{g_s}{e^{\beta \cdot p \cdot u} / \lambda_s + \theta_s} \quad (\text{A.19})$$

Appendix B

Partition function for the Grand-Canonical ensemble

$$\ln Z_s(T, V, \mu_s) = \frac{\Delta V g_s}{2\pi^2 \hbar^3} \int_0^\infty \theta_s p^2 dp \ln \left(1 + \theta_s \cdot \lambda_s \cdot e^{-\beta \cdot E} \right) \quad (\text{B.1})$$

Replacing the logarithm with its Taylor expansion:

$$\ln(1 + \theta_s x) = - \sum_{k=1}^{\infty} \frac{(-1 \cdot \theta_s \cdot x)^k}{k} \quad (\text{B.2})$$

converging under the assumption $|x| < 1$ i.e. for $\lambda_s \cdot e^{-\beta \cdot E} < 1 \Rightarrow \mu_s < E$:

$$\ln Z_s(T, V, \mu_s) = \frac{\Delta V g_s}{2\pi^2 \hbar^3} \int_0^\infty \theta_s p^2 dp \sum_{k=1}^{\infty} \left(\frac{(-\theta_s \lambda_s e^{-\beta \cdot E})^k}{k} \right) \quad (\text{B.3})$$

$$\ln Z_s(T, V, \mu_s) = \frac{\Delta V g_s}{2\pi^2 \hbar^3} \sum_{k=1}^{\infty} \frac{(\theta_s \lambda_s)^k}{k} \int_0^\infty p^2 dp e^{-k\beta \cdot E} \quad (\text{B.4})$$

We can now compute the integration

$$\ln Z_s(T, V, \mu_s) = \frac{\Delta V g_s}{2\pi^2 \hbar^3} \sum_{k=1}^{\infty} \frac{(\theta_s \lambda_s)^k}{k} \left[\frac{p^3}{3} \cdot e^{-k\beta \cdot E} \Big|_0^\infty - \int_0^\infty dp \frac{p^3}{3} e^{-k\beta \cdot E} (-k\beta) \frac{dE}{dp} \right] \quad (\text{B.5})$$

While the first term vanishes at the 0 and ∞ we can use:

$$E = \sqrt{p^2 + m_s^2} \Rightarrow \frac{dE}{dp} = \frac{1}{2\sqrt{p^2 + m_s^2}} \cdot 2p \equiv \frac{p}{E} \quad (\text{B.6})$$

Which yields:

$$\ln Z_s(T, V, \mu_s) = \frac{\Delta V g_s}{2\pi^2 \hbar^3} \sum_{k=1}^{\infty} \frac{(\theta_s \lambda_s)^k}{k} \int_0^{\infty} dp \frac{p^3}{3} e^{-k\beta \cdot E(k\beta)} \frac{p}{E} \quad (\text{B.7})$$

We can substitute p with E :

$$\ln Z_s(T, V, \mu_s) = \frac{\Delta V g_s}{2\pi^2 \hbar^3} \sum_{k=1}^{\infty} \frac{(\theta_s \lambda_s)^k}{k} \int_{m_s}^{\infty} \frac{E}{p} \cdot \frac{p}{E} dE \frac{\sqrt{E^2 - m_s^2}^3}{3} e^{-k\beta \cdot E(k\beta)} \quad (\text{B.8})$$

Using $x = k\beta E$:

$$\ln Z_s(T, V, \mu_s) = \frac{\Delta V g_s}{2\pi^2 \hbar^3} \sum_{k=1}^{\infty} \frac{(\theta_s \lambda_s)^k}{k} \int_{m_s}^{\infty} dk\beta E \frac{[(k\beta E)^2 - (k\beta m_s)^2]^{\frac{3}{2}}}{3(k\beta)^3} e^{-x} \quad (\text{B.9})$$

$$\ln Z_s(T, V, \mu_s) = \frac{\Delta V g_s}{2\pi^2 \hbar^3} \sum_{k=1}^{\infty} \frac{(\theta_s \lambda_s)^k}{k} \frac{m_s^2}{k\beta} \int_{k\beta m_s}^{\infty} dx \frac{[x^2 - (k\beta m_s)^2]^{\frac{3}{2}}}{3(k\beta m_s)^2} e^{-x} \quad (\text{B.10})$$

Using $w_s = k\beta m_s$:

$$\ln Z_s(T, V, \mu_s) = \frac{\Delta V g_s}{2\pi^2 \hbar^3} \sum_{k=1}^{\infty} \frac{(\theta_s \lambda_s)^k}{k} \frac{m_s^2}{k\beta} \int_{w_s}^{\infty} dx \frac{[x^2 - w_s^2]^{\frac{3}{2}}}{3 \cdot w_s^2} e^{-x} \quad (\text{B.11})$$

$$\ln Z_s(T, V, \mu_s) = \frac{\Delta V g_s}{2\pi^2 \hbar^3} \sum_{k=1}^{\infty} \frac{(\theta_s \lambda_s)^k \cdot m_s^2}{k^2 \beta} \int_{w_s}^{\infty} dx \frac{w_s^3 [\frac{x^2}{w_s^2} - 1]^{\frac{3}{2}}}{3 \cdot w_s^2} e^{-x} \quad (\text{B.12})$$

$$\ln Z_s(T, V, \mu_s) = \frac{\Delta V g_s}{2\pi^2 \hbar^3} \sum_{k=1}^{\infty} \frac{(\theta_s \lambda_s)^k \cdot m_s^2 \cdot w_s}{3k^2 \beta} \int_{w_s}^{\infty} dx [\frac{x^2}{w_s^2} - 1]^{\frac{3}{2}} e^{-x} \quad (\text{B.13})$$

Defining $y_s = x/w_s$:

$$\ln Z_s(T, V, \mu_s) = \frac{\Delta V g_s}{2\pi^2 \hbar^3} \sum_{k=1}^{\infty} \frac{(\theta_s \lambda_s)^k \cdot m_s^2 \cdot w_s}{3k^2 \beta} \int_1^{\infty} w_s dy [y^2 - 1]^{\frac{3}{2}} e^{-w_s \cdot y} \quad (\text{B.14})$$

Introducing the modified Bessel function:

$$K_n(q) = \frac{\sqrt{\pi}}{(n - \frac{1}{2})!} \left(\frac{q}{2}\right)^n \int_0^{\infty} dy (y^2 - 1)^{n - \frac{1}{2}} e^{-q \cdot y} \quad (\text{B.15})$$

Which for $n \equiv 2$ is:

$$K_2(q) = \frac{\sqrt{\pi}}{(2 - \frac{1}{2})!} \left(\frac{q}{2}\right)^2 \int_0^\infty dy (y^2 - 1)^{2 - \frac{1}{2}} e^{-q \cdot y} \quad (\text{B.16})$$

$$K_2(q) = \frac{\sqrt{\pi}}{\left(\frac{3}{2}\right)!} \frac{q^2}{4} \int_0^\infty dy (y^2 - 1)^{\frac{3}{2}} e^{-q \cdot y} \quad (\text{B.17})$$

$$K_2(q) = \frac{\sqrt{\pi}}{\frac{3\sqrt{\pi}}{4}} \frac{q^2}{4} \int_0^\infty dy (y^2 - 1)^{\frac{3}{2}} e^{-q \cdot y} \quad (\text{B.18})$$

$$K_2(q) = \frac{q^2}{3} \int_0^\infty dy (y^2 - 1)^{\frac{3}{2}} e^{-q \cdot y} \quad (\text{B.19})$$

Now looking at Eq. B.14 we can identify a structure which is exactly like the one shown in Eq. B.19:

$$\ln Z_s(T, V, \mu_s) = \frac{\Delta V g_s}{2\pi^2 \hbar^3} \sum_{k=1}^{\infty} \frac{(\theta_s \lambda_s)^k \cdot m_s^2}{k^2 \beta} \left[\frac{w_s^2}{3} \int_1^\infty dy [y^2 - 1]^{\frac{3}{2}} e^{-w_s \cdot y} \right] \quad (\text{B.20})$$

$$\ln Z_s(T, V, \mu_s) = \frac{\Delta V g_s}{2\pi^2 \hbar^3} \sum_{k=1}^{\infty} \frac{(\theta_s \lambda_s)^k \cdot m_s^2}{k^2 \beta} K_2(y) \quad (\text{B.21})$$

We can conclude that for the Grand-Canonical ensemble the partition function can be written as:

$$\ln Z_s(T, V, \mu_s) = \frac{\Delta V g_s}{2\pi^2 \hbar^3} \sum_{k=1}^{\infty} \frac{(\theta_s \lambda_s)^k \cdot m_s^2}{k^2 \beta} K_2(k \beta m_s) \quad (\text{B.22})$$

Appendix C

The Cooper-Frye formula

The number of particles created in the fireball for each species was already obtained in Eq. A.17. The same can be done for the species s by using geometrical considerations (and using the phase-space distribution as in Eq. A.19) and summing over all particle currents passing through a hermetical hyper-surface Σ surrounding the collision site:

$$\langle N_s \rangle = \int_{\Sigma} d^3 \sigma(x) j_s^\mu(x) \quad (C.1a)$$

$$j_s^\mu(x) = \frac{1}{(2\pi\hbar)^3} \int d^3 p u^\mu f_s(x, p) \quad (C.1b)$$

$$\langle N_s \rangle = \int_{\Sigma} d^3 \sigma(x) \left(\frac{1}{(2\pi\hbar)^3} \int d^3 p u^\mu f_s(x, p) \right) \quad (C.1c)$$

The goal of this approach is to count the number of particles that flew through the closed surface surrounding the collision. In principle this can be independent on the size of the surface as long as enough time passes from the time of the collision so that even slower particles can be considered. For $t \rightarrow \infty$ all particles created in the collision are expected to pass through the surface, giving the possibility to compute the total number of particles created. By replacing the particle velocity u^μ with $u^\mu = \frac{p^\mu}{E}$:

$$\langle N_s \rangle = \int_{\Sigma} d^3 \sigma(x) \left(\frac{1}{(2\pi\hbar)^3} \int d^3 p \frac{p^\mu}{E} f_s(x, p) \right) \quad (C.2)$$

We can obtain now the momentum dependent particle distribution for the species s by differentiating in $d^3 p$ and taking out E :

$$E \frac{d \langle N_s \rangle}{d^3 p} = \frac{1}{(2\pi\hbar)^3} \int_{\Sigma} d^3 \sigma(x) p f_s(x, p) \quad (C.3)$$

This expression can be further refined by introducing kinematic variables such as the rapidity y , the pseudo-rapidity η , the transverse and longitudinal (to the beam axis) momentum p_T and p_L , the transverse mass m_T :

$$y = \frac{1}{2} \cdot \ln \frac{E + p_L}{E - p_L} \quad (\text{C.4a})$$

$$\eta = \frac{1}{2} \cdot \ln \frac{E + u_L}{E - u_L} \quad (\text{C.4b})$$

$$p_T = \sqrt{p_x^2 + p_y^2}, \text{ being } p_z \text{ along the beam direction} \quad (\text{C.4c})$$

$$m_T = \sqrt{m^2 + p_T^2} \equiv \sqrt{m^2 + p_x^2 + p_y^2} \quad (\text{C.4d})$$

$$m_T dm_T \equiv p_T dp_T \quad (\text{C.4e})$$

Which gives the expression in its final form:

$$E \frac{d\langle N_s \rangle}{d^3 p} \equiv E \frac{d\langle N_s \rangle}{dy p_T dp_T d\phi} \equiv E \frac{d\langle N_s \rangle}{dym_T dm_T d\phi} = \frac{1}{(2\pi\hbar)^3} \int_{\Sigma} d^3 \sigma(x) p f_s(x, p) \quad (\text{C.5})$$

Appendix D

The TOF Quality Assurance

An example of the TOF QA is reported here:

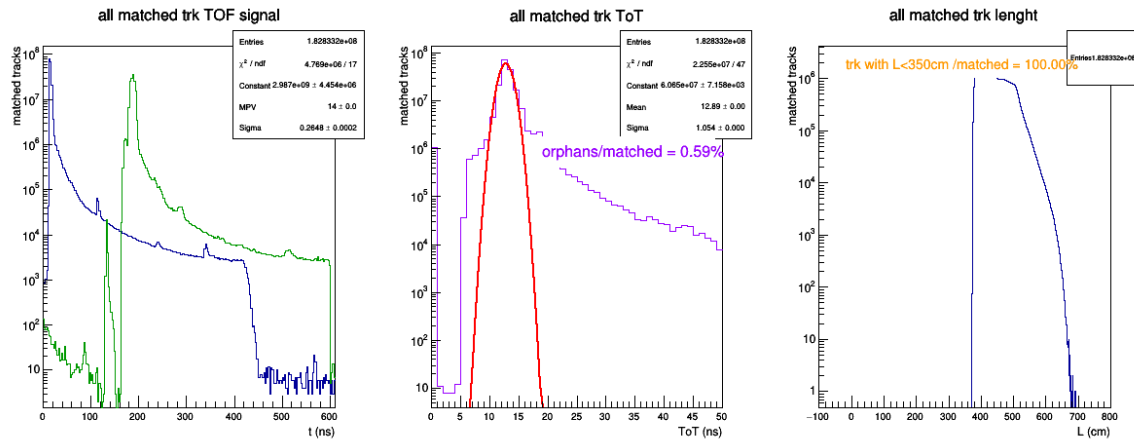


Fig. D.1 Track Properties

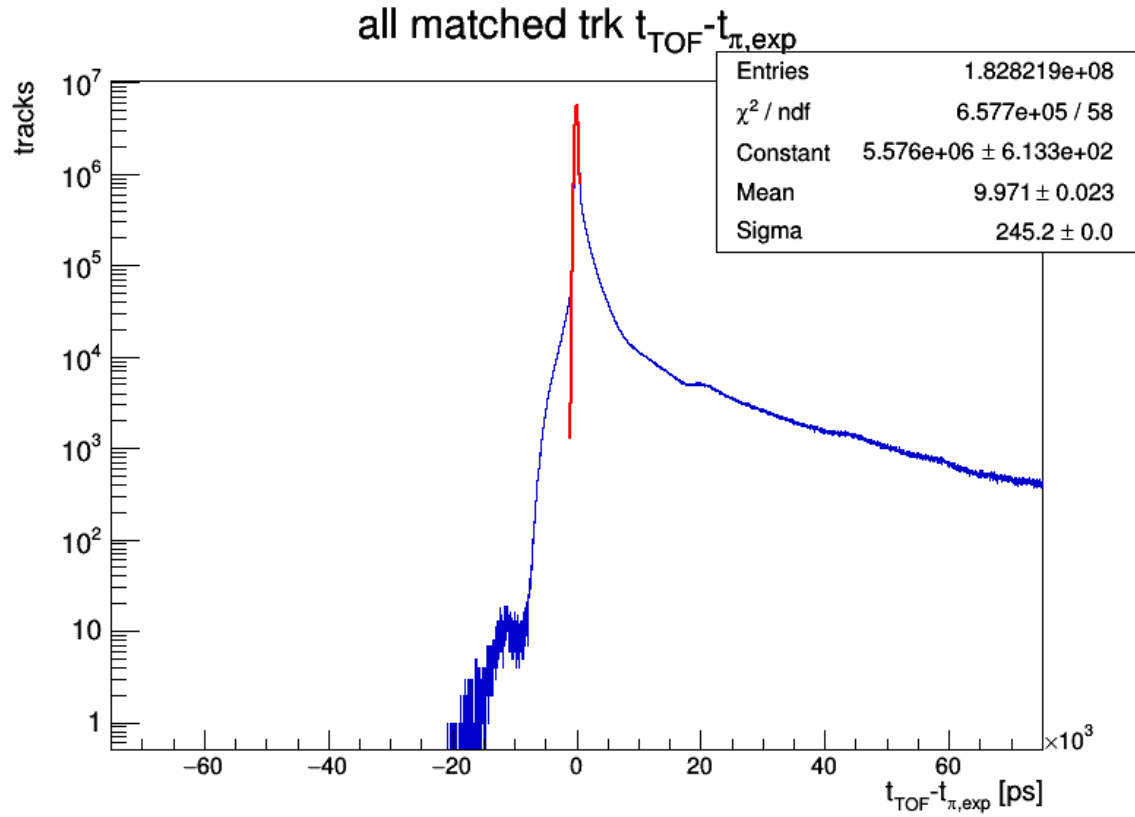


Fig. D.2 TOF time

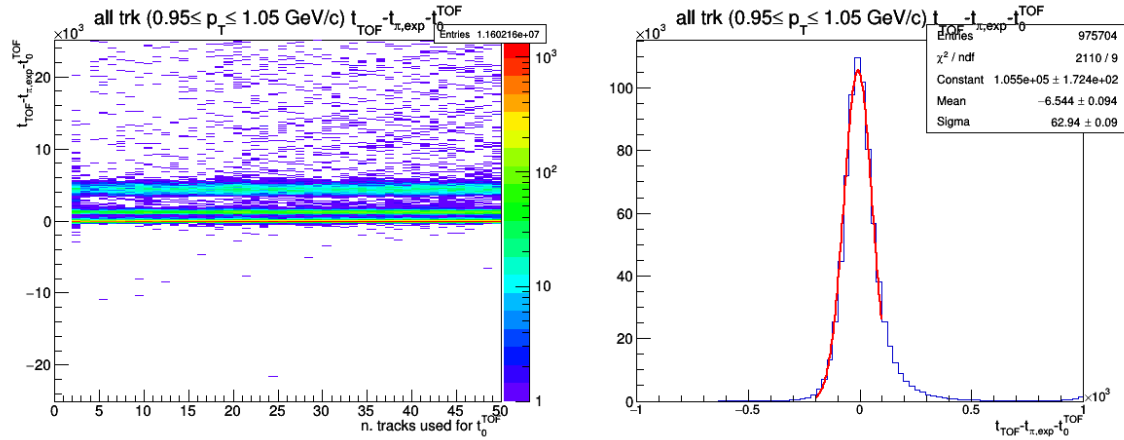
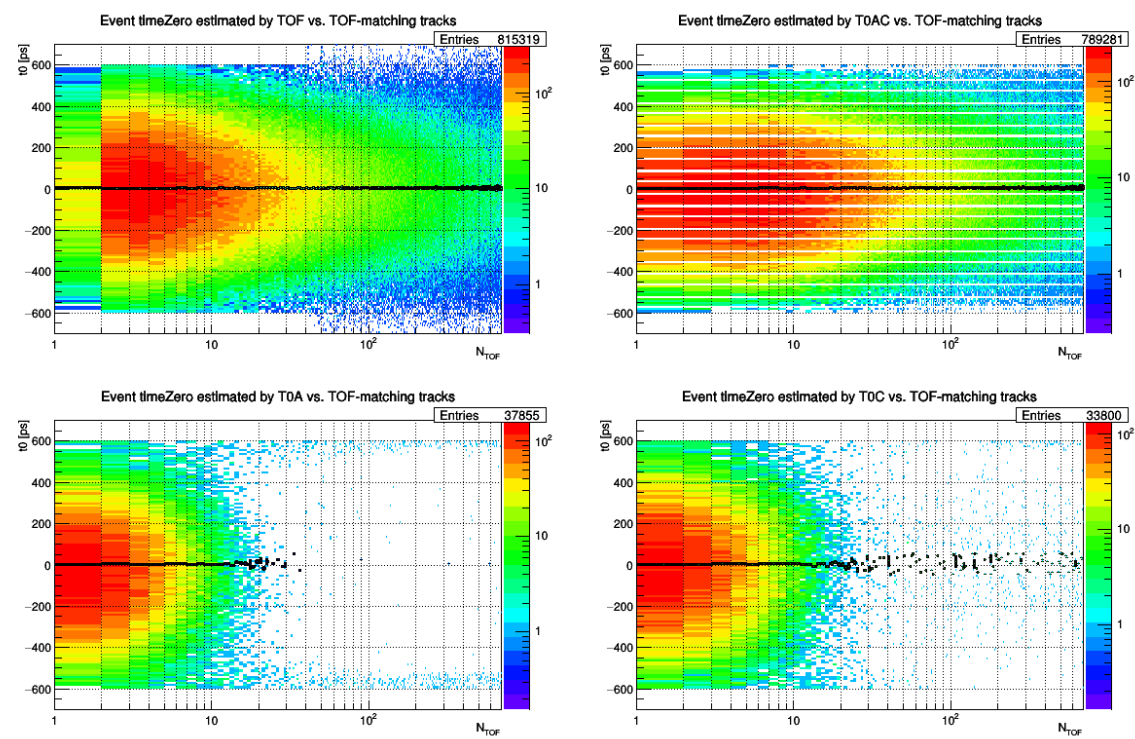


Fig. D.3 TOF resolution

Fig. D.4 t_{ev} vs Multiplicity

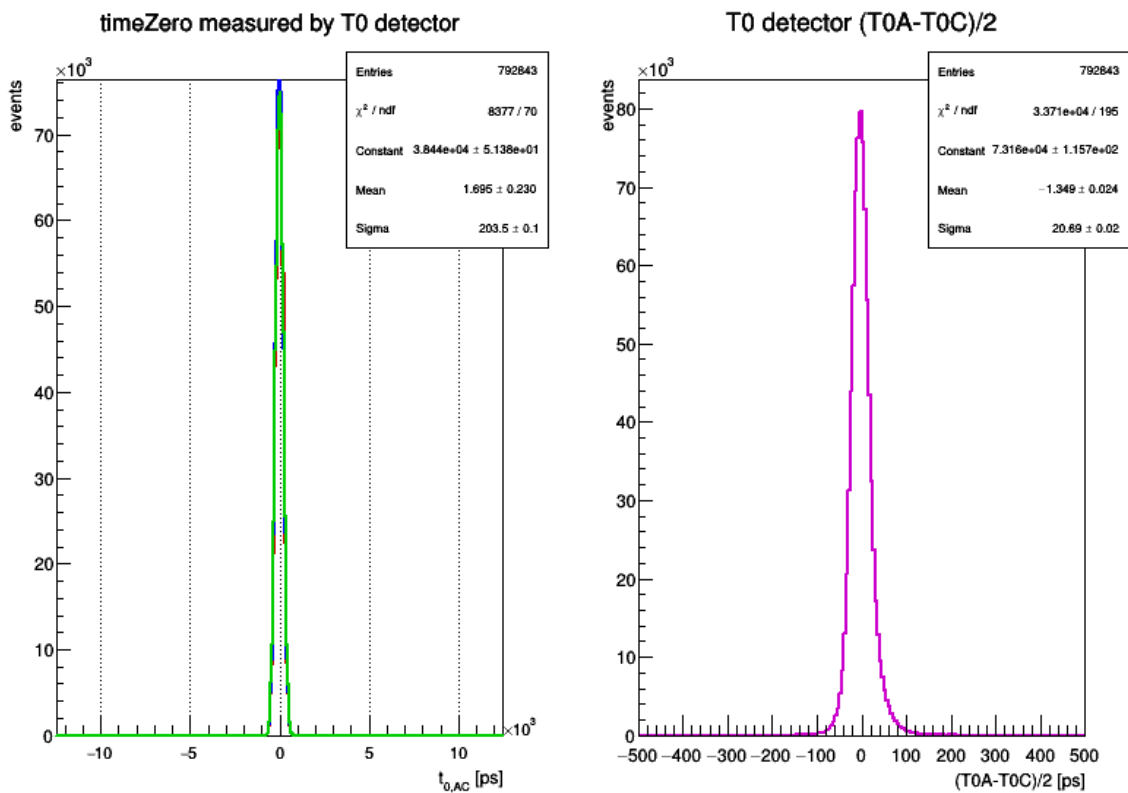


Fig. D.5 T0 Detector

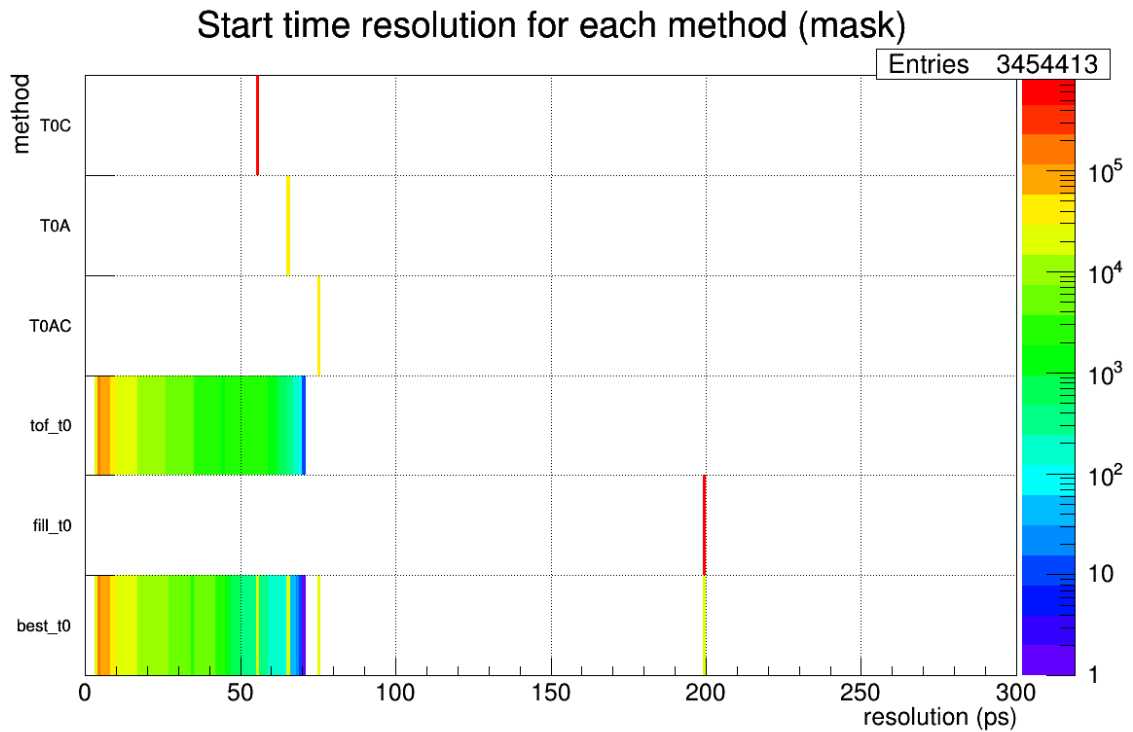


Fig. D.6 Start Time Resolution

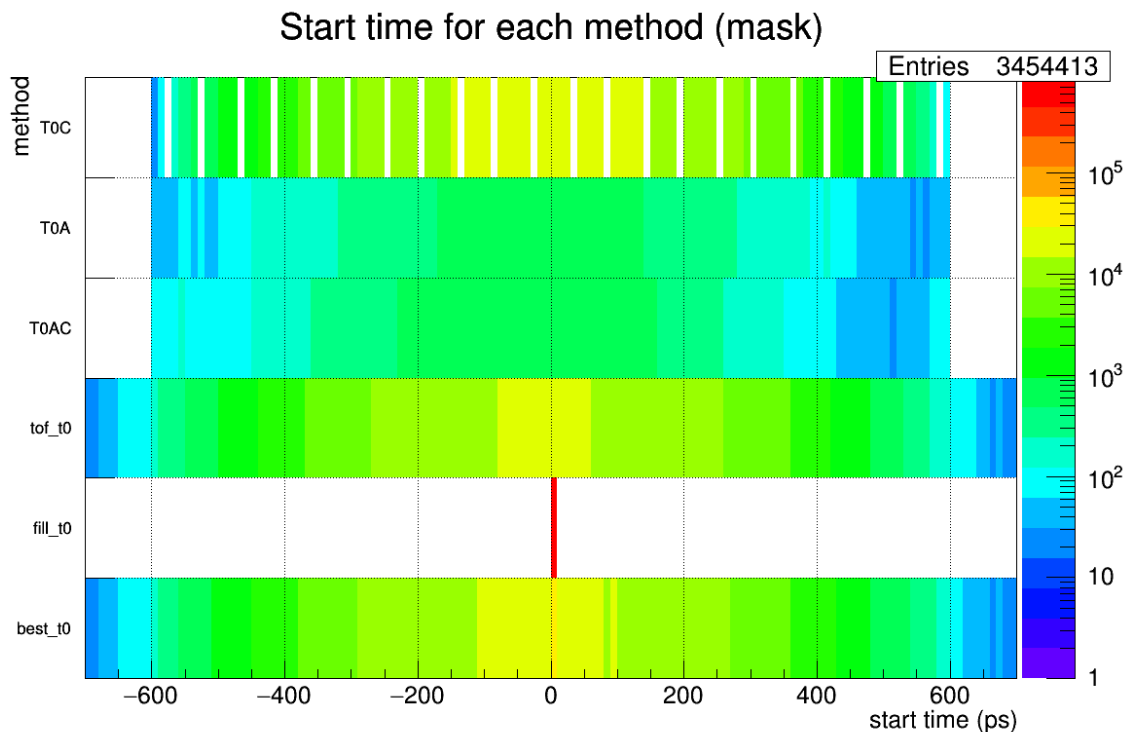


Fig. D.7 Start Time Methods

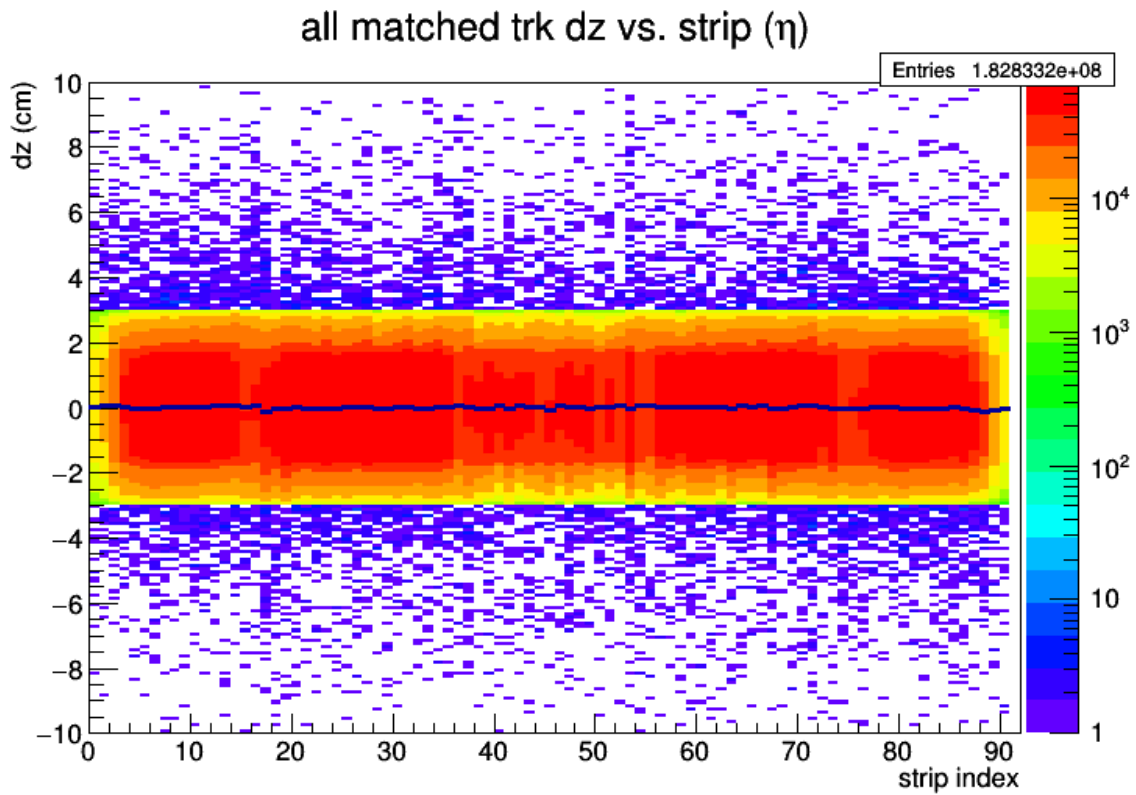


Fig. D.8 Profile DZ vs Strip Number

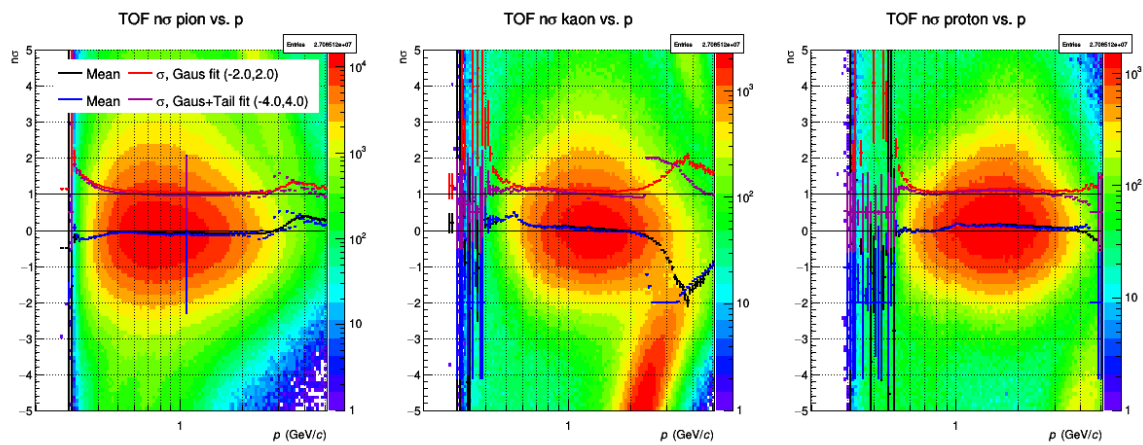


Fig. D.9 PID sigmas Start Time

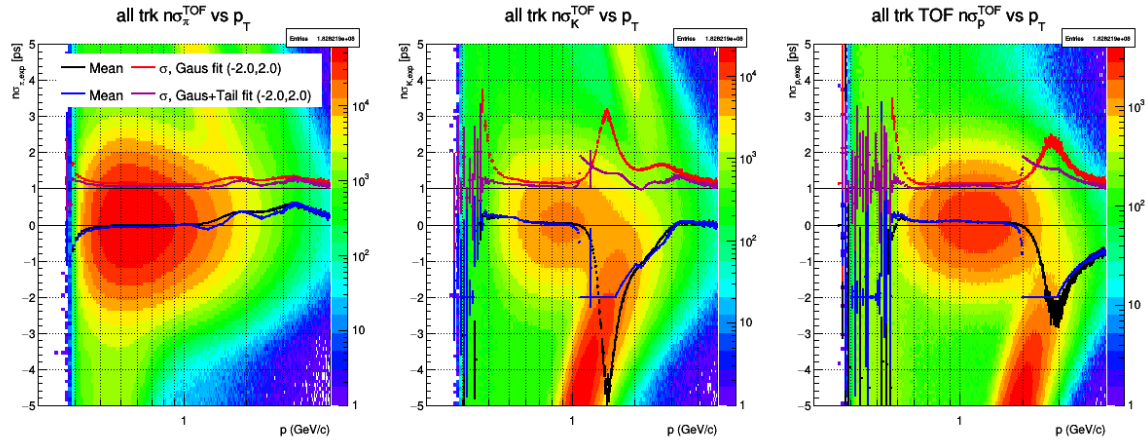


Fig. D.10 PID sigmas

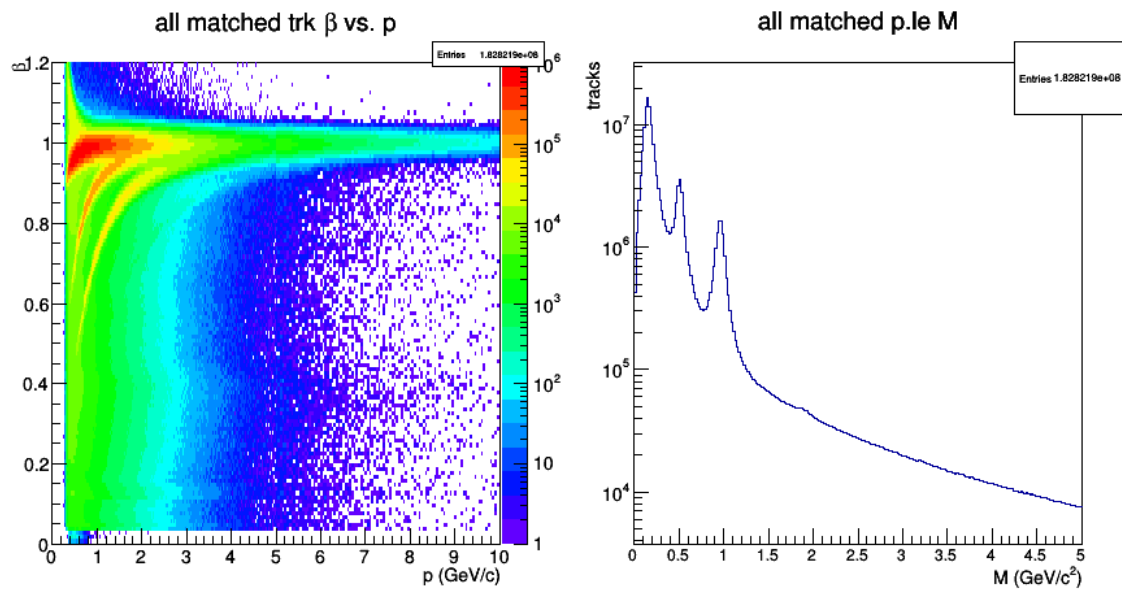


Fig. D.11 PID

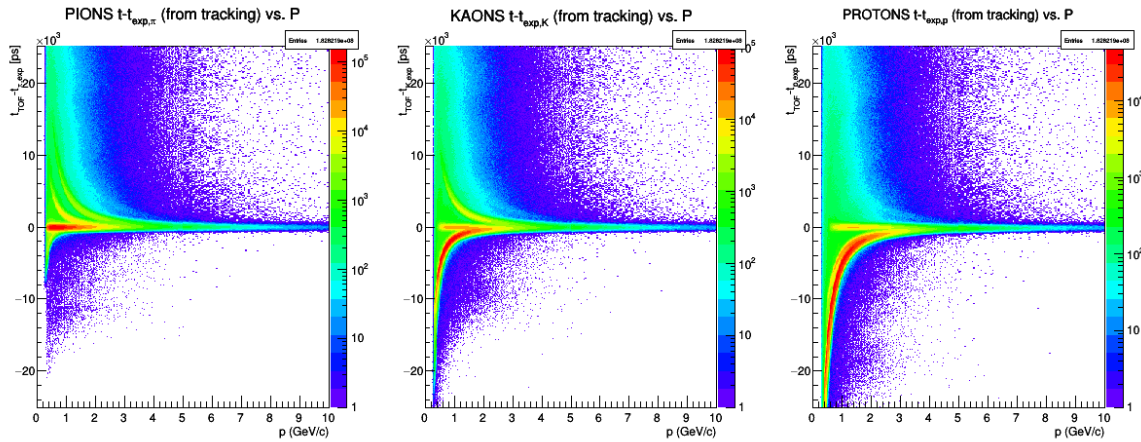


Fig. D.12 PID Expected Times

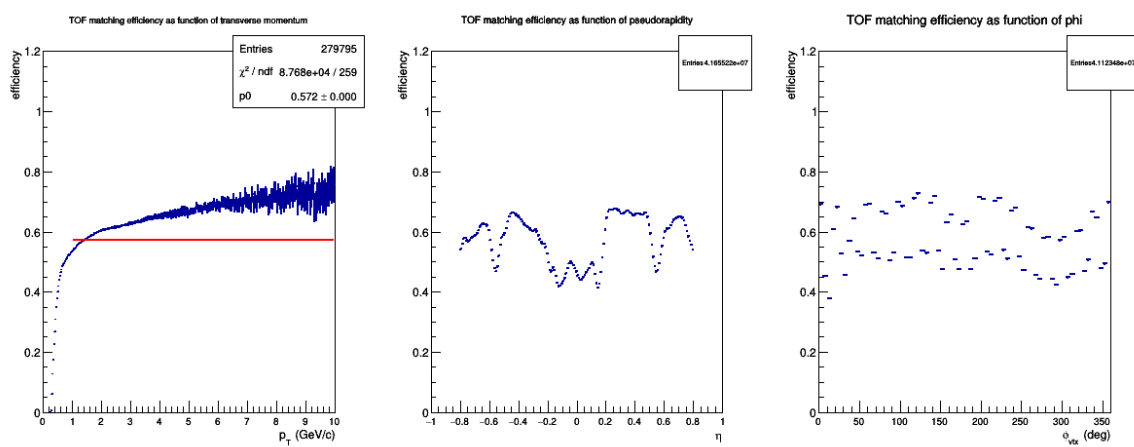


Fig. D.13 Matching Efficiency

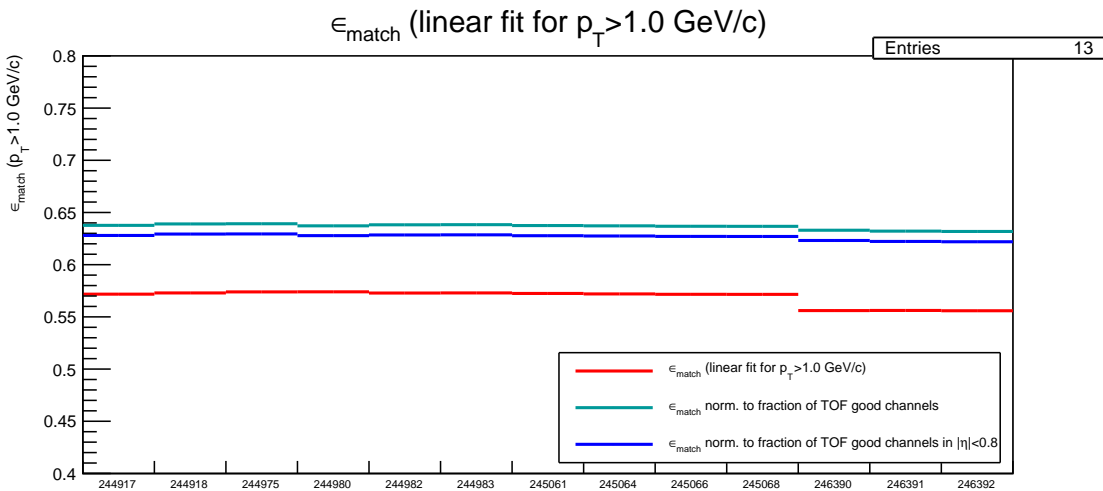


Fig. D.14 Matching Efficiency Summary

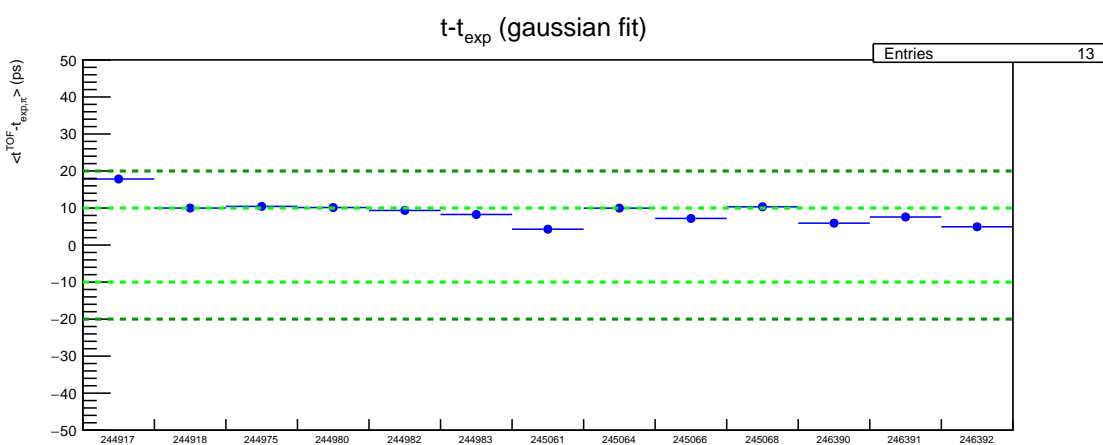


Fig. D.15 Peak Difference Time Vs Run

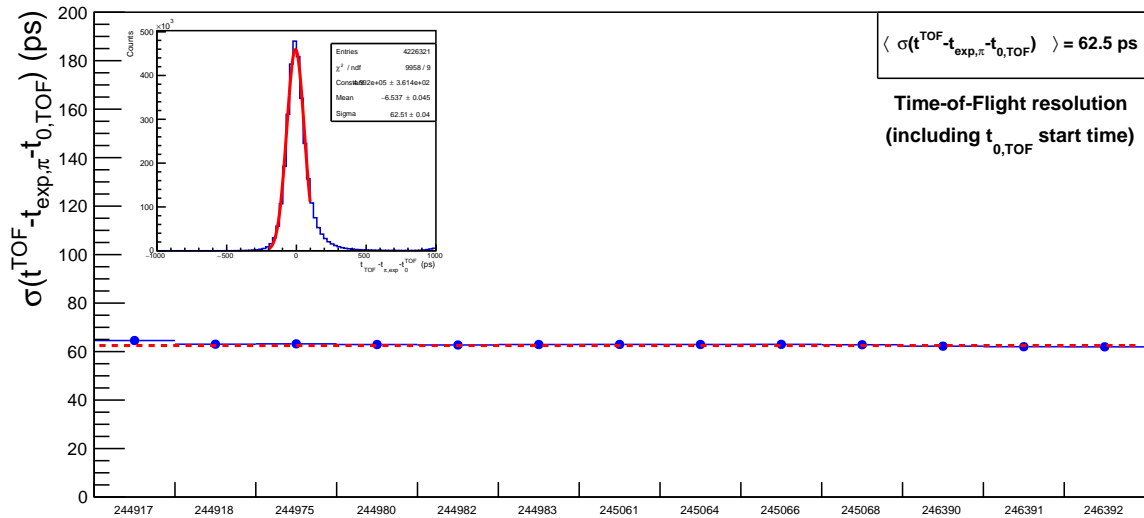


Fig. D.16 Resolution

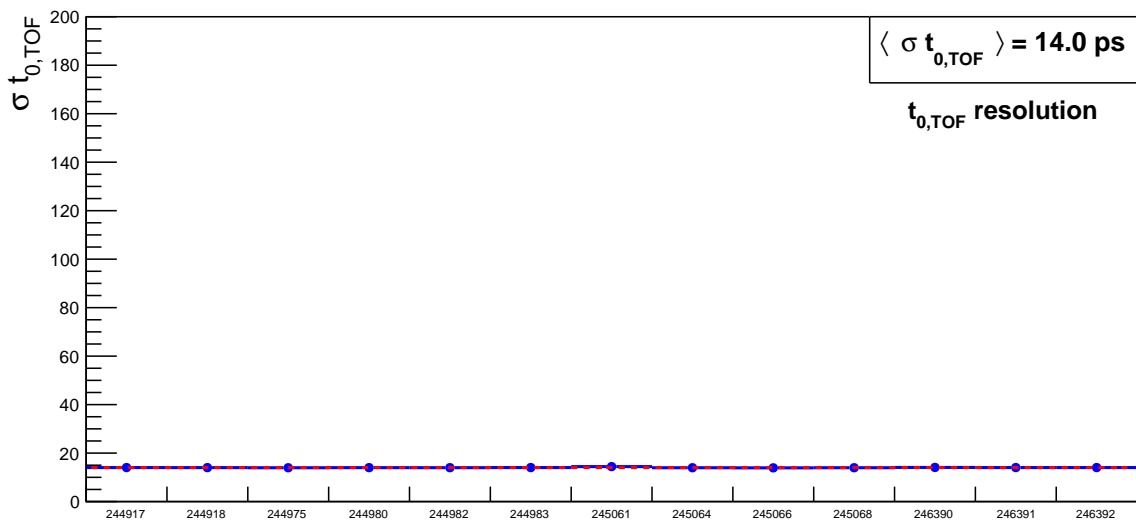


Fig. D.17 Resolution

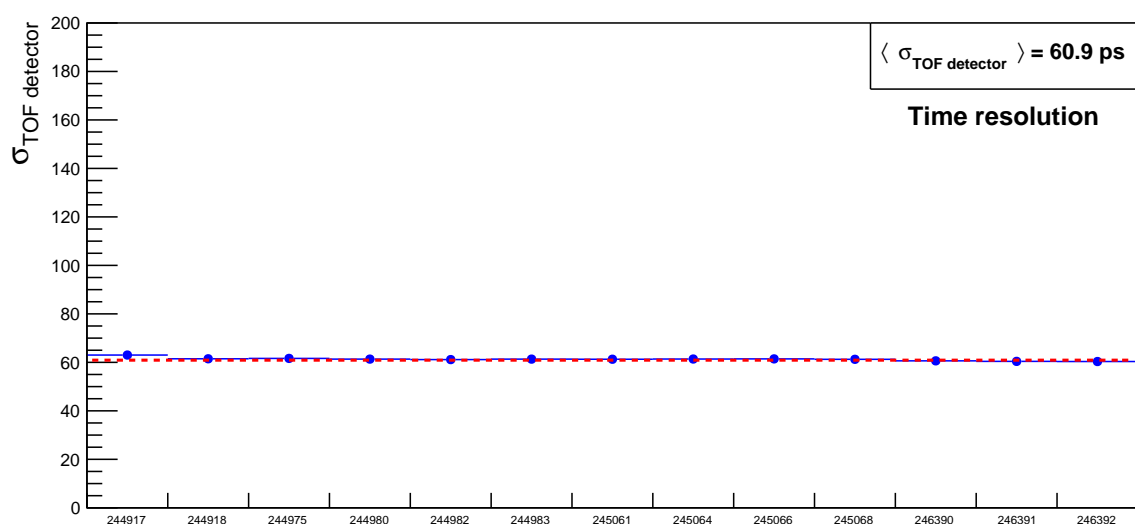


Fig. D.18 Resolution

Appendix E

Efficiency in pp collisions at $\sqrt{s} = 5.02 \text{ TeV}$

In this appendix are reported the efficiencies of π , K and p as measured in pp collisions at $\sqrt{s} = 5.02 \text{ TeV}$ and defined in Section 6.3.

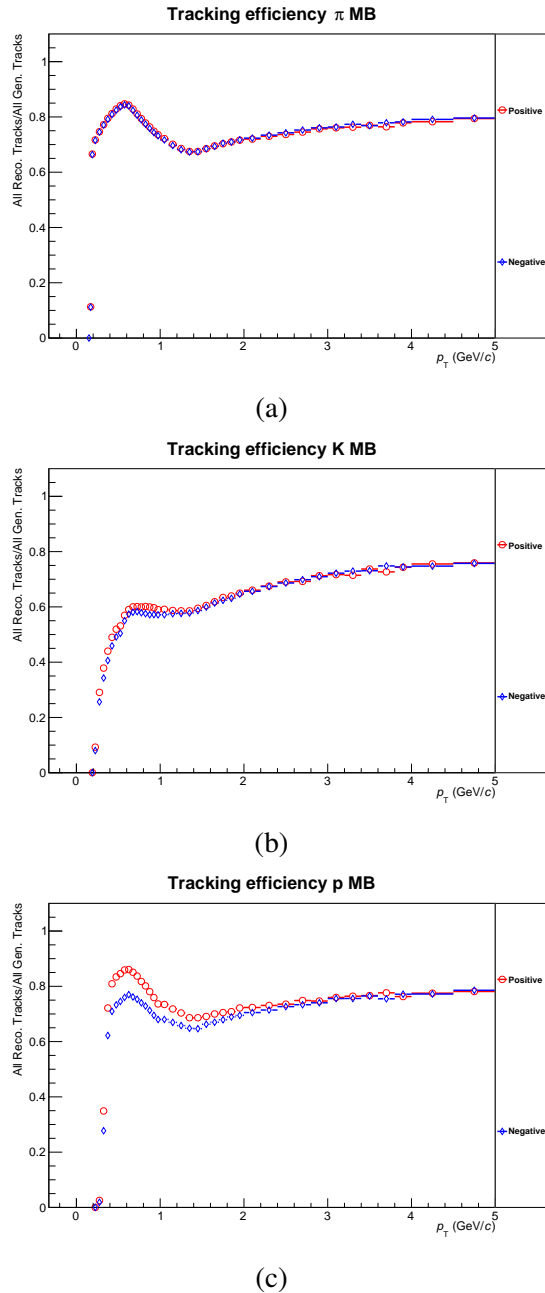


Fig. E.1 Tracking efficiency as measured in pp collisions at $\sqrt{s_{NN}} = 5.02$ TeV for identified π^\pm, K^\pm, p and \bar{p} as a function of p_T .

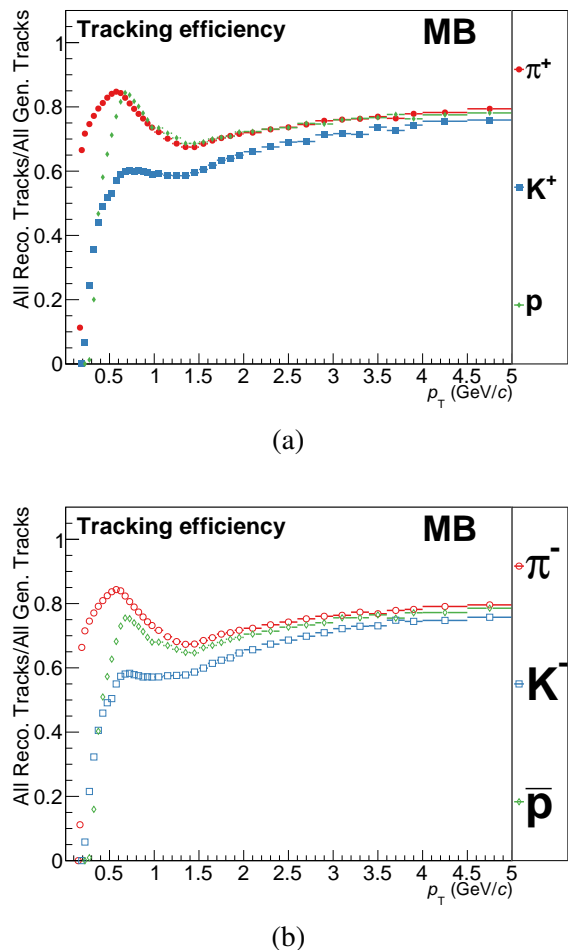


Fig. E.2 Tracking efficiency as measured in pp collisions at $\sqrt{s_{\text{NN}}} = 5.02 \text{ TeV}$ for identified π^\pm, K^\pm, p and \bar{p} as a function of p_T , comparison among different particle species of the same charge.

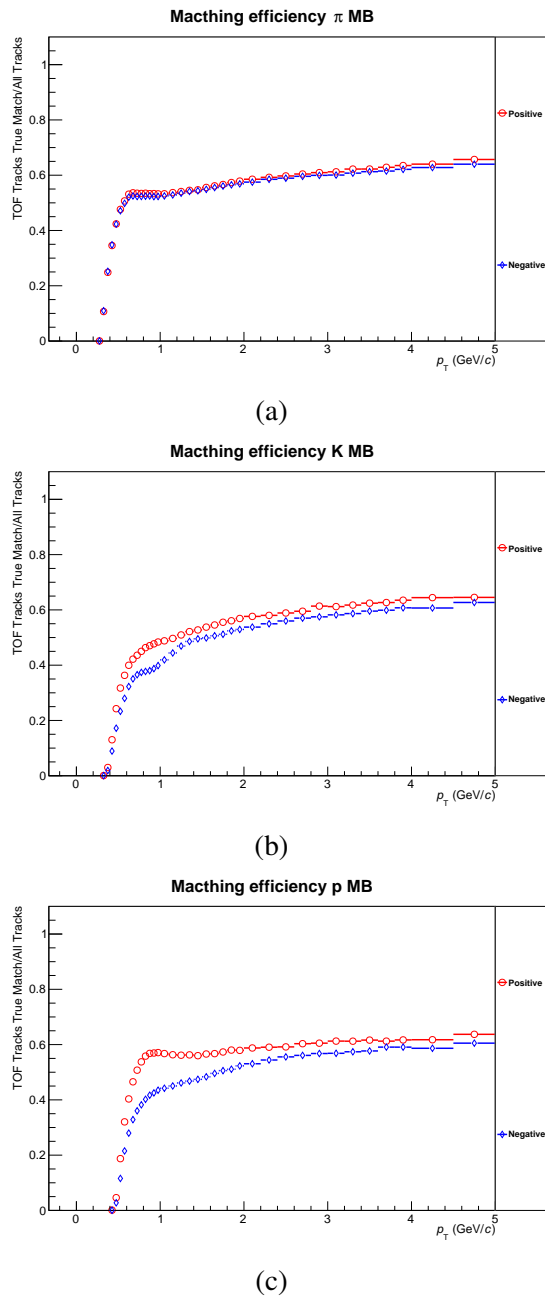


Fig. E.3 Matching efficiency as measured in pp collisions at $\sqrt{s_{\text{NN}}} = 5.02$ TeV for identified π^\pm, K^\pm, p and \bar{p} as a function of p_T .

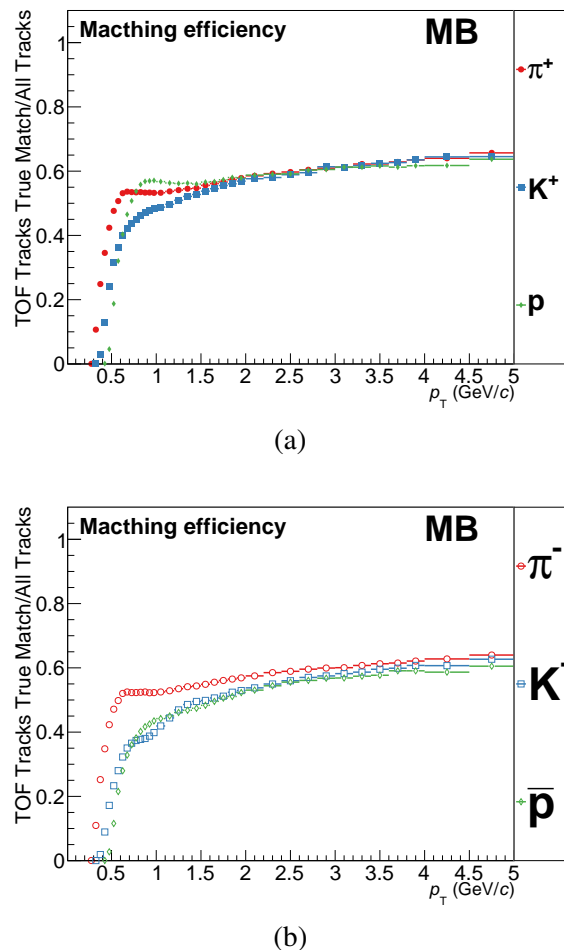


Fig. E.4 Matching efficiency as measured in pp collisions at $\sqrt{s_{\text{NN}}} = 5.02 \text{ TeV}$ for identified π^\pm, K^\pm, p and \bar{p} as a function of p_T , comparison among different particle species of the same charge.

Appendix F

Cut variation in pp collisions

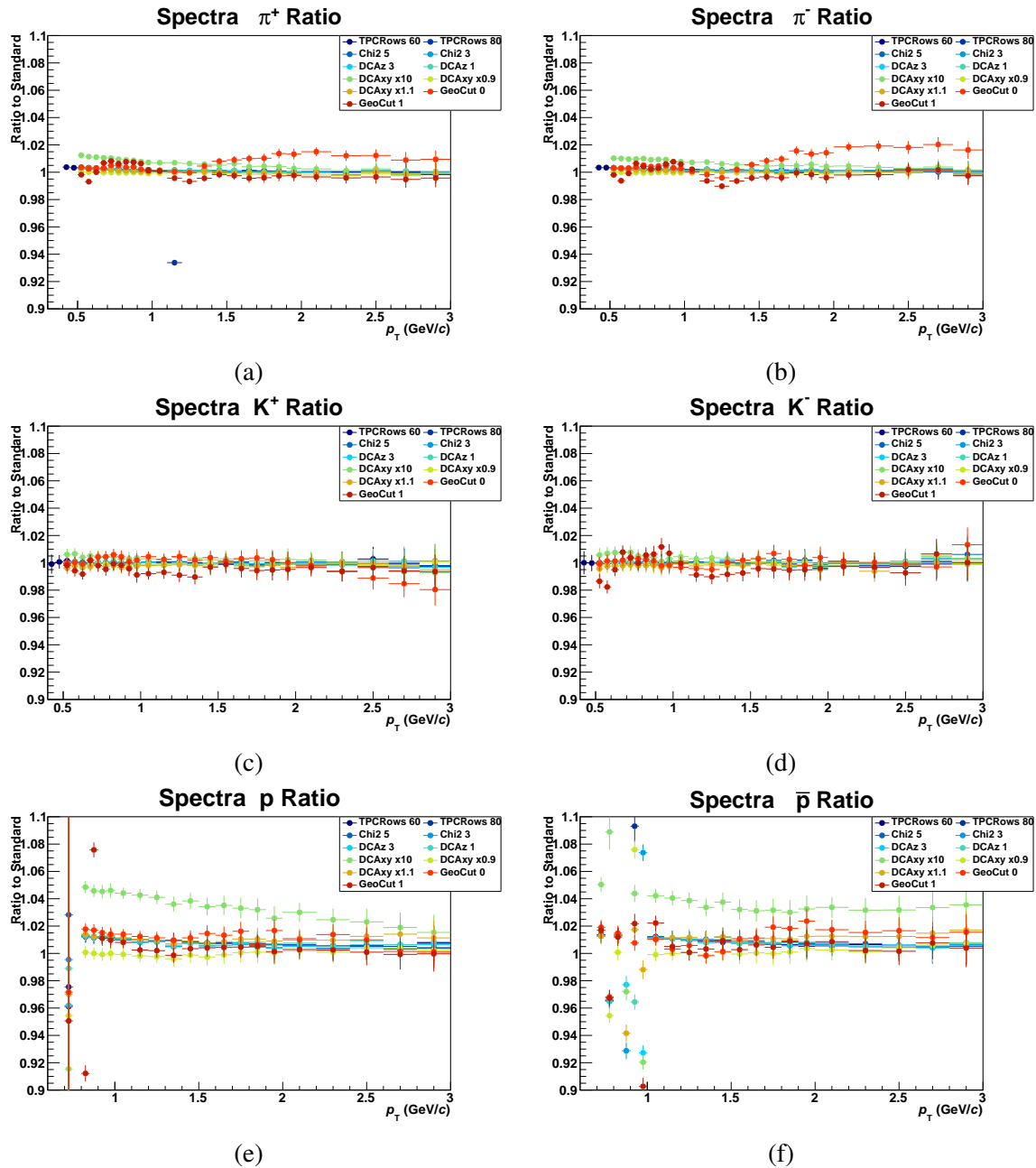


Fig. F.1 Ratio between the spectra obtained with modified track cuts (as in Table 6.2) and the standard one for MB pp collisions.

Appendix G

PID variation in pp collisions

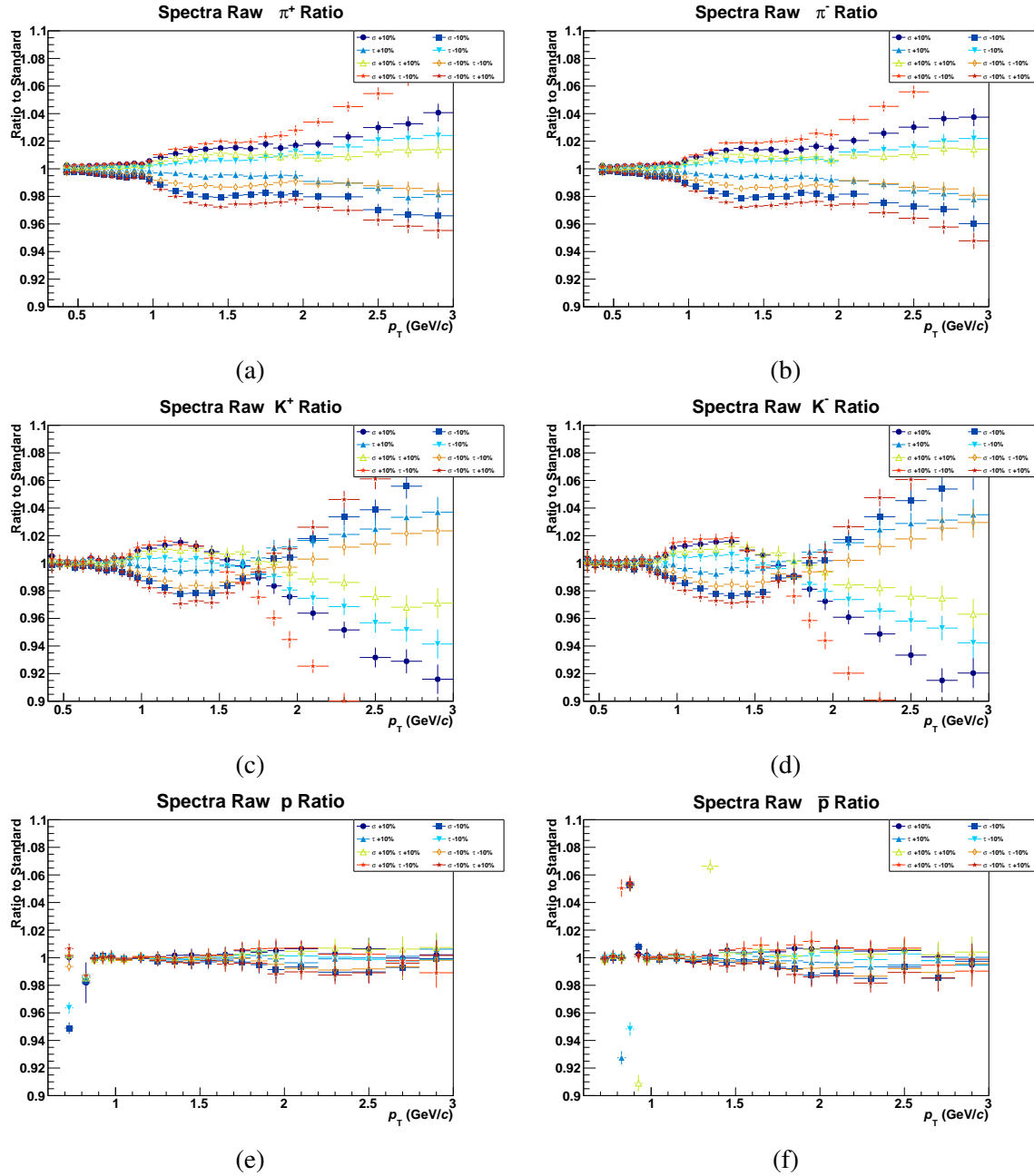


Fig. G.1 Ratio between the spectra obtained with modified TOF signal parameters and the standard one for MB pp collisions.

Appendix H

Systematic uncertainties in pp

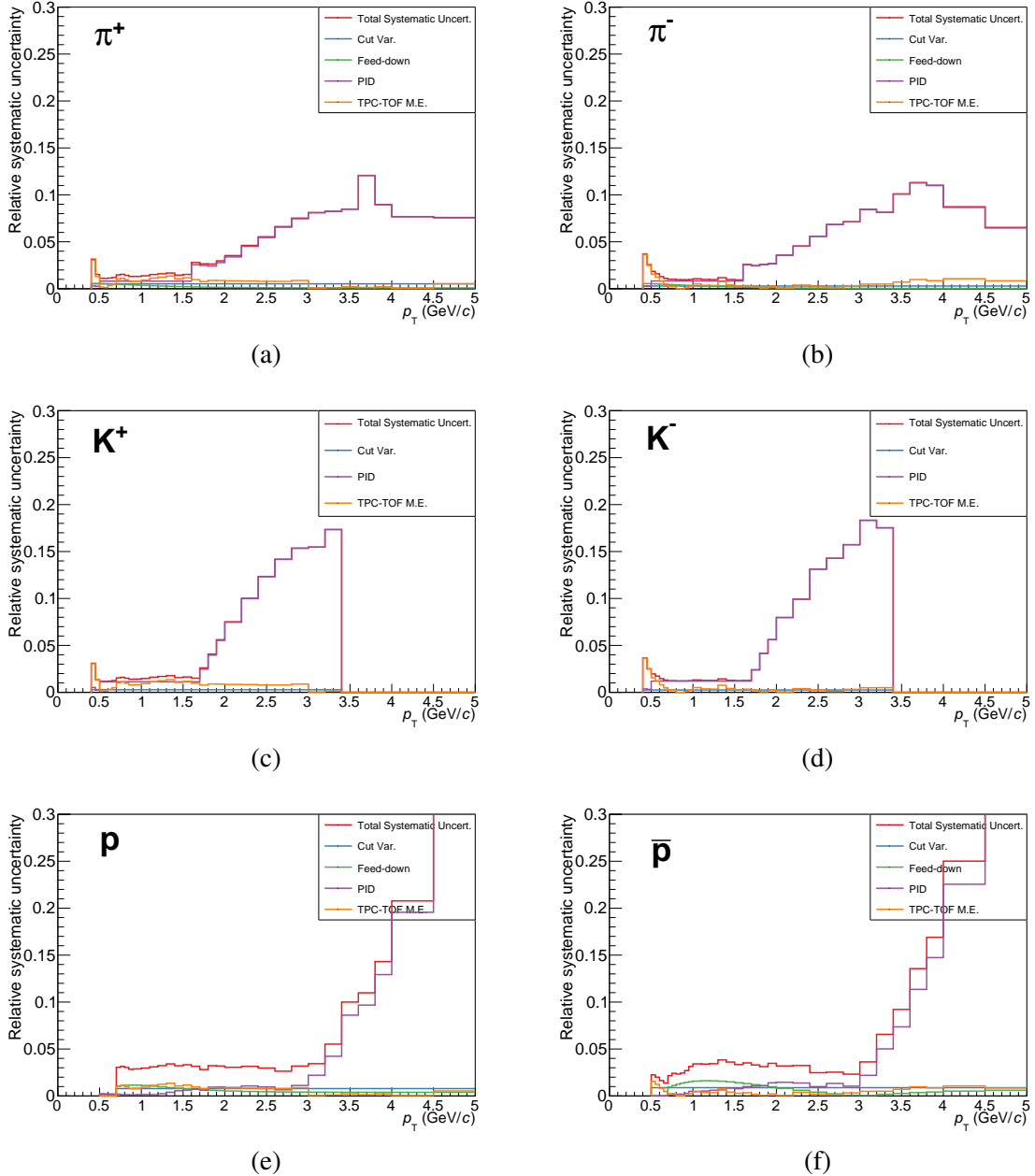


Fig. H.1 Systematic uncertainty on the particle spectra as measured in pp collisions at $\sqrt{s} = 5.02$ TeV.